ADVANCES IN TERRESTRIAL PALEOECOLOGY FROM INTRATOOTH STABLE ISOTOPE PROFILES IN TOOTH ENAMEL AND TUSK DENTIN

by

Kevin Toshio Uno

A dissertation submitted to the faculty of
The University of Utah
in partial fulfillment of the requirements for the degree of

Doctor of Philosophy

in

Geology

Department of Geology and Geophysics

The University of Utah

December 2012

The University of Utah Graduate School

STATEMENT OF DISSERTATION APPROVAL

The dissertation of **Kevin Toshio Uno**

has been approved by the following supervisory committee members:

Thure E. Cerling	, Chair	**October 3, 2012** Date Approved
Francis H. Brown	, Member	**October 3, 2012** Date Approved
David S. Chapman	, Member	**October 5, 2012** Date Approved
James R. Ehleringer	, Member	**October 3, 2012** Date Approved
Daniel C. Fisher	, Member	Date Approved

and by **D. Kip Solomon**, Chair of the Department of **Geology and Geophysics**

and by Charles A. Wight, Dean of The Graduate School.

ABSTRACT

Stable carbon and oxygen isotope analysis of tooth enamel is one of the primary tools available for studying terrestrial mammals and ecosystems in the geologic past. Carbon isotope ratios record the proportion of C_3 versus C_4 vegetation in diet, and by extension, landscape vegetation. Oxygen isotope ratios are related to the isotope ratio of meteoric water and animal physiology and feeding ecology. The carbon isotope ratio in fossil enamel from 9.9 to 3 Ma was measured in ~450 teeth representing nine herbivore lineages to study dietary and vegetation change during this interval in East Africa. Results indicate that differential rates of diet change from C_3-dominated to mixed C_3-C_4 and C_4-dominated diets between different lineages began as early as 9.9 Ma.

The carbon-14 (^{14}C) concentration in metabolically inert tissues formed since *ca.* 1955 can be used to determine the date the tissue formed, or tissue growth rate if multiple samples are taken along the tissue growth axis. This method has applications to stable isotope (paleo)ecology and wildlife forensics. ^{14}C-derived growth rates in enamel and tusk dentin elucidate the time represented in periodic growth increments and provide insight into enamel maturation.

Changes in the isotope ratios of diet and body water, driven by seasonal variability in vegetation and climate (e.g., precipitation), cause variation in isotope ratios along the growth axis of elephant molars and tusks. Isotopic variation in tusk dentin and

tail hair profiles of an extant African elephant are compared. Both profiles serve as a proxy for seasonal changes in vegetation and precipitation. Diagenesis leads to overprinting of the primary isotopic signal in fossil tusks, but not in fossil enamel. However, the process of enamel formation blurs the primary input signal. Combined forward and inverse modeling of intratooth isotope profiles in enamel can be used to reconstruct seasonal variability in diet, vegetation, and climate once appropriate model parameters are established. These parameters are determined for elephant and mammoth molars using ^{14}C data, micro-CT, and histological methods. Application of the models to profiles from fossil proboscidean molar plates provides a means for studying seasonality in ancient ecosystems.

TABLE OF CONTENTS

LIST OF TABLES

Table

ACKNOWLEDGMENTS

The research I present in this dissertation was completed through collaboration with many other scientists under the guidance of an excellent supervisory committee. Foremost, I thank Thure Cerling, who served as a wonderful mentor and advisor throughout my masters and doctoral studies. I also thank the other members of my doctoral committee, Frank Brown, David Chapman, Jim Ehleringer, and Dan Fisher. In particular, I thank Dan Fisher for sharing his ideas and unparalleled knowledge about the histological, morphological, and isotopic information contained within proboscidean tusks and molars.

My training as a scientist has included work in the laboratory, out in the field, and in museums. I wish to acknowledge Thure Cerling, Craig Cook, Brad Erkkila, Diego Fernandez, Naomi Levin, Ben Passey, Jay Quade, Alan Rigby, Adam Rountrey, and Kip Solomon, all of whom helped train me in the lab. I thank Dan Davis and Blake Hethmon for assistance in the lab preparing samples for isotope analysis. I thank Frank Brown, Thure Cerling, Scott Hynek, Naomi Levin, and Tetsuya Sakai for training me in the field. I also wish to acknowledge colleagues from the National Museums of Kenya (KNM) and from Japan who helped train me in vertebrate paleontology. From the KNM, I thank Kyalo Manthi, Mary Muungu, Francis Kirera, and Emma Mbua. Japanese colleagues Masato Nakatsukasa, Yutaka Kunimatsu, and Hideo Nakaya supported my work on the

late Miocene fossils from the Samburu Hills and Nakali. I also thank John M. Harris and Meave Leakey for assistance in fossil identification of the Lothagam material.

My education has been marked by opportunities presented to me by many of those mentioned above, but none of these would have been seized upon without the lifelong support I've received from my parents, Toshio and Roberta Uno. I thank them for their sacrifices and hard work that allowed me to pursue an education in the earth sciences. Finally, I thank my wife Claire Uno for her unwavering support. During graduate school, I have been primarily focused on becoming a better scientist. Claire's intelligence, kindness, and selflessness have been a constant reminder that being a good scientist begins with being a good person who possesses these qualities. She's also a great copy editor who never seems to tire of reading about isotopes.

CHAPTER 1

INTRODUCTION

Since the late Miocene, terrestrial ecosystems in East Africa have experienced dramatic changes driven primarily by interactions between tectonics and climate at global and regional scales (Cane and Molnar, 2001; deMenocal, 1995; Haug and Tiedemann, 1998; Sepulchre et al., 2006; Trauth et al., 2005). Broadly speaking, the defining characteristic of ecological change in the region has been increased climate variability, superimposed over a long-term trend towards aridification that led to the expansion of open habitats in the Plio-Pleistocene. Isotopic evidence from the Omo-Turkana and Awash Basins indicates that C_4 grasses have been the dominant herbaceous cover in these open habitats since the latest Miocene and early Pliocene (Cerling et al., 2003a; Levin et al., 2011). Changes in the vegetation and landscape through time were accompanied by changes in fauna, with large-bodied grazers becoming more common from approximately 5 to 6 Ma onward. Within this interval of long-term ecological change towards more heterogeneous and open landscapes lies the origin and evolution of many mammalian genera, including our own lineage, *Homo*.

The evolution of any lineage is tightly linked to its ecology and environment. To that end, decades of research on East African paleoenvironments by paleontologists,

anthropologists, palynologists, paleobotanists, geologists, geochronologists, and geochemists have focused not only on elucidating hominin evolution, but also understanding the paleoenvironmental and paleoclimatic context in which human evolution occurred. Marine records and modeling studies have contributed to our general understanding of the timing, paleoclimatic drivers, and effects of increased climate variability and aridification on African climate and vegetation (Cane and Molnar, 2001; deMenocal, 1995; Feakins et al., 2005; Schefuß et al., 2003).

Terrestrial sediments offer additional paleoenvironmental and paleoclimatic proxies such as fossil soils, vertebrates, and plants that provide direct evidence of the ecology at a finer scale than marine records. Furthermore, late Neogene rifting in East Africa has interspersed hundreds of volcanic ashes within the fluvio-lacustrine sediments that can be directly dated isotopically, or more often, geochemically correlated to other dated ashes. Together, the terrestrial proxies and robust age control provide the tools needed to evaluate the role of climatic and ecological change on mammalian evolution. An outstanding question that relates to ecological change is how the timing and frequency of precipitation may have influenced the establishment of savannah and grassland ecosystems in the early Pliocene. This period of ecological change corresponds to an adaptive radiation in suids and grazing bovids, and the initial diversification of hominins in East Africa (Bobe and Behrensmeyer, 2004). To explore the relationship between seasonality of precipitation and the establishment of savannah and grassland ecosystems, environments that are integrally tied to hominin evolution, a proxy for seasonal variability in vegetation or precipitation is needed.

Over the past 30 years or so, stable carbon and oxygen isotope analysis of tooth enamel has emerged as one of the primary geochemical tools for studying fossil and recent terrestrial environments. Carbon isotope ratios in fossil herbivore tooth enamel record the proportion of C_3 versus C_4 vegetation in diet (Lee-Thorp and dan der Merwe, 1987), which because of dietary specialization often does not reflect the actual proportion of C_3 versus C_4 vegetation in the ecosystem. Oxygen isotope ratios reflect body water composition, which to first order is determined by meteoric water, but also is influenced by animal physiology and behavior (Kohn, 1996) as well as aridity (Levin et al., 2006). The technique has been widely used to study mammalian diet and ecology at various time scales in ancient ecosystems (Cerling et al., 1997; Morgan and Kingston, 1994; Quade et al., 1992; Wang et al., 1994), and recent isotopic studies on extant mammalian herbivore clades have revealed dietary and physiological differences that further refine interpretation of isotopic data from their extinct relatives (e.g.,Cerling et al., 1999; Cerling et al., 2003b; Cerling et al., 2008; Harris and Cerling, 2002; Levin et al., 2006). A single sample drilled along the growth axis of a tooth provides a snapshot of herbivore diet and body water over the period in which the tooth formed. Serial sampling along the growth axis of a tooth, referred to here as an intratooth profile, provides a time series of information.

The research compiled in this dissertation is aimed at developing methods to extract high-resolution stable isotope time series from teeth that enable investigation of the magnitude and frequency of seasonal changes in diet and body water and by extension, vegetation and precipitation. Intratooth profiles from tooth enamel and tusk dentin have been used in previous studies to evaluate seasonality of climate (e.g., Fricke

and O'Neil, 1996; Koch et al., 1989) . The isotope time series in enamel is blurred, or attenuated and shifted, due to the protracted nature of enamel formation and the sampling geometry used to collect enamel powder for isotopic analysis. The approach taken to unblurring or recovering the signal is through inverse modeling, which is described in greater detail below. Reaching the modeling step in Chapter 5 requires establishing model parameters that describe enamel maturation. Thus, Chapters 3 and 4 explore enamel growth rates and how isotopic information is recorded in metabolically inert tissues with simpler growth processes such as elephant tail hair and tusk dentin.

Before delving into high-resolution records in molars and tusks, I give an example in Chapter 2 of the utility of carbon isotopes in exploring the evolution of mammalian diets in East Africa over the past 10 to 3 Ma. In this chapter, my colleagues, who include paleoanthropologists Yutaka Kunimatsu, Meave Leakey, and Masato Naktsukasa, paleontologists John M. Harris and Hideo Nakaya, geochemist Thure Cerling, and I utilize the method of taking a single enamel sample from a tooth to reconstruct paleodiet. We build upon earlier studies that document global dietary change in herbivores associated with the late Miocene to Pliocene expansion of C_4 grasslands (Cerling et al., 1997; Latorre et al., 1997; Passey et al., 2002; Quade et al., 1992). An important question that has not been addressed in previous studies is how different herbivore lineages in the same ecosystem adapted to the new menu item, C_4 grasses. What we discovered from analyzing some 450 teeth representing nine herbivore lineages was that the rates of dietary change vary considerably through time. Ancestors of horses, the equids, had diets comprised of up to 65 % C_4 grasses by 9.9 Ma, which represents the oldest evidence of C_4-dominated diets in East Africa. The hippos, rhinos, and bovids also

found their way to the C_4 table early on (~9.6 to 9.3 Ma), while proboscideans (gomphotheres and elephants) did so by ~7.5 Ma and the suids by 6.5 Ma. The fossil enamel data from the two older fossil sites, Nakali (9.9 Ma) and the Samburu Hills (9.6 to 9.3 Ma), are particularly important because there are no soil carbonate data from these sites and there is in general limited isotopic data from this time period (10 to 8 Ma) in East Africa.

In Chapter 3, my colleagues, who include Samuel Andanje, Patrick Omondi, and Moses Litoroh from the Kenya Wildlife Service, George Wittemyer and Sir Iain Douglas-Hamilton of Save the Elephants, paleontologist Dan Fisher, geochemists Thure Cerling and Jay Quade, and I enlist a radioactive isotope, carbon-14 (^{14}C), to determine the ages and growth rates of teeth, tusks, and other biologic tissues. This method has applications to stable isotope ecology and paleoecology and to wildlife forensics. In the study, we take advantage of bomb-curve ^{14}C, an unintended gift to the geochemical community from early Cold War era (1950s to 1963) above-ground thermonuclear weapons testing. The energy released into the atmosphere by the bombs resulted in the production of a suite of radioactive isotopes, including ^{14}C, whose fallout serves as an exceptional tracer in the biosphere. The ^{14}C concentration in the atmosphere (as $^{14}CO_2$) nearly doubled in the northern hemisphere by the time the test ban went into effect in 1963. Since that time, there has been a steady decline in the concentration of atmospheric $^{14}CO_2$ as it has been absorbed into the oceans, taken up by plants for photosynthesis, and diluted by ^{14}C-free fossil fuel CO_2 emissions (Hua and Barbetti, 2004; Levin and Hesshaimer, 2006). The uptake of ^{14}C by a plant means that its tissue ^{14}C concentration reflects that of the atmosphere at the time the tissue formed. This is

also true for herbivores that eat plants (and presumably the carnivores that eat the herbivores). We show that the concentration of ^{14}C in metabolically inert herbivore tissues such as hair, horns, and teeth, record the date when the tissue formed simply by matching it to the atmospheric concentration of ^{14}C along the bomb-curve. Furthermore, serial sampling ($n \geq 2$) teeth, tusks, and horn along their growth axes enables us to determine tissue growth rates.

The ^{14}C study was initiated to understand growth rates of elephant molars and tusks, but other applications of the method are born from this study. The most socially relevant is the use of this method to combat the illegal trade in elephant ivory. Recent escalation of elephant poaching for ivory, driven mostly by demand in China, seriously threatens populations across Africa, Asia, and the Indian subcontinent. Often, smugglers or dealers of ivory attempt to forge documentation to mask illegal ivory as "antique", which under the Convention of International Trade in Endangered Species (CITES) laws for African elephant ivory in the US means it is older than 1947. The ^{14}C method for dating ivory can be used to determine the true age of the ivory back to ~1953. If confiscated ivory contains any bomb-derived ^{14}C, it must be younger than 1953 and therefore is illegal.

In Chapter 4, intratooth isotope profiles in elephant tusk dentin reveal details of dietary variability that previously were undocumented in tusks at an approximately weekly resolution. My colleagues, who include Dan Fisher, Thure Cerling, George Wittemyer, Sir Ian Douglas-Hamilton, and I are presented with a unique opportunity in which we are able to "ground truth" multiyear carbon and oxygen isotope tusk dentin profiles with coeval rainfall, remote sensing vegetation (NDVI), and GPS data. We also

use measured coeval isotope profiles in tail hair from the same elephant, R37, who, until her death in 2006, was matriarch of the Swahili family that lives in and around the Samburu, Buffalo Springs, and Shaba National Reserves in Kenya. Comparison of weekly sampled tail hair and ivory illustrates the striking similarity in the isotope profiles. It also suggests that physiological mechanisms, possibly related to turnover of carbon and oxygen in the blood bicarbonate pool or to maturation of dentin, may lead to some attenuation of the isotope signal in tusk dentin. The carbon isotope profiles from the tusk track seasonal diet change associated with the biannual rains in Kenya and also serve as a proxy for the seasonal precipitation. Results show that high-resolution tusk profiles have great potential for studies of unfossilized dentin; in most fossilized dentin, diagenesis overprints the primary isotopic input signal from diet or body water, precluding application of this method to fossil tusk dentin. However, results from this chapter still make a significant contribution to the overarching goal of extracting seasonal records from fossil molar enamel. This is because we also have one of R37's molars, for which the R37 tusk profiles serve as a proxy for the primary input signal that is being sought from an intratooth profile in the R37 molar enamel.

In Chapter 5, we introduce an elephant named Misha, whose teeth and tusks were made available to my colleagues and I after her death at Utah's Hogle Zoo in Salt Lake City, UT. Misha was translocated from the Bay Area in California to Salt Lake City in April 2005, which imparted a near-instantaneous isotopic shift recorded in her molars and tusks. In this chapter, my colleagues, who include those from Chapter 4 plus Hogle Zoo veterinarian Nancy Carpenter, and I evaluate coeval molar and tusk profiles in elephants. We use forward and inverse models, written by former Cerling Lab member Ben Passey,

that mathematically describe tooth enamel formation. The modeling component allows reconstruction of the estimated primary (carbon or oxygen) input signal in molars, which gives the best estimate for the frequency and magnitude of environmental seasonality. The model requires measurement of enamel maturation parameters. Density profiles in developing elephant molar plates generated by micro-computed tomography (Micro-CT) provide two of three parameters and thin sections and measurement on the surface of molar plates provide the third. Maturation parameters are determined where possible or estimated for elephant and mammoth molars. The tusk profiles from R37 and Misha serve as proxies for the primary input signals to which the inverse modeled results from their molar profiles are compared. The original models were developed for continuously growing teeth and assume a constant growth rate, which has not been verified in proboscidean molar plates. Thus, Chapter 5 also addresses growth rates of elephant and mammoth molar plates using histological methods.

We obtain inversion results from four proboscidean molar profiles, including two fossil mammoth molar plates. Results from the Misha profile indicate that the model performs well in recovering the overall structure and amplitude of the primary input signal, but that instantaneous diet switches from predominantly C_3 to C_4 diets are still somewhat blurred. Although an instantaneous diet shift of this magnitude (~8 ‰) is unlikely to occur in a natural ecosystem, it illustrates model limitations.

Unblurring an enamel isotope profile through inverse modeling yields the estimated primary input signal required to evaluate seasonal environmental variability in ancient environments. Inverse methods are necessary because the blurring induced by enamel maturation can impart quasi-sinusoidal profiles from nonsinusoidal inputs, which

can lead to incorrect interpretations of seasonality (Passey and Cerling, 2004; Zazzo et al., 2005). The research in Chapter 5 establishes inverse modeling of isotope profiles in molar plates belonging to the *Loxodonta*, *Elephas*, and *Mammthus* clades of proboscideans as a means for evaluating seasonal variation in climate and vegetation of past environments.

1.1 References

Bobe, R., and Behrensmeyer, A. K., 2004, The expansion of grassland ecosystems in Africa in relation to mammalian evolution and the origin of the genus Homo: Palaeogeography, Palaeoclimatology, Palaeoecology, v. 207, no. 3-4, p. 399-420.

Cane, M. A., and Molnar, P., 2001, Closing of the Indonesian seaway as a precursor to east African aridification around 3–4 million years ago: Nature, v. 411, no. 6834, p. 157-162.

Cerling, T., Harris, J., and Leakey, M., 1999, Browsing and grazing in elephants: The isotope record of modern and fossil proboscideans: Oecologia, v. 120, no. 3, p. 364-374.

-, 2003a, Isotope paleoecology of the Nawata and Nachukui Formations at Lothagam, Turkana Basin, Kenya, *in* Leakey, M. G., and Harris, J. M., eds., Lothagam: The Dawn of Humanity in Eastern Africa: New York, Columbia University Press, p. 605-623.

Cerling, T., Harris, J., and Passey, B., 2003b, Diets of East African Bovidae based on stable isotope analysis: Journal Information, v. 84, no. 2, p. 456-470.

Cerling, T. E., Harris, J. M., Hart, J. A., Kaleme, P., Klingel, H., Leakey, M. G., Levin, N. E., Lewison, R. L., and Passey, B. H., 2008, Stable isotope ecology of the common hippopotamus: Journal of Zoology, v. 276, no. 2, p. 204-212.

Cerling, T. E., Harris, J. M., MacFadden, B. J., Leakey, M. G., Quade, J., Eisenmann, V., and Ehleringer, J. R., 1997, Global vegetation change through the Miocene/Pliocene boundary: Nature, v. 389, no. 6647, p. 153-158.

deMenocal, P. B., 1995, Plio-Pleistocene African Climate: Science, v. 270, no. 5233, p. 53-59.

Feakins, S. J., deMenocal, P. B., and Eglinton, T. I., 2005, Biomarker records of late Neogene changes in northeast African vegetation: Geology, v. 33, no. 12, p. 977-980.

Feakins, S. J., deMenocal, P. B., and Eglinton, T. I., 2005, Biomarker records of late Neogene changes in northeast African vegetation: Geology, v. 33, no. 12, p. 977-980.

Fricke, H. C., and O'Neil, J. R., 1996, Inter-and intra-tooth variation in the oxygen isotope composition of mammalian tooth enamel phosphate: Implications for palaeoclimatological and palaeobiological research: Palaeogeography, Palaeoclimatology, Palaeoecology, v. 126, no. 1, p. 91-99.

Harris, J., and Cerling, T., 2002, Dietary adaptations of extant and Neogene African suids: Journal of Zoology, v. 256, no. 1, p. 45-54.

Haug, G. H., and Tiedemann, R., 1998, Effect of the formation of the Isthmus of Panama on Atlantic Ocean thermohaline circulation: Nature, v. 393, p. 673-676.

Hua, Q., and Barbetti, M., 2004, Review of tropospheric bomb ^{14}C data for carbon cycle modeling and age calibration purposes: Radiocarbon, v. 46, no. 3, p. 1273-1298.

Koch, P. L., Fisher, D. C., and Dettman, D., 1989, Oxygen isotope variation in the tusks of extinct proboscideans: A measure of season of death and seasonality: Geology, v. 17, no. 6, p. 515-519.

Kohn, M. J., 1996, Predicting animal $d^{18}O$: Accounting for diet and physiological adaptation: Geochimica et Cosmochimica Acta, v. 60, no. 23, p. 4811-4829.

Latorre, C., Quade, J., and McIntosh, W. C., 1997, The expansion of C4 grasses and global change in the late Miocene: Stable isotope evidence from the Americas: Earth and Planetary Science Letters, v. 146, no. 1-2, p. 83-96.

Lee-Thorp, J. A., and dan der Merwe, N. J., 1987, Carbon isotope analysis of fossil bone apatite: South African Journal of Science, v. 83, no. 11, p. 712-715.

Levin, I., and Hesshaimer, V., 2006, Radiocarbon; a unique tracer of global carbon cycle dynamics: Radiocarbon, v. 42, no. 1, p. 69-80.

Levin, N. E., Brown, F. H., Behrensmeyer, A. K., Bobe, R., and Cerling, T. E., 2011, Paleosol carbonates from the Omo Group: Isotopic records of local and regional environmental change in East Africa: Palaeogeography, Palaeoclimatology, Palaeoecology, v. 307, no. 1-4, p. 75-89.

Levin, N. E., Cerling, T. E., Passey, B. H., Harris, J. M., and Ehleringer, J. R., 2006, A stable isotope aridity index for terrestrial environments: Proceedings of the National Academy of Sciences of the United States of America, v. 93, no. 30, p. 11201-11205.

Morgan, M., and Kingston, J., 1994, Carbon isotopie evidence for the emergence of C4 plants in the Neogene from Pakistan and Kenya: Nature, v. 367, p. 162-165.

Passey, B. H., and Cerling, T. E., 2004, Response to the comment by MJ Kohn on "Tooth enamel mineralization in ungulates: Implications for recovering a primary isotopic time-series" by BH Passey and TE Cerling (2002): Geochimica et Cosmochimica Acta, v. 68, no. 2, p. 407-410.

Passey, B. H., Cerling, T. E., Perkins, M. E., Voorhies, M. R., Harris, J. M., and Tucker, S. T., 2002, Environmental change in the Great Plains; an isotopic record from fossil horses: Journal of Geology, v. 110, no. 2, p. 123-140.

Quade, J., Cerling, T. E., Barry, J. C., Morgan, M. E., Pilbeam, D. R., Chivas, A. R., Lee-Thorp, J. A., and van der Merwe, N. J., 1992, A 16-Ma record of paleodiet using carbon and oxygen isotopes in fossil teeth from Pakistan: Chemical Geology; Isotope Geoscience Section, v. 94, no. 3, p. 183-192.

Schefuß, E., Schouten, S., Jansen, J. H. F., and Damsté, J. S. S., 2003, African vegetation controlled by tropical sea surface temperatures in the mid-Pleistocene period: Nature, v. 422, no. 6930, p. 418-421.

Sepulchre, P., Ramstein, G., Fluteau, F., Schuster, M., Tiercelin, J. J., and Brunet, M., 2006, Tectonic uplift and Eastern Africa aridification: Science, v. 313, no. 5792, p. 1419-1423.

Trauth, M. H., Maslin, M. A., Deino, A., and Strecker, M. R., 2005, Late Cenozoic moisture history of East Africa: Science, v. 309, no. 5743, p. 2051-2053.

Wang, Y., Cerling, T. E., and MacFadden, B. J., 1994, Fossil horses and carbon isotopes: new evidence for Cenozoic dietary, habitat, and ecosystem changes in North America: Palaeogeography, Palaeoclimatology, Palaeoecology, v. 107, no. 3-4, p. 269-279.

Zazzo, A., Balasse, M., and Patterson, W. P., 2005, High-resolution $d^{13}C$ intratooth profiles in bovine enamel: Implications for mineralization pattern and isotopic attenuation: Geochimica et Cosmochimica Acta, v. 69, no. 14, p. 3631-3642.

CHAPTER 2

LATE MIOCENE TO PLIOCENE CARBON ISOTOPE RECORD OF DIFFERENTIAL DIET CHANGE AMONG EAST AFRICAN HERBIVORES

This chapter was first published in April, 2011 in the *Proceedings of the National Academy of Sciences*, Vol. 108, no. 16, p 6509–6514. It is reprinted here with authorization from the National Academy of Sciences as described in section 3a of the PNAS License to Publish.

Late Miocene to Pliocene carbon isotope record of differential diet change among East African herbivores

Kevin T. Uno[a,1], Thure E. Cerling[a,b], John M. Harris[c], Yutaka Kunimatsu[d], Meave G. Leakey[e], Masato Nakatsukasa[d,f], and Hideo Nakaya[f]

[a]Department of Geology and Geophysics, University of Utah, Salt Lake City, UT 84112; [b]Department of Biology, University of Utah, Salt Lake City, UT 84112; [c]George C. Page Museum, Los Angeles, CA 90036; [d]Laboratory of Physical Anthropology, Kyoto University, Kyoto 606-8502, Japan; [e]Turkana Basin Institute, Stony Brook University, Stony Brook, NY 11790; and [f]Department of Earth and Environmental Sciences, Kagoshima University, Kagoshima 890-0065, Japan

Edited by David Pilbeam, Harvard University, Cambridge, MA, and approved March 5, 2011 (received for review December 14, 2010)

Stable isotope and molecular data suggest that C_4 grasses first appeared globally in the Oligocene. In East Africa, stable isotope data from pedogenic carbonate and fossil tooth enamel suggest a first appearance between 15–10 Ma and subsequent expansion during the Plio-Pleistocene. The fossil enamel record has the potential to provide detailed information about the rates of dietary adaptation to this new resource among different herbivore lineages. We present carbon isotope data from 452 fossil teeth that record differential rates of diet change from C_3 to mixed C_3/C_4 or C_4 diets among East African herbivore families at seven different time periods during the Late Miocene to the Pliocene (9.9–3.2 Ma). Significant amounts of C_4 grasses were present in equid diets beginning at 9.9 Ma and in rhinocerotid diets by 9.6 Ma, although there is no isotopic evidence for expansive C_4 grasslands in this part of the Late Miocene. Bovids and hippopotamids followed suit with individuals that had C_4-dominated (>65%) diets by 7.4 Ma. Suids adopted C_4-dominated diets between 6.5 and 4.2 Ma. Gomphotheriids and elephantids had mostly C_3-dominated diets through 9.3 Ma, but became dedicated C_4 grazers by 6.5 Ma. Deinotheriids and giraffids maintained a predominantly C_3 diet throughout the record. The sequence of differential diet change among herbivore lineages provides ecological insight into a key period of hominid evolution and valuable information for future studies that focus on morphological changes associated with diet change.

carbon isotopes | herbivore diet | bioapatite | paleodiet | mammal

Stable carbon isotope ratios from fossil tooth enamel, pedogenic carbonates, and terrestrial plant biomarkers are commonly used to determine the relative amounts of C_3 and C_4 vegetation in ancient habitats (1–4). These paleovegetation proxies integrate over different spatial and temporal scales, and each proxy has inherent strengths and weaknesses when used to reconstruct the relative amounts of C_3 and C_4 vegetation in ancient habitats (5, 6).

Carbon isotopes from fossil enamel of East African herbivores indicate C_3 diets and presumably, C_3 environments, in the records from Buluk, Fort Ternan, and the Tugen Hills that range in age from 17 to ~9 Ma (7–9). An exception is carbon isotope data from four equid teeth from Chorora, Ethiopia, dated at 10.7–10.1 Ma, which indicate a mixed C_3/C_4 diet (10). Previously published isotope data on enamel from the Nakali, Namurungule, Nawata, and Nachukui formations (included and expanded significantly here) indicate a shift toward C_4-dominated diets between 9.6 and 4.2 Ma (7). The previously published fossil enamel $\delta^{13}C$ record from East Africa shows that herbivores incorporated C_4 vegetation into their diets as early as ~10 Ma and is generally consistent with the Late Miocene (8–6 Ma) global expansion of C_4 vegetation documented in the Siwaliks, North America, and South America (1, 11–14).

Early to early Late Miocene pedogenic carbonate records from fossil sites in East Africa include Rusinga Island (15), the Lothidok Hills (16), Fort Ternan (17), the Tugen Hills (2), and Lothagam (7). All carbon isotope data from pedogenic carbonates older than 9 Ma indicate C_3 environments, with the exception of the Tugen Hills (2). No pedogenic carbonates have been found in the Nakali Formation, and none have been sampled from the Namurungule Formation in the Samburu Hills. The earliest robust evidence for C_4 vegetation from pedogenic carbonate is in the Lower Nawata Formation (7.4 Ma) at Lothagam, where the $\delta^{13}C$ values (−9.0 to −2.2‰) indicate C_3 to mixed C_3/C_4 environments that included significant amounts of C_4 grass (7). Although isotope records from Late Miocene pedogenic carbonates are rare, abundant records show that C_4 grasses became widespread during the Late Pliocene to Pleistocene throughout East Africa (ref. 5 and references therein).

Feakins et al. (4) analyzed the $\delta^{13}C$ values of *n*-alkanoic acids in sediments from a Gulf of Aden core (Deep Sea Drilling Project Site 231) that coincide with two time periods represented in our record. The biomarker record shows input of predominantly C_3-derived leaf waxes at 9.4 Ma and 5–15% C_4 vegetation from 3.8 to 3.2 Ma (4). The data from the Gulf of Aden core record a noncontinuous, regional-scale signal that is well dated with high temporal resolution. Collectively, the fossil enamel, pedogenic carbonate, and biomarker records from East Africa indicate C_3-dominated ecosystems throughout the Middle and Late Miocene and an expansion of C_4 grasses in the Late Pliocene and Pleistocene. However, none of these previously published datasets provides a detailed record of the response of the fauna during this period.

We use stable carbon isotope ratios from fossil tooth enamel identified from family to species level (*SI Appendix*, Table S1) to evaluate rates of change in herbivore diets from the Late Miocene to the Early Pliocene from three fossil localities in East Africa (Fig. 1). The sites range in age from 9.9 to 3.2 Ma; lithostratigraphy, radiometric ages, and stratigraphic intervals where samples were collected are shown in Fig. 2. The stable isotope data address two important issues in the East African fossil record. First, they illustrate the diverse paleoecological response of large herbivores to paleoenvironmental change associated with the appearance of C_4 grasses during a key period of hominid evolution. Paleoenvironmental context is integral to understanding East African hominid emergence, radiation, and evolution from the Late Miocene onward. All sites in this study have yielded important hominid material. Nakali and the Samburu Hills, located in the Suguta Valley, Kenya, have yielded the Late Miocene hominids *Nakalipithecus nakayami* (18) and *Samburupithecus kiptalami* (19), respectively, which likely represent stem

Author contributions: K.T.U., T.E.C., J.M.H., Y.K., M.G.L., M.N., and H.N. designed research; K.T.U., T.E.C., J.M.H., Y.K., M.G.L., M.N., and H.N. performed research; K.T.U., T.E.C., J.M.H., and M.G.L. analyzed data; and K.T.U. wrote the paper.

The authors declare no conflict of interest.

This article is a PNAS Direct Submission.

[1]To whom correspondence should be addressed. E-mail: kevin.uno@utah.edu.

This article contains supporting information online at www.pnas.org/lookup/suppl/doi:10.1073/pnas.1018435108/-/DCSupplemental.

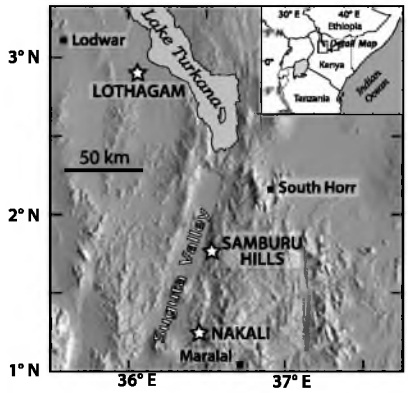

Fig. 1. Map of northern Kenya showing the three fossil localities in the Suguta Valley and the Turkana Basin.

hominines (23). With *Chororapithecus abyssinicus*, these are the only known East African hominids between 11 and 9 Ma (24). The third site, Lothagam, is located west of Lake Turkana in northern Kenya (Fig. 1). The Nawata and Nachukui formations at Lothagam have yielded hominid material dated at ~5 and 3.5 Ma. The older specimens are attributed to Hominidae indet., whereas the younger specimens are likely *Kenyanthropus platyops* or, possibly, *Australopithecus* cf *Au. afarensis* (25) (*SI Appendix*, Table S2). Second, the stable isotope record of diet change will allow paleontologists to compare the timing and rate of diet change to morphological changes associated with the dietary shift toward C_4 grazing in herbivore lineages. Examples of craniodental and postcranial ecomorphic characteristics influenced by the transition from browsing to grazing include tooth morphology (i.e., hypsodonty, enamel thickness, and size), jaw structure, and forelimb bone length (26, 27).

Results and Discussion

Carbon Isotope Data by Age. We use the terms "C_3-dominated diet" for $\delta^{13}C$ values < −8‰, "mixed C_3/C_4 diet" for −8‰ to −2‰, and "C_4-dominated diet" for values > −2‰. These delineations are based on estimated paleoatmospheric $\delta^{13}C$ values and an enrichment factor of 14.1‰ between diet and enamel (*SI Appendix*, Table S3) (28, 29). A Shapiro–Wilk test for normality demonstrates that the data are not distributed normally (*SI Appendix*, Table S4). Thus, the median and range of $\delta^{13}C$ values are more appropriate than the mean and SD for describing central location and variance. Mann–Whitney *U* test results indicate significant shifts ($P < 0.05$) in the median $\delta^{13}C$ value between successive age increments (i.e., 9.9–9.6 Ma) where there are more than five isotope analyses within a family (*SI Appendix*, Table S5). All isotopic results are reported in *SI Appendix*, Table S6; a summary is presented in Table 1.

The $\delta^{13}C$ values of 113 herbivore fossil teeth from the Nakali Formation (9.9 Ma) range from −12.3 to −0.9‰ and have a median value of −9.4‰. Of the 113 samples, 94 indicate C_3-dominated diets (Fig. 3). Ten of 11 samples that have $\delta^{13}C$ values > −7‰ come from the Upper Member. This includes three Upper Member equid teeth that range from −1.8 to −0.9‰, suggesting diets of ~65% C_4 grass. None of the samples with confirmed placement in the Lower Member ($n = 28$) have $\delta^{13}C$ values > −8‰. Thus, C_4 grasses were absent from the diets of all confirmed Lower Member taxa and were in high-enough abundance to comprise the majority of the diet of some Upper Member equids. Although C_4 grass was available by 9.9 Ma at Nakali, most herbivores were exploiting C_3 trees, shrubs, forbs, sedges, or grasses.

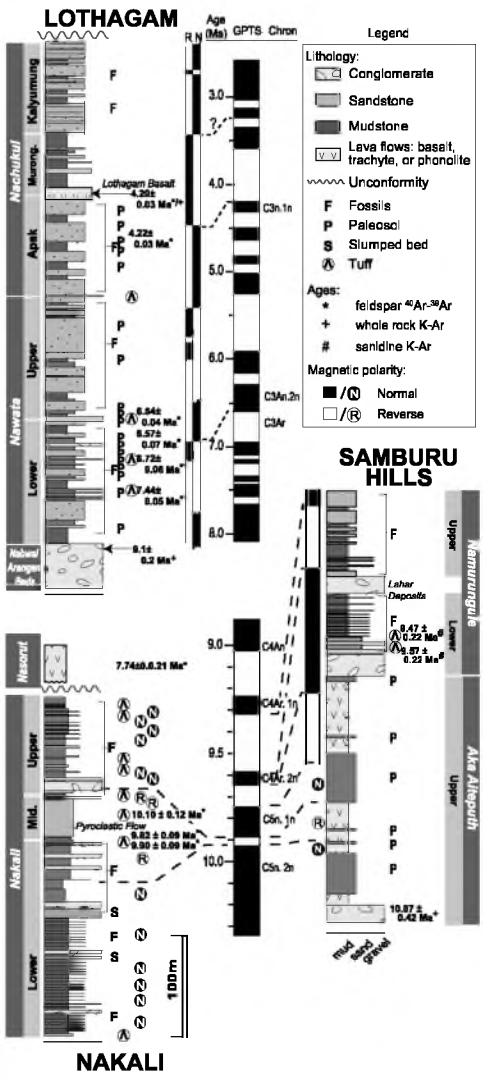

Fig. 2. Lithostratigraphy, magnetostratigraphy, and radiometric ages from Nakali, the Samburu Hills, and Lothagam. Geomagnetic Polarity Time Scale (GPTS) changes at the break between 9.0 and 8.0 Ma. The uppermost age from the Nakali Formation (10.10 ± 0.12 Ma) is from a pyroclastic flow and essentially synchronous with the two slightly younger ages below. Modified from refs. 18, 19, and 20–22.

In stark contrast to the Nakali (9.9 Ma) taxa, more than 80% ($n = 103$) of Namurungule taxa (9.6–9.3 Ma) consumed C_4 grass (Fig. 3). The range of $\delta^{13}C$ values in the Lower and Upper members of the Namurungule Formation are indistinguishable (Table 1), but the $\delta^{13}C$ histogram for Lower Namurungule taxa is bimodal with peaks at −7 and −1‰. This is the earliest evidence for niche partitioning into C_3 and C_4 diets at the ecosystem scale in the East African fossil record. The Upper Namurungule histogram is not well defined (Fig. 3). The distribution of $\delta^{13}C$ values from the Lower Nawata is also bimodal with peaks at −7‰ and −2‰. The Upper Nawata $\delta^{13}C$ histogram is unimodal and skewed left. The Apak $\delta^{13}C$ histogram is also unimodal and

Table 1. Median, range, and number of $\delta^{13}C$ values for herbivore families by age

Formation or member (age)	Family	Median (‰)	Range (‰)	*N*
Kaiyumung	All taxa	−1.8	−11.1 to +0.8	13
(3.2 Ma)	Rhinocerotidae	+0.5	−0.6 to +0.8	3
	Bovidae	—	−6.6 and −2.0	2
	Suidae	−1.5	−2.9 to −0.2	6
	Giraffidae	−9.4	—	1
	Deinotheriidae	−11.1	—	1
Apak	All taxa	−2.4	−12.5 to −0.2	53
(4.2 Ma)	Equidae	−1.0	−1.8 to −0.2	5
	Rhinocerotidae	−2.4	−11.2 to −2.0	11
	Bovidae	+2.2	−5.8 to −0.4	6
	Hippopotamidae	−4.4	−8.2 to −0.9	7
	Suidae	−2.9	−5.9 to −1.5	13
	Gomphotheriidae	−0.9	−2.2 to −0.7	4
	Elephantidae	−0.8	−1.1 to −0.2	5
	Deinotheriidae	—	−12.5 and −12.0	2
Upper Nawata	All taxa	−2.9	−12.2 to +0.9	79
(6.5 Ma)	Equidae	−0.2	−0.5 to +0.5	6
	Rhinocerotidae	−8.0	−10.9 to −1.3	13
	Bovidae	−3.3	−9.0 to +0.2	7
	Hippopotamidae	−2.7	−7.6 to +0.9	28
	Suidae	−5.8	−9.1 to −2.0	12
	Giraffidae	−12.2	—	1
	Elephantidae	−1.1	−2.1 to +0.3	11
	Deinotheriidae	−11.4	—	1
Lower Nawata	All taxa	−5.1	−11.4 to +2.2	91
(7.4 Ma)	Equidae	−0.9	−3.8 to +0.4	14
	Rhinocerotidae	−9.1	−11.0 to −4.0	15
	Bovidae	−4.2	−7.3 to +2.2	6
	Hippopotamidae	−4.3	−9.2 to −0.7	29
	Suidae	−7.2	−9.6 to −5.6	14
	Giraffidae	−9.8	−11.4 to −8.1	4
	Gomphotheriidae	−2.1	−3.9 to +0.7	4
	Elephantidae	−3.2	−6.2 to −1.0	4
	Deinotheriidae	−9.7	—	1
Upper Namurungule	All taxa	−5.0	−10.7 to +0.2	34
(9.3 Ma)	Equidae	−1.9	−4.8 to +0.2	13
	Rhinocerotidae	—	−9.7 and −4.9	2
	Bovidae	—	−7.6 and −2.1	2
	Hippopotamidae	−5.6	−6.5 to −3.8	3
	Suidae	−7.9	−8.4 to −5.1	3
	Giraffidae	−7.6	−10.7 to −7.3	3
	Gomphotheriidae	−8.2	−9.1 to −4.6	8
Lower Namurungule	All taxa	−5.6	−10.4 to +0.7	69
(9.6 Ma)	Equidae	−2.1	−6.6 to +0.7	24
	Rhinocerotidae	−4.4	−9.6 to −1.0	12
	Bovidae	−6.1	−10.3 to −3.7	6
	Hippopotamidae	−6.6	−8.5 to −5.2	6
	Suidae	−6.5	−7.4 to −3.5	7
	Giraffidae	−7.7	−8.7 to −6.3	7
	Gomphotheriidae	—	−10.3 and −6.3	2
	Deinotheriidae	−9.5	−9.8 to −8.9	5
Nakali	All taxa	−9.4	−12.3 to −0.9	113
(9.9 Ma)	Equidae	−8.6	−10.5 to −0.9	35
	Rhinocerotidae	−9.3	−11.6 to −6.5	11
	Bovidae	−10.4	−11.8 to −8.1	10
	Hippopotamidae	−9.7	−11.2 to −8.0	14
	Suidae	−8.6	−10.8 to −6.3	15
	Giraffidae	−9.8	−12.3 to −8.0	15
	Gomphotheriidae	−7.7	−9.6 to −6.9	7
	Deinotheriidae	−10.4	−11.7 to −9.5	6

skewed left (Fig. 3). No histogram is plotted for the Kaiyumung because of the relatively small sample size (n = 13). The $\delta^{13}C$ data record a dietary transition from nearly all C_3 at 9.9 Ma to mixed C_3/C_4 from 9.6 to 7.4 Ma to predominantly mixed C_3/C_4 to

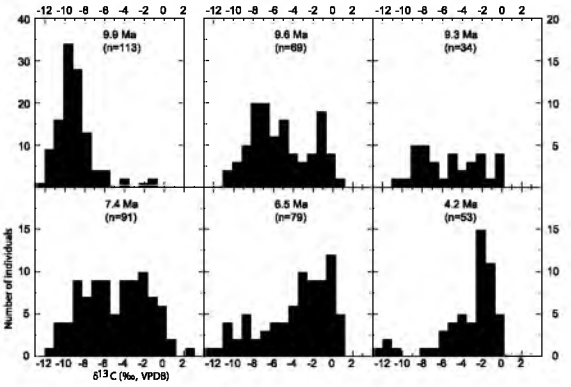

Fig. 3. Histograms of $\delta^{13}C$ values of fossil enamel from all herbivore taxa by age. Note the different vertical axis for the 9.9 Ma population.

C_4-dominated diets from 6.5 Ma onward (Fig. 3). Advancing temporally from 10 to 3 Ma through the isotope record requires moving spatially within the Kenya Rift between the three sites (Fig. 1). Available data suggest differences in physiographic settings (e.g., paleoelevation and location in the Rift Valley) between the three sites that would have affected paleoclimatic variables such as temperature, precipitation, aridity, and seasonality (18, 20, 30, 31). None of the sites overlap in age; hence, it is not possible to discern the influence of local (i.e., site-specific) versus regional climate on vegetative structure at each site. Therefore, the temporal shift in $\delta^{13}C$ toward more positive values may also be partly attributed to local physiographic influences on paleoclimate. The carbon isotope data are a single, albeit valuable, component for reconstructing the paleoecology of fossil sites. In the absence of additional geochemical, taxonomic, taphonomic, and lithofacies data from all sites, we refrain from a comprehensive reconstruction of paleoenvironment at each site and focus on diet change in herbivore lineages.

Carbon Isotope Data by Family. ***Equidae.*** The majority of Nakali Formation equids have C_3-dominated diets. Nine have intermediate $\delta^{13}C$ values (−7.8 to −4.1‰) indicative of a mixed C_3/C_4 diet, and three specimens collected within the upper 30 m of the Nakali Formation have values that range from −1.8 to −0.9‰ (Fig. 4). These three specimens comprise the earliest C_4-dominated diets from the East African fossil record. Lower Namurungule equids display a greater range in $\delta^{13}C$ values than equids in the Upper Namurungule. The ranges of $\delta^{13}C$ values in both the Lower and Upper Nawata are small, 4.2‰ and 1.0‰, respectively. Equids from the Apak have a median $\delta^{13}C$ value of −1.0‰ (n = 5) and a range of 1.6‰. No equids were sampled from the Kaiyumung.

The equids were the first to incorporate significant amounts of C_4 grass into their diet at 9.9 Ma. Beginning at 9.6 Ma, the isotope record shows a rapid transition toward dedicated C_4 grazing characterized by an increasing median and a decreasing range of $\delta^{13}C$ values through time (Fig. 4). Nearly three-fourths of the Nakali equids have C_3-dominated diets, but not a single equid from the Lower Namurungule has a C_3 diet. Between 9.6 and 9.3 Ma, the minimum $\delta^{13}C$ value increases from −6.6 to −4.8‰, indicating a shift away from C_3 vegetation in diet. By 6.5 Ma, equids were dedicated C_4 grazers, as are extant equids.

Isotopic data are supported by mesowear analysis of fossil teeth, which is a fast, qualitative method for determining diet preference (browse vs. graze) using two morphological criteria. Cusp shape describes the buccal apices of molar cusps as sharp,

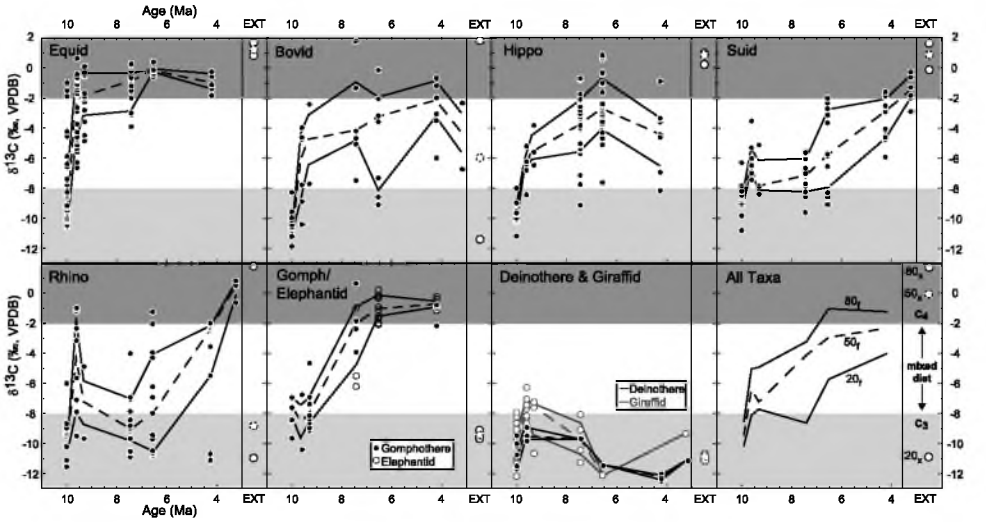

Fig. 4. The $\delta^{13}C$ value vs. age (Ma) for nine herbivore families and for all taxa. Data points represent individual samples. Lines are the 20th, 50th (dashed), and 80th percentile $\delta^{13}C$ values for fossil (f) populations. White circles to the right of the fossil data for each family indicate the 20th, 50th (dashed), and 80th percentile $\delta^{13}C$ values for extant (x and EXT) herbivores from Northern Kenya (32). The δ13C values from extant herbivores are corrected by +1.5‰ for recent changes in atmospheric $\delta^{13}C$ values.

round, or blunt, and occlusal relief describes the height of the valley between them (33). Sharp-to-round cusp shape and high occlusal relief, akin to serrations on a knife, are common in extant browsers. Round or blunt cusp shape and low occlusal relief are common in extant grazers. Nakaya et al. (34) found that 85% (n = 68) of upper molars from Nakali equids have high occlusal relief and that 92% (n = 60) have a sharp or round cusp shape, suggesting a diet of C_3 browse, not C_3 graze. In contrast, in the Namurungule Formation, 52% (n = 54) of upper molars have low occlusal relief and 97% (n = 36) have a round or blunt cusp shape, suggesting grazing diets. The isotope and mesowear results suggest that the East African equid diet transitioned from C_3 browsing (with some minor amounts of C_4 grazing) at 9.9 Ma to a C_4-dominated grazing diet by 7.4 Ma. However, in the absence of mesowear (or microwear) data for other lineages that eventually include C_4 grass in their diets, prior or continued use of C_3 grass cannot be ruled out.

Rhinocerotidae. All but one of the Nakali rhinocerotids had C_3-dominated diets. The $\delta^{13}C$ values of Lower Namurungule rhinocerotids (−9.6 to −1.0‰) indicate a range of C_3- to C_4-dominated diets. The range in $\delta^{13}C$ values of rhinocerotids increases from the Lower Nawata to the Upper Nawata and decreases slightly in the Apak. In the Kaiyumung, three rhinocerotid samples have a median $\delta^{13}C$ value of +0.5‰.

Some rhinocerotids adopt a C_4-dominated diet by 9.6 Ma. However, unlike the equids, the rhinocerotids maintain a diverse diet ranging from C_3- to C_4-dominated diets through 4.2 Ma (Fig. 4). In the Lower Namurungule, half of the population (potentially *Ceratotherium* sp.) has a mixed C_3/C_4 to C_4-dominated diet (−3.2 to −1.0‰), and the other half has a mixed C_3/C_4 to C_3-dominated diet (−9.6 to −5.7‰), suggesting niche partitioning in the rhinocerotid diet as early as 9.6 Ma. By the Apak, mixed diets become less common in the record than C_3- or C_4-dominated diets, a profile that more closely resembles the dietary niche partitioning among the extant African rhinoceros where the white, *Ceratotherium*, is a grazer, and the black, *Diceros*, is a browser. Only the grazing rhinocerotid, *Ceratotherium* sp., is present at 3.2 Ma in the Kaiyumung.

Bovidae. The median $\delta^{13}C$ value of Nakali bovids (−10.4‰; n = 10) is, along with the deinotheriids, the lowest among all East African lineages at 9.9 Ma. The median $\delta^{13}C$ value increases to −6.1‰ (n = 6) in Lower Namurungule bovids and appears to increase further in the two bovids analyzed from the Upper Namurungule ($\delta^{13}C$ values = −7.6‰ and −2.1‰). This trend continues through bovids from the Lower Nawata, Upper Nawata, and Apak. Two bovids analyzed from the Kaiyumung have $\delta^{13}C$ values of −6.6‰ and −2.1‰.

Even in the Late Miocene and Early Pliocene, bovids were taxonomically diverse (*SI Appendix* and references therein), which is reflected isotopically in the range of diets after 9.9 Ma. The highest $\delta^{13}C$ value from each age population increases incrementally from the Lower Namurungule to the Lower Nawata (Fig. 4). As with the rhinocerotids, the bovids show a diverse diet throughout most of their record, despite being represented by a relatively limited sample size (n = 39). Although bovid fossils are abundant, especially at Lothagam, many are horn cores or postcranial elements, whereas teeth suitable for isotope analysis are rare. Future stable isotope work between and within the bovid tribes has great potential for elucidating their dietary preferences and radiation.

Hippopotamidae. Nakali hippopotamids have a median $\delta^{13}C$ value of −9.7‰ whereas in Lower Namurungule hippopotamids the median $\delta^{13}C$ value is −6.6‰. Three hippopotamids from the Upper Namurungule have a median $\delta^{13}C$ value of −5.6‰. By the Lower Nawata, the median $\delta^{13}C$ value is −3.8‰ (n = 29) and in the Upper Nawata the median increases to −2.7‰ (n = 28). In the Apak, the median $\delta^{13}C$ value is −4.4‰ (n = 7) and the range is from −8.2 to −0.9‰ (Fig. 4). No hippopotamids were analyzed from the Kaiyumung.

Kenyapotamus coryndoni had a C_3 diet at 9.9 Ma, but by 9.6 Ma it was a mixed C_3/C_4 feeder and only one individual had a C_3 diet. Hippopotamids from 9.3 Ma incorporated even more C_4 grass into their diet than those from 9.6 Ma. By 7.4 Ma, *Kenyapotamus* is replaced by *Archaeopotamus* species that exploit nearly the entire $\delta^{13}C$ range of C_3 to C_4 vegetation (Fig. 4). Hippopotamid diet remains diverse through the remainder of the record at Lothagam. The common extant hippopotamus in East Africa is primarily a grazer, but individuals display a diverse diet ranging from −13.7 to +1.5‰, with a mean value of −3.5 ± 1.7‰ (35).

Suidae. Nakali Formation suids have a median $\delta^{13}C$ value of −8.6‰ (n = 15), a value that increases to −6.5‰ (n = 6) in Lower Namurungule suids. The three suids from the Upper Namurungule have a median $\delta^{13}C$ value of −7.9‰. At Lothagam, suid $\delta^{13}C$ values increase from the Lower Nawata to the Upper Nawata and still further in the Apak and the Kaiyumung.

Between 9.9 and 3.2 Ma, suids make a slow transition from a C_3- to a C_4-dominated diet (Fig. 4). Only 2 of 15 nyanzachoeres from 9.9 Ma have minor amounts of C_4 grass in their diet, but by 9.6 Ma all have some C_4 grass in their diet. Suid diet remains fairly static through the Lower Nawata and is even slightly more reliant on C_3 vegetation at 9.3 and 7.4 Ma than at 9.6 Ma. In the Upper Nawata, *Nyanzochoerus syticus* has a wide dietary range, but that of *N. australis* is C_4-dominated. By 4.2 Ma, the suids have mixed C_3/C_4 to C_4-dominated diets. Kaiyumung nyanzachoeres and notochoeres have C_4-dominated diets with a relatively restricted range of $\delta^{13}C$ values. Extant East African suids occupy a wide range of ecosystems from closed canopy forests to mosaic grassland/woodlands, and their diets reflect the wide range of habitats that they occupy. Extant suids from the Turkana Basin have C_4-dominated diets (36).

Giraffidae. Giraffids have a C_3-dominated diet from 9.9 to 3.2 Ma with the exception of six values from 9.6 and 9.3 Ma in the Namurungule Formation, where the maximum value is −6.3‰. No giraffids were sampled from the Apak, and the sole giraffid value from the Kaiyumung is −9.4‰. *Giraffa camelopordalis*, the extant giraffe, has been extirpated from the Turkana Basin, but elsewhere in Africa it and the Okapi have C_3-dominated diets.

Gomphotheriidae and Elephantidae. Results for these two proboscidean lineages are discussed together and shown on the same plot (Fig. 4) because of general morphological similarities and because neither family is present throughout the entire record. In general, gomphotheriid $\delta^{13}C$ values indicate C_3-dominated diets from 9.9 to 9.3 Ma. By 7.4 Ma, no gomphotheriids or elephantids have C_3 diets, and they occupy nearly the entire $\delta^{13}C$ range of mixed C_3/C_4 to C_4 diet (Fig. 4). Between 7.4 and 6.5 Ma, they become dedicated grazers. The Apak exhibits the highest taxonomic diversity of gomphotheriids and elephantids, but the lowest range of $\delta^{13}C$ values, suggesting that, shortly before their extinction, gomphotheriids and elephantids were competing directly with each other for food. In complete contrast to their Plio-Pleistocene relatives, the extant elephantids, *Loxodonta africana* and *Elephas maximus*, are primarily browsers (37, 38).

Deinotheriidae. Deinotheriids are extinct proboscideans that had two downward-curving tusks in the lower jaw, and they are relatively rare throughout the record. From the $\delta^{13}C$ values available (Table 1), it appears that they maintain a C_3 diet throughout the record, in agreement with previous interpretations of diet based on carbon isotope data and low crowned tooth morphology (37, 39). The $\delta^{13}C$ values from this taxon, like those of *Giraffa*, are useful for defining the C_3 end member at a given fossil locality.

Patterns of Differential Diet Change. The carbon isotope data illustrate patterns of diet change in nine herbivore lineages, but do not reveal underlying drivers of the observed changes. We compiled isotope data from fossil and extant herbivore teeth in northern Kenya and summarized diet change patterns in herbivore lineages over the last 10 million years in East Africa (Fig. 4). The perissodactyls rapidly shift to C_4-dominated diets. The equids' shift begins around 9.9 Ma, and the rhinocerotids' by 9.6 Ma. However, the rhinocerotids and equids differ in that rhinocerotids have C_3-, mixed C_3/C_4, and C_4-dominated diets from 9.6 until 4.2 Ma, when mixed C_3/C_4 diets disappear from the record, whereas the equids become dedicated C_4 grazers sometime between 9.3 and 7.4 Ma (Fig. 4). Two proboscidean families, the gomphotheriids and elephantids, make a similar shift to C_4 grazing that begins later than that of the equids (Fig. 4). At some time in the last million years or so, elephantids return to C_3-dominated diets (37). The deinotheriids, a third proboscidean family, maintain a C_3-dominated diet up to their demise in the Pleistocene. Among the artiodactyls, bovids shift to a mixed C_3/C_4 diet by 9.6 Ma and to a wide range of diets by 7.4 Ma, including individuals with C_4-dominated diets. This diversity in diet may have contributed to their successful radiation in the Pliocene and Pleistocene in East Africa. Likewise, hippopotamids transition from a C_3 diet to a mixed C_3/C_4 diet between 9.9 and 9.3 Ma. By 7.4 Ma, their diets had become quite diverse and remain so today (35). The suids incorporate small amounts of C_4 grass into their diet by 9.6 Ma, but do not begin their shift toward a C_4-dominated diet until 6.5 Ma (Fig. 4).

The underlying driver of the diverse dietary response to C_4 grass among lineages can broadly be attributed to paleoenvironmental change. Paleoenvironmental records in East Africa from 10 to ~5.5 Ma are essentially limited to sites in this study and in the Tugen Hills. At present, the discontinuous and incomplete paleoenvironmental record renders linkages to diet change weak. This is in contrast to the continuous, multiproxy paleoenvironmental records from 8 to 5 Ma in the Siwalik Hills of India and Pakistan, where a spatiotemporally continuous isotopic record of soil carbonates and a rich, coeval faunal collection, which includes isotope data from enamel, show that long-term climate change resulted in major faunal turnover (12). Building a multiproxy data set from existing East African sites during this time period has the potential of elucidating the primary drivers of herbivore diet change related to changes in paleoenvironment and paleoclimate.

Conclusions

From the Late Miocene through the Pliocene, East African herbivore families exhibit differential rates of diet change from C_3-dominated to mixed C_3/C_4 or C_4-dominated diets. C_4 grasses were available by 9.9 Ma at Nakali, but of the population sampled (n = 113), only a dozen equids, a single rhinocerotid, and two suids and gomphotheriids, had mixed C_3/C_4 or C_4-dominated diets. By 9.6 Ma, 80% of the sampled fauna, which includes the equids, rhinocerotids, bovids, hippopotamids, gomphotheriids, and suids, were incorporating C_4 grass into their diets. The paleosol record indicates mosaic environments from 7.4 to 4.2 Ma, but there is no evidence for long-lived, ecosystem-scale C_4 grasslands. With the exception of deinotheriids and giraffids, all sampled lineages incorporate significant amounts (>50%) of C_4 grasses into their diet by 6.5 Ma. The change from C_3 to mixed C_3/C_4 or C_4-dominated diets between 9.9 and 9.3 Ma took place within a single species in both equids and hippopotamids. High rates of dietary change later in the record (9.3–3.2 Ma) likely occurred in conjunction with major habitat change that, in turn, produced faunal change, including the appearance of stem hominins in the fossil record. The timing and rates of morphological change (e.g., craniodental and postcranial) can be evaluated with respect to the ~7-million-year isotope record of diet change presented here.

Materials and Methods

Stable isotope ratios are reported as δ values relative to the Pee Dee Belemnite (PDB) standard using permil (‰) notation where $\delta^{13}C = (R_{sample}/R_{standard} - 1) \times 1{,}000$, and R_{sample} and $R_{standard}$ are the $^{13}C/^{12}C$ ratios in the sample and in the standard, respectively, and the $\delta^{13}C$ value of PDB is defined as 0‰. The $\delta^{13}C$ isotope ratios of enamel were measured at the Stable Isotope Ratio Facility for Ecological Research at the University of Utah on a Finnigan 252 isotope ratio mass spectrometer. The SD of an internal carbonate standard (Carrara marble) analyzed with these samples was 0.2‰ (n = 63). Additional details of the sampling and analytical methods are provided in *SI Appendix*. Taxonomic identification of mammalian fauna from the Nakali, Namurungule, Nawata, and (Lothagam) Nachukui formations is presented in *SI Appendix*, Table S2, and reviewed in *SI Appendix* (18, 30, 40–51). We analyzed fossil enamel from large herbivores listed in *SI Appendix*, Table S1. Many are identified only by family because permission to sample specimens

for stable isotope analysis is often restricted to fragmentary material that precludes identification at the genus or species level. A Simpson Index shows that the fauna from Nakali and Namurungule formations are similar at the family, genus, and species levels at 82, 78, and 50%, respectively (30, 52). Significant faunal turnover occurs between 9.3 and 7.4 Ma.

ACKNOWLEDGMENTS. We thank the Government of Kenya and the National Museums of Kenya (KNM) for permission to sample fossil material from Nakali, the Samburu Hills, and Lothagam. This work would not be possible without the contributions of the KNM and Koobi Fora Research Project field crews and the KNM preparation and curatorial staff, especially Dr. E. Mbua and M. Muungu. K.T.U. thanks F. H. Brown, T. Sakai, and N. E. Levin for assistance in the field and insightful discussion. We thank A. K. Behrensmeyer and an anonymous reviewer whose critical comments significantly improved the manuscript. This work was supported by National Science Foundation Grant BCS-0621542 and Japan Society for the Promotion of Science Grants 19107007 and 22255006.

1. Quade J, et al. (1992) A 16-Ma record of paleodiet using carbon and oxygen isotopes in fossil teeth from Pakistan. *Chem Geol Isot Geosci Sect* 94:183–192.
2. Kingston JD, Hill A, Marino BD (1994) Isotopic evidence for neogene hominid paleoenvironments in the Kenya rift valley. *Science* 264:955–959.
3. Cerling TE, Quade J, Wang Y, Bowman JR (1989) Carbon isotopes in soils and palaeosols as ecology and palaeoecology indicators. *Nature* 341:138–139.
4. Feakins SJ, deMenocal PB, Eglinton TI (2005) Biomarker records of late Neogene changes in northeast African vegetation. *Geology* 33:977–980.
5. Ségalen L, Lee-Thorp JA, Cerling T (2007) Timing of C_4 grass expansion across sub-Saharan Africa. *J Hum Evol* 53:549–559.
6. Kingston JD (2007) Shifting adaptive landscapes: Progress and challenges in reconstructing early hominid environments. *Am J Phys Anthropol* 134(Suppl 45):20–58.
7. Cerling T, Harris J, Leakey M (2003) Isotope paleoecology of the Nawata and Nachukui Formations at Lothagam, Turkana Basin, Kenya. *Lothagam: The Dawn of Humanity in Eastern Africa*, pp 605–623.
8. Cerling TE, Harris JM, Ambrose SH, Leakey MG, Solounias N (1997) Dietary and environmental reconstruction with stable isotope analyses of herbivore tooth enamel from the Miocene locality of Fort Ternan, Kenya. *J Hum Evol* 33:635–650.
9. Morgan M, Kingston J (1994) Carbon isotope evidence for the emergence of C_4 plants in the Neogene from Pakistan and Kenya. *Nature* 367:162–165.
10. Bernor RL, Kaiser TM, Nelson SV (2004) The oldest Ethiopian Hipparion (Equinae, Perissodactyla) from Chorora: Systematics, paleodiet and paleoclimate. *Courier Forschungsinstitut Senckenberg* 246:213–226.
11. Cerling TE, et al. (1997) Global vegetation change through the Miocene/Pliocene boundary. *Nature* 389:153–158.
12. Badgley C, et al. (2008) Ecological changes in Miocene mammalian record show impact of prolonged climatic forcing. *Proc Natl Acad Sci USA* 105:12145–12149.
13. Wang Y, Cerling TE, MacFadden BJ (1994) Fossil horses and carbon isotopes: New evidence for Cenozoic dietary, habitat, and ecosystem changes in North America. *Palaeogeogr Palaeoclimatol Palaeoecol* 107:269–279.
14. Latorre C, Quade J, McIntosh WC (1997) The expansion of C_4 grasses and global change in the late Miocene: Stable isotope evidence from the Americas. *Earth Planet Sci Lett* 146:83–96.
15. Bestland EA, Krull ES (1999) Palaeoenvironments of Early Miocene Kisingiri volcano Proconsul sites: Evidence from carbon isotopes, palaeosols and hydromagmatic deposits. *J Geol Soc London* 156:965–976.
16. Cerling TE (1992) Development of grasslands and savannas in East Africa during the Neogene. *Global Planet Change* 5:241–247.
17. Cerling TE, Quade J, Ambrose SH, Sikes NE (1991) Fossil soils, grasses, and carbon isotopes from Fort Ternan, Kenya: Grassland or woodland? *J Hum Evol* 21:295–306.
18. Kunimatsu Y, et al. (2007) A new Late Miocene great ape from Kenya and its implications for the origins of African great apes and humans. *Proc Natl Acad Sci USA* 104:19220–19225.
19. Sawada Y, et al. (1998) K-Ar ages of Miocene Hominoidea (Kenyapithecus and Samburupithecus) from Samburu Hills, northern Kenya. *Comptes Rendus de l'Academie des Sciences, Serie II. Sciences de la Terre et des Planetes* 326:445–451.
20. Sakai T, et al. (2010) Climate shift recorded at around 10 Ma in Miocene succession of Samburu Hills, northern Kenya Rift, and its significance. *Geological Society, London, Special Publications* 342(1):109–127.
21. McDougall I, Feibel CS (1999) Numerical age control for the Miocene-Pliocene succession at Lothagam, a hominoid-bearing sequence in the northern Kenya Rift. *J Geol Soc London* 156:731–745.
22. Feibel C (2003) Stratigraphy and depositional history of the Lothagam sequence. *Lothagam: The Dawn of Humanity in Eastern Africa*, pp 17–29.
23. Harrison T (2010) Dendropithecoidea, Proconsuloidea, and Hominoidea. *Cenozoic Mammals of Africa*, eds Werdelin L, Sanders WJ (University of California Press, Berkeley, CA), pp 429–469.
24. Suwa G, Kono RT, Katoh S, Asfaw B, Beyene Y (2007) A new species of great ape from the late Miocene epoch in Ethiopia. *Nature* 448:921–924.
25. Leakey M, Walker A (2003) The Lothagam hominids. *Lothagam: The Dawn of Humanity in Africa*, pp 249–257.
26. Stromberg CAE (2006) Evolution of hypsodonty in equids: Testing a hypothesis of adaptation. *Paleobiology* 32:236–258.
27. Cerling T, Harris J, Leakey M (2005) *Environmentally Driven Dietary Adaptations in African Mammals. A History of Atmospheric CO_2 and Its Effects on Plants, Animals, and Ecosystems, Ecological Studies*, eds Baldwin IT, et al. (Springer, Berlin), Vol 177, pp 258–272.
28. Cerling T, Harris J (1999) Carbon isotope fractionation between diet and bioapatite in ungulate mammals and implications for ecological and paleoecological studies. *Oecologia* 120:347–363.
29. Tipple B, Meyers S, Pagani M (2010) Carbon isotope ratio of Cenozoic CO_2: A comparative evaluation of available geochemical proxies. *Paleoceanography* 25.
30. Tsujikawa H (2005) The palaeoenvironment of Samburupithecus kiptalami based on its associated fauna. *Afr Stud Monogr* (Suppl 32):51–62.
31. Leakey M, Harris J (2003) *Lothagam: The Dawn of Humanity in Eastern Africa* (Columbia University Press, New York).
32. Cerling T, Harris J, Leakey M, Mudidia N (2003) Stable isotope ecology of Northern Kenya, with emphasis on the Turkana Basin. *Lothagam: The Dawn of Humanity in Eastern Africa*, pp 583–603.
33. Fortelius M, Solounias N (2000) Functional characterization of ungulate molars using the abrasion-attrition wear gradient: A new method for reconstructing paleodiets. *Am Mus Novit* 3301:1–36.
34. Nakaya H, et al. (2008) Late Miocene paleoenvironmental change of hominoid sites in Kenya: Mesowear analysis of Hipparion cheek teeth, paper presented at the 33rd *International Geological Congress at Oslo 2008*.
35. Cerling TE, et al. (2008) Stable isotope ecology of the common hippopotamus. *J Zool* 276:204–212.
36. Harris J, Cerling T (2002) Dietary adaptations of extant and Neogene African suids. *J Zool* 256:45–54.
37. Cerling T, Harris J, Leakey M (1999) Browsing and grazing in elephants: The isotope record of modern and fossil proboscideans. *Oecologia* 120:364–374.
38. Sukumar R, Ramesh R (1995) Elephant foraging: Is browse or grass more important? *A Week with Elephants*, eds Daniel JC, Datye H (Bombay Natural History Society, Bombay and Oxford University Press, New Delhi), pp 368–374.
39. Sanders W, Gheerbrant E, Harris J, Saegusa H, Delmer C (2010) Proboscidea. *Cenozoic Mammals of Africa*, eds Werdelin L, Sanders WJ (University of California Press, Berkeley, CA), pp 161–251.
40. Aguirre E, Alberdi MT (1974) Hipparion remains from the northern part of the Rift Valley; Kenya. *Proc K Ned Akad Wet, B Palaeontol Geol Phys Chem* 77:146–157.
41. Aguirre E, Leakey P (1974) Nakali; nueva fauna de Hipparion del Rift Valley de Kenya. *Estudios Geologicos (Madrid)* 30:219–227.
42. Aguirre E, Guerin C (1974) First discovery of a Iranotherlinae (Mammalia, Perissodactyla, Rhinocerotidae) in Africa: Kenyatherium bishopi Nov. gen. Nov. sp. Training Vallesian (Upper Miocene) of Nakala (Kenya) (Translated from French). *Estudios Geologicos (Madrid)* 30:229–233.
43. Flynn LJ, Sabatier M (1984) A muroid rodent of Asian affinity from the Miocene of Kenya. *J Vertebr Paleontol* 3:160–165.
44. Benefit B, Pickford M (1986) Miocene fossil cercopithecoids from Kenya. *Am J Phys Anthropol* 69:441–464.
45. Morales J, Pickford M (2006) A large Percrocutid carnivore from the Late Miocene (ca. 10–9 Ma) of Nakali, Kenya. *Annales de Paleontologie* 92(4):359–366.
46. Nakaya H, Pickford M, Nakano Y, Ishida H (1984) The late Miocene large mammal fauna from the Namurungule Formation, Samburu Hills, northern Kenya. *Afr Stud Monogr* (Suppl 2):87–131.
47. Nakaya H, Pickford M, Yasui K, Nakano Y (1987) Additional large mammalian fauna from the Namurungule Formation, Samburu Hills, northern Kenya. *Afri Stud Monogr* (Suppl 5):79–130.
48. Nakaya H, Watade M (1990) Hipparion from the upper Miocene Namurungule Formation, Samburu Hills, Kenya: Phylogenetic significance of newly discovered skull. *Geobios* 23:195–219.
49. Nakaya H (1994) Faunal change of late Miocene Africa and Eurasia: Mammalian fauna from the Namurungule Formation, Samburu Hills, northern Kenya. *Afri Stud Monogr* (Suppl 20):1–103.
50. Tsujikawa H (2005) The updated late Miocene large mammal fauna from Samburu Hills, northern Kenya. *Afr Stud Monogr* (Suppl 32):1–50.
51. Werdelin L, Sanders W (2010) *Cenozoic Mammals of Africa* (University of California Press, Berkeley, CA).
52. Nakaya H, Tsujikawa H (2006) Late Cenozoic mammalian biostratigraphy and faunal change. *Human Origins and Environmental Backgrounds*, pp 59–70.

Supplementary Information

SI Text

Stable Carbon Isotopes in Plants and Teeth

Photosynthetic pathway primarily determines the $\delta^{13}C$ value of a plant. Today in East Africa trees and shrubs use the more primitive and common C_3 pathway, or Calvin cycle, and have a $\delta^{13}C$ value of -23 to -36‰, whereas nearly all grasses and some sedges below 3000 m elevation use the more derived C_4 pathway, or Hatch-Slack cycle, and have a $\delta^{13}C$ value of -14 to -10‰ (1-3). The difference in the $\delta^{13}C$ values between C_3 and C_4 plants is due to the different metabolic pathways plants use to fix atmospheric CO_2 (4). The ~13 ‰ range in $\delta^{13}C$ values of C_3 plants is controlled by environmental conditions. The most negative $\delta^{13}C$ values are found in closed canopy forests (5). The most commonly cited mechanism is the "canopy effect" where respired CO_2 is recycled within the canopy (6). Xeric conditions can lead to $\delta^{13}C$ values several permil more positive than the mean C_3 value. In Kenya, modern C_3 plants from open forests and bushlands have $\delta^{13}C$ values of -27.8 ± 0.3 ‰ and -27.0 ± 0.2 ‰, respectively. C_3 plants from Mpala, Kenya sampled in 1998 have an average value of -24.6 ‰ (n=15) (7) . Crassulacean Acid Metabolism (CAM) is a third photosynthetic pathway that some plants use in some arid ecosystems, but it is much less common than the C_3 and C_4 pathways. CAM plants are not widely consumed by extant herbivores in East Africa, and therefore are not considered further here.

During tooth formation, carbon derived from diet is incorporated into enamel as carbonate anions. The difference between the stable isotope ratio of these two phases, the $\delta^{13}C$ of diet ($\delta^{13}C_{diet}$) and $\delta^{13}C$ value of enamel ($\delta^{13}C_{enamel}$), is expressed as an

enrichment factor, $\varepsilon^{*}_{diet\text{-}enamel}$, where $\varepsilon^{*}_{diet\text{-}enamel} = [(\delta^{13}C_{enamel} + 1000)/(\delta^{13}C_{diet} + 1000) - 1] * 1000$. The asterisk on ε^{*} indicates that isotopic enrichment between the two phases is not necessarily limited to equilibrium fractionation processes. The $\varepsilon^{*}_{diet\text{-}enamel}$ for large ruminant ungulates is 14.1 ± 0.5‰ (3). In non-ruminant herbivores, the enrichment between diet and enamel ($\varepsilon^{*}_{diet\text{-}enamel}$) is slightly smaller (12 to 14‰; Passey et al. (8)). However, we use an $\varepsilon^{*}_{diet\text{-}enamel}$ of 14.1‰ for all samples in the preceding discussion. Herbivores with diets that consist of a mixture of C_3 and C_4 vegetation will have intermediate $\delta^{13}C$ values that depend on the mixing proportion of the two plant types.

The $\delta^{13}C$ values of C_3 and C_4 diets

Plants fix atmospheric CO_2 to form biomass, and therefore the $\delta^{13}C$ value of atmospheric CO_2 ($\delta^{13}C_{atm}$) must also be measured or estimated in order to determine a threshold enamel $\delta^{13}C$ value ($\delta^{13}C_{enamel}$) that indicates the presence of C_4 in diet. The current $\delta^{13}C_{atm}$ value is about -8.2‰, but has fluctuated between -6.8 to -4.9‰ over the last 20 Ma (9, 10). We use $\delta^{13}C$ values of the atmosphere ($\delta^{13}C_{atm}$) based on North Atlantic benthic Foraminifera to calculate $\delta^{13}C$ values of enamel ($\delta^{13}C_{enamel}$) for pure C_3 and pure C_4 diets based on the age of the sediments at each site (10). We use the mean $\delta^{13}C_{atm}$ value from the upper limit of the 90% confidence interval from the high resolution or three million year time-averaged benthic Foraminifera record as a conservative value to calculate a maximum $\delta^{13}C_{enamel}$ value for a pure C_3 diet (Table S2). The range of maximum $\delta^{13}C_{enamel}$ values for a pure C_3 diet is from -7.7 to -8.2‰, and the mean is -7.9 ± 0.2‰. We use the lower limit of the 90% confidence interval $\delta^{13}C_{atm}$ value from each

time period to conservatively calculate a $\delta^{13}C_{enamel}$ value for a pure C_4 diet. The $\delta^{13}C_{enamel}$ range for a pure C_4 diet is from +2.4 to +3.1‰, and the mean is 2.9 ± 0.2‰.

Statistical Analysis

The $\delta^{13}C$ values are derived from mixed C_3-C_4 ecosystems where the distribution of the $\delta^{13}C$ value of plants is bimodal, and therefore not normally distributed. A Shapiro-Wilk test for normality demonstrates that the data are not distributed normally by age group (Table S2). Only data from one of seven age groups, the Upper Namurungule (9.3 Ma, n= 34), satisfy the null hypothesis of normality. Thus, the median and range of $\delta^{13}C_{enamel}$ (hereafter, $\delta^{13}C$) values are more appropriate than the mean and standard deviation for describing central location and variance of each population. We apply the nonparametric Mann-Whitney *U* test to check for significant difference in the median $\delta^{13}C$ values within each family between successive time periods. The test is only applied to groups with at least five samples per time period.

Mann-Whitney *U* test results indicate significant shifts ($p < 0.05$) in the median $\delta^{13}C$ value between successive age increments (i.e., 9.9 to 9.6 Ma) where there are more than five isotope analyses within a family (Table S3). Shifts in diet do not occur synchronously between families throughout the record. Significant changes in the median $\delta^{13}C$ value occur between 9.9 and 9.6 Ma for all families except gomphotheriids; between 9.6 and 7.4 Ma for hippopotamids ($p = 0.008$) and rhinocerotids ($p = 0.003$); between 9.3 and 7.4 Ma for gomphotheriids and elephantids ($p = 0.0016$); between 7.4 and 6.5 Ma for equids ($p = 0.013$) and hippopotamids ($p = 0.011$); between 6.5 and 4.2 Ma for equids ($p = 0.045$), hippopotamids ($p = 0.039$) and suids ($p = 0.022$); and between 4.2 and 3.2 Ma for suids ($p = 0.011$) (Table S3).

Geology and Age Control

The Nakali Formation is a 340 m thick sequence of volcanoclastic sediments divided into three members (Lower, Middle, and Upper). The Nakali area (1.1850° N, 36.3756° E) was first investigated in 1969 by Emiliano Aguirre and Phillip Leakey (11), but little work was done on the geology of the Nakali Formation until the Japan-Kenya Paleoanthropological Expedition started work there in 2002. The formation is exposed over a ~16 km^2 area on the eastern flank of the Suguta Valley. North-south trending post-depositional normal faults divide the area structurally into three blocks (western, central, and eastern). The Nakali Formation is underlain by the Alengerr tuffs (10.6 ± 0.40 Ma) and overlain unconformably by the Nasorut volcanic sequence (7.74 ± 0.21 Ma) (12). The Lower Member transitions from a lacustrine facies consisting of turbidites and debrites at the base to a fluvio-lacustrine facies near the top of the member. Two $^{40}Ar/^{39}Ar$ ages from single anorthoclase grains separated from a pumiceous tuff at the top of the Lower Member are 9.90 ± 0.09 Ma and 9.82 ± 0.09 Ma (Figure 2). The Middle Member is a 40 m thick pyroclastic flow deposit that has yielded a $^{40}Ar/^{39}Ar$ age on anorthoclase $^{40}Ar/^{39}Ar$ age of 10.10 ± 0.12 Ma. The Upper Member is composed of primarily fluvio-lacustrine deposits interbedded with sparse debris flows and lapilli tuffs (12). A majority of the fauna comes from this member, including the hominoid fossils. Reversed polarity in the Middle Member where the isotopically dated samples were collected securely places the Lower Member in chron C5n.2n, the Middle Member in C5n.1r, and the Upper Member in C5n.1n. The isotopic age data; paleomagnetic data; and evidence for rapid sedimentation; which includes turbidites, debrites, debris flows,

lahars, tuffs, and a lack of paleosols; suggests that a single age of 9.9 Ma is most appropriate for the Nakali fauna.

In the Samburu Hills 60 kilometers north of Nakali, five formations make up a non-continuous succession of Neogene sedimentary and volcanic rocks spanning from 19.2 to 4.1 Ma (Figure 1 and (13)). The geology of the area was first described by Baker (14) and since 1980, the Samburu Hills and adjacent Nachola areas have been studied by the Japan-Kenya Paleoanthropological Expedition team (15, 16). The Late Miocene Namurungule Formation is exposed in the western part of the Samburu Hills, near the eastern edge of the Suguta valley (1.7033° N, 36.5262° E). The 100 to 200 m thick formation is divided into a Lower Member and an Upper Member, which are separated by a 14 to 30 m thick lahar (17, 18). The Namurungule Formation is underlain conformably by the Aka Aiteputh Formation, and unconformably overlain by the Kongia Formation (7.3–5.3 Ma)(18). A whole rock K-Ar age on an Upper Aka Aiteputh basalt flow below the contact with the Namurungule has an age of 10.07 ± 0.42 Ma (Fig. 5 of (18)). The Upper Aka Aiteputh contains red calcareous paleosols interbedded with basaltic lavas, and the contact with the Lower Namurungule is defined by a 3 m thick poorly-sorted conglomerate (18). K-Ar ages on sanidine from two pumice-rich tuffs that bracket the hominoid bearing sediments of the Lower Namurungule are 9.57 ± 0.22 Ma and 9.47 ± 0.22 Ma, respectively (19). Based on isotopic age data, paleomagnetic data, and sedimentary facies from the Upper Aka Aiteputh through the Namurungule Formation, Sawada et al. (19) place the Lower Namurungule in chron C4Ar. 2n (9.64 to 9.58 Ma) and the Upper Namurungule in chrons C4Ar.2r to C4Ar.1n, which range from 9.58 to 9.31 Ma (Figure 2). Thus we use an age of 9.6 Ma for the Lower Namurungule

fauna and 9.3 Ma for the Upper Namurungule fauna. Saneyoshi et al. (18) provide a detailed review of the geology and depositional environment of the Namurungule Formation.

Lothagam is located in the Turkana Basin approximately 55 km east-southeast of the town of Lodwar, and 140 km north-northwest of the Samburu Hills (Figure 1; 2.9098° N, 36.0455° E). The area (approximately 5 by 10 km) is interpreted as an uplifted footwall block that exposes sediments deposited in the Kerio Basin from the Middle Miocene to the Pliocene (20). Today, two north-south trending ridges define the area. Fossil-bearing sediments are exposed between the ridges and on their flanks. The eastern ridge is a horst called Lothagam Hill (or Lothsegam in the Turkana language) and is the more prominent of the two. The first detailed geological and paleontological study at Lothagam was led by Patterson in 1967 and subsequent work by Behrensmeyer (21) and Powers (22) refined the stratigraphic framework and age. A more comprehensive study of the fauna and geology at Lothagam resulted from a four-year field campaign led by M.G. Leakey from 1989 to 1993 (23). The geologic component of the most recent campaign included determining precise radiometric ages throughout the entire 900 m section by McDougall and Feibel (24), classification of paleosols by Wynn (25), stable isotope analysis of pedogenic carbonates (26), and revision of the stratigraphy by Feibel (27) that built upon the previous work of Powers (22) and Behrensmeyer (21).

In the present study, the Late Miocene to Pliocene fauna from Lothagam come from the Upper and Lower Members of the Nawata Formations and the Apak and Kaiyumung Members of the Nachukui Formation. The Nawata Formation is bounded below by the volcanic Nabwal Arangan Formation. Basalt and phonolite whole rock K-

Ar dates from this formation range from 14.2 ± 0.2 Ma at the base to 9.1 ± 0.2 at the top of the formation (Figure 2; (24)). The Nawata Formation is split into an Upper and a Lower Member. The base of the 137 m thick Lower Nawata member consists of alluvial plain sediments and poorly sorted gravel conglomerates interpreted as ephemeral stream deposits (27). The upper part of the Lower Nawata contains fluvial deposits characteristic of a perennial river system. Paleosols are present throughout the Lower Nawata and are primarily vertisols with occasional calcaric fluvisols or calcaric regosols (25). Carbon isotope values of 14 pedogenic carbonates from 11 paleosols in the Lower Nawata range from -9.0 to -2.2 ‰. These data represent C_3-dominated to mixed C_3/C_4 ecosystems, the latter of which contains significant amounts of C_4 biomass (26). One tuffaceous bed from a series of altered tuffs called the Lower Markers in the lower half of this member has an arithmetic mean $^{40}Ar/^{39}Ar$ age on 33 alkali feldspar crystals of 7.44 ± 0.05 Ma, which we use as an age for all Lower Nawata fauna (24). A majority of the Lower Nawata fauna comes from above this dated tuff.

The informally named Marker Tuff designates the base of the Upper Nawata and provides the only datable material from the Upper Nawata. Ten single crystal alkali feldspars from Marker Tuff yield an arithmetic mean $^{40}Ar/^{39}Ar$ age of 6.54 ± 0.04 Ma (24). The 125 m thick Upper Nawata contains abundant thick, multi-storied sandstones that may suggest increased reworking of sediments due to decreased subsidence rates in the basin (27). The Upper Nawata contains fewer paleosols than the Lower Nawata, despite similar overall thicknesses. Carbon isotope values of five pedogenic carbonates from four paleosols in the Upper Nawata range from -5.9 to -1.3 ‰, which indicate mixed C_3/C_4 ecosystems (26).

The 400 m thick Nachukui Formation overlies the Nawata Formation, probably conformably, and is divided into five members at Lothagam (24). The formation is part of the Plio-Pleistocene Omo Group, which also includes the Koobi Fora and the Shungura Formations (28). Fauna in this study are from the basal Apak Member and the Kaiyumung Member, neither of which are present in the original type sections from West Turkana. Sites of similar age to the Kaiyumung are present in the Nachukui Formation (e.g., at Lomekwi) along the west side of Lake Turkana.

The Apak Member is a ~100 m thick sequence of fluvial to lacustrine sandstones with occasional mudstones and eight paleosols (24, 25). The upper part of the Apak Member is lacustrine deposits of Lonyumun Lake age (4.1 Ma). The arithmetic mean $^{40}Ar/^{39}Ar$ age of two alkali feldspars from pumice is 4.22 ± 0.03 Ma (24). We use this as the age for all Apak Member fauna. Carbon isotope values of seven pedogenic carbonates from five paleosols in the Apak Member range from -9.4 to -3.0 ‰, which indicate C_3-dominated to mixed C_3/C_4 ecosystems (26). The Lothagam Basalt, assigned an age of 4.20 ± 0.03 Ma based on $^{40}Ar/^{39}Ar$ and K/Ar dating, overlies the Apak Member and underlies the Muruongori Member.

Age spectra from whole rock and plagioclase $^{40}Ar/^{39}Ar$ ages from one sample (K86-2899B) indicate excess argon, probably due to incomplete degassing of the glass component of the basalt at the time of eruption (24). Therefore, the age assigned to the Lothagam Basalt is a maximum age. Stratigraphic and geochemical correlation place the Lothagam Basalt in the Gombe Group Basalts, all of which have reversed polarity that place it securely in the Gilbert Chron (29). In all locations where the Gombe Group

Basalts and Moiti Tuff are both present, the tuff overlies the basalt. Thus the age of Moiti tuff, 3.97 ± 0.03, provides a minimum age constraint for the basalts (30).

Fluvial sediments of the 94 m thick Kaiyumung Member conformably overlie the Muruongori Member, but there may be depositional hiatuses within these members. The absence of volcanic deposits in the Kaiyumung Member precludes isotopic dating and correlation by tephrastratigraphy. In particular, the absence of the Moiti, Lokochot, and Tulu Bor tuffs dated at 3.97, 3.60, and 3.48 Ma, respectively, indicates that this time period is missing either due to depositional hiatus or erosion. The Lokochot Tuff and the Tulu Bor Tuff are present at Echawe less than 20 km to the south in the region, and both are present in the Baringo Basin at Kipcherere (31); the Tulu Bor Tuff has also been identified west of Kanapoi and in a fault along the eastern margin of Napedet about 17 km west of Lothagam and the Naibar Tuff, which is only slightly older than the Moiti Tuff (McDougall et al. submitted) is exposed in Naiyenapunedebu about 4 km north of the northern exposures of the Kaiyumung Member. This suggests that the reversed polarity section in the Kaiyumung Member is the Kaena (2An.lr) or Mammoth (2An.2r) subchron of the Gauss magnetochron (2An), and therefore we use an age of 3.2 Ma for the Kaiyumung fauna.

Fauna

Equidae. A single equid species is recognized from the Nakali and Namurungule Formations as member of the three-toed Hipparionini tribe, and has previously been alternately referred to as *Hipparion primigenium, H. sitifense, "Cormohipparion" perimense, H. africanum,* and *H.* aff. *africanum* (12, 32–36). In a recent review of

African Equidae, Bernor et al. (37) reject the use of the genus *Hipparion* for all late Miocene African equids, with the exception of those from Sahabi, Libya, and instead use "*Cormohipparion*" or *?"Sivalhippus"*. Therefore, we refer to this taxon as "*Cormohipparion*" aff. *africanum*. The authors note that this part of the Miocene was a period of rapid diversification within the equids, and that the Namurungule equids may be the sister taxon to the genus *Eurygnathohippus* represented by at least three species from Lothagam. *"Cormohipparion"* cf. *primigenium* is rare in the Lower Nawata and absent in the Upper Nawata and Nachukui Formation, whereas *Eurygnathohippus turkanense* and *Eu. feibeli* are ubiquitous in the Upper and Lower Members of the Nawata Formation. In the Apak and Kaiyumung Members of the Nachukui Formation, *Eu.* spp. indet. (small and large forms) are present (38).

Rhinocerotidae. *Kenyatherium bishopi* is the most common rhinocerotid species at Nakali, which is where the type specimen was discovered (39). At least one other species is present, although it has only been identified to family (12). At least five rhinocerotids have been identified over the past three decades from the Namurungule Formation. In the Lower Namurungule, *Brachypotherium sp., Kenyatherium bishopi, Chilotheridium pattersoni*, *Paradiceros mukirii,* and most recently, *Ceratotherium* sp.?, have been identified (32, 33, 35, 36, 40, 41). Fossil material from the Upper Namurungule has only been identified to family. A recent review of African rhinocerotids by Geraads (41) is in agreement with the presence of *K. bishopi* in the Nakali Formation, but suggests that only two rhinocerotids are present in the Namurungule, *K. bishopi* and *Ceratotherium* sp.?

At Lothagam, three rhinocerotid species have been identified. *Brachypotherium lewisi* is the common rhinocerotid in both Members of the Nawata Formation. *Ceratotherium* sp.? is also present (42). *Diceros praecox* first occurs in the Upper Nawata. *D. praecox* and *Ceratotherium* sp.? occur in the Apak Member, but only *Ceratotherium* sp.? specimens have been found in the Kaiyumung Member of the Nachukui Formation (42).

Gomphotheriidae and Elephantidae. Two gomphotheriids, *Anancus* sp. and *Choerolophodon ngorora* (advanced morph), have been identified at Nakali (12, 39, 43). *C. ngorora* and *Tetralophodon* sp. nov are present in the Lower Namurungule (36, 43). As of yet, *Tetralophodon* sp. nov is the only gomphotheriid to come from the Upper Namurungule (36). Elephantids first appear at Lothagam in the Lower Nawata, where *A. kenyensis* is accompanied by the elephantids *Stegotetrabelodon orbus* and *Primelephas gomphotheroides* (44). In the Upper Nawata there is *A. kenyensis*, a trilophodont gomphotheriid (gen. et sp. indet.), *S. orbus*, and *Elephas nawatensis*, which Sanders et al. (43) refer to as *Primelephas korotorensis*. The greatest diversity from these two families occurs in the Apak Member, where there is *A. kenyensis*, *S. orbus*, *Elephas ekorensis* (and cf. *E. ekorensis*), *Loxodonta* sp. indet., and two unidentified elephantids, *Elephas* gen. et sp. incertae sedis A and *E.* gen. et sp. incertae sedis B (44). No gomphotheriid or elephantid specimens have been recovered from the Kaiyumung Member.

Bovidae. Bovids from Nakali include *Tragelaphini* gen. indet., *Boselaphini* gen. indet., and *Gazella* sp. indet. (12, 39). From the Lower Namurungule come *Boselaphini*

gen. et sp. nov., *Tragoportax* sp., *Pachytragus* sp., *Antidorcas* sp., and *Bovidae* gen. indet. (35, 36). The Upper Namurungule has one boselaphine (gen. indet.) and at least two antilopines, *Antidorcas* sp., *Gazella* sp., and *Antilopini* gen. indet. (35, 36). Gentry (45) reports the boselaphine *Miotragocerus* sp. aff. *M. cyrenaicus*, in the Lower Namurungule and the Nawata Formation. There is a high diversity of bovids throughout the Lothagam sequence that includes seventeen species and nine tribes (46). They are the most abundant terrestrial herbivore throughout the succession. Aepycerotini (impalas) are the most common bovid, but decline in abundance throughout the succession, while the Boselaphini decline sharply between the Lower and Upper Nawata. Other tribes present include Tragelaphini, Bovini, Reduncini, Hippotragini, Alcelaphini, Antilopini, and Neotragini (SI Table 1). Harris (46) provides a detailed description and review of the Lothagam bovids.

Hippopotamidae. Only one hippopotamid species, the bunodont *Kenyapotamus coryndoni*, has been identified from the Nakali and Namurungule Formations (12, 32-36). *K. coryndoni* material from both sites is mostly isolated or fragmentary teeth. An exception is a mandible from the Namurungule (KNM-SH 15857) that reveals a narrow muzzle and lower jaw morphology similar to that of *Archaeopotamus lothagamensis* from the Lower Nawata (47). In addition to this relatively rare hippopotamid, the larger *Archaeopotamus harvardi* is present from the Lower Nawata through the Apak Member of the Nachukui Formation. *A. harvardi* is the predominant hippopotamid taxon at Lothagam, where hippopotamids comprise 27% of all mammalian fauna from the

succession (48). A third hippopotamid, *Hippopotamus* aff. *H. protamphibius*, comes from the Apak Member exclusively (48).

Suidae. Nakali suids are identified only to genus as *Nyanzachoerus* spp., but their presence at this site is significant because it pushes their first appearance back to 9.9 Ma in East Africa (12). Two suids, a smaller form identified as *Nyanzachoerus* cf. *N. devauxi* and larger form, *Nyanzachoerus* sp. (large), come from the Namurungule Formation (36). The latter is similar to *N. syrticus* (49). The smaller form is present in both members, while the placement of the larger form is uncertain (36). In the Lower Nawata, there is one kubanochoere that is similar to unpublished mandibles from Nakoret with extremely large premolars. *N. devauxi* is present throughout the Nawata Formation, but not in the Nachukui Formation (49). *N. syrticus* (conspecific with *N. tulotos*) and *N.* cf. *syrticus*, are also present in the Nawata Formation, and Harris and Leakey (49) note an increase in size and complexity of the upper third molar in Upper Nawata specimens compared to those from the Lower Nawata. Rare potamochoere and cainochoere material also comes from the Nawata Formation. *Nyanzachoerus* cf. *N. australis* appears in the Upper Nawata and is dominant in the Apak Member of the Nachukui. The youngest nyanzachoere to appear in the Lothagam sequence is *N. pattersoni* (= *N. kanamensis)*, which occurs in the Kaiyumung Member. *Notochoerus* is thought to have evolved from the nyanzachoere lineage (50). *Notochoerus jaegeri* first appears at Lothagam in the Apak Member. *Notochoerus euilus* follows, first in the uppermost part of the Apak Member (*Not.* cf. *euilus*), and then as the common suid in the Kaiyumung Member (49).

Deinotheriidae. Deinotheriid material has been recovered from the Nakali Formation and from all members of the Namurungule, Nawata, and Nachukui Formations. All material is identified as *Deinotherium bozasi* or *D.* cf. *bozasi* (12, 35, 36, 51).

Giraffidae. East African giraffids are interpreted as browsers throughout the geologic record, with the exception of the Pliocene sivatheres (52, 53). The Nakali Formation has yielded two giraffids, *Palaeotragus* cf. *germaini* and ?*Samotherium* sp. (12). These taxa are also found in the Lower and Upper Namurungule (35, 36). Although giraffids are rare at Lothagam, *P. germaini* and *Palaeotragus* sp. occur throughout the Nawata Formation. These taxa are replaced by a more progressive giraffid, *Giraffa stillei*, in the lower part of the Apak Member. *G. stillei* is present through the Kaiyumung Member (54).

Sampling Methods. For all fossil teeth housed in the National Museum of Kenya's (KNM) paleontology collection in Nairobi, enamel was removed using a Dremel® battery-powered drill with diamond powder or carbide bits. One to four mg of powdered enamel was removed from a non-diagnostic part of the tooth, often along fractured enamel surfaces, in a ~1 mm wide groove or pit. Broken teeth are ideal for sampling because it is easy to distinguish enamel from dentin, cementum, or matrix material along fractured enamel surfaces that are normal to the enamel-dentin or cementum-dentin junction curved plane. A subset of samples is tooth fragments that were collected in the field at Lothagam. Enamel powder was collected either by removing dentin, cementum,

and matrix material and subsequently crushing the fossil enamel with a mortar and pestle, or by the aforementioned Dremel technique.

Whenever possible, the third molar was sampled because it forms during adulthood and therefore is the best representative of an individual's diet. We treat samples from different teeth of an individual (maxilla or mandible) as discrete samples because each tooth represents a different time period.

Laboratory Methods. Powdered enamel samples were digested in 100 % H_3PO_4 (phosphoric acid) off-line for 36 hours at 25°C in sealed vessels, or online using a Finnigan CarboFlo®. For off-line reactions, 15–50 mg of enamel powder was reacted in the presence of silver wool or foil. The CarboFlo® system is a hybrid positive pressure/vacuum system with a common acid bath (CAB). Approximately 500 μg of fossil enamel is weighed out into a silver capsule, which is used as a precautionary measure to oxidize any SO_2 produced during digestion in phosphoric acid. The silver capsules are dropped into the CAB from an autosampler carousel. The sample reacts in the CAB, which is stirred vigorously at 90° C for 10 minutes. A 60 ml/min stream of He sweeps the liberated H_2O and CO_2 through a dry ice/ethanol trap to remove water and then through a liquid nitrogen (LN) trap to collect the CO_2. Following the 10 minute reaction period, the LN trap is isolated from positive pressure and evacuated with a rotary vacuum pump to ~10^{-3} Torr. The LN trap is removed and the CO_2 is cryogenically transferred to a microvolume held at -170°C. Once transferred to the microvolume, the CO_2 is analyzed through the dual inlet system on the mass spectrometer. Internal

laboratory enamel and Carrara carbonate standards are used for data correction of samples.

A subset of enamel samples representing all sites was treated with 3% H_2O_2 for 15-30 minutes, rinsed three times with DI, and dried overnight at 60°C. The difference in $\delta^{13}C$ values between treated and untreated samples was less than ±1 ‰ for most samples. Loss of sample material during treatment was on the order of one to several milligrams. Due to the limited amount of sample (~1–4 mg) collected from the KNM accessioned teeth and minimal effect of treatment and the loss of sample associated with treatment, remaining samples were not treated.

References:

1. Tieszen LL, Senyimba MM, Imbamba SK, & Troughton JH (1979) The distribution of C3 and C4 grasses and carbon isotope discrimination along an altitudinal and moisture gradient in Kenya. *Oecologia* 37(3):337-350.
2. Young HJ & Young TP (1983) Local Distribution of C_3 and C_4 Grasses in Sites of Overlap on Mount Kenya. *Oecologia* 58(3):373-377.
3. Cerling T & Harris J (1999) Carbon isotope fractionation between diet and bioapatite in ungulate mammals and implications for ecological and paleoecological studies. *Oecologia* 120(3):347-363.
4. Farquhar G, Ehleringer J, & Hubick K (1989) Carbon isotope discrimination and photosynthesis. *Annual Review of Plant Biology* 40(1):503-537.
5. Cerling TE, Hart JA, & Hart TB (2004) Stable isotope ecology in the Ituri Forest. *Oecologia* 138(1):5-12.
6. van der Merwe N & Medina E (1991) The canopy effect, carbon isotope ratios and foodwebs in Amazonia. *Journal of Archaeological Science* 18(3):249-259.
7. Cerling T, Harris J, & Passey B (2003) Diets of East African Bovidae based on stable isotope analysis. *Journal Information* 84(2):456-470.
8. Passey B, *et al.* (2005) Carbon isotope fractionation between diet, breath CO2, and bioapatite in different mammals. *Journal of Archaeological Science* 32(10):1459-1470.
9. Passey B, *et al.* (2009) Strengthened East Asian summer monsoons during a period of high-latitude warmth? Isotopic evidence from Mio-Pliocene fossil mammals and soil carbonates from northern China. *Earth and Planetary Science Letters* 277(3-4):443-452.
10. Tipple B, Meyers S, & Pagani M (2010) Carbon isotope ratio of Cenozoic CO2: A comparative evaluation of available geochemical proxies. *Paleoceanography* 25(3).
11. Aguirre E & Leakey P (1974) Nakali; nueva fauna de Hipparion del Rift Valley de Kenya. *Estudios Geologicos (Madrid)* 30(2-3):219-227.
12. Kunimatsu Y, *et al.* (2007) A new late Miocene great ape from Kenya and its implications for the origins of African great apes and humans. *Proceedings of the National Academy of Sciences* 104(49):19220-19225.
13. Sawada Y, *et al.* (2006) The Ages and Geological Backgrounds of Miocene Hominoids Nacholapithecus, Samburupithecus, and Orrorin from Kenya. *Human origins and environmental backgrounds*:71-96.
14. Baker BH (1963) Geology of the Baragoi area; degree sheet 27, N.E. quarter. *Report - Republic of Kenya, Mines and Geological Department* 53.
15. Ishida H (1984) Outline of 1982 survey in Samburu Hills and Nachola area, northern Kenya. *African Studies Monographs, Supplementary Issue* (2):1-13.
16. Ishida H (1987) Outline the Third Season, 1984, of the Palaeoanthropological Expedition Team to the Samburu Hills and Nachola Areas, Northern Kenya. *African Studies Monographs, Supplementary Issue* (5):1-6.
17. Tateishi M (1987) Sedimentary facies of the Miocene in the Samburu Hills, northern Kenya. *African Study Monographs, Supplementary Issue* 5:59-77.
18. Saneyoshi M, Nakayama K, Sakai T, Sawada Y, & Ishida H (2006) Half graben filling processes in the early phase of continental rifting: The Miocene Namurungule Formation of the Kenya Rift. *Sedimentary Geology* 186(1-2):111-131.
19. Sawada Y, *et al.* (1998) K-Ar ages of Miocene Hominoidea (Kenyapithecus and Samburupithecus) from Samburu Hills, northern Kenya. *Comptes Rendus de l'Academie des Sciences, Serie II.Sciences de la Terre et des Planetes* 326(6):445-451.
20. McDougallL I & Feibel CS (1999) Numerical age control for the Miocene-Pliocene succession at Lothagam, a hominoid-bearing sequence in the northern Kenya Rift. *Journal of the Geological Society* 156(4):731-745.
21. Behrensmeyer A (1976) Lothagam Hill, Kanapoi, and Ekora: A general summary of stratigraphy and faunas. *Earliest Man and Environments in the Lake Rudolf Basin: Stratigraphy, Paleoecology, and Evolution*:163-170.
22. Powers DW (1980) Geology of the Mio-Pliocene sediments of the Lower Kerio river valley, Kenya. PhD (Princeton, Princeton).

23. Leakey M & Harris J (2003) *Lothagam: the dawn of humanity in eastern Africa* (Columbia Univ Pr).
24. McDougall I & Feibel CS (1999) Numerical age control for the Miocene-Pliocene succession at Lothagam, a hominoid-bearing sequence in the northern Kenya Rift. *Journal of the Geological Society* 156(4):731-745.
25. Wynn JG (2003) Miocene and Pliocene paleosols of Lothagam. *Lothagam: The dawn of humanity in eastern Africa. Columbia University Press, New York, pp31-42*, eds Leakey MG & Harris JM (Columbia University Press, New York), Vol Lothagam: The dawn of humanity in Eastern Africa, pp 31-42.
26. Cerling T, Harris J, & Leakey M (2003) Isotope paleoecology of the Nawata and Nachukui Formations at Lothagam, Turkana Basin, Kenya. *Lothagam: The Dawn of Humanity in Eastern Africa*, eds Leakey MG & Harris JM (Columbia University Press, New York), pp 605-623.
27. Feibel C (2003) Stratigraphy and depositional history of the Lothagam Sequence. *Lothagam: The Dawn of Humanity in Eastern Africa*, eds Leakey MG & Harris JM (Columbia University Press, New York), pp 17-29.
28. Feibel CS, Brown FH, & McDougall I (1989) Stratigraphic context of fossil hominids from the Omo group deposits: Northern Turkana Basin, Kenya and Ethiopia. *American Journal of Physical Anthropology* 78(4):595-622.
29. Haileab B, Brown FH, McDougall I, & Gathogo PN (2004) Gombe Group basalts and initiation of Pliocene deposition in the Turkana depression, northern Kenya and southern Ethiopia. *Geological Magazine* 141(1):41-53.
30. McDougall I & Brown F (2008) Geochronology of the pre-KBS Tuff sequence, Omo Group, Turkana Basin. *Journal of the Geological Society* 165(2):549-562.
31. Namwamba F (1993) Tephrostratigraphy of the Chemeron Formation, Baringo Basin, Kenya. MS (University of Utah, Salt Lake City).
32. Nakaya H, Pickford M, Nakano Y, & Ishida H (1984) The late Miocene large mammal fauna from the Namurungule Formation, Samburu Hills, northern Kenya. *African Studies Monographs, Supplementary Issue* (2):87-131.
33. Nakaya H, Pickford M, Yasui K, & Nakano Y (1987) Additional large mammalian fauna from the Namurungule Formation, Samburu Hills, northern Kenya. *African Studies Monographs, Supplementary Issue* (5):79-130.
34. Nakaya H & Watade M (1990) Hipparion from the upper Miocene Namurungule Formation, Samburu Hills, Kenya; phylogenetic significance of newly discovered skull. *Geobios* 23(2):195-219.
35. Nakaya H (1994) Faunal change of late Miocene Africa and Eurasia: mammalian fauna from the Namurungule Formation, Samburu Hills, northern Kenya. *African Studies Monographs, Supplementary Issue* (20):1-103.
36. Tsujikawa H (2005) The updated late Miocene large mammal fauna from Samburu Hills, northern Kenya. *African Studies Monographs, Supplementary Issue* (32):1-50.
37. Bernor R, Armour-Chelu M, Gilbert H, Kaiser T, & Schulz E (2010) Equidae. *Cenozoic Mammals of Africa*, eds Werdelin L & Sanders WJ (University of California Press, Berkeley), pp 685-721.
38. Bernor R & Harris J (2003) Systematics and evolutionary biology of the Late Miocene and Early Pliocene hipparionine equids from Lothagam, Kenya. *Lothagam: The Dawn of Humanity in Africa*, eds Leakey MG & Harris JM (Columbia University Press, New York), pp 387-413.
39. Aguirre E & Guerin C (1974) Premiere decouverte d'un Iranotheriinae (Mammalia, Perissodactyla, Rhinocerotidae) en Afrique; Kenyatherium bishopi nov. gen. nov. sp. de la formation vallesienne (Miocene superieur) de Nakali (Kenya). *Estudios Geologicos (Madrid)* 30(2-3):229-233.
40. Nakaya H & Watabe M (1990) Hipparion from the upper Miocene Namurungule Formation, Samburu Hills, Kenya: Phylogenetic significance of newly discovered skull. *Geobios* 23(2):195-219.
41. Geraads D (2010) Rhinocerotidae. *Cenozoic Mammals of Africa*, eds Werdelin L & Sanders WJ (University of California Press, Berkeley), pp 669-683.
42. Harris J & Leakey M (2003) Lothagam Rhinocerotidae. *Lothagam: The Dawn of Humanity in Africa*, eds Leakey MG & Harris JM (Columbia University Press, New York), pp 371-385.

43. Sanders W, Gheerbrant E, Harris J, Saegusa H, & Delmer C (2010) Proboscidea. *Cenozoic Mammals of Africa*, eds Werdelin L & Sanders WJ (University of California Press, Berkeley), pp 161-251.
44. Tassy P (2003) Elephantoidea from Lothagam. *Lothagam: The Dawn of Humanity in Africa*, eds Leakey MG & Harris JM (Columbia University Press, New York), pp 331-358.
45. Gentry A (2010) Bovidae. *Cenozoic Mammals of Africa*, eds Werdelin L & Sanders WJ (University of California Press, Berkeley), pp 741-796.
46. Harris J (2003) Bovidae from the Lothagam Succession. *Lothagam: The Dawn of Humanity in Eastern Africa*, eds Leakey MG & Harris JM (Columbia University Press, New York), pp 531-579.
47. Weston E & Boisserie J (2010) Hippopotamidae. *Cenozoic Mammals of Africa*, eds L W & WJ S (University of California Press, Berkeley), pp 853-871.
48. Weston E (2003) Fossil hippopotamidae from Lothagam. *Lothagam: The Dawn of Humanity in Africa*, eds Leakey MG & Harris JM (Columbia University Press, New York), pp 441-483.
49. Harris J & Leakey M (2003) Lothagam Suidae. *Lothagam: The Dawn of Humanity in Africa*, eds Leakey MG & Harris JM (Columbia University Press, New York), pp 485-522.
50. Bishop L (2010) Suiodea. *Cenozoic Mammals of Africa*, eds Werdelin L & Sanders WJ (University of California Press, Berkeley), pp 821-842.
51. Harris J (2003) Deinotheres from the Lothagam Succession. *Lothagam: The Dawn of Humanity in Eastern Africa*, ed Leakey MG (Columbia University Press, New York), pp 359-362.
52. Harris J, Solounias N, & Geraads D (2010) Giraffoidea. *Cenozoic Mammals of Africa*, eds Werdelin L & Sanders WJ (University of California Press, Berkeley), pp 797-811.
53. Cerling T, Harris J, & Leakey M (2005) Environmentally Driven Dietary Adaptations in African Mammals. *A History of Atmospheric CO_2 and Its Effects on Plants, Animals, and Ecosystems,* Ecological Studies, eds Baldwin IT, Caldwell MM, Heldmaier G, Jackson RB, Lange OL, Mooney HA, Schulze ED, Sommer U, Ehleringer JR, Denise Dearing M, *et al.* (Springer-Verlag), Vol 177, pp 258-272.
54. Harris J (2003) Lothagam Giraffids. *Lothagam: The Dawn of Humanity in Africa*, eds Leakey MG & Harris JM (Columbia University Press, New York), pp 523-530.

Table S1. Large herbivore fauna analyzed for $\delta^{13}C$ values from the Nakali, Namurungule, Nawata, and Nachukui Formations.

Order	Family	Tribe or Subfamily	Species	Site:	Nakali	Samburu Hills		Lothagam		Lothagam		Total # by Family
				Formation:	Nakali	Namurungule		Nawata		Nachukui		
				Member:	--	Lower	Upper	Lower	Upper	Apak	Kaiyum.	
Proboscidea												
	Deinotheriidae		Deinotherium bozasi & D. cf. bozasi		6	5		1	1	2	1	
			Number analyzed		**6**	**5**	**0**	**1**	**1**	**2**	**1**	**16**
	Gomphotheriidae		Anancus kenyensis							4		
			Anancus sp.		1							
			Tetralophodon sp. nov.		1		1					
			Choerolophodon ngorora		4							
			Gomphotheriidae gen. et sp. indet.		1	2	7	4				
			Number analyzed		**7**	**2**	**8**	**4**	**0**	**4**	**0**	**25**
	Elephantidae		Stegotetrabelodon orbus							1		
			Stegotetrabelodon sp.					2	1	1		
			Primelephas gomphotheroides						1			
			Primelephas or S. orbus					1	3			
			Elephantidae gen. et sp. indet.					1	6	3		
			Number analyzed		**0**	**0**	**0**	**4**	**11**	**5**	**0**	**20**
Perissodactyla												
	Equidae		"Cormohipparion" aff. africanum		35	24	13					
			Eurygnathohippus turkanense					1	2			
			Eurygnathohippus feibeli					1				
			Eurygnathohippus sp.					12	4	5		
			Number analyzed		**35**	**24**	**13**	**14**	**6**	**5**	**0**	**97**
Perissodactyla (cont.)												
	Rhinocerotidae											
			Chilotheridium pattersoni			4?						
			Kenyatherium bishopi		11							
			Brachypotherium lewisi				1	11	5	1		
			Ceratotherium sp.			?		2	4	1	3	
			Diceros praecox						4	3		
			Rhinocerotidae gen. et. sp. indet.			8	1	2		6		
			Number analyzed		**11**	**12**	**2**	**15**	**13**	**11**	**3**	**67**
Artiodactyla												
	Bovidae	Tragelaphini	Tragelaphini gen. & sp. indet.		6			1	2			
		Boselaphini	Boselaphini gen. & sp. indet.		1	5						
		Reduncini	Reduncini gen. & sp. indet.					3	1		1	
		Hippotragini	Hippotragini gen. et sp. indet.					1				
		Alcelaphini	Alcelaphini gen. & sp. indet.						1			
		Aepycerotini	Aepyceros sp.						1		1	
		Antilopini	Gazella sp. indet.			1						
			Antilopini gen. et sp. indet.				1					
			Bovidae gen. et sp. indet.		3		1	1	2	6		
			Number analyzed		**10**	**6**	**2**	**6**	**7**	**6**	**2**	**39**
	Giraffidae											
		Samotherinae	? Samotherium sp.		4							
		Palaeotraginae	Palaeotragus germaini					2				
			Palaeotragus cf. germaini			4						
			Palaeotragus sp.					2	1			
			Giraffa stillei								1	
			Giraffidae gen. et sp. indet.		11	3	3					
			Number analyzed		**15**	**7**	**3**	**4**	**1**	**0**	**1**	**31**
	Hippopotamidae		Kenyapotamus cf. coryndoni		7	6	3					
			Archaeopotamus lothagamensis					2	1			
			Archaeopotamus harvardi					4	2			
			Archaeopotamus sp. indet.					2				
			Hippopotamidae gen. et sp. indet.		7			21	25	7		
			Number analyzed		**14**	**6**	**3**	**29**	**28**	**7**	**0**	**87**
Artiodactyla (cont.)												
	Suidae		Nyanzachoerus spp.		3							
			Nyanzachoerus syrticus					5	8			
			Nyanzachoerus cf. Ny. syrticus			3	2					
			Nyanzachoerus cf. Ny. australis						2	3		
			Nyanzachoerus pattersoni								1	

Order	Family	Tribe or Subfamily	Species	Site:	Nakali	Samburu Hills		Lothagam		Lothagam		Total # by Family
				Formation:	Nakali	Namurungule		Nawata		Nachukui		
				Member:	--	Lower	Upper	Lower	Upper	Apak	Kaiyum.	
			Nyanzachoerus devauxi					5	1			
			Nyanzachoerus jaegeri							4		
			Notochoerus euilus & N. cf. euilus								5	
			Suidae gen. et sp. indet.		12	4	1	4	1	6		
			Number analyzed		**15**	**7**	**3**	**14**	**12**	**13**	**6**	**70**
			Total Number Specimens by Site		**113**	**69**	**34**	**91**	**79**	**53**	**13**	**452**

Taxa from the Nakali Formation are compiled from Aguirre & Alberdi, 1974; Aguirre & Leakey, P., 1974; Aguirre & Guerin, 1974; Flynn, 1984; Be

Table S2. Mammalian Fauna from the Nakali, Namurungule, Nawata, and Nachukui Formations by Member. Nakali Formation taxa are compiled fr

Order	Family	Tribe or Subfamily	Species	Site:	Nakali	Samburu Hills		Lothagam		Lothagam	
				Formation:	Nakali	Namurungule		Nawata		Nachukui	
				Member:	--	Lower	Upper	Lower	Upper	Apak	Kaiyum.
Proboscidea											
	Deinotheriidae		Deinotherium bozasi & D. cf. bozasi		X	9	8	1	1	1	1
			Number Deinotheriidae taxa		**1**	**1**	**1**	**1**	**1**	**1**	**1**
	Gomphotheriidae		Anancus kenyensis					1	2	3	
			Anancus sp.		X						
			Tetralophodon sp. nov.			3	6				
			Choerolophodon ngorora		X	1					
			Gomphotheriidae gen. et sp. indet.							1	
			Number Gomphotheriidae taxa		**2**	**2**	**1**	**1**	**1**	**2**	**0**
	Elephantidae		Stegotetrabelodon orbus					8	1	2	
			Primelephas gomphotheroides					3			
			Primelephas or S. orbus					7			
			Elephas nawatensis						2		
			Elephas ekorensis & cf. E. ekorensis							2	
			Loxodonta sp. indet. (?aff. L. exoptata)							3	
			Elephantidae gen. et sp. indet.					2		1	
			Elephantidae gen. & sp. incertae sedis A						1	1	
			Elephantidae gen. & sp. incertae sedis B							1	
			Number Elephantidae taxa		**0**	**0**	**0**	**4**	**3**	**6**	**0**
Perissodactyla											
	Equidae		"Cormohipparion" aff. africanum		X	107	44				
			"Cormohipparion" cf. "C". primigenium					2			
			Eurygnathohippus turkanense					30	16		
			Eurygnathohippus feibeli					13	24		
			Eurygnathohippus sp. indet. (large)							8	8
			Eurygnathohippus sp. indet. (small)							5	1
			Number Equidae taxa		**1**	**1**	**1**	**3**	**2**	**2**	**2**
	Rhinocerotidae										
			Chilotheridium pattersoni			21					
			Paradiceros mukirii			19	7				
			Kenyatherium bishopi		X	3					
			Brachypotherium lewisi					20	11	2	
			Ceratotherium sp.			?	?	2	6	1	4
			Diceros praecox						4	5	
			Iranotheriinae sp. nov.			10					
			Rhinocerotidae gen. et sp. indet.		X	29	10				
			Number Rhinocerotidae taxa		**2**	**5**	**2**	**2**	**3**	**3**	**1**
	Chalicotheriidae		Chalicotheriidae gen. et sp. indet.				1				
			Number Chalicotheriidae taxa		**0**	**0**	**1**	**0**	**0**	**0**	**0**
Artiodactyla											
	Bovidae	Tragelaphini	Tragelaphus kyaloae						1	7	3
			Tragelaphus cf. T. scriptus								1
			Tragelaphini gen. & sp. indet		X						
		Bovini	Simatherium aff. S. kohllarsoni							1	4
		Boselaphini	Tragoportax cf. T. cyrenaicus					7	1	2	
			Tragoportax sp. A					4	2		
			Tragoportax sp. B					1	2		
			Tragoportax sp. indet			5					
			Boselaphini gen. & sp. indet.		X	47					
Artiodactyla (cont.)											
		Reduncini	Kobus presigmoidalis					4	13	4	1
			Kobus laticornis						10		
			Menelikia leakeyi					4	3		
		Hippotragini	Praedamalis ?sp.					2	4		
			Hippotragus sp.					2	2	1	
		Alcelaphini	Damalacra sp. A					4	23	4	
			Damalacra sp. B					2	2	3	2
		Aepycerotini	Aepyceros premelampus					72	58	20	9
		Antilopini	Pachytragus sp.			16					

Order	Family	Tribe or Subfamily	Species	Site:	Nakali	Samburu Hills		Lothagam		Lothagam	
				Formation:	Nakali	Namurungule		Nawata		Nachukui	
				Member:	--	Lower	Upper	Lower	Upper	Apak	Kaiyum.
			Gazella sp. indet.		X		12	1	2	3	
			?Antidorcus sp.			1	2				
			Antilopini gen. et sp. indet.				1				
		Neotragini	Raphiceros sp.					1	1	2	
			Madoqua sp.					1	3	1	
			Bovidae gen. et sp. indet.		X	9	27	25	6		
			Number Bovidae taxa		**4**	**5**	**4**	**14**	**16**	**11**	**6**
	Giraffidae										
		Samotherinae	? Samotherium sp.		X	15	6				
		Sivatherinae	cf. Sivatherium sp.					1			
		Palaeotraginae	Palaeotragus germaini					5	5		
			Palaeotragus cf. germaini		X	84	21				
			Palaeotragus sp.					7	4		
		Giraffinae	Giraffa stillei							9	3
			Number Giraffidae taxa		**2**	**2**	**2**	**3**	**2**	**1**	**1**
	Hippopotamidae		Kenyapotamus coryndoni		X	9	2				
			Archaeopotamus lothagamensis					6			
			Archaeopotamus harvardi					85	63	14	15
			Archaeopotamus sp. indet.					5	3		3
			Hippopotamus cf. H. protamphibius							5	
			Hippopotamidae gen. et sp. indet.		X						
			Number Hippopotamidae taxa		**2**	**1**	**1**	**3**	**2**	**2**	**2**
	Suidae		cf. Kubanochoerus sp.			?X	?X	1			
			Nyanzachoerus spp.		X			1	5		
			Nyanzachoerus syrticus & cf. syrticus			?X	?X	82	49	2	
			Nyanzachoerus devauxi & cf. devouxi			16	6	28	7		
			Nyanzachoerus cf. Ny. australis						4	15	
			Nyanzachoerus pattersoni								3
			Notochoeruss jaegeri							2	
			Notochoerus euilus & No. cf. euilus							1	21
			cf. Potamochoeroides sp.					2	1		
			Cainochoerus cf. C. africanus						1		
			Number Suidae taxa		**?2**	**3**	**3**	**5**	**6**	**4**	**2**
	Tragulidae		Tragulidae indet.				1				
			Number Tragulidae taxa		**0**	**0**	**1**	**0**	**0**	**0**	**0**
Primates											
	Cercopithecinae		Parapapio lothagamensis					76	31		
			cf. Parapapio sp. indet.							4	1
			Theropithecus brumpti & cf. brumpti								12
			Theropithecus oswaldi								
			Theropithecus darti								
			cf.Theropithecus								
			Number Cercopithecinae taxa		**0**	**0**	**0**	**1**	**1**	**1**	**2**
Primates (cont.)											
	Colobinae		Cercopithecoides kerioensis							?1	
			Colobinae species A					4	3		
			Colobinae species B					8	8		
			Colobinae species C							2	
			Colobinae gen. indet. & sp. indet. (small)					4	4		
			Colobinae gen. indet. & sp. indet. (large)								1
			Microcolobus sp.		X						
			Number Colobinae taxa		**1**	**0**	**0**	**3**	**3**	**1**	**1**
	small non-cercopithecoid catarrhine gen. indet. A				X						
	small non-cercopithecoid catarrhine gen. indet. B				X						
	Hominoidea		Nakalipithecus nakayamai		12						
			Hominoidea sp.		X						
			Samburupithecus kiptalami			1					
			Hominidae indet.						2	1	
			Australopithecus cf A. afarensis								4
			Number Hominoidea taxa		**2**	**1**	**0**	**0**	**1**	**1**	**1**
Rodentia											
	Rhyzomyidae		Nakalimys lavocati		X						

Order	Family	Tribe or Subfamily	Species	Site:	Nakali	Samburu Hills		Lothagam		Lothagam	
				Formation:	Nakali	Namurungule		Nawata		Nachukui	
				Member:	--	Lower	Upper	Lower	Upper	Apak	Kaiyum.
			Number Rhyzomyidae taxa		**1**	**0**	**0**	**0**	**0**	**0**	**0**
	Thryonomyidae		Paraphiomys sp.		X	1					
			Paraphiomys chororensis					1			
			Paraulacodus sp.			2					
			Paraulacodus cf. P. johanesi					1			
			Thyronomys cf. T. gregorianus								1
			Thyronomys sp. (small)						5		
			Number Thryonomyidae taxa		**1**	**2**	**2**	**2**	**1**	**0**	**1**
	Muridae		Abudhabia sp.						1		
			Karnimata jacobsi sp. nov.					4			
			Saidomys sp.						1		
			Muridae gen. et sp. indet.					1			
			Number Muridae taxa		**0**	**0**	**0**	**2**	**2**	**0**	**0**
	Hystricidae		Hystrix sp. (small)					1			
			Hystrix sp. (large)								1
			Number Hystricidae taxa		**0**	**0**	**0**	**1**	**0**	**0**	**1**
	Sciuridae		Kubwaxerus pattersoni					6			
			Number Sciuridae taxa		**0**	**0**	**0**	**1**	**0**	**0**	**0**
Lagomorpha											
	Leporidae		Alilepus sp.					4			
			Serengetilagus praecapensis							1	
			Number Leporidae taxa		**0**	**0**	**0**	**1**	**0**	**1**	**0**
Carnivora											
	Mustelidae		Mustelidae gen. et sp. indet.		X						
			Ekorus ekakeran					2			
			Erokomellivora lothagamensis						1		
			Mellivoranae gen. et sp. indet.					1	1		
			Vishnuonyx angololensis					1			
			Number Mustelidae taxa		**1**	**0**	**0**	**3**	**2**	**0**	**0**
Carnivora (cont.)											
	Hyaenidae		Hyaenidae gen. et sp. indet.		X	5	2				
			Ictitherium ebu					1		1	
			Hyaenictitherium cf. H. parvum					1	2		
			cf. Hyanictis sp.					3	1	1	
			Ikelohyaena cf. I. abronia					1		1	
			Number Hyaenidae taxa		**1**	**1**	**1**	**4**	**2**	**3**	**0**
	Percrocutidae		Percrocuta leakeyi		X						
			Number Percrocutidae taxa		**1**	**0**	**0**	**0**	**0**	**0**	**0**
	Amphicyonidae		Amphicyonidae gen. et sp. indet.			X?	X?				
			Amphicyonidae sp. A					3			
			Amphicyonidae sp. B						1		
			Number Amphicyonidae taxa		**0**	**1**	**1**	**1**	**1**	**0**	**0**
	Felidae		Machairodontinae gen. et sp. indet.			X					
			Lokotunjailurus emageritus					16	13		
			Metailurus cf. Metailurus sp.					1	6		
			Dinofelis sp.					4	8	6	
	Felidae		Dinofelis aronoki								1
			Leptailurus or Caracal sp.								1
			Number Felidae taxa		**0**	**1**	**1**	**3**	**3**	**1**	**2**
	Viverrdae		Viverra cf. V. leakeyi					1			
			Viverinae sp. indet.					1			
			Viverinae gen. et sp. indet. (large)					1	1		
			Genetta sp. A					2			
			Genetta sp. B						1		
			Number Viverridae taxa		**0**	**0**	**0**	**4**	**2**	**0**	**0**
	Canidae		cf. Canis sp.								1
			Number Canidae taxa		**0**	**0**	**0**	**0**	**0**	**0**	**1**
Hyracoidea											

Order	Family	Tribe or Subfamily	Species	Site:	Nakali	Samburu Hills		Lothagam		Lothagam	
				Formation:	Nakali	Namurungule		Nawata		Nachukui	
				Member:	--	Lower	Upper	Lower	Upper	Apak	Kaiyum.
	Procaviidae		cf. Heterohyrax sp.		X						
	Pliohyracidae		Parapliohyrax gen indet.			1					
			Number Procaviidae taxa		**1**	**1**	**1**	**0**	**0**	**0**	**0**
			Total Number taxa		**23**	**27**	**23**	**62**	**54**	**40**	**24**

Table S3. Calculated $\delta^{13}C$ values (‰) for enamel based on C3 and C4 diets using an enrichment factor of 14.1‰ from Cerling and Harris (1999). The $\delta^{13}C$ values for paleoatmospheric CO2 are the maximum and minimum (90% confidence interval) values determined by Tipple et al, 2010 using the high resolution and 3 Ma benthic foraminifera records

Age (Ma)	Formation/ Member	$\delta^{13}C$ atm CO_2 high est.	$\delta^{13}C$ atm CO_2 low est.	$\delta^{13}C$ pl Avg. C3_pl	$\delta^{13}C$ pl Max. C3_pl	$\delta^{13}C$ pl Avg. C4_pl	$\delta^{13}C$ en Avg. C3_en	$\delta^{13}C$ en Max. C3_en	$\delta^{13}C$ en Avg. C4_en	Tipple et al., 2010 dataset
present		-8.2	--	-27.3	-24.5	-12.8	-13.4	-10.5	1.3	high res benthic
3.2	Kaiyumung	-5.7	-6.4	-24.8	-22.1	-11.1	-10.9	-8.1	3.1	high res benthic
4.2-4.3	Apak	-5.9	-6.6	-25.0	-22.2	-11.2	-11.0	-8.2	2.9	3myr benthic
6.6-6.5	U. Nawata	-5.8	-7.0	-24.9	-22.2	-11.7	-11.0	-8.2	2.4	high res benthic
7.6-7.4	L. Nawata	-5.3	-6.5	-24.4	-21.7	-11.2	-10.5	-7.7	3.0	high res benthic
9.6-9.3	Namurungule	-5.5	-6.7	-24.6	-21.8	-11.3	-10.6	-7.8	2.8	high res benthic
10.0-9.8	Nakali	-5.3	-6.5	-24.5	-21.7	-11.2	-10.5	-7.7	3.0	high res benthic
10.0-3.0	All sites	-5.6	-6.6	-24.7	-21.9	-11.3	-10.8	-7.9	2.9	high res benthic

Avg. = average; en = enamel; est. =estimate; Max. =maximum pl =plant

Table S4. Shapiro-Wilk test for normality of $\delta^{13}C$ data by age. H_0 = data is from the Normal distribution; Small p-values reject H_0.

AGE	W	p value	Normal?	n
3.2	0.8115	0.0094	no	13
4.2	0.8125	<0.0001	no	53
6.5	0.9163	<0.0001	no	79
7.4	0.9704	0.0343	no	91
9.3	0.9502	0.1246	yes	34
9.6	0.9519	0.0010	no	69
9.9	0.8523	<0.0001	no	113
ALL	0.9452	<0.0001	no	452

Table S5. Mann-Whitney U test results comparing medians for each family by between time periods. Time periods are listed at the top of each column in Ma. Values in **bold** are significanty different at the 95% level ($p < 0.05$). To perform the test, a minimum of 5 individuals was required for each population.

	3.2 vs. 4.2		4.2 vs. 6.5		6.5 vs. 7.4		7.4 vs. 9.3		7.4 vs. 9.6		9.3 vs. 9.6		9.3 vs. 9.9		9.6 vs. 9.9	
Family	χ^2	**p**	χ^2	**p**	χ^2	**p**	χ^2	**p**	χ^2	**p**	χ^2	**p**	χ^2	**p**	χ^2	**p**
bovid	--	--	1.65	0.1985	0.18	0.6682	--	--	2.08	0.1495	--	--	--	--	7.35	**0.0067**
dein	--	--	--	--	--	--	--	--	--	--	--	--	--	--	5.63	**0.0176**
equid	--	--	4.03	**0.0446**	6.12	**0.0133**	0.72	0.3957	--	--	0.85	0.3562	--	--	30.01	**<0.0001**
ele+gom	--	--	0.01	0.9349	2.56	0.1096	9.94	**0.0016**	--	--	--	--	0	1.0	--	--
giraffid	--	--	--	--	--	--	--	--	--	--	--	--	--	--	11.21	**0.0008**
hippo	--	--	4.25	**0.0392**	6.44	**0.0111**	--	--	7.13	**0.0076**	--	--	--	--	11.44	**0.0007**
rhino	--	--	2.73	0.0987	0.39	0.5339	--	--	8.57	**0.0034**	--	--	--	--	11.04	**0.0009**
suid	6.47	**0.0109**	5.24	**0.0221**	1.49	0.2226	--	--	2.52	0.1127	--	--	--	--	11.69	**0.0006**

Table S6. Carbon isotope data of fossil enamel from the Nakali, Namurungule, Nawata, and Nachukui Formations. Capital and lower case letters indicate upper and lower teeth, respectively; c= canine, d = deciduous, i= incisor, p= premolar, m=molar, molar frag= premolar or molar fragment, and x= tooth position unknown.

$\delta^{13}C$	Taxon	Part	Fm./Mbr.	Sample	Age (Ma)
Bovidae					
-8.1	Alcelaphini?	Mx	Nakali	KNM-NA 284	9.9
-9.5	Boselaphini gen. indet.	m3	Nakali	KNM-NA 42	9.9
-11.2	Bovidae gen. indet.	m frag	Nakali	NA60-12039	9.9
-10.3	Bovidae gen. indet.	molar frag	Nakali	NA11-12243	9.9
-11.8	Tragelaphini gen. indet.	mx	Nakali	KNM-NA 43	9.9
-10.7	Tragelaphini gen. indet.	mx	Nakali	NA3-12231	9.9
-10.6	Tragelaphini gen. indet.	molar frag	Nakali	NA2-7745	9.9
-10.5	Tragelaphini gen. indet.	Mx	Nakali	KNM-NA 44	9.9
-10.1	Tragelaphini gen. indet.	molar frag	Nakali	KNM-NA 48	9.9
-9.9	Tragelaphini gen. indet.	M frag	Nakali	KNM-NA 47	9.9
-10.3	Boselaphini gen. indet.	M1 frag	L. Namarungule	KNM-SH-41903	9.6
-8.8	Boselaphini gen. indet.	M3	L. Namarungule	KNM-SH 37890	9.6
-4.4	Boselaphini gen. indet.	p3 & p4	L. Namarungule	KNM-SH 15735	9.6
-3.7	Boselaphini gen. indet.	M1 frag	L. Namarungule	KNM-SH 15726	9.6
-7.6	Boselaphini sp. small	mx	L. Namarungule	KNM-SH 40125	9.6
-4.5	Gazella sp.	dp4	L. Namarungule	KNM-SH-15736	9.6
-7.6	Antilopini gen. indet.	m1	U. Namarungule	KNM-SH-38324	9.3
-2.1	Bovidae gen. indet.	M2	U. Namarungule	KNM-SH 12334	9.3
-4.5	Bovidae gen. indet.	molar frag	L. Nawata	LOTH-125	7.4
2.2	Hippotragini gen. indet.	m3	L. Nawata	KNM-LT 25432	7.4
-4.9	Reduncini	m1	L. Nawata	KNM-LT 207	7.4
-4.0	Reduncini	m3	L. Nawata	KNM-LT 23624	7.4
-1.0	Reduncini	m1	L. Nawata	KNM-LT 13007	7.4
-7.3	Tragelaphini gen. indet.	m3	L. Nawata	KNM-LT 182	7.4
-9.0	Aepyceros	molar frag	U. Nawata	LOTH-152	6.5
0.2	Alcelaphini	M frag	U. Nawata	KNM-LT 517	6.5
-3.3	Bovidae gen. indet.	molar frag	U. Nawata	LOTH-45	6.5
-2.9	Bovidae gen. indet.	molar frag	U. Nawata	LOTH-41	6.5
-1.8	Reduncini	m frag	U. Nawata	KNM-LT 23693	6.5
-8.5	Tragelaphini gen. indet.	m frag	U. Nawata	KNM-LT 28777	6.5
-7.2	Tragelaphini gen. indet.	m3	U. Nawata	KNM-LT 23613	6.5
-5.8	Bovidae gen. indet.	molar frag	Apak	LOTH-59	4.2
-3.3	Bovidae gen. indet.	molar frag	Apak	LOTH-111	4.2
-2.8	Bovidae gen. indet.	molar frag	Apak	LOTH-103	4.2
-1.7	Bovidae gen. indet.	molar frag	Apak	LOTH-106	4.2
-0.9	Bovidae gen. indet.	molar frag	Apak	LOTH-119	4.2
-0.4	Bovidae gen. indet.	molar frag	Apak	LOTH-100	4.2
-6.6	Aepyceros sp.	m frag	Kaiyumung	KNM-LT 28736	3.2
-2.1	Bovini or Reduncini	m frag	Kaiyumung	KNM-LT 26040	3.2
Deinotheriidae					
-11.7	Deinotherium bozasi	m2	Nakali	KNM-NA 1	9.9
-11.5	Deinotherium bozasi	molar frag	Nakali	KNM-NA 3	9.9
-10.7	Deinotherium bozasi	m3	Nakali	KNM-NA 2	9.9
-10.1	Deinotherium bozasi	p4	Nakali	KNM-NA 47142	9.9
-10.0	Deinotherium bozasi	M3	Nakali	KNM-NA 259(B)	9.9
-9.5	Deinotherium bozasi	mx	Nakali	KNM-NA 47136	9.9
-9.8	Deinotherium bozasi	m3	L. Namarungule	KNM-SH 15783	9.6
-9.6	Deinotherium bozasi	m2	L. Namarungule	KNM-SH 12304	9.6
-9.5	Deinotherium bozasi	molar frag	L. Namarungule	KNM-SH 12306	9.6
-9.0	Deinotherium bozasi	m2	L. Namarungule	KNM-SH 12305	9.6
-8.9	Deinotherium bozasi	M1	L. Namarungule	KNM-SH 38331	9.6
-9.7	Deinotherium bozasi	molar frag	L. Nawata	KNM-LT 26346	7.4

$\delta^{13}C$	Taxon	Part	Fm./Mbr.	Sample	Age (Ma)
Deinotheriidae (cont.)					
-11.4	Deinotherium bozasi	molar frag	U. Nawata	KNM-LT 26344	6.5
-12.5	Deinotherium bozasi	molar frag	Apak	KNM-LT 23806	4.2
-12.0	Deinotherium bozasi	molar frag	Apak	KNM-LT 26345	4.2
-11.1	Deinotherium bozasi	dp4	Kaiyumung	KNM-LT 23677	3.2
Elephantidae					
-5.5	Elephantidae gen indet.	molar frag	L. Nawata	LOTH-137	7.4
-6.2	Stegotetrabelodon or Primelephas	dpx	L. Nawata	KNM-LT 26332	7.4
-1.0	Stegotetrabelodon sp.	molar frag	L. Nawata	KNM-LT 26336	7.4
-1.0	Stegotetrabelodon sp.	molar frag	L. Nawata	KNM-LT 26336	7.4
-2.1	Elephantidae gen indet.	molar frag	U. Nawata	LOTH-159	6.5
-1.5	Elephantidae gen indet.	molar frag	U. Nawata	LOTH-158	6.5
-0.9	Elephantidae gen indet.	molar frag	U. Nawata	LOTH-176	6.5
-0.3	Elephantidae gen indet.	molar frag	U. Nawata	LOTH-162	6.5
-0.2	Elephantidae gen indet.	molar frag	U. Nawata	LOTH-171	6.5
-0.1	Elephantidae gen indet.	molar frag	U. Nawata	LOTH-154	6.5
-1.6	Primelephas sp.	molar frag	U. Nawata	KNM-LT 23783	6.5
-2.0	S.t.belodon or Primelephas	molar frag	U. Nawata	LOTH-64.b	6.5
-1.2	S.t.belodon or Primelephas	molar frag	U. Nawata	LOTH-64.a	6.5
-1.1	S.t.belodon or Primelephas	molar frag	U. Nawata	LOTH-64	6.5
0.3	Stegotetrabelodon sp.	molar frag	U. Nawata	LOTH-66	6.5
-0.4	Elephantidae gen indet.	molar frag	Apak	LOTH-118	4.2
-0.2	Elephantidae gen indet.	molar frag	Apak	LOTH-61	4.2
-0.8	Primelephas sp.	M3	Apak	KNM-LT 26323	4.2
-0.9	Stegotetrabelodon orbus	dp4	Apak	KNM-LT 26337	4.2
-1.1	Stegotetrabelodon sp.		Apak	WT 2632	4.2
Equidae					
-10.5	"Cormohipparion" aff. africanum	m3	Nakali	NA34-11993	9.9
-10.5	"Cormohipparion" aff. africanum	Mx	Nakali	NA36 12305	9.9
-10.4	"Cormohipparion" aff. africanum	m2	Nakali	KNM-NA 179	9.9
-10.2	"Cormohipparion" aff. africanum	P4	Nakali	KNM-NA 173	9.9
-10.1	"Cormohipparion" aff. africanum	M3	Nakali	KNM-NA 47181	9.9
-10.1	"Cormohipparion" aff. africanum	P3 or P4	Nakali	KNM-NA 240	9.9
-10.0	"Cormohipparion" aff. africanum	P2	Nakali	KNM-NA 171	9.9
-9.9	"Cormohipparion" aff. africanum	P3	Nakali	KNM-NA 156	9.9
-9.8	"Cormohipparion" aff. africanum	P4	Nakali	KNM-NA 181	9.9
-9.6	"Cormohipparion" aff. africanum	p4	Nakali	KNM-NA 165	9.9
-9.6	"Cormohipparion" aff. africanum	m2	Nakali	NA52-12224	9.9
-9.5	"Cormohipparion" aff. africanum	m3	Nakali	KNM-NA 47153	9.9
-9.4	"Cormohipparion" aff. africanum	M3	Nakali	NA52-11929	9.9
-9.4	"Cormohipparion" aff. africanum	M1	Nakali	KNM-NA 47180	9.9
-9.2	"Cormohipparion" aff. africanum	M3	Nakali	KNM-NA 155	9.9
-9.1	"Cormohipparion" aff. africanum	M2	Nakali	KNM-NA 47273	9.9
-9.1	"Cormohipparion" aff. africanum	mx	Nakali	KNM-NA 47267	9.9
-8.6	"Cormohipparion" aff. africanum	P3	Nakali	KNM-NA 184	9.9
-8.5	"Cormohipparion" aff. africanum	P2	Nakali	KNM-NA 47272	9.9
-8.4	"Cormohipparion" aff. africanum	M1	Nakali	KNM-NA 232	9.9
-8.3	"Cormohipparion" aff. africanum	M2	Nakali	KNM-NA 170	9.9
-8.3	"Cormohipparion" aff. africanum	M3	Nakali	KNM-NA 241	9.9
-8.2	"Cormohipparion" aff. africanum	p2	Nakali	KNM-NA 47270	9.9
-7.8	"Cormohipparion" aff. africanum	M3	Nakali	KNM-NA 47159	9.9
-7.7	"Cormohipparion" aff. africanum	p3	Nakali	KNM-NA 177	9.9
-7.4	"Cormohipparion" aff. africanum	M1 or M2	Nakali	KNM-NA 152	9.9
-7.3	"Cormohipparion" aff. africanum	m2	Nakali	KNM-NA 162	9.9
-6.5	"Cormohipparion" aff. africanum	M3	Nakali	NA5-11913	9.9
-6.3	"Cormohipparion" aff. africanum	px	Nakali	KNM-NA 47274	9.9

$\delta^{13}C$	Taxon	Part	Fm./Mbr.	Sample	Age (Ma)
Equidae (cont.)					
-5.8	"Cormohipparion" aff. africanum	P3	Nakali	NA52-12223	9.9
-4.5	"Cormohipparion" aff. africanum	M3	Nakali	KNM-NA 47169	9.9
-4.1	"Cormohipparion" aff. africanum	Px	Nakali	KNM-NA 47275	9.9
-1.8	"Cormohipparion" aff. africanum	m3	Nakali	KNM-NA 47161_a	9.9
-1.4	"Cormohipparion" aff. africanum	m2 or m3	Nakali	KNM-NA 47179	9.9
-0.9	"Cormohipparion" aff. africanum	M1or M2	Nakali	KNM-NA 47249	9.9
-6.6	"Cormohipparion" aff. africanum	mx	L. Namarungule	KNM-SH 14774	9.6
-6.2	"Cormohipparion" aff. africanum	mx	L. Namarungule	KNM-SH 15648	9.6
-5.5	"Cormohipparion" aff. africanum	Mx or P4	L. Namarungule	KNM-SH 15653	9.6
-5.3	"Cormohipparion" aff. africanum	p3	L. Namarungule	KNM-SH 14773	9.6
-5.1	"Cormohipparion" aff. africanum	P4	L. Namarungule	KNM-SH 15656	9.6
-4.8	"Cormohipparion" aff. africanum	dP	L. Namarungule	KNM-SH 12302	9.6
-4.7	"Cormohipparion" aff. africanum	m1	L. Namarungule	KNM-SH 40132	9.6
-4.5	"Cormohipparion" aff. africanum	M2	L. Namarungule	KNM-SH 12246	9.6
-4.2	"Cormohipparion" aff. africanum	M2	L. Namarungule	KNM-SH 12248	9.6
-3.7	"Cormohipparion" aff. africanum	unkn	L. Namarungule	KNM-SH 18007	9.6
-2.8	"Cormohipparion" aff. africanum	m3	L. Namarungule	KNM-SH 12287	9.6
-2.6	"Cormohipparion" aff. africanum	M1	L. Namarungule	KNM-SH 15662	9.6
-1.7	"Cormohipparion" aff. africanum	dP2	L. Namarungule	KNM-SH 15706	9.6
-1.6	"Cormohipparion" aff. africanum	mx	L. Namarungule	KNM-SH 12203	9.6
-1.4	"Cormohipparion" aff. africanum	m2	L. Namarungule	KNM-SH 12266	9.6
-1.2	"Cormohipparion" aff. africanum	M2	L. Namarungule	KNM-SH 12245	9.6
-1.0	"Cormohipparion" aff. africanum	M1	L. Namarungule	KNM-SH 15818	9.6
-1.0	"Cormohipparion" aff. africanum	M1 or M2	L. Namarungule	KNM-SH 14763	9.6
-0.7	"Cormohipparion" aff. africanum	M3	L. Namarungule	KNM-SH 15664	9.6
-0.7	"Cormohipparion" aff. africanum	m2	L. Namarungule	KNM-SH 38436	9.6
-0.6	"Cormohipparion" aff. africanum	m2	L. Namarungule	KNM-SH 12283	9.6
-0.6	"Cormohipparion" aff. africanum	M2	L. Namarungule	KNM-SH 12242	9.6
-0.3	"Cormohipparion" aff. africanum	M3	L. Namarungule	KNM-SH 15652	9.6
0.7	"Cormohipparion" aff. africanum	M3	L. Namarungule	KNM-SH 15658	9.6
-4.8	"Cormohipparion" aff. africanum	M1	U. Namarungule	KNM-SH 12202	9.3
-4.4	"Cormohipparion" aff. africanum	mx or p4	U. Namarungule	KNM-SH 15650	9.3
-3.5	"Cormohipparion" aff. africanum	M1	U. Namarungule	KNM-SH 12241	9.3
-2.8	"Cormohipparion" aff. africanum	M2	U. Namarungule	KNM-SH 12243	9.3
-2.7	"Cormohipparion" aff. africanum	mx	U. Namarungule	KNM-SH 12252	9.3
-2.2	"Cormohipparion" aff. africanum	m3	U. Namarungule	KNM-SH 15649	9.3
-1.9	"Cormohipparion" aff. africanum	m3	U. Namarungule	KNM-SH 12260	9.3
-1.8	"Cormohipparion" aff. africanum	m1	U. Namarungule	KNM-SH 12261	9.3
-1.6	"Cormohipparion" aff. africanum	unkn	U. Namarungule	KNM-SH 12249	9.3
-0.5	"Cormohipparion" aff. africanum	M3	U. Namarungule	KNM-SH 12247	9.3
-0.4	"Cormohipparion" aff. africanum	P4	U. Namarungule	KNM-SH 12205	9.3
-0.3	"Cormohipparion" aff. africanum	Mx	U. Namarungule	KNM-SH 12239	9.3
0.2	"Cormohipparion" aff. africanum	Mx or Px	U. Namarungule	KNM-SH 12244	9.3
-1.9	Eurygnathohippus feibeli	molar frag	L. Nawata	KNM-LT 23107	7.4
-3.8	Eurygnathohippus sp.	molar frag	L. Nawata	LOTH-133	7.4
-3.0	Eurygnathohippus sp.	mx	L. Nawata	LOTH-83	7.4
-2.9	Eurygnathohippus sp.	molar frag	L. Nawata	LOTH-128	7.4
-1.4	Eurygnathohippus sp.	I	L. Nawata	LOTH-77	7.4
-1.1	Eurygnathohippus sp.	M frag	L. Nawata	LOTH-40	7.4
-0.8	Eurygnathohippus sp.	Mx	L. Nawata	LOTH-94	7.4
-0.7	Eurygnathohippus sp.	molar frag	L. Nawata	LOTH-124	7.4
-0.6	Eurygnathohippus sp.	Mx	L. Nawata	LOTH-82	7.4
-0.6	Eurygnathohippus sp.	molar frag	L. Nawata	LOTH-123	7.4
-0.2	Eurygnathohippus sp.	molar frag	L. Nawata	LOTH-130	7.4
-0.1	Eurygnathohippus sp.	P3 or M3	L. Nawata	LOTH-91	7.4
0.4	Eurygnathohippus sp.	molar frag	L. Nawata	LOTH-127	7.4
-2.9	Eurygnathohippus turkanense	M1	L. Nawata	KNM-LT 25436	7.4
-0.1	Eurygnathohippus feibeli	m1	U. Nawata	KNM-LT 25475	6.5

$\delta^{13}C$	Taxon	Part	Fm./Mbr.	Sample	Age (Ma)
Equidae (cont.)					
-0.5	Eurygnathohippus sp.	molar frag	U. Nawata	LOTH-47	6.5
-0.3	Eurygnathohippus sp.	molar frag	U. Nawata	LOTH-48	6.5
-0.3	Eurygnathohippus sp.	Mx	U. Nawata	LOTH-50	6.5
-0.1	Eurygnathohippus sp.	molar frag	U. Nawata	LOTH-54	6.5
0.5	Eurygnathohippus turkanense	P3	U. Nawata	KNM-LT 25484	6.5
-0.2	Eurygnathohippus sp.	molar frag	Apak	LOTH-57	4.2
-1.8	Euygnathohippus sp.	molar frag	Apak	LOTH-110	4.2
-1.3	Euygnathohippus sp.	molar frag	Apak	LOTH-97	4.2
-1.0	Euygnathohippus sp.	molar frag	Apak	LOTH-101	4.2
-0.5	Euygnathohippus sp.	molar frag	Apak	LOTH-120	4.2
Giraffidae					
-9.4	Sivatherium maurusium	unkn	Kaiyumung	WT 17472	3.2
-12.3	Giraffidae gen. indet.	m1 or m2	Nakali	KNM-NA 47190	9.9
-11.5	Giraffidae gen. indet.	P3	Nakali	KNM-NA 47189	9.9
-11.3	Giraffidae gen. indet.	molar frag	Nakali	KNM-NA 47183	9.9
-10.8	Giraffidae gen. indet.	molar frag	Nakali	KNM-NA 325	9.9
-10.8	Giraffidae gen. indet.	m frag	Nakali	NA16-11974	9.9
-9.8	Giraffidae gen. indet.	molar frag	Nakali	KNM-NA 45720	9.9
-9.8	Giraffidae gen. indet.	molar frag	Nakali	NA37 12205	9.9
-9.5	Giraffidae gen. indet.	molar frag	Nakali	NA11-12008	9.9
-9.1	Giraffidae gen. indet.	m3	Nakali	KNM-NA 47191	9.9
-8.7	Giraffidae gen. indet.	molar frag	Nakali	KNM-NA 47150	9.9
-8.3	Giraffidae gen. indet.	mx	Nakali	NA1-11960	9.9
-11.0	Samotherium (?)	m1 or m2	Nakali	KNM-NA 292	9.9
-11.0	Samotherium (?)	M1 or M2	Nakali	KNM-NA 201	9.9
-9.6	Samotherium (?)	m3	Nakali	KNM-NA 275	9.9
-8.0	Samotherium (?)	M1 or M2	Nakali	KNM-NA 290	9.9
-8.2	Giraffidae gen. indet.	Mx	L. Namarungule	KNM-SH-37898	9.6
-7.5	Giraffidae gen. indet.	M1or M2	L. Namarungule	KNM-SH 37895	9.6
-6.3	Giraffidae gen. indet.	mx	L. Namarungule	KNM-SH-37897	9.6
-8.7	Palaeotragus cf. germaini	m3 frag	L. Namarungule	KNM-SH 15846	9.6
-8.4	Palaeotragus cf. germaini	M3 frag	L. Namarungule	KNM-SH 12234	9.6
-7.7	Palaeotragus cf. germaini	M1	L. Namarungule	KNM-SH 14759	9.6
-7.1	Palaeotragus cf. germaini	p3	L. Namarungule	KNM-SH 12232	9.6
-10.7	Giraffidae gen. indet.	Px frag	U. Namarungule	KNM-SH 12238	9.3
-7.6	Giraffidae gen. indet.	m3	U. Namarungule	KNM-SH 12229_A	9.3
-7.3	Giraffidae gen. indet.	p4	U. Namarungule	KNM-SH 12233	9.3
-10.5	Palaeotragus germaini	M3	L. Nawata	KNM-LT 26262	7.4
-9.1	Palaeotragus germaini	M3	L. Nawata	KNM-LT 414	7.4
-11.4	Palaeotragus sp.	molar frag	L. Nawata	KNM-LT 23639	7.4
-8.1	Palaeotragus sp.	molar frag	L. Nawata	KNM-LT 23150	7.4
-12.2	Palaeotragus sp.	m1	U. Nawata	KNM-LT 29066	6.5
Gomphotheriidae					
-8.5	Anancus sp.	unkn	Nakali	KNM-NA 260	9.9
-9.6	Choerolophodon ngorora	M1	Nakali	KNM-NA 4	9.9
-7.7	Choerolophodon ngorora	M2	Nakali	KNM-NA 47146	9.9
-7.0	Choerolophodon ngorora	mx	Nakali	KNM-NA 86	9.9
-8.4	Choerolophodon sp.	molar frag	Nakali	KNM-NA 47137	9.9
-7.6	Gomphotheriidae gen. indet.	unkn	Nakali	KNM-NA 6	9.9
-6.9	Tetralophodon sp.	m2	Nakali	KNM-NA 47397	9.9
-10.4	Gomphotheriidae gen. indet.	m1	L. Namarungule	KNM-SH 12377	9.6
-6.7	Gomphotheriidae gen. indet.	dm or dM	L. Namarungule	KNM-SH 15781	9.6
-9.1	Gomphotheriidae gen. indet.	molar frag	U. Namarungule	KNM-SH 12380	9.3
-9.0	Gomphotheriidae gen. indet.	molar frag	U. Namarungule	KNM-SH 12374	9.3

$\delta^{13}C$	Taxon	Part	Fm./Mbr.	Sample	Age (Ma)
Gomphotheriidae (cont.)					
-8.6	Gomphotheriidae gen. indet.	M2	U. Namarungule	KNM-SH 12373	9.3
-8.4	Gomphotheriidae gen. indet.	M1	U. Namarungule	KNM-SH 12309	9.3
-7.4	Gomphotheriidae gen. indet.	molar frag	U. Namarungule	KNM-SH 12379	9.3
-6.9	Gomphotheriidae gen. indet.	P4	U. Namarungule	KNM-SH 12310	9.3
-4.6	Gomphotheriidae gen. indet.	M2	U. Namarungule	KNM-SH 12307	9.3
-8.1	Tetralophodon sp.	unkn	U. Namarungule	KNM-SH 12308	9.3
-3.9	Gomphotheriidae gen. indet.	M frag	L. Nawata	LOTH-84	7.4
-2.4	Gomphotheriidae gen. indet.	molar frag	L. Nawata	LOTH-75	7.4
-1.8	Gomphotheriidae gen. indet.	molar frag	L. Nawata	LOTH-72	7.4
0.7	Gomphotheriidae gen. indet.	M frag	L. Nawata	LOTH-90	7.4
-2.2	Anancus kenyensis	dP4	Apak	KNM-LT 28567	4.2
-0.9	Anancus kenyensis	m1	Apak	KNM-LT 361	4.2
-0.8	Anancus kenyensis	M frag	Apak	KNM-LT 23790	4.2
-0.7	Anancus kenyensis	m3	Apak	KNM-LT 341	4.2
Hippopotamidae					
-10.3	Hippopotamidae gen. indet.	molar frag	Nakali	KNM-NA 146	9.9
-10.1	Hippopotamidae gen. indet.	m frag	Nakali	NA3-11953	9.9
-10.0	Hippopotamidae gen. indet.	m3	Nakali	KNM-NA 250 (C)	9.9
-9.7	Hippopotamidae gen. indet.	tusk frag	Nakali	KNM-NA 250 (A)	9.9
-9.7	Hippopotamidae gen. indet.	m3	Nakali	KNM-NA 47284	9.9
-9.0	Hippopotamidae gen. indet.	p4	Nakali	NA28-11970	9.9
-8.0	Hippopotamidae gen. indet.		Nakali	KNM-NA 143	9.9
-11.2	Kenyapotamus coryndoni	Mx frag	Nakali	KNM-NA 47283	9.9
-10.2	Kenyapotamus coryndoni	mx	Nakali	KNM-NA 45756	9.9
-9.8	Kenyapotamus coryndoni	Mx	Nakali	KNM-NA 47292	9.9
-9.7	Kenyapotamus coryndoni	m3	Nakali	KNM-NA 45735	9.9
-9.5	Kenyapotamus coryndoni	m3	Nakali	KNM-NA 246	9.9
-9.1	Kenyapotamus coryndoni	p4 or p3	Nakali	KNM-NA 45754	9.9
-9.1	Kenyapotamus coryndoni	mx	Nakali	KNM-NA 192	9.9
-8.5	Kenyapotamus coryndoni	M1	L. Namarungule	KNM-SH 14789	9.6
-6.8	Kenyapotamus coryndoni	mx	L. Namarungule	KNM-SH 18001	9.6
-6.8	Kenyapotamus coryndoni	p3	L. Namarungule	KNM-SH-40142	9.6
-6.4	Kenyapotamus coryndoni	M1	L. Namarungule	KNM-SH 15851	9.6
-6.2	Kenyapotamus coryndoni	m3	L. Namarungule	KNM-SH 14792	9.6
-5.2	Kenyapotamus coryndoni	m3	L. Namarungule	KNM-SH 15850	9.6
-6.5	Kenyapotamus coryndoni	m3	U. Namarungule	KNM-SH-15857	9.3
-5.6	Kenyapotamus coryndoni	tusk	U. Namarungule	SHS-188	9.3
-3.8	Kenyapotamus coryndoni	tusk	U. Namarungule	SHS-189	9.3
-3.4	Archaeopotamus harvardi	I	L. Nawata	KNM-LT 23270	7.4
-2.6	Archaeopotamus harvardi	p4	L. Nawata	KNM-LT 23872	7.4
-2.2	Archaeopotamus harvardi	P3	L. Nawata	KNM-LT 23269	7.4
-0.7	Archaeopotamus harvardi	P3	L. Nawata	KNM-LT 23831	7.4
-7.8	Archaeopotamus lothagamensis	tusk	L. Nawata	KNM-LT 23879	7.4
-2.1	Archaeopotamus lothagamensis	m3	L. Nawata	KNM-LT 22864	7.4
-4.1	Archaeopotamus sp indet.	p4	L. Nawata	KNM-LT 8585	7.4
-2.2	Archaeopotamus sp. indet.	M3	L. Nawata	KNM-LT 23874	7.4
-9.2	Hippopotamidae gen. indet.	molar frag	L. Nawata	LOTH-92	7.4
-7.9	Hippopotamidae gen. indet.	Px	L. Nawata	LOTH-135	7.4
-7.2	Hippopotamidae gen. indet.	M frag	L. Nawata	LOTH-78	7.4
-5.8	Hippopotamidae gen. indet.	PM3, M1, dP3, C	L. Nawata	LOTH-93	7.4
-5.7	Hippopotamidae gen. indet.	PM3, M1, dP3, C	L. Nawata	LOTH-93	7.4
-5.5	Hippopotamidae gen. indet.	M frag	L. Nawata	LOTH-74	7.4
-5.4	Hippopotamidae gen. indet.	molar frag	L. Nawata	LOTH-126	7.4
-5.4	Hippopotamidae gen. indet.	PM3, M1, dP3, C	L. Nawata	LOTH-93	7.4
-5.1	Hippopotamidae gen. indet.	Px	L. Nawata	LOTH-95	7.4
-5.0	Hippopotamidae gen. indet.	molar frag	L. Nawata	LOTH-122	7.4

$\delta^{13}C$	Taxon	Part	Fm./Mbr.	Sample	Age (Ma)
Hippopotamidae (cont.)					
-4.2	Hippopotamidae gen. indet.	molar frag	L. Nawata	LOTH-138	7.4
-4.0	Hippopotamidae gen. indet.	M frag	L. Nawata	LOTH-81	7.4
-3.8	Hippopotamidae gen. indet.	molar frag	L. Nawata	LOTH-85	7.4
-3.4	Hippopotamidae gen. indet.	molar frag	L. Nawata	LOTH-69	7.4
-3.2	Hippopotamidae gen. indet.	tusk	L. Nawata	LOTH-86	7.4
-3.1	Hippopotamidae gen. indet.	I	L. Nawata	LOTH-89	7.4
-3.0	Hippopotamidae gen. indet.	tusk	L. Nawata	LOTH-86	7.4
-2.8	Hippopotamidae gen. indet.	tusk	L. Nawata	LOTH-71	7.4
-2.1	Hippopotamidae gen. indet.	molar frag	L. Nawata	LOTH-69	7.4
-1.7	Hippopotamidae gen. indet.	tusk	L. Nawata	LOTH-87	7.4
-0.7	Hippopotamidae gen. indet.	M frag	L. Nawata	LOTH-73	7.4
-2.4	Archaeopotamus harvardi	tusk	U. Nawata	KNM-LT 23856	6.5
-1.0	Archaeopotamus harvardi	M2	U. Nawata	KNM-LT 409	6.5
-5.2	Archaeopotamus lothagamensis	m2	U. Nawata	KNM-LT 23871	6.5
-7.6	Hippopotamidae gen. indet.	Px	U. Nawata	LOTH-42	6.5
-5.2	Hippopotamidae gen. indet.	tusk	U. Nawata	LOTH-56	6.5
-5.1	Hippopotamidae gen. indet.	molar frag	U. Nawata	LOTH-172	6.5
-4.7	Hippopotamidae gen. indet.	dx & mx	U. Nawata	LOTH-49	6.5
-4.3	Hippopotamidae gen. indet.	M3	U. Nawata	LOTH-44	6.5
-3.7	Hippopotamidae gen. indet.	molar frag	U. Nawata	LOTH-151	6.5
-3.6	Hippopotamidae gen. indet.	molar frag	U. Nawata	LOTH-51	6.5
-3.2	Hippopotamidae gen. indet.	molar frag	U. Nawata	LOTH-173	6.5
-3.2	Hippopotamidae gen. indet.	dP and P	U. Nawata	LOTH-65	6.5
-3.1	Hippopotamidae gen. indet.	molar frag	U. Nawata	LOTH-150	6.5
-3.1	Hippopotamidae gen. indet.	molar frag	U. Nawata	LOTH-51	6.5
-2.9	Hippopotamidae gen. indet.	molar frag	U. Nawata	LOTH-160	6.5
-2.8	Hippopotamidae gen. indet.	P2	U. Nawata	LOTH-55	6.5
-2.6	Hippopotamidae gen. indet.	dI	U. Nawata	LOTH-68	6.5
-2.6	Hippopotamidae gen. indet.	dx & mx	U. Nawata	LOTH-49	6.5
-2.5	Hippopotamidae gen. indet.	M	U. Nawata	LOTH-43	6.5
-1.6	Hippopotamidae gen. indet.	molar frag	U. Nawata	LOTH-168	6.5
-1.0	Hippopotamidae gen. indet.	molar frag	U. Nawata	LOTH-175	6.5
-1.0	Hippopotamidae gen. indet.	molar frag	U. Nawata	LOTH-174	6.5
-0.6	Hippopotamidae gen. indet.	tusk	U. Nawata	LOTH 87	6.5
-0.4	Hippopotamidae gen. indet.	molar frag	U. Nawata	LOTH-156	6.5
-0.3	Hippopotamidae gen. indet.	molar frag	U. Nawata	LOTH 157	6.5
0.6	Hippopotamidae gen. indet.	molar frag	U. Nawata	LOTH-46	6.5
0.8	Hippopotamidae gen. indet.	molar frag	U. Nawata	LOTH-153	6.5
0.9	Hippopotamidae gen. indet.	molar frag	U. Nawata	LOTH-165	6.5
-8.2	Hippopotamidae gen. indet.	molar frag	Apak	LOTH-112	4.2
-7.0	Hippopotamidae gen. indet.	M	Apak	LOTH-99	4.2
-4.6	Hippopotamidae gen. indet.	molar frag	Apak	LOTH-104	4.2
-4.4	Hippopotamidae gen. indet.	molar frag	Apak	LOTH-62	4.2
-3.6	Hippopotamidae gen. indet.	molar frag	Apak	LOTH-102	4.2
-3.3	Hippopotamidae gen. indet.	molar frag	Apak	LOTH-63	4.2
-0.9	Hippopotamidae gen. indet.	molar frag	Apak	LOTH-109	4.2
Rhinocerotidae					
-11.6	Rhinocerotidae gen indet.	M3	Nakali	KNM-NA 47424	9.9
-11.2	Rhinocerotidae gen indet.	M2	Nakali	KNM-NA 89_a	9.9
-10.3	Rhinocerotidae gen indet.	M3	Nakali	KNM-NA 255(C)	9.9
-9.6	Rhinocerotidae gen indet.	m1	Nakali	KNM-NA 106	9.9
-9.4	Rhinocerotidae gen indet.	unkn	Nakali	KNM-NA 104	9.9
-9.3	Rhinocerotidae gen indet.	unkn	Nakali	KNM-NA 93	9.9
-9.2	Rhinocerotidae gen indet.	M1 or M2	Nakali	KNM-NA 47406	9.9
-9.1	Rhinocerotidae gen indet.	unkn	Nakali	KNM-NA 92	9.9
-9.0	Rhinocerotidae gen indet.	M3	Nakali	KNM-NA 47534	9.9

$\delta^{13}C$	Taxon	Part	Fm./Mbr.	Sample	Age (Ma)
Rhinocerotidae (cont.)					
-8.7	Rhinocerotidae gen indet.	molar frag	Nakali	KNM-NA 47419	9.9
-6.5	Rhinocerotidae gen indet.	M3	Nakali	KNM-NA 47409	9.9
-2.4	Brachypotherium sp.	m3	L. Namarungule	KNM-SH 12143	9.6
-5.7	Chilotheridium pattersoni	m3	L. Namarungule	KNM-SH 15769	9.6
-3.2	Chilotheridium pattersoni	mx	L. Namarungule	KNM-SH 15751	9.6
-1.0	Chilotheridium pattersoni	M3	L. Namarungule	KNM-SH 15831	9.6
-1.0	Chilotheridium pattersoni	M3	L. Namarungule	KNM-SH 15832	9.6
-7.1	Elasmotherinae	M1 or M2	L. Namarungule	KNM-SH 15824	9.6
-1.2	Elasmotherinae	M3	L. Namarungule	KNM-SH 15828	9.6
-9.6	Rhinocerotidae gen indet.	p3 or p4	L. Namarungule	KNM-SH 15768	9.6
-8.1	Rhinocerotidae gen indet.	unkn	L. Namarungule	KNM-SH 15767	9.6
-8.0	Rhinocerotidae gen indet.	m1	L. Namarungule	KNM-SH 15749	9.6
-8.0	Rhinocerotidae gen indet.	M2	L. Namarungule	KNM-SH 15833	9.6
-2.4	Rhinocerotidae gen indet.	m1	L. Namarungule	KNM-SH 15757	9.6
-9.7	Brachypotherium sp.	mx frag	U. Namarungule	KNM-SH 12145	9.3
-4.9	Rhinocerotidae gen indet.	mx frag	U. Namarungule	KNM-SH 12378	9.3
-11.0	Brachypotherium lewisi	m frag	L. Nawata	KNM-LT 86	7.4
-10.6	Brachypotherium lewisi	m frag	L. Nawata	KNM-LT 23960	7.4
-10.6	Brachypotherium lewisi	M2	L. Nawata	KNM-LT 22874	7.4
-9.7	Brachypotherium lewisi	m frag	L. Nawata	KNM-LT 24290	7.4
-9.2	Brachypotherium lewisi	M3	L. Nawata	KNM-LT 24290	7.4
-9.1	Brachypotherium lewisi	m frag	L. Nawata	KNM-LT 28735	7.4
-8.5	Brachypotherium lewisi	m frag	L. Nawata	KNM-LT 23965	7.4
-7.9	Brachypotherium lewisi	m	L. Nawata	KNM-LT 81	7.4
-7.1	Brachypotherium lewisi	M3	L. Nawata	KNM-LT 93	7.4
-7.0	Brachypotherium lewisi	m frag	L. Nawata	KNM-LT 26280	7.4
-4.0	Brachypotherium lewisi	P2	L. Nawata	KNM-LT 99	7.4
-9.8	Ceratotherium sp.	M2	L. Nawata	KNM-LT-89-en	7.4
-9.1	Ceratotherium sp.	M2	L. Nawata	KNM-LT 89	7.4
-8.9	Rhinocerotidae gen indet.	molar frag	L. Nawata	LOTH-70	7.4
-7.1	Rhinocerotidae gen indet.	PM, PM, M	L. Nawata	LOTH-121	7.4
-10.9	Brachypotherium lewisi	molar frag	U. Nawata	KNM-LT-95	6.5
-9.8	Brachypotherium lewisi	p1	U. Nawata	KNM-LT 23967	6.5
-9.5	Brachypotherium lewisi	P2	U. Nawata	KNM-LT 22872	6.5
-8.0	Brachypotherium lewisi	M3	U. Nawata	KNM-LT 30651	6.5
-7.0	Brachypotherium lewisi	p1	U. Nawata	KNM-LT 23962	6.5
-10.8	Ceratotherium sp.	m1 frag	U. Nawata	KNM-LT 96	6.5
-4.0	Ceratotherium sp.	molar frag	U. Nawata	KNM-LT-23772-en	6.5
-2.1	Ceratotherium sp.	m2?	U. Nawata	KNM-LT 26278	6.5
-1.3	Ceratotherium sp.	m1	U. Nawata	KNM-LT 82	6.5
-10.7	Diceros praecox	P	U. Nawata	KNM-LT 23961	6.5
-10.5	Diceros praecox	m1	U. Nawata	KNM-LT 84	6.5
-6.3	Diceros praecox	m frag	U. Nawata	KNM-LT 26285	6.5
-4.3	Diceros praecox	M1	U. Nawata	KNM-LT 23665	6.5
-5.5	Brachypotherium lewisi	molar frag	Apak	KNM-LT-90	4.2
-2.4	Ceratotherium sp.	m frag	Apak	KNM-LT 83	4.2
-10.7	Diceros praecox	M3	Apak	KNM-LT 28563	4.2
-3.6	Diceros praecox	m1	Apak	KNM-LT 28762	4.2
-2.5	Diceros praecox	m3	Apak	KNM-LT 23971	4.2
-11.2	Rhinocerotidae gen indet.	molar frag	Apak	LOTH-58	4.2
-2.4	Rhinocerotidae gen indet.	molar frag	Apak	LOTH-117	4.2
-2.3	Rhinocerotidae gen indet.	molar frag	Apak	LOTH-117	4.2
-2.2	Rhinocerotidae gen indet.	molar frag	Apak	LOTH-117	4.2
-2.1	Rhinocerotidae gen indet.	molar frag	Apak	LOTH-115	4.2
-2.0	Rhinocerotidae gen indet.	molar frag	Apak	LOTH-116	4.2
-0.6	Ceratotherium sp.	P2	Kaiyumung	KNM-LT 23969	3.2
0.5	Ceratotherium sp.	p2	Kaiyumung	KNM-LT 23968	3.2
0.8	Ceratotherium sp.	molar frag	Kaiyumung	KNM-LT-26283	3.2

$\delta^{13}C$	Taxon	Part	Fm./Mbr.	Sample	Age (Ma)
Suidae					
-10.8	Nyanzachoerus sp.	molar frag	Nakali	KNM-NA 47644	9.9
-9.8	Nyanzachoerus sp.	m frag	Nakali	NA38-11901	9.9
-9.1	Nyanzachoerus sp.	p4	Nakali	KNM-NA 47643	9.9
-9.0	Nyanzachoerus sp.	m3	Nakali	KNM-NA 45736	9.9
-8.8	Nyanzachoerus sp.	M3	Nakali	KNM-NA 47246	9.9
-8.7	Nyanzachoerus sp.	M1 or M2	Nakali	NA10-12008	9.9
-8.6	Nyanzachoerus sp.	Px	Nakali	KNM-NA 45737	9.9
-8.6	Nyanzachoerus sp.	m3	Nakali	KNM-NA 47242	9.9
-8.5	Nyanzachoerus sp.	m2	Nakali	KNM-NA 45743	9.9
-8.5	Nyanzachoerus sp.	molar frag	Nakali	KNM-NA 47280	9.9
-8.5	Nyanzachoerus sp.	p3 or p4	Nakali	KNM-NA 45739A	9.9
-8.2	Nyanzachoerus sp.	m frag	Nakali	NA12-12033	9.9
-8.2	Nyanzachoerus sp.	molar frag	Nakali	KNM-NA 45755	9.9
-7.8	Nyanzachoerus sp.	p4	Nakali	KNM-NA 47305	9.9
-6.3	Nyanzachoerus sp.	mx	Nakali	KNM-NA 47278	9.9
-7.4	Nyanzachoerus aff. syrticus	M1	L. Namarungule	KNM-SH 12418	9.6
-6.6	Nyanzachoerus aff. syrticus	M2	L. Namarungule	KNM-SH 18003	9.6
-3.5	Nyanzachoerus aff. syrticus	M1	L. Namarungule	KNM-SH 14760	9.6
-7.0	Nyanzachoerus sp.	molar frag	L. Namarungule	KNM-SH 18006	9.6
-6.5	Nyanzachoerus sp.	M1	L. Namarungule	KNM-SH 41910	9.6
-6.0	Nyanzachoerus sp.	m2	L. Namarungule	KNM-SH 40152	9.6
-5.3	Nyanzachoerus sp.	Mx frag	L. Namarungule	SH 6218 99	9.6
-7.9	Nyanzachoerus aff. syrticus	M3 frag	U. Namarungule	KNM-SH 12400	9.3
-5.1	Nyanzachoerus aff. syrticus	m2 frag	U. Namarungule	KNM-SH 12399	9.3
-8.4	Nyanzachoerus sp.	m2	U. Namarungule	KNM-SH 12420	9.3
-8.3	Nyanzachoerus devauxi	m3	L. Nawata	KNM-LT 26127	7.4
-8.3	Nyanzachoerus devauxi	m3	L. Nawata	KNM-LT 26116	7.4
-7.9	Nyanzachoerus devauxi	M3	L. Nawata	KNM-LT 110	7.4
-7.0	Nyanzachoerus devauxi	m3	L. Nawata	KNM-LT 303	7.4
-5.6	Nyanzachoerus devauxi	molar frag	L. Nawata	KNM-LT 22967	7.4
-9.6	Nyanzachoerus syrticus	m3	L. Nawata	KNM-LT 26115	7.4
-7.7	Nyanzachoerus syrticus	molar frag	L. Nawata	LOTH-132	7.4
-7.2	Nyanzachoerus syrticus	molar frag	L. Nawata	LOTH-129	7.4
-7.1	Nyanzachoerus syrticus	p4	L. Nawata	KNM-LT 26122	7.4
-5.7	Nyanzachoerus syrticus	m3	L. Nawata	KNM-LT 301	7.4
-8.6	Suidae gen. indet.	molar frag	L. Nawata	LOTH-134	7.4
-6.7	Suidae gen. indet.	i	L. Nawata	LOTH-96	7.4
-6.1	Suidae gen. indet.	molar frag	L. Nawata	LOTH-131	7.4
-6.1	Suidae gen. indet.	molar frag	L. Nawata	LOTH-80	7.4
-3.6	Nyanzachoerus cf. australis	M3	U. Nawata	KNM-LT 23627	6.5
-2.3	Nyanzachoerus cf. australis	m3	U. Nawata	KNM-LT 285	6.5
-5.7	Nyanzachoerus devauxi	M3	U. Nawata	KNM-LT 29096	6.5
-9.1	Nyanzachoerus syrticus	P4	U. Nawata	KNM-LT 26088	6.5
-8.6	Nyanzachoerus syrticus	M1	U. Nawata	KNM-LT 26088	6.5
-8.3	Nyanzachoerus syrticus	M2	U. Nawata	KNM-LT 26088	6.5
-6.5	Nyanzachoerus syrticus	m frag	U. Nawata	KNM-LT 24084	6.5
-5.9	Nyanzachoerus syrticus	molar frag	U. Nawata	KNM-LT 7709	6.5
-5.8	Nyanzachoerus syrticus	M2	U. Nawata	LOTH-67	6.5
-3.1	Nyanzachoerus syrticus	molar frag	U. Nawata	KNM-LT 23743	6.5
-2.7	Nyanzachoerus syrticus	M3	U. Nawata	KNM-LT 23747	6.5
-2.0	Suidae gen. indet.	molar frag	U. Nawata	LOTH-140	6.5
-4.0	Notochoerus jaegeri	M3	Apak	KNM-LT 311	4.2
-5.9	Nyanzachoerus cf. australis	m3	Apak	KNM-LT 26076	4.2
-2.6	Nyanzachoerus cf. australis	M3	Apak	KNM-LT 26092	4.2
-2.5	Nyanzachoerus cf. australis	M3	Apak	KNM-LT 26092	4.2
-1.9	Nyanzachoerus cf. australis	molar frag	Apak	LOTH-98	4.2

$\delta^{13}C$	Taxon	Part	Fm./Mbr.	Sample	Age (Ma)
Suidae (cont.)					
-1.8	Nyanzachoerus cf. australis	molar frag	Apak	KNM-LT 308	4.2
-1.5	Nyanzachoerus cf. australis	M3	Apak	KNM-LT 26084	4.2
-4.8	Suidae gen. indet.	molar frag	Apak	LOTH-105	4.2
-4.7	Suidae gen. indet.	molar frag	Apak	LOTH-105	4.2
-4.6	Suidae gen. indet.	molar frag	Apak	LOTH-105	4.2
-4.2	Suidae gen. indet.	I	Apak	LOTH-114	4.2
-2.9	Suidae gen. indet.	molar frag	Apak	LOTH-107	4.2
-2.5	Suidae gen. indet.	M	Apak	LOTH-113	4.2
-2.0	Notochoerus euilus	m3	Kaiyumung	KNM-LT 289	3.2
-1.8	Notochoerus euilus	m3	Kaiyumung	KNM-LT 23767	3.2
-1.2	Notochoerus euilus	M3	Kaiyumung	KNM-LT 26074	3.2
-0.5	Notochoerus euilus	M3	Kaiyumung	KNM-LT 24050	3.2
-0.2	Notochoerus euilus	m3	Kaiyumung	KNM-LT 26596	3.2
-2.9	Nyanzachoerus pattersoni	M3	Kaiyumung	KNM-LT 26137	3.2

CHAPTER 3

BOMB-CURVE RADIOCARBON MEASUREMENTS OF RECENT BIOLOGIC TISSUES AND APPLICATIONS TO STABLE ISOTOPE ECOLOGY AND PALEOECOLOGY, AND TO WILDLIFE FORENSICS

3.1 Abstract

Above-ground thermonuclear weapons testing from 1952 through 1962 nearly doubled the concentration of radiocarbon (^{14}C) in the atmosphere. As a result, organic material formed during or after this period can be radiocarbon dated using the abrupt rise and steady fall of the ^{14}C concentration in the atmosphere known as the bomb-curve. We test the accuracy of Accelerator Mass Spectrometry radiocarbon dating of various herbivore (n=26) and plant (n=3) tissues collected on known dates between 1905 and 2008 in equatorial East Africa. Herbivore samples include apatite from tooth enamel and tusk dentin, collagen from tusk dentin, soft tissue from a tusk pulp cavity, and keratin from hair and horn. Plant samples are annual grasses. Herbivore and plant samples formed after 1955 are dated at -0.8 ± 0.7 years of collection for apatite (n=5), -1.2 years for collagen (n=1), -0.7 years for soft tissue (n=1), 0.3 ± 0.6 years for plants (n=3), and -1.3 ± 1.8 years for hair and horn (n=11). ^{14}C ages from dentin apatite and collagen from

the same tissue sample yield indistinguishable ages, as does NaOCl-treated and untreated dentin apatite. Results from four hair samples older than 1955 have high age uncertainties ranging from 17 to 231 years largely due to the Suess effect (e.g., Tans et al., 1979). The results demonstrate that ^{14}C dating of post-1955 animal tissues and plants is an accurate method for determining time of tissue formation.

^{14}C dating of tissues has applications to stable isotope (paleo)ecology and wildlife forensics. We use data from 41 additional samples to determine growth rates in upper and lower hippopotamus canines (1.9 to 7.5 cm/year) and in elephant tusks (4.1 to 5.1 cm/year), molar enamel (1.4 to 1.6 cm/year), and tail hair (0.8 mm/day). Establishing growth rates from ^{14}C ages improves interpretations of serial stable isotope data for (paleo)ecological studies. Growth rates can also be used to calculate the time interval represented in periodic histological structures in dental tissues, which in turn may be used as chronometers in fossil teeth. We determine a time interval of 10.3 ± 1.8 days between hippo canine perikymata and confirm the weekly periodicity of second-order growth increments in African elephant tusks. Finally, bomb-curve ^{14}C dating of confiscated animal tissues can be used to determine if trade in the item is legal, since many CITES trade restrictions are based on the age of the tissue. We demonstrate that ^{14}C dating can be a powerful forensic tool to combat illegal trade in animal parts.

3.2 Introduction

Carbon-14 (^{14}C) is produced in the atmosphere primarily by neutron interaction with ^{14}N through the reaction $^{14}N + n \rightarrow {}^{14}C + p$. This occurs naturally from secondary neutron flux generated by cosmic rays, and anthropogenically by high neutron flux from

nuclear fission in bombs or to a lesser degree, nuclear reactors. Atmospheric ^{14}C is oxidized to CO_2, which enters the terrestrial biosphere through assimilation into plant biomass. Other living organisms incorporate ^{14}C into their tissues by consuming plants or organisms that consume plants. ^{14}C enters the oceans as CO_2 through air-sea exchange and subsequent vertical mixing, and becomes part of the biologically available DIC pool.

Following the inception of thermonuclear weapons testing, periodic measurement of atmospheric ^{14}C concentrations began at stations around the world. These data document the abrupt rise and steady fall of ^{14}C concentration in the atmosphere known as the bomb-curve. The atmospheric ^{14}C concentration and its regional variation are well known for the last 60 years (Hua and Barbetti, 2004; Levin and Kromer, 2004). These measurements have culminated in large data sets that have proven extremely useful for studying the atmosphere, biosphere, ocean circulation, and carbon cycling (Broecker et al., 1985; Broecker and Walton, 1959; Hua and Barbetti, 2004; Levin and Hesshaimer, 2006; Nydal, 1968; Nydal and Lövseth, 1983).

Previous studies testing bomb-curve ^{14}C dating are largely limited to tree rings and selected mammal tissues. Alpha-cellulose ^{14}C measurements of individual tree rings have been combined with atmospheric $^{14}CO_2$ measurements to develop ^{14}C age calibration data sets (Hua and Barbetti, 2004; Hua et al., 1999). Vogel et al. (2002) calculated a ^{14}C age within one year of the known age for a palm leaf (ca. 1964) and determined growth rates for several plants of unknown ages. Geyh (2001) found human bone collagen and animal leather are less suitable for bomb-curve dating than hair, which could be used to determine age of death within ~2 years. Forensics research to determine year of birth has focused on tissues that undergo little to no *in vivo* remodeling or

turnover. Multiple studies show human tooth enamel and dentin can be reliably used to calculate birth year (Buchholz and Spalding, 2010; Cook et al., 2006; Spalding et al., 2005; Ubelaker et al., 2006; Wang et al., 2010) and proteins in the crystalline portions of eye lenses also provide accurate birth year estimates (Lynnerup et al., 2008). Vogel et al. (2002) found that radiocarbon in basal tusk collagen yields calibrated ages that date to the year before the known date of death for five elephants. Sideras-Haddad and Brown (2002) similarly explored the use of ^{14}C dating in elephant tusks but do not specify whether tusk collagen or apatite was analyzed.

Here we use animal and plant tissues of known ages to expand significantly on previous studies to show that from 1955 to present, ^{14}C-calibrated ages accurately record the date in which the tissues formed. Given the appropriate sampling strategy, ^{14}C-calibrated ages can be used to determine year of birth or death, and age at death. In addition to dating material, multiple ^{14}C- calibrated ages along continuously growing tissues such as teeth and hair can be used to determine growth rates and resolve the periodicity in growth increments in teeth and tusks.

We demonstrate the accuracy of bomb-curve ^{14}C dating based on results from 30 apatite, collagen, keratin, soft tissue, and plant samples. Maximum accuracy with respect to the known age is achieved by using hair, horn, tooth enamel, and tusk dentin, all of which undergo little to no turnover or remodeling after formation. Samples collected from the proximal, or most recently formed, portion of the tissue can be used to determine date of collection, which is often, but not always, death. Serially sampling along the growth axis of continuously growing hair and teeth (i.e., molars, tusks, and canines) can be used to determine tissue growth rate. To accomplish this, we use ^{14}C

ages from an additional 41 samples from *Hippopotamus amphibius* (hippo) canine enamel and *Loxodonta africana* (elephant) tusk collagen, tusk and molar apatite, and tail hair keratin. We provide examples of how ^{14}C ages from these mammal tissues can be used in stable isotope (paleo)ecology and wildlife forensics. In stable isotope ecology, growth rates are necessary to convert distance along the growth axis of a tooth or tusk to time, which enables comparison of isotope data with time series data (e.g., temperature, rainfall, or remote sensing data such as NDVI). ^{14}C-derived growth rates from extant species are used to evaluate the period of time (e.g., days or weeks) represented in growth increments in dental tissues, providing a basis for establishing a chronometer in fossil teeth. This can provide chronologic control for intratooth stable isotope and histological studies that aim to evaluate seasonal environmental variability in past environments. We demonstrate that ^{14}C dating can be used in wildlife forensics to determine age of confiscated animal tissues, which in many cases is equivalent to date of death. For many animal parts, such as ivory and rhino horn, this often determines whether trade of the item, defined here as sale, purchase, import, export, or re-export, is legal according to international regulations.

3.3 Materials and Methods

3.3.1 Sample description

Herbivore and plant samples were collected for ^{14}C analysis from the field or museum collections between 1971 and 2009 and span known ages of 1905 to 2008. Summary sample information is listed in Table 3.1, and more detailed sample information, including sample and species identification, known age, geographic location

and coordinates, and specimen location is provided in Appendix B. Hair sampled for this study was determinate body hair from primates and ungulates and indeterminate tail hair from elephants and one ungulate. The horn sample comes from an oryx; the soft tissue sample was from tissue dried onto the pulp cavity of an elephant tusk. Collagen is from elephant tusk and molar dentin. Apatite samples are from elephant molar enamel and tusk dentin, and from hippo canine enamel. Three annual grass samples are from Kenya.

3.3.2 Sampling plan for determining growth rates

The structure and growth processes of hair and teeth were considered in devising sampling plans that minimized the time averaging in tissues. For elephant tail hair, a 3 to 5 mm segment of hair was cut from the proximal and distal end. Each sample represents approximately 4 to 6 days based on the growth rate of 0.81 ± 0.11 mm/day for female elephant tail hair determined by Wittemyer et al. (2009). Elephant tusks are continuously growing, modified incisors made up of dentin with a cementum outer layer. Enamel is deposited at the tip of the tusk, though this is rarely if ever present in adult individuals due to normal wear. Dentin is deposited throughout life along the conical pulp cavity surface, and incremental growth features representing annual, weekly (or fortnightly), and daily intervals are present in proboscidean tusks (e.g., Fisher et al., 1996). Dentin was removed from longitudinally-cut tusks by drilling along a 1 mm wide path parallel to growth increments. Distances are measured along the tusk axis from the horn of the pulp cavity to the tip of the tusk (Figure 3.1A). Sample position is determined by where the growth increments intersect the tusk axis.

Tooth enamel undergoes a more protracted formation process than tusk dentin. An immature enamel matrix is initially secreted by ameloblast cells, followed by a prolonged period of maturation of weeks to months (e.g., table 1 in Kohn, 2004). Like tooth dentin, enamel contains incremental growth features, and each new layer forms subparallel to the enamel-dentin junction of the tooth (Dean, 2000). We mitigate the problem of enamel maturation using the smoothing parameter provided in the ^{14}C age-calibration software, described below. We also minimize the time averaging by drilling ~1- to 10-mm-wide sample paths through the entire thickness of enamel, oriented parallel to incremental growth features (i.e., perikymata) visible on the outer enamel surface.

Elephant cheek teeth (i.e., premolars and molars) consist of a battery of thick, enamel-covered plates. Plates grow from the initial occlusal surface toward the cervical margin, making the base the youngest part (Figure 3.1B). All length measurements in this study begin at the cervical margin. Multiple plates are forming at any given time, exclusive of the very beginning and end of molar formation. When enamel maturation is complete, cementum forms on the outer surface of the plate and eventually all plates are cemented together to form the molar (Figure 3.1B). We use at least two ^{14}C ages per plate to determine vertical growth rates in six plates from two individuals. One molar is from a male elephant, TE-95, and was collected in Tsavo East National Park shortly after death around 1964. The other is R37, a female from Samburu National Reserve in Kenya who died on September 26, 2006. Both molars are lower third molars (m3), or sixth molars according to the system devised by Laws (1966).

Hippo canines, often referred to as tusks, grow continuously throughout the life of the individual. We use the term canine throughout this paper to avoid confusion with

elephant tusks. We determine growth rates for five canines (four lower and one upper) from four individuals that died between 1971 and 2007. Distances are measured from the proximal end along the outer curve of the canine because measurement along this surface is most convenient and unambiguous, as opposed to the inner curve or the midline (Figure 3.1C).

3.3.3 Sample preparation

Keratin (hair and horn) samples were wiped with ethanol to remove adhering contaminants. For hair, approximately 3-5 mg were cut from the proximal end of the hair. For horn, approximately 4 mg of material was removed from the inner part at the base of the horn using a Dremel® tool. Samples were loaded into 9-mm quartz tubes (precombusted to 900° C) with ~100 mg of CuO and Ag foil. They were evacuated on a vacuum line, sealed with a torch, and combusted at 850°C for 4 hours. An organic ^{14}C blank, Rio Frio charcoal, was prepared along with the unknowns.

Tusk collagen was isolated from 28 to 50 mg of drilled, powdered dentin by treatment with 0.25 or 0.5 M HCl for at least 4 hours. Acid was refreshed at least once during the reaction period. Treated powder was centrifuged, neutralized with NaOH, rinsed 5 times with ultra-pure water, and dried overnight at 60°C. Collagen was combusted by the same method as the keratin.

Apatite from enamel and dentin was removed with a Dremel® tool equipped with a 1-mm-diameter bit. Prior to removing sample powder, an area in excess of the actual milling area was prepared by milling away the outermost ~0.2 mm of enamel to expose a clean enamel surface. Approximately 90 to 210 mg of powder was transferred into pre-

combusted glassware, evacuated on a vacuum line, and digested offline with 105% H_3PO_4 in sealed vessels at 90° C for 2 hours or until the reaction was complete. Two elephant tusk dentin samples were split and treated with excess 3% NaOCl for 30 minutes to remove organics. Treated samples were rinsed three times in ultra-pure water, dried overnight at 60°C, and digested in the same manner as untreated samples. An inorganic ^{14}C blank, Carrara marble or IAEA-C1, was prepared along with the unknowns.

Evolved CO_2 from combustion or acid digestion was cryogenically extracted on a vacuum line to remove water and other contaminants. SO_2, commonly present in enamel samples, was removed by reducing it onto silver: sample gas was either passed across hot (~500° C) Ag-Cu wool or a piece of precombusted Ag foil was placed in the break-seal tube with the extracted CO_2 sample and heated at 60° C for at least 24 hours. In most cases, extracted CO_2 was split (~2:1) and sealed into precombusted 6-mm-diameter Pyrex tubes. The larger aliquot was graphitized using the Fe-Zn reduction method and pressed into a target containing ~1 mg carbon. For smaller sample masses, no split was made, and all extracted CO_2 was graphitized.

3.3.4 Does ^{14}C vary based on tissue type or pretreatment?

Two elephants with known dates of death provide an opportunity to test for variation in ^{14}C concentration based on tissue type. From R37, we measured ^{14}C in tail hair, soft tissue from the tusk pulp cavity, tusk collagen, 3% NaOCl-treated tusk apatite, and untreated tusk apatite. We sampled the proximal end of a tail hair collected the day after death. The soft tissue sample was from pulp cavity tissue that dried onto the surface of the pulp cavity of the tusk. The collagen and two apatite samples are from the same

aliquot of dentin drilled from the tusk pulp cavity margin. We also measured ^{14}C in collagen, 3% NaOH-treated apatite, and untreated apatite from the same aliquot of dentin from the tusk pulp cavity margin of Misha, who died at Utah's Hogle Zoo in September 2008.

3.3.5 ^{14}C and $\delta^{13}C$ measurement

Seventy-one samples were analyzed for ^{14}C concentration on a 2.5MV General Ionex or a 3.0MV National Electrostatics Corporation Accelerator Mass Spectrometer (AMS) at the University of Arizona with an external precision of ~0.4%. Stable carbon isotope ratios were determined from the remaining extracted CO_2 split at the University of Arizona on a VG Isotech Optima Spectrometer (IRMS). For smaller ^{14}C samples that lacked a CO_2 split, carbon isotope ratios were determined on additional sample material using online (e.g., Costech 4010 Elemental Analyzer or Finnigan CarboFlo) methods at the University of Utah's Stable Isotope Ratio Facility for Environmental Research on an MAT-252 IRMS. All samples were analyzed along with internal lab standards calibrated to international standards, and precision of sample $\delta^{13}C$ values is <0.2 ‰. The $\delta^{13}C$ data were used for fractionation corrections of ^{14}C.

3.3.6 Calculation and reporting of bomb-curve ^{14}C-calibrated ages

All data are reported as fraction modern carbon ($F^{14}C$) following the recommended convention for post-bomb ^{14}C measurements (Reimer et al., 2004) where

$$F^{14}C = (A_S/0.95\ A_{OX}) \times (0.975/0.981)^2 \times [(1+\delta^{13}C_{OX}/1000) / (1+ \delta^{13}C_S/1000)]^2, \qquad (1)$$

A is the activity or $^{14}C/^{12}C$ ratio, and the subscripts S and OX are for the sample and the oxalic acid standard. Where appropriate, we also use the $\Delta^{14}C$ notation, expressed in permil notation (‰), where

$$\Delta^{14}C = [(F^{14}C)\, e^{\lambda(1950\text{-year})} - 1] \times 1000, \qquad (2)$$

λ is 1/8267 year, and year is the year the sample was analyzed.

As nearly all samples are from equatorial East Africa and range in age from 1905 to 2008, age calibration necessitates the use of the Northern Hemisphere Zone 3 (NH3), Southern Hemisphere (SH), and Levin datasets (Hua and Barbetti, 2004; Levin et al., 2008; Levin and Kromer, 2004). Grass samples from low-latitude southern hemisphere sites (1° to 3° S) have known ages that bracket the steep rise in the bomb-curve. These were selected for ^{14}C measurement to test whether samples from this region fall on the NH3 or SH1 curve. The Northern Hemisphere Zone 2 (NH2) and Levin datasets are used for age calibration on the tusk from Misha.

Calibrated ^{14}C ages were determined using the CALIBomb program (Reimer and Reimer, 2010). The program prepends the bomb calibration data sets with 300 years of INTCAL04 data. Two important parameters used for calculating ages with CALIBomb are resolution and smoothing. Resolution determines the minimum length of time in years that is required to distinguish separate calibrated ranges. We use the default value of 0.2 years for all samples. Smoothing is set to the duration over which the sample forms. We use 0.5 years for teeth and tusks based on our sampling geometry and the time over which these tissues form. The smoothing period for hair is 0.5 years, and this

is determined based on the approximate maximum turnover time of carbon in the tail hair (Cerling et al., 2007). For annual grasses, a smoothing period of 0.1 years is used.

3.3.7 Selection of ^{14}C-calibrated ages

$F^{14}C$ values near or above 1.10 will intersect the bomb curve twice and yield at least two possible calibrated ^{14}C ages for the NH2, NH3, or SH1 data sets. This is true for $F^{14}C$ values near or above 1.06 using the Levin data set. Resolution and smoothing values less than 0.2 may result in more than two possible ages. In this study, the calibrated ^{14}C age closer to known ages of the samples was selected. For samples in which the age is uncertain, there are several ways to select the appropriate ^{14}C age. First, if the approximate date of death or collection is known (e.g., 5 to 15 years), the correct age can often be selected. For example, using the NH3 data set and resolution and smoothing values of 0.2 and 0.5, respectively, a hair sample with an $F^{14}C$ value of 1.150 $\pm$ 0.002 yields calibrated ^{14}C age of 1958.72 $\pm$ 0.07 (1σ) or 1990.83 $\pm$ 0.42. If it is known that the sample was collected around or before 1965, then the younger age, 1990.83, can be rejected.

If there is no information about the date of death or collection, measuring the ^{14}C content at two or more positions along the growth axis of the hair (or other tissue) can be used to determine the appropriate calibrated ^{14}C age. Cook et al. (2006) and Wang et al. (2010) describe this method and show it works well in human teeth using combined enamel apatite and dentin collagen $F^{14}C$ values from the same tooth. We provide a brief summary here and show in the results and discussion sections that the method is applicable for multiple keratin, apatite, and collagen $F^{14}C$ values from a single sample.

Samples from the proximal and distal ends of a growing tissue such as hair, horn, or tooth will give two different $F^{14}C$ values. If the proximal $F^{14}C$ value is greater than the distal value, then the tissue formed during the rise of the bomb-curve, between 1955 and 1965. Given the opposite, whereby the proximal $F^{14}C$ value is less than the distal value, the tissue formed during the fall of the bomb-curve, between 1965 and present. For samples separated by a very short time period (< ~1 year), this technique of measuring two or more samples along the growth axis of the tissue may not be able to resolve the appropriate age, especially for tissues formed after ~1995.

3.4. Results

3.4.1 $F^{14}C$ and ^{14}C-calibrated ages for samples with known ages

The $F^{14}C$ values plotted against the known age clearly show that the $F^{14}C$ in herbivore and plant samples tracks the $F^{14}C$ of atmospheric CO_2 during the period in which the tissue formed for samples collected after 1955 (Figure 3.2). The NH3 and SH1 calibration curves are plotted in Figure 3.2 because we present data from samples from both regions. The NH3 data set is appended with the Levin data set (NH3+Levin) beginning at 1999.50 to permit ^{14}C age calibration through 2006. The two curves, NH3+Levin and SH1, differ significantly prior to ~1970 due to bomb testing locations and atmospheric circulation, and subtle differences of 4-5 ‰ continue to persist after 1970. Pre-1970 keratin and plant samples are confirmed (or in several cases presumed) to have been collected from the Southern Hemisphere and track the SH1 curve extremely well, with the exception of a single outlier, sample L10830, discussed in Section 3.4.3.

In Figure 3.3A, we show the known age versus the calibrated ^{14}C age for all samples (n=22) collected from 1955 to 2006. The ^{14}C ages for Misha, who died in 2008, could not be calculated because there are no existing published calibration data sets that extend beyond 2006 (Levin et al., 2008). Figure 3.3B includes four samples collected between 1905 and 1953 and illustrates the inaccuracy of ^{14}C ages before 1955. The mean residual, calculated from the difference between the ^{14}C age and known age, for 11 keratin samples collected after 1955 is -1.3 ± 1.8 (1σ) years. For apatite samples (n = 5), the mean residual is -0.8 ± 0.7 years; for grasses (n = 3), it is 0.3 ± 0.6 years. For the soft tissue and collagen samples, the residuals are -0.7 and -1.2 years, respectively. Tissues formed during the steeper parts of the bomb curve (i.e., 1960 to 1995) tend to have residuals less than 2 years (Figure 3.3C). The ^{14}C data for all samples with known ages are provided in Table 3.2.

3.4.2 Tissue growth rates from ^{14}C ages

We use multiple ^{14}C ages from elephant tail hair, molar plates, tusks, and hippo canines to calculate tissue growth rates (Table 3.3). The period of growth for some canines and both tusks continued beyond 1997, when ^{14}C data becomes sparse for both the NH3 and the SH1 data sets. For example, in the SH1 data set, there are no ^{14}C data between 1996.95 and 2001.0, and the NH3 data set has only two ^{14}C values between 1996.95 and its terminus in 1999.5. Thus, we use the Levin data set to calibrate ^{14}C ages for samples younger than 1960 that have an $F^{14}C \leq 1.110$.

3.4.2.1 Hippo canines. We calculate growth rates for five hippo canines using a total of 17 enamel ^{14}C ages, and the total amount of time recorded in each tusk ranges

from 7.8 to 11.5 years (Figures 3.4A and 3.4B, Table 3.3). Multiple ages were determined along the lower and upper canines of one individual, presumed to be a juvenile or young adult based on canine shape and size, that died in Queen Elizabeth National Park in Uganda in 1971. Five ^{14}C ages from the lower canine (KL (L)) and three from the upper (2KL (U)) give linear growth rates of 3.35 ± 0.25 cm/year and 1.94 ± 0.31 cm/year, respectively (Figure 3.4A). The lower canine has a total length of 37.2 cm, representing 11.1 years of growth; the upper canine (17.0 cm) represents 8.8 years of growth. The $F^{14}C$ values in each canine are highest in the middle section, indicating the bomb peak is recorded in these canines (Table 3.2).

Growth rates for three lower canines, all presumed to be from males based on canine size or field observations, are calculated based on ^{14}C ages from samples drilled within 5 cm of the proximal and distal ends (Table 3.3). Sample K11-KF, from the Koobi Fora spit at Lake Turkana, Kenya, yields a growth rate of 4.51 ± 0.21 cm/year and spans 7.6 years between 1972 and 1980 (Table 3.3). The other two canines, TSV-291 and K08-201, were collected near the town of Mtito Andei which lies just outside of Tsavo National Park, in 1996 and October 2007, respectively. Although the site is located in the SH1 region, paucity of data from 1996 to 2007 precludes use of the SH1 data set, and we use the NH3 and Levin data sets instead to calculate ages, as discussed in Section 3.3. Sample TSV-291 yields a growth rate of 7.47 ± 0.88 cm/year based on ^{14}C ages using the NH3 data set (Figure 3.4B). Sample K08-201 yields a growth rate of 4.87 ± 0.34 cm/year based on ^{14}C ages using the NH3 and Levin data sets (Figure 3.4B). The higher uncertainties from Tsavo canines are a result of the shallower slope of the bomb curve (-7 ‰/year) from 1990 to present and annual fluctuations of up to 30‰.

The growth rates determined in four lower canines range from 3.35 to 7.47 cm/year. Passey et al. (2005) measured growth rates of lower canines on two female hippos at the Toledo Zoo by notching the tooth at the gum line and measuring the distance from the gum line the following year. Growth rates from the 48- and 8- year-old females were 1.35 cm/year and 2.9 cm/year, respectively. These are lower than the average values determined in this study. This is likely due to differences in canine growth rates between male and female hippos and for the 48-year-old individual, age.

3.4.2.2 Elephant tusks. We calculate tusk growth rates for two female elephants using ^{14}C ages from collagen. Growth rates are 4.13 ± 0.39 cm/year and 5.10 ± 0.74 cm/year for R37 and Misha, respectively (Figure 3.4C and Table 3.3). We use linear growth rates because they best fit the data from the two tusks, although a second-order polynomial also describes tusk growth in R37. Since there is no calibrated ^{14}C age for the youngest data point for Misha, we use September 8, 2008, her known date of death.

Assuming an age at death of 53 ± 5 years old for R37 based on tooth wear (Laws, 1966; Lee et al., 2012), her tusk represents growth from 25 to 53 years of age, whereas Misha's tusk represents growth from 13 to 28 years of age. Thus, the difference in growth rate between the two tusks may be explained by ontogeny, whereby growth rates during early adulthood are 20% higher than those later in life. The difference may also relate to captive versus wild diet and stress levels. Although linear growth rates are appropriate for the time represented in the two tusks, our data suggest for tusks that record multiple ontogenetic stages (e.g., juvenile, adolescent, and adult), growth rates are not linear. Mastodon tusks show nonlinear growth rates based on measurements of annual incremental thicknesses and lengths over ~30 years (Fisher et al., 2008; Fisher, 2008).

The ^{14}C ages can also be used to calculate the number of years represented in a tusk. Using the distal ^{14}C ages and the known dates of death for R37 and Misha, the tusks represent 28.6 and 14.8 years, respectively (Table 3.3). Interestingly, this accounts for 54% and 53% of their total lifespans, suggesting similar overall rates of wear between the two female elephants. Our data are limited to two female elephants; multiple ^{14}C ages from individual tusks that grew between 1955 and 2005, particularly those from males and those that capture multiple ontogenetic stages, are necessary to provide an understanding of variation in tusk growth rate as a function of sex and age.

3.4.2.3 Elephant molars. We calculate vertical growth rates along six plates from two molars using 16 ^{14}C ages. These growth rates are time-averaged mineralization rates of enamel, which may differ from molar extension rate. The latter is determined by the extension of the molar plate as new dentin and immature enamel are formed, while the former represents the difference between the average ages of the enamel volumes sampled at each position along the plate. If molar extension and enamel maturation processes were constant throughout molar formation, then mineralization and extension rates would be equal. Figure 3.5A shows sample locations in the m3 from TE-95. Twelve ^{14}C ages were used to determine growth rates from four TE-95 plates (2, 4, 7, and 9), and four ages come from two plates in R37's m3. Growth rates from both molars range from 1.39 ± 0.27 to 1.63 ± 0.14 cm/year (Table 3.3; Figures 3.5B and 3.5C). The rates fall within the range of those determined histologically for the extinct Columbian mammoth (*Mammuthus columbi)*: 1.3 to 2.2 cm/year (Dirks et al., 2012; Metcalfe and Longstaffe, 2012). The ^{14}C data do not reveal whether growth rates are linear or not; however, Dirks et al. (2012) show that for two extinct proboscidean species, *M. columbi*

and a dwarf elephant, *Palaeoloxodon cypriotes*, growth rates are highest near the initial occlusal surface and decrease toward the cervical margin.

A single ^{14}C age from the posterior plate (11) of TE-95 that was forming when the elephant died yields an age of 1963.5 ± 0.1 years (Figure 3.5A). Two collagen dates from TE-95 dentin provide additional information about molar formation. One sample, TE-95 Rm6.7-1.3-C, is near the cervical margin of plate 7, and it yields a date of 1961.5 ± 0.8 years, which is ~1.5 years younger than the adjacent enamel (Figure 3.5A). The second sample, TE-95 Rm6-Root-C, is from the mesial root and yields a date of 1964.2 ± 0.1, which is the best estimate for the date of death. Total time represented in unworn molar plates from TE-95 is 7.3 ± 0.6 years, and total time represented in an m3 is >10 years based on ^{14}C dates from TE-95 and R37 (Table 3.3). The thick enamel and the long time intervals represented in a single plate or entire molar make fossil proboscidean teeth excellent candidates for intratooth stable isotope profiles in paleoecology (e.g., Metcalfe et al., 2011).

3.4.2.4 Elephant tail hair. Only one of two tail hairs sampled provides a reasonable growth rate. Sample TSV-171, collected on July 17, 1998 from a female African elephant in Tsavo National Park, yields a growth rate of 0.81 ± 0.77 (2σ) mm/day (Table 3.3). Wittemyer et al. (2009) used independent methods to calculate a growth rate of 0.81 ± 0.11 mm/day for female African elephants (n=38). The similarity of the two growth rates suggests a consistent offset between ^{14}C in elephant hair and $^{14}CO_2$ in the atmosphere as reported in the calibration data set (e.g., SH1). The offset between the measured (102.7 ± 1.2 ‰) and expected (95.8 ± 4.4 ‰) $\Delta^{14}C$ value is approximately 7 ‰. We discuss several possibilities for the enriched ^{14}C in Section

3.5.3. The second tail hair was collected from R37 within days of her death in September 2006. The proximal and distal ends of the 304-mm-long hair have nearly identical values of 74.3 ± 1.2 ‰ ($F^{14}C$ = 1.0820) and 72.5 ± 1.2 ‰ ($F^{14}C$ = 1.0803), and the higher value in the proximal end precludes calculating a growth rate. Similar to the two hair samples from TSV-171, the R37 tail hair is enriched in $\Delta^{14}C$ compared to expected values based on the date of death. Growth rates determined by independent methods from R37 tail hairs collected between 2001 and 2006 range from 0.56 to 0.62 mm/day.

3.4.3 ^{14}C variation based on tissue type or pretreatment

Four tissue types were sampled at death from two elephants to test for variation in ^{14}C based on tissue type. Collagen and apatite from tusk dentin sampled from the pulp cavity margin (e.g., the tissue forming at time of death) show indistinguishable $F^{14}C$ values (Table 3.4). The $F^{14}C$ values can be used to calculate a ^{14}C-calibrated date for R37, and the collagen and apatite ages fall within a range of less than 0.4 years. We tested whether treating tusk apatite with 3% NaOCl had any effect on $\Delta^{14}C$ values. Treated and untreated apatite samples from Misha have nearly identical $\Delta^{14}C$ values while those from R37 differ by 5.6‰, but fall within the range of 2σ error (Table 3.4). The data suggest treatment to oxidize organics prior to acid digestion is not necessary.

We also analyzed the proximal end of a tail hair (R37-prox-K) and soft tissue from R37's tusk pulp cavity (R37-PC-tissue). The $F^{14}C$ value in the tail hair is anomalously high, resulting in an older date than the actual date of death (Table 3.4). The soft tissue sample has a $\Delta^{14}C$ value of 43.7 ‰ and a ^{14}C-calibrated date of 2006.04, which is the closest to the actual date of death of all R37 tissues analyzed.

3.5 Discussion

3.5.1 Applications to stable isotope (paleo)ecology

3.5.1.1 ^{14}C-correlated stable isotope profiles. Serial sampling or intratooth stable isotope profiles of enamel yield information about seasonal change in diet and water use, which relate to seasonality of precipitation and vegetation. This has been suggested and employed as tool for (paleo)dietary and (paleo)ecological reconstruction in modern and fossil mammalian teeth (Fricke and O'Neil, 1996; Higgins and MacFadden, 2009; Hynek et al., 2012; Koch et al., 1989; Metcalfe et al., 2011; Passey and Cerling, 2002). In ungulate molars, tooth height and growth rate determine total formation time, which is generally no more than 2-3 years (Hoppe et al., 2004; Kohn, 2004). However, continuously growing teeth from large mammals (e.g., hippo canines and elephant tusks) and elephant molars form over years to decades, and therefore can be used to evaluate long-term dietary and seasonality changes (Codron et al., 2012; Koch et al., 1989; Passey and Cerling, 2002), and can capture ontogenetic transitions such as weaning (Rountrey et al., 2007).

We show that intratooth stable isotope profiles from two hippos that died nearly 11 years apart can be concatenated (with sufficient overlap) using ^{14}C data from the distal end of the younger hippo (K08-201) and the proximal end of the older hippo (TSV-291) (Figure 3.6). Both canines were collected from the same region near Tsavo National Park, and presumably record similar habitats within or near the Park. The proximal $F^{14}C$ value for TSV-291 and the distal $F^{14}C$ value for K08-201 are nearly identical (Table 3.2) and therefore yield similar ^{14}C ages (Figure 3.4B). Together, the profiles give an 18-year record of hippo ecology from Tsavo West National Park. The dominant feature in the

$\delta^{13}C$ record from TSV-291 is a rapid decrease of 5.4‰, indicating a switch to a C_3 diet of browse beginning in the latter part of 1995, followed by a 4‰ increase in $\delta^{18}O$ during the last half year of the hippo's life in 1996 (Figure 3.6). The onset of the $\delta^{13}C$ shift coincides with the beginning of a prolonged drought that persisted until April of 1997. The K08-201 canine suggests that C_3-dominated diets persisted among hippos in this region until the year 2000, when the diet returns to predominantly C_4 vegetation.

Overlapping isotope profiles from multiple teeth based on bomb-curve ^{14}C ages can provide long-term ecological records of a taxon or region. These records may be useful for tracking decadal (or longer) scale changes in land-use, climate, or life history patterns, and thus have potential application in wildlife ecology and conservation. Understanding how ecological change, such as periods of drought or seasonal precipitation, affects intratooth isotope profiles in extant taxa will also provide insight for interpreting profiles in fossil teeth.

3.5.1.2 Determining periodicity of incremental growth features from ^{14}C growth rates. Periodic incremental growth features in tooth enamel and dentin (e.g., perikymata, striae of Retzius, and Andresen lines) can be used as accurate chronometers if the time interval represented by each increment is known (Dean and Scandrett, 1996). In human and some other hominin teeth, perikymata visible on the surface of a tooth usually represent a period of 7 or 8 days (Reid and Dean, 2006). In proboscidean tusks, three hierarchical incremental growth features are present: first-order increments have annual periodicity, second-order are weekly in elephants and mammoths (fortnightly in mastodons), and third-order are daily (Fisher, 1987; Fisher, 2001).

Here we use ^{14}C growth rates to determine the time interval represented in hippo canine perikymata and to confirm the weekly time interval represented in elephant tusk dentin. By establishing a chronometer, the teeth can provide information about the timing of tooth development and other aspects of life history. The chronometer is also critical for interpreting intratooth stable isotope profiles in fossil teeth, where one of the primary goals is to determine the magnitude, duration, and periodicity of seasonal changes in past environments.

The distance between perikymata (n=158) was measured along sections of hippo canine K11-KF using a plugin (Inc Meas v1.2) in ImageJ software (Figure 3.7). Mean increment width is 1.27 ± 0.21 mm, and given the growth rate of 45.1 mm/year, each increment represents 10.3 ± 1.8 (2σ) days (Appendix B). Other hippo canines for which ^{14}C growth rates were determined either lacked visible perikymata (KL and 2KL) or photos for making measurements (TSV-291 and K08-201).

In the R37 tusk, we measured the thickness of second-order increments on a transversely-cut thin section located 2 mm from the horn of the pulp cavity using the same ImageJ plugin (Figure 3.8). The average growth rate determined from histological measurements is 103.0 ± 28.9 μm/week (Appendix B). To compare the histologically determined tusk growth with the ^{14}C growth rate measured along the tusk axis, the angle (θ) between the growth increments and tusk axis was measured in multiple locations and determined to be 7.53 ± 0.3°(Figure 3.1A). Using the trigonometric relationship between the tusk axis and a line perpendicular to the growth increments, the ^{14}C tusk growth rate is converted to the same orientation as the histological measurements and yields a growth rate of 105 ± 11 μm/week (Appendix B). This is remarkably close to the histologically

determined rate of 103 ± 29 μm/week, providing independent evidence for weekly periodicity of second-order growth increments in elephant tusk dentin.

The period recorded in growth increments in modern teeth and tusks can be applied with caution to similar taxa in the fossil record that cannot be bomb-curve radiocarbon dated, and thus provides a chronometer in fossil teeth. This is particularly useful for intratooth stable isotope profiles or histological data that are used to evaluate seasonality (e.g., Koch et al., 1989). The period between increments may differ between modern and fossil teeth.

3.5.2 Application of ^{14}C dating to wildlife forensics

The international trade in animal parts, defined here as sale, purchase, import, export, or re-export, is a booming industry estimated to value $5-15 billion annually (Roe et al., 2002). While corresponding numbers for the illegal trade are not known, the United Nations Environment Program estimated its value in 1998 to be on the order of $5-8 billion per year, while other sources argue the current value is twice this amount (US Department of State, 2007). The Convention of International Trade of Endangered Species (CITES) treaty was enacted in 1973 to prohibit international trade in animal parts from endangered species listed in Appendix 1 of the treaty. International trade of raw Asian and African elephant ivory has been banned since they were added to Appendix 1 in 1975 and 1989, respectively, with the exception of limited sales of African ivory from selected African countries in 1997, 2002, and most recently, in 2008 when 110 tons of ivory from South Africa, Botswana, Namibia, and Zimbabwe were sold to China and Japan. The demand for ivory remains high, especially in Asia, despite the ban and other

efforts to eliminate illegal trade. As a result, there has been a significant increase in poaching of African elephants since 2006 (CITES, 2010; Wasser et al., 2010).

One way in which recent, illegally procured ivory is brought to market is by cosmetically aging raw or worked ivory. For example, in the United States, interstate trade is legal for raw or worked African ivory (e.g., carved statues or figurines) if it was imported before 1989. Worked ivory imported after 1989 must be at least 100 years old for interstate trade to be legal. Trade of raw African ivory imported since 1989 is banned in accordance with the CITES treaty, the Endangered Species Act of 1973, and the African Elephant Conservation Act of 1988. Laws are similar for Asian elephant ivory, except the cut-off year is 1976. In the European Union, there are similar laws with different date criteria established through CITES and the European Commission Regulation (EC) 338/97 of 1997: Worked ivory imported prior to 1947 can be traded within the European Union, while all trade of raw ivory is illegal.

Given the dependence of trade status on the age date of ivory, we propose ^{14}C dating of ivory be employed as a wildlife forensics tool to assess whether trade is legal. Our results show that ivory apatite and collagen are both suitable for ^{14}C dating (Table 3.4), but since collagen requires less powdered ivory (~25 to 50 mg) than apatite (150 mg) for analysis, collagen may be preferable. Since there are at least two possible ages for each $F^{14}C$ value, if the question of the age date of ivory is not simply whether the animal part is prebomb or postbomb, then at least two samples must be taken from the specimen and the orientation of the growth axis (for tusks, hair, or horn) must be known to ascertain the correct age date (see Section 3.3.7). If this is not possible, measurements

of other radionuclides associated with nuclear weapons testing (i.e., ^{90}Sr, ^{228}Th, and ^{232}Th isotopes) may be useful for determining the correct ^{14}C age date.

Other forensic tools have been developed for geolocating the origin of ivory, such as DNA (Wasser et al., 2004), stable isotope analysis ($\delta^{13}C$, $\delta^{15}N$, $^{87}Sr/^{86}Sr$) of ivory (Van der Merwe et al., 1990; Vogel et al., 1990), and measurements of Schreger bands (bands formed of alternating layers of apatite with orientations at about right angles to one another) to differentiate between Asian and African elephant ivory (Trapani and Fisher, 2003). For confiscated ivory with an unknown origin, combined geolocating and ^{14}C dating forensic tools can serve to determine the source and age date of ivory and, as a result, whether trade is legal. In addition, this information can help identify where and when areas are being exploited for illegal trade, information critical for directing conservation and antipoaching resources.

The ^{14}C dating method can be extended to other animal parts such as hair and horn (e.g., from rhinos) as indicated by our results on keratin samples of known age date (Table 3.2). The increase in the number of AMS and beta-counting facilities capable of making ^{14}C measurements over recent decades has resulted in lower analytical costs and faster sample turnaround times, making ^{14}C measurements a practical forensic tool in the effort to end illegal trade in animal parts.

3.5.3 Limitations of ^{14}C age dating of tissues

Our results show calibrated ^{14}C ages are consistent with known ages of biologic tissues that undergo little or no remodeling and are formed after 1955. Here we discuss two problematic samples to elucidate potential complications of the method. It is clear

from the data that tissues formed prior to ~1955 are not suitable for bomb-curve ^{14}C dating (Figure 3.2B). One sample of primate hair from *Cercopithecus mitis* (blue monkey) was reportedly collected in the Congo in 1962, but has a $F^{14}C$ of 0.9749 ± 0.0023, which clearly indicates it formed prior to 1955. Nearly 70% of the blue monkey's diet is from fruit, leaves, and other vegetation, so significant dietary contribution from plant material more than several years old at any time is unlikely (Cords, 1986). Hair from other primates, including two other *C. mitis*, yielded ^{14}C age dates consistent with known dates, further suggesting that diet is not responsible for the age date discrepancy. The most likely explanation is that the date of museum accession, which we used as the known age date of the sample, does not reflect the date of death.

The ^{14}C age dates from the proximal ends of two elephant tail hairs are older than their known ages due to enriched $\Delta^{14}C$ values (Table 3.2). Three factors that may contribute to this include diet, physiology, and ecosystem dynamics. Extant African elephants are predominantly browsers, and they incorporate woody vegetation into their diet, especially during periods of drought when the nutritional quality of vegetation decreases. Woody vegetation such as twigs, branches, or bark, may be several to tens of years old and have higher $\Delta^{14}C$ values. During wet periods, elephant diets include as much as 50% annual grasses (Cerling et al., 2009), and this could result in more accurate $\Delta^{14}C$ values of keratin. Collagen, apatite, and soft tissue sampled at death from R37 do not show the ~20 ‰ enrichment seen in the proximal tail hair sample, suggesting partitioning of carbon between different tissues (Table 3.4). Determining ^{14}C ages at a higher spatial resolution from a tail hair with a known collection date, known dietary

input (e.g., percent graze vs. browse) based on field observations and carbon stable isotopes, and corresponding fecal samples that can be ^{14}C dated could address this issue.

3.6 Conclusions

In this study, we show bomb-curve ^{14}C can be used to accurately date keratin, collagen, apatite, and bulk plant tissue, and we provide examples of applications of the technique to stable isotope (paleo)ecology and wildlife forensics. Hair, horn, enamel, dentin, and grasses that formed between 1955 and 2008 have been accurately dated (-0.9 ± 1.4 years) for 21 samples of known age using bomb-curve ^{14}C. Sampling teeth, tusks, and horn parallel to growth increments minimizes time averaging in tissues to provide greater age dating precision. We calculated growth rates of elephant tail hair, tusks, molars, and hippo canines from multiple ^{14}C ages measured along tissue growth axes. ^{14}C measurements from NaOCl-treated dentin, untreated dentin, and collagen from two elephant tusks yield indistinguishable ages, indicating both apatite and collagen are suitable for bomb-curve ^{14}C dating, and that treatment of dentin apatite to remove organics is not necessary for ^{14}C measurement. Our results, particularly the ability to establish growth rates in teeth and tusks, have the following immediate and novel applications to stable isotope (paleo)ecology and wildlife forensics.

We concatenated intratooth $\delta^{13}C$ and $\delta^{18}O$ profiles from two hippo tusks using ^{14}C ages to establish a tie-point, resulting in an 18-year composite stable isotope record. The $\delta^{13}C$ data show a major shift in hippo diet from C_4 grasses to C_3 browse associated with the onset of a 2-year drought from 1995 through 1996. Records such as these can be used

to study long-term (i.e., multidecadal) population, climate, or ecosystem dynamics that would not be feasible from a single intratooth profile, exclusive of proboscidean tusks.

Growth rates from bomb-curve ^{14}C dating can be used to determine the time represented in periodic growth increments. We calculated a periodicity of 10.3 ± 1.8 days between perikymata along a lower hippo canine from ^{14}C–based canine growth rate. Elephant tusk growth rates based on ^{14}C ages and histological measurements are 105 ± 11 and 103 ± 29 μm/week, respectively, confirming the weekly periodicity of second-order growth increments in African elephant tusk dentin. Determining the time represented in periodic growth increments in teeth of extant taxa provides a potential chronometer in fossil teeth, where knowledge of growth rate is critical to interpretation of intratooth stable isotope profiles or histological data related to life history.

^{14}C dating of raw or worked animal hair, horn, teeth, or tusk can be used to establish sample age date and in many cases date of death of an animal, which can determine whether trade (e.g., sale, import, export, or re-export) is legal according to CITES and national regulations. Poaching for elephant tusks and rhino horn has increased significantly since 2006. Turnaround time and cost of ^{14}C measurements have decreased in the past decades and therefore make it an accessible wildlife forensics tool. Combined with geolocation (e.g., DNA, stable isotope, histological) forensic techniques, ^{14}C dating of animal parts can help budget-limited government agencies and NGOs determine how and where to direct conservation and antipoaching resources.

3.7 Acknowledgments

We thank the Office of the President of the Republic of Kenya, the Kenya Wildlife Service, and the Samburu and Buffalo Springs County Councils for permission to conduct this research. We thank the Kenya Wildlife Service; Save The Elephants; the National Museums of Kenya; the Field Museum of Natural History; Prince Kaleme at Centre de Recherche en Sciences Naturelles, Lwiro, DRC; Nancy Carpenter at Utah's Hogle Zoo; Hans Klingel; and Francis Kirera for sample collection or providing access to collections. We thank Adam Rountrey for furnishing a copy of the plug-in (IncMeas v1.2) used to measure growth increments in ImageJ and Kendra Chritz, Audrey Copeland, Blake Hethmon, and Jared Singer for assistance with sample preparation. This project was supported by National Science Foundation grants EAR-0819611, BCS-0621542, the National Geographic Society, and by a University of Utah Graduate Research Fellowship. Stable isotope analyses were carried out at the University of Arizona and in the SIRFER facility at the University of Utah. This work was carried out under CITES permits US831854/9, 02US053837/9, and 07US159997/9.

3.8 References

Broecker, W. S., Peng, T. H., Ostlund, G., and Stuiver, M., 1985, The distribution of bomb radiocarbon in the ocean: Journal of Geophysical Research, v. 90, no. C4, p. 6953-6970.

Broecker, W. S., and Walton, A., 1959, Radiocarbon from nuclear tests: Science, v. 130, p 309-314.

Buchholz, B., and Spalding, K., 2010, Year of birth determination using radiocarbon dating of dental enamel: Surface and Interface Analysis, v. 42, no. 5, p. 398-401.

Cerling, T. E., Ayliffe, L. K., Dearing, M. D., Ehleringer, J. R., Passey, B. H., Podlesak, D. W., Torregrossa, A. M., and West, A. G., 2007, Determining biological tissue turnover using stable isotopes: The reaction progress variable: Oecologia, v. 151, no. 2, p. 175-189.

Cerling, T. E., Wittemyer, G., Ehleringer, J. R., Remien, C. H., and Douglas-Hamilton, I., 2009, History of Animals using Isotope Records (HAIR): A 6-year dietary history of one family of African elephants: Proceedings of the National Academy of Sciences, v. 106, no. 20, p. 8093.

CITES, 2010, Monitoring of illegal hunting in elephant range states, (CoP15, Doc. 44.2 Rev. 1, 2010).

Codron, J., Codron, D., Sponheimer, M., Kirkman, K., Duffy, K. J., Raubenheimer, E. J., Mélice, J. L., Grant, R., Clauss, M., and Lee-Thorp, J. A., 2012, Stable isotope series from elephant ivory reveal lifetime histories of a true dietary generalist: Proceedings of the Royal Society B: Biological Sciences, v. 279, p. 2433-2441.

Cook, G. T., Dunbar, E., Black, S. M., and SHENG, X., 2006, A preliminary assessment of age at death determination using the nuclear weapons testing 14C activity of dentine and enamel: Radiocarbon, v. 48, no. 3, p. 305-313.

Cords, M., 1986, Interspecific and intraspecific variation in diet of two forest guenons, Cercopithecus ascanius and C. mitis: The Journal of Animal Ecology, p. 811-827.

Dean, M., 2000, Incremental markings in enamel and dentine: What they can tell us about the way teeth grow: Development, Function and Evolution of Teeth, p. 119-130.

Dean, M., and Scandrett, A., 1996, The relation between long-period incremental markings in dentine and daily cross-striations in enamel in human teeth: Archives of oral biology, v. 41, no. 3, p. 233-241.

Dirks, W., Bromage, T. G., and Agenbroad, L. D., 2012, The duration and rate of molar plate formation in *Palaeoloxodon cypriotes* and *Mammuthus columbi* from dental histology: Quaternary International, v. 255, p. 79-85.

Fisher, D., Beld, S., Rountrey, A., Allmon, W., and Nester, P., 2008, Tusk record of the North Java mastodon: Palaeontographica Americana, v. 61, p. 417-463.

Fisher, D. C., 1987, Mastodon procurement by paleoindians of the Great Lakes Region: Hunting or scavenging?, *in* Nitecki, M. H., and Nitecki, D. V., eds., The Evolution of Human Hunting: New York, Plenum, p. 309-421.

-, 2001, Season of death, growth rates, and life history of North American mammoths: Proceedings of the international conference on mammoth site studies., p. 121-135.

-, 2008, Taphonomy and paleobiology of the Hyde Park mastodon: Palaeontographica Americana, v. 61, p. 197-289.

Fisher, D. C., and Fox, D. L., 2007, Season of Death of the Dent Mammoths, *in* Brunswig, R. H., and Pitblado, B. L., eds., From the Dent Prairie to the Peaks of the Rockies: Recent Paleoindian Research in Colorado: Boulder, University of Colorado Press, p. 123-153.

Fisher, D. C., Shoshani, J., and Tassy, P., 1996, Extinction of proboscideans in North America: The Proboscidea: Evolution and palaeoecology of elephants and their relatives., p. 296-315.

Fricke, H. C., and O'Neil, J. R., 1996, Inter-and intra-tooth variation in the oxygen isotope composition of mammalian tooth enamel phosphate: Implications for palaeoclimatological and palaeobiological research: Palaeogeography, Palaeoclimatology, Palaeoecology, v. 126, no. 1, p. 91-99.

Geyh, M. A., 2001, Bomb radiocarbon dating of animal tissues and hair: Radiocarbon, v. 43, p. 723-730.

Higgins, P., and MacFadden, B. J., 2009, Seasonal and geographic climate variabilities during the Last Glacial Maximum in North America: Applying isotopic analysis and macrophysical climate models: Palaeogeography, Palaeoclimatology, Palaeoecology, v. 283, no. 1, p. 15-27.

Hoppe, K. A., Stover, S. M., Pascoe, J. R., and Amundson, R., 2004, Tooth enamel biomineralization in extant horses: Implications for isotopic microsampling: Palaeogeography, Palaeoclimatology, Palaeoecology, v. 206, no. 3, p. 355-365.

Hua, Q., and Barbetti, M., 2004, Review of tropospheric bomb ^{14}C data for carbon cycle modeling and age calibration purposes: Radiocarbon, v. 46, no. 3, p. 1273-1298.

Hua, Q., Barbetti, M., Worbes, M., Head, J., and Levchenko, V. A., 1999, Review of radiocarbon data from atmospheric and tree-ring samples for the period 1945-1997 AD: IAWA journal, v. 20, p. 261-284.

Hynek, S. A., Passey, B. H., Prado, J. L., Brown, F. H., Cerling, T. E., and Quade, J., 2012, Small mammal carbon isotope ecology across the Miocene–Pliocene boundary, northwestern Argentina: Earth and Planetary Science Letters, v. 321, p. 177-188.

Koch, P., Fisher, D., and Dettman, D., 1989, Oxygen isotope variation in the tusks of extinct proboscideans: A measure of season of death and seasonality: Geology, v. 17, no. 6, p. 515.

Kohn, M. J., 2004, Comment: Tooth enamel mineralization in ungulates: Implications for recovering a primary isotopic time-series, by BH Passey and TE Cerling (2002): Geochimica et Cosmochimica Acta, v. 68, no. 2, p. 403-406.

Laws, R., 1966, Age criteria for the African elephant, Loxodonta a. africana: East African Wildlife Journal, v. 4, p. 1-37.

Lee, P. C., Sayialel, S., Lindsay, W. K., and Moss, C. J., 2012, African elephant age determination from teeth: Validation from known individuals: African Journal of Ecology, v. 50, p. 9-20.

Levin, I., Hammer, S., Kromer, B., and Meinhardt, F., 2008, Radiocarbon observations in atmospheric CO2: Determining fossil fuel CO2 over Europe using Jungfraujoch observations as background: Science of the Total Environment, v. 391, no. 2-3, p. 211-216.

Levin, I., and Hesshaimer, V., 2006, Radiocarbon; a unique tracer of global carbon cycle dynamics: Radiocarbon, v. 42, no. 1, p. 69-80.

Levin, I., and Kromer, B., 2004, The tropospheric $^{14}CO_2$ level in mid-latitudes of the Northern Hemisphere (1959-2003): Radiocarbon, v. 46, no. 3, p. 1261-1272.

Lynnerup, N., Kjeldsen, H., Heegaard, S., Jacobsen, C., and Heinemeier, J., 2008, Radiocarbon dating of the human eye lens crystallines reveal proteins without carbon turnover throughout life: PLoS One, v. 3, no. 1, p. e1529.

Metcalfe, J. Z., and Longstaffe, F. J., 2012, Mammoth tooth enamel growth rates inferred from stable isotope analysis and histology: Quaternary Research, v. 77, p. 424-432.

Metcalfe, J. Z., Longstaffe, F. J., Ballenger, J. A. M., and Haynes Jr, C. V., 2011, Isotopic paleoecology of Clovis mammoths from Arizona: Proceedings of the National Academy of Sciences, v. 108, no. 44, p. 17916-17920.

Nydal, R., 1968, Further investigation on the transfer of radiocarbon in nature: Journal of Geophysical Research, v. 73, no. 12, p. 3617-3635.

Nydal, R., and Lövseth, K., 1983, Tracing bomb 14C in the atmosphere 1962–1980: Journal of Geophysical Research, v. 88, no. C6, p. 3621-3642.

Passey, B. H., and Cerling, T. E., 2002, Tooth enamel mineralization in ungulates; implications for recovering a primary isotopic time-series: Geochimica et Cosmochimica Acta, v. 66, no. 18, p. 3225-3234.

Passey, B. H., Cerling, T. E., Schuster, G. T., Robinson, T. F., Roeder, B. L., and Krueger, S. K., 2005, Inverse methods for estimating primary input signals from time-averaged isotope profiles: Geochimica Et Cosmochimica Acta, v. 69, no. 16, p. 4101-4116.

Reid, D., and Dean, M., 2006, Variation in modern human enamel formation times: Journal of Human Evolution, v. 50, no. 3, p. 329-346.

Reimer, P. J., Brown, T. A., and Reimer, R. W., 2004, Discussion: Reporting and calibration of post-bomb ^{14}C data: Radiocarbon, v. 46, p. 1299-1304.

Reimer, R., and Reimer, P., 2010, CALIBomb - calibration of post-bomb C-14 data. http://calib.qub.ac.uk/.

Roe, D., Mulliken, T., Milledge, S., Mremi, J., Mosha, S., and Grieg-Gran, M., 2002, Making a killing or making a living: Wildlife trade, trade controls, and rural livelihoods, IIED and TRAFFIC: Biodiversity and Livelihoods, v. 6, 109 p.

Rountrey, A. N., Fisher, D. C., Vartanyan, S., and Fox, D. L., 2007, Carbon and nitrogen isotope analyses of a juvenile woolly mammoth tusk: Evidence of weaning: Quaternary International, v. 169, p. 166-173.

Sideras-Haddad, E., and Brown, T., 2002, Dating Studies of Elephant Tusks Using Accelerator Mass Spectrometry: Lawrence Livermore National Laboratory (LLNL), Livermore, CA.

Spalding, K. L., Buchholz, B. A., Bergman, L. E., Druid, H., and Frisén, J., 2005, Forensics: Age written in teeth by nuclear tests: Nature, v. 437, no. 7057, p. 333-334.

Tans, P., De Jong, A., and Mook, W., 1979, Natural atmospheric ^{14}C variation and the Suess effect: Nature, v. 280, p. 826-828.

Trapani, J., and Fisher, D. C., 2003, Discriminating proboscidean taxa using features of the Schreger pattern in tusk dentin: Journal of Archaeological Science, v. 30, no. 4, p. 429-438.

Ubelaker, D. H., Buchholz, B. A., and Stewart, J. E. B., 2006, Analysis of artificial radiocarbon in different skeletal and dental tissue types to evaluate date of death: Journal of Forensic Sciences, v. 51, no. 3, p. 484-488.

US Department of State, 2007, Countering Multi-billion Dollar Illegal Wildlife Trade Focus of Government-backed Global Coalition, Bureau of Oceans and International Environmental and Scientific Affairs, Nairobi, Kenya.

Van der Merwe, N., Lee-Thorp, J., Thackeray, J., Hall-Martin, A., Kruger, F., Coetzee, H., Bell, R., and Lindeque, M., 1990, Source-area determination of elephant ivory by isotopic analysis: Nature, v. 346, no. 6286, p. 744-746.

Vogel, J., Eglington, B., and Auret, J., 1990, Isotope fingerprints in elephant bone and ivory: Nature, v. 346, no. 6286, p. 747-749.

Vogel, J., Fuls, A., and Visser, E., 2002, Accurate dating with radiocarbon from the atom bomb tests: South African Journal of Science, v. 98, p. 437-438.

Wang, N., Shen, C., Ding, P., Yi, W., Sun, W., Liu, K., Ding, X., Fu, D., Yuan, J., and Yang, X., 2010, Improved application of bomb carbon in teeth for forensic investigation: Radiocarbon, v. 52, no. 2, p. 706-716.

Wasser, S., Poole, J., Lee, P., Lindsay, K., Dobson, A., Hart, J., Douglas-Hamilton, I., Wittemyer, G., Granli, P., and Morgan, B., 2010, Elephants, ivory, and trade: Science, v. 327, no. 5971, p. 1331-1332.

Wasser, S. K., Shedlock, A. M., Comstock, K., Ostrander, E. A., Mutayoba, B., and Stephens, M., 2004, Assigning African elephant DNA to geographic region of origin: Applications to the ivory trade: Proceedings of the National Academy of Sciences, v. 101, no. 41, p. 14847-14852.

Wittemyer, G., Cerling, T. E., and Douglas-Hamilton, I., 2009, Establishing chronologies from isotopic profiles in serially collected animal tissues: An example using tail hairs from African elephants: Chemical Geology, v. 267, no. 1-2, p. 3-11.

Table 3.1. Summary of tissue, type, and number of samples. All animal tissues are from primates, ungulates, or elephants. Detailed sample information is presented in Appendix B.

Tissue	Type	known age (n)	unknown age (n)
keratin	tail hair	4	1
	body hair	11	0
	horn	1	0
collagen	tusk dentin	2	7
	molar dentin	0	2
connective tissue	tusk pulp cavity	1	0
apatite	canine enamel	3	12
	tusk dentin	2	0
	treated tusk dentin	2	0
	molar enamel	0	19
bulk plant tissue	annual grass	3	0
	TOTAL:	29	41

Table 3.2. ^{14}C results for all samples, given as $F^{14}C$ with 2σ error. Certainty is based on age calibration from Calibomb software. Ages are given in Gregorian calendar years (yrs).

Sample ID	Tissue	F14C	2σ	14C Age (yr)	2σ (yr)	certainty	Known Age (yr)	uncert. (yr)	14C-Known age (yrs)	Data Set	δ13C
KL-1-E	bioapatite	1.5136	0.0012	1970.59	0.5	0.89	1971.50	0.5	-0.9	SH1	-0.9
TSV-291-(2-3)	bioapatite	1.1006	0.0012	1996.86	0.6	0.87	1996.50	2.0	0.4	NH3	-5.7
R37-PC-DEN	bioapatite	1.0577	0.0033	2005.67	0.9	0.76	2006.74	0.0	-1.1	Levin	-11.9
K08-201-(2-3)	bioapatite	1.0652	0.0012	2006.47	0.1	0.05	2007.22	2.0	-0.8	Levin	-4.8
Misha-PC-DEN	bioapatite	1.0383	0.0012	NA	0.0	NA	2008.69	--	--	Levin	-14.1
R37-PC-DEN(T)	bioapatite	1.0633	0.0033	2005.33	1.3	0.85	2006.74	0.0	-1.4	Levin	-11.9
Misha-PC-DEN(T)	bioapatite	1.0386	0.0012	NA	0.0	0.00	2008.69	--	--	Levin	-14.1
T. triandra_071962	bulk plant	1.2174	0.0022	1962.20	0.3	0.14	1962.54	0.2	-0.3	SH1	-10.2
H. nyassae_011964	bulk plant	1.6183	0.0028	1964.85	0.1	0.05	1964.06	0.2	0.8	SH1	-11.1
T. triandra_051964	bulk plant	1.5861	0.0027	1964.75	0.3	0.24	1964.37	0.2	0.4	SH1	-9.9
R37-PC-tissue	PC tissue	1.0513	0.0012	2006.04	0.0	0.01	2006.74	0.0	-0.7	Levin	-19.0
R37-PC-C	collagen	1.0592	0.0037	2005.52	1.1	0.80	2006.74	0.0	-1.2	Levin	-19.3
Misha-PC-C	collagen	1.0414	0.0012	NA	0.0	NA	2008.69	--	--	Levin	-22.7
FMNH-20754	keratin	0.9733	0.0022	1800.74	150.7	1.00	1905.91	2.0	-105.2	SH1	-20.7
MAM-3528	keratin	0.9894	0.0028	1865.35	54.1	0.89	1930.92	2.0	-65.6	NH3	-20.7
MAM-3559	keratin	0.9852	0.0038	1849.84	49.9	0.49	1932.42	2.0	-82.6	SH1	-22.5
LP878	keratin	0.9700	0.0022	1722.94	72.9	1.00	1953.63	2.0	-230.7	SH1	-21.7
LP2989	keratin	0.9990	0.0023	1954.66	2.0	0.98	1956.93	2.0	-2.3	SH1	-22.2
L10335	keratin	1.1553	0.0025	1959.60	0.2	0.10	1960.63	2.0	-1.0	SH1	-23.2
L10830	keratin	0.9749	0.0023	1944.49	7.5	0.18	1962.42	2.0	-17.9	SH1	-21.4
L13873	keratin	1.3603	0.0027	1963.59	0.1	0.09	1964.51	2.0	-0.9	SH1	-15.0
L15346	keratin	1.5713	0.0031	1966.50	2.1	1.00	1966.18	2.0	0.3	SH1	-23.5
L16286	keratin	1.5773	0.0030	1968.04	0.3	0.78	1967.16	2.0	0.9	SH1	-23.7

Sample ID	Tissue	F14C	2σ	14C Age (yr)
OHORN-1974	keratin	1.4032	0.0012	1975.02
L3791	keratin	1.2916	0.0026	1980.17
MAM-8759	keratin	1.1717	0.0025	1989.22
TSV-171-Prox-K	keratin	1.1107	0.0012	1996.71
R37-DIST-K	keratin	1.0803	0.0012	2002.46
R37-prox-K	keratin	1.0821	0.0012	2001.93
TSV-171-Dist-K	keratin	1.1188	0.0012	1995.99
Misha-MID1-C	collagen	1.0613	0.0033	2005.45
Misha-MID2-C	collagen	1.0789	0.0037	2002.54
Misha-Tip-c	collagen	1.1281	0.0012	1994.04
R37-MID1-C	collagen	1.0855	0.0038	2001.42
R37-MID2-C	collagen	1.1077	0.0038	1996.54
R37-MID3-C	collagen	1.2017	0.0041	1985.54
R37-Tip-C	collagen	1.3262	0.0043	1978.13
TE-95 Rm6-Root-C	collagen	1.5055	0.0025	1964.24
TE-95 Rm6.7-1.3-C	collagen	1.2024	0.0022	1961.49
2KL-145-E	bioapatite	1.5019	0.0034	1964.23
2KL-43-E	bioapatite	1.5387	0.0029	1969.47
2KL-95-E	bioapatite	1.6120	0.0031	1967.07
K11-KF-190/200	bioapatite	1.4418	0.0033	1973.55
K11-KF-40/50	bioapatite	1.3093	0.0031	1979.01
KL-15.5-E	bioapatite	1.6080	0.0036	1964.99
KL-17-E	bioapatite	1.5639	0.0035	1964.58

Table 3.2 Continued

2σ (yr)	certainty	Known Age (yr)	uncert. (yr)	14C-Known age (yrs)	Data Set	δ13C
0.7	0.89	1974.50	1.0	0.5	NH3	-10.3
0.8	0.87	1982.45	2.0	-2.3	SH1	-22.5
1.1	0.75	1988.50	2.0	0.7	SH1	-23.1
0.1	0.30	1998.54	2.0	-1.8	SH1	-22.8
0.6	0.79	2005.39	0.2	-2.9	Levin	-21.6
0.9	0.79	2006.74	0.0	-4.8	Levin	-21.0
0.8	0.93	--	--	--	SH1	-17.9
1.1	0.84	--	--	--	Levin	-21.2
1.5	0.82	--	--	--	Levin	-14.7
1.0	0.88	--	--	--	NH1	-19.8
1.5	0.81	--	--	--	Levin	-18.2
1.0	0.93	--	--	--	NH3	-17.9
1.3	0.71	--	--	--	NH3	-20.3
0.8	0.96	--	--	--	NH3	-18.1
0.1	0.06	--	--	--	SH1	-16.9
0.8	0.40	--	--	--	SH1	-17.0
0.1	0.05	--	--	--	SH1	-1.6
0.7	0.92	--	--	--	SH1	-2.9
0.5	0.71	--	--	--	SH1	-3.1
0.7	0.93	--	--	--	NH3	0.7
0.4	0.87	--	--	--	NH3	0.5
0.4	0.26	--	--	--	SH1	-0.8
0.2	0.19	--	--	--	SH1	-0.8

Table 3.2 Continued

Sample ID	Tissue	F14C	2σ	14C Age (yr)	2σ (yr)	certainty	Known Age (yr)	uncert. (yr)	14C-Known age (yrs)	Data Set	δ13C
KL-24-E	bioapatite	1.2354	0.0030	1962.49	0.2	0.12	--	--	--	SH1	0.1
KL-31.5-E	bioapatite	1.1782	0.0012	1959.95	0.2	0.08	--	--	--	SH1	-0.2
KL-8-E	bioapatite	1.5760	0.0035	1968.07	0.3	0.77	--	--	--	SH1	-0.5
R37-Lm6.10-1.6	bioapatite	1.1840	0.0021	1987.28	1.0	0.92	--	--	--	NH3	-10.5
R37-Lm6.10-5.0	bioapatite	1.1971	0.0022	1986.29	1.2	0.86	--	--	--	NH3	-10.8
R37-Lm6.3-0.7	bioapatite	1.2726	0.0022	1980.54	0.6	0.80	--	--	--	NH3	-10.7
R37-Lm6.7-1.0	bioapatite	1.2247	0.0022	1984.15	0.8	0.45	--	--	--	NH3	-10.6
R37-Lm6.7-7.3	bioapatite	1.2916	0.0022	1979.63	0.4	0.80	--	--	--	NH3	-10.9
TE-95 Rm5.7-1.7	bioapatite	0.9828	0.0025	1952.46	1.9	0.01	--	--	--	SH1	-8.0
TE-95 Rm6.11-2.3	bioapatite	1.3395	0.0022	1963.51	0.1	0.03	--	--	--	SH1	-6.8
TE-95 Rm6.2-1.1	bioapatite	1.1381	0.0027	1959.34	0.3	0.18	--	--	--	SH1	-8.1
TE-95 Rm6.2-7.5	bioapatite	1.0007	0.0025	1954.99	1.5	1.00	--	--	--	SH1	-7.9
TE-95 Rm6.4-1.5	bioapatite	1.1634	0.0021	1959.73	0.2	0.10	--	--	--	SH1	-7.6
TE-95 Rm6.4-6.2	bioapatite	1.0411	0.0020	1956.39	0.2	0.14	--	--	--	SH1	-7.4
TE-95 Rm6.4-9.5	bioapatite	0.9942	0.0019	1954.26	2.2	0.20	--	--	--	SH1	-7.6
TE-95 Rm6.7-1.3	bioapatite	1.2764	0.0029	1963.07	0.3	0.17	--	--	--	SH1	-7.7
TE-95 Rm6.7-10.1	bioapatite	1.0532	0.0025	1957.67	0.4	1.00	--	--	--	SH1	-7.9
TE-95 Rm6.9-10.4	bioapatite	1.1230	0.0020	1959.07	0.1	0.07	--	--	--	SH1	-7.7
TE-95 Rm6.9-2.0	bioapatite	1.4317	0.0025	1963.89	0.1	0.15	--	--	--	SH1	-6.6
TE-95 Rm6.9-4.2	bioapatite	1.2131	0.0021	1962.13	0.3	0.15	--	--	--	SH1	-7.5
TE-95 Rm6.9-5.8	bioapatite	1.1802	0.0020	1961.65	0.0	0.00	--	--	--	SH1	-7.6
TE-95 Rm6.9-8.3	bioapatite	1.1408	0.0020	1959.38	0.2	0.18	--	--	--	SH1	-7.6
TSV-291-(56-57)	bioapatite	1.1646	0.0012	1989.63	0.9	0.74	--	--	--	NH3	-2.9
K08-201-(49-50)	bioapatite	1.1032	0.0012	1996.83	2.0	0.86	--	--	--	NH3	-4.8

Table 3.3. Summary of growth rates determined from ^{14}C dating of hair, teeth, and tusks.

Sample ID	Growth rate ± 2σ	Length (cm)	Proximal ^{14}C age	Distal ^{14}C age	Total time in tissue (yrs.)
Tail hair keratin (mm/day)					
TSV-171	0.81 ± 0.77	31.4	1996.7	1996.0	0.7
R37	NA		2002.5	2001.9	—
Hippo canine apatite (cm/yr)					
2KL (upper)	1.94 ± 0.31	17.0	1969.5	1964.2	8.8
KL	3.35 ± 0.25	37.2	1960.0	1970.6	11.1
K11-KF	4.51 ± 0.41	35.0	1979.0	1972.4	7.8
K08-201	4.87 ± 0.34	56.0	2006.5	1996.8	11.5
TSV-291	7.47 ± 0.88	60.0	1996.9	1989.6	8.0
Elephant tusk collagen (cm/yr)					
Misha	5.11 ± 0.75	73.0	2008.7	1993.9	14.8
R37	4.13 ± 0.39	115.6	2005.5	1978.1	26.6
Elephant molar apatite (cm/yr)					
TE-95 Rm6.2	1.49 ± 0.54	10.1	1959.3	1955.0	6.8
TE-95 Rm6.4	1.46 ± 0.59	11.6	1959.7	1954.3	7.9
TE-95 Rm6.7	1.63 ± 0.14	12.3	1963.1	1957.1	7.5
TE-95 Rm6.9	1.62 ± 0.14	11.1	1963.9	1959.1	6.9
R37 Lm6.7	1.39 ± 0.27	7.8	1984.2	1979.6	5.6
R37 Lm6.10	1.61 ± 1.19	5.9	1988.4	1986.3	3.7

Table 3.4. Comparison of ^{14}C data from different tissue types collected at death from two elephants. Comparison of ^{14}C values from treated and untreated apatite and collagen from both individuals show no significant difference between tissues or treatments.

Sample ID	Part	Tissue	$F^{14}C$	2σ	$\Delta^{14}C$	2σ (‰)	^{14}C Age	2σ (yrs.)	Data set	Known Age	^{14}C-Known age (yrs.)
Misha-PC-C	tusk	collagen	1.0414	0.0012	33.8	1.2	—	—	—	2008.69	—
Misha-PC-DEN	tusk	apatite	1.0383	0.0012	30.8	1.2	—	—	—	2008.69	—
Misha-PC-DEN(T)	tusk	apatite	1.0386	0.0012	31.1	1.2	—	—	—	2008.69	—
R37-PC-C	tusk	collagen	1.0592	0.0037	51.5	3.7	2005.52	1.06	Levin	2006.74	-1.2
R37-PC-DEN	tusk	apatite	1.0577	0.0033	50.0	3.3	2005.67	0.91	Levin	2006.74	-1.1
R37-PC-DEN(T)	tusk	apatite	1.0633	0.0033	55.6	3.3	2005.33	1.26	Levin	2006.74	-1.4
R37-PC-tissue	soft tissue	PC tissue	1.0513	0.0012	43.7	1.2	2006.04	0.02	Levin	2006.74	-0.7
R37-prox-K	tail hair	keratin	1.0821	0.0012	74.3	1.2	2001.93	0.89	Levin	2006.74	-4.8

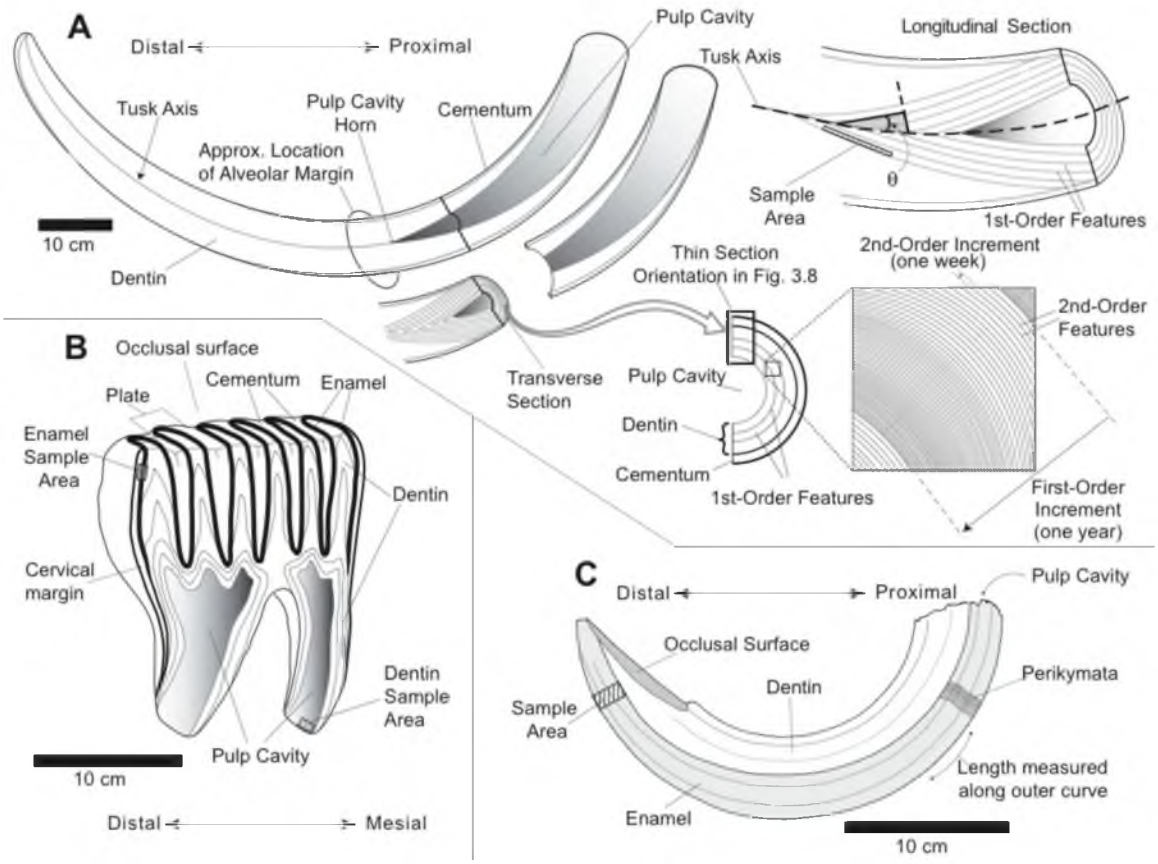

Figure 3.1. Schematic diagrams of sampled teeth illustrate structural features, periodic growth increments (in A and C), and sampling strategy. Hatched area in each figure (A-C) shows approximate size of sample area. A) Upper left: longitudinally-cut elephant tusk with incremental growth features shown at proximal end; Upper right: detail of proximal end showing the geometric relationship (angle θ) between the tusk axis and the trace of dentin increments in the plane of longitudinal section; Lower right: Transverse view illustrating first- and second-order growth increments. B) Longitudinally-cut elephant molar comprised of six enamel plates; and C) a lateral view of a lower hippo canine with perikymata shown over a representative interval (~2cm). A) and B) are modified from (Fisher and Fox, 2007).

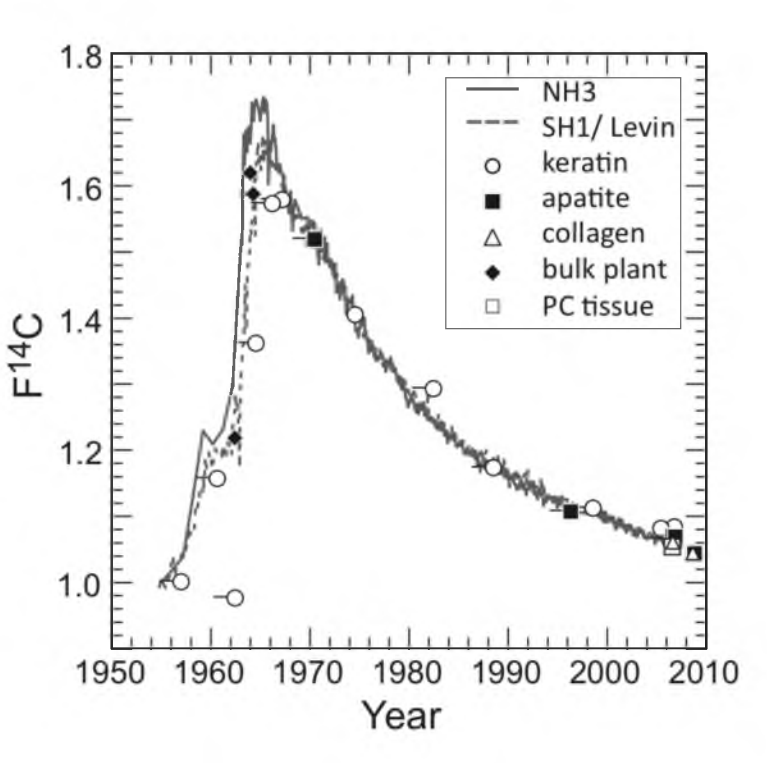

Figure 3.2. Fraction modern carbon ($F^{14}C$) vs. year for samples with a known date of death or collection. Y-axis error bars are smaller than the symbols; one-way x-axis error bars on some samples represent potential offset of up to two years between the actual date of death and date of collection or accession.

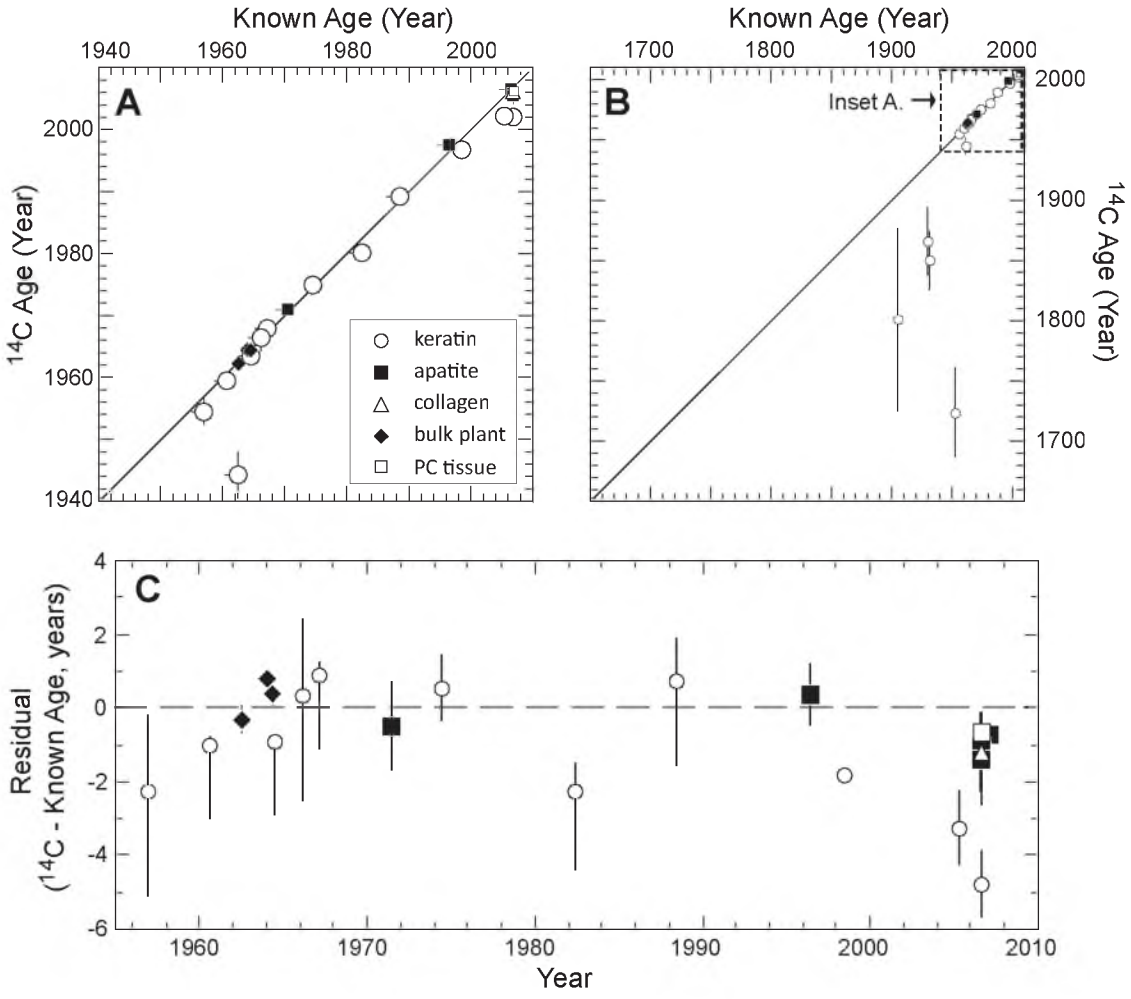

Figure 3.3. ^{14}C Age vs. Known Age for tissue or plant samples from specimens with a known date of death for A) samples younger than 1955 (n=23) and B) all samples (n=27). Y-axis error bars are 2σ; one-way x-axis error bars on some samples represent potential offset of up to two years between the actual date of death and date of collection or accession. C) Residuals of known age samples by tissue type. 2σ error bars are calculated based on combined ^{14}C age and known age (e.g., date of collection or death) uncertainties.

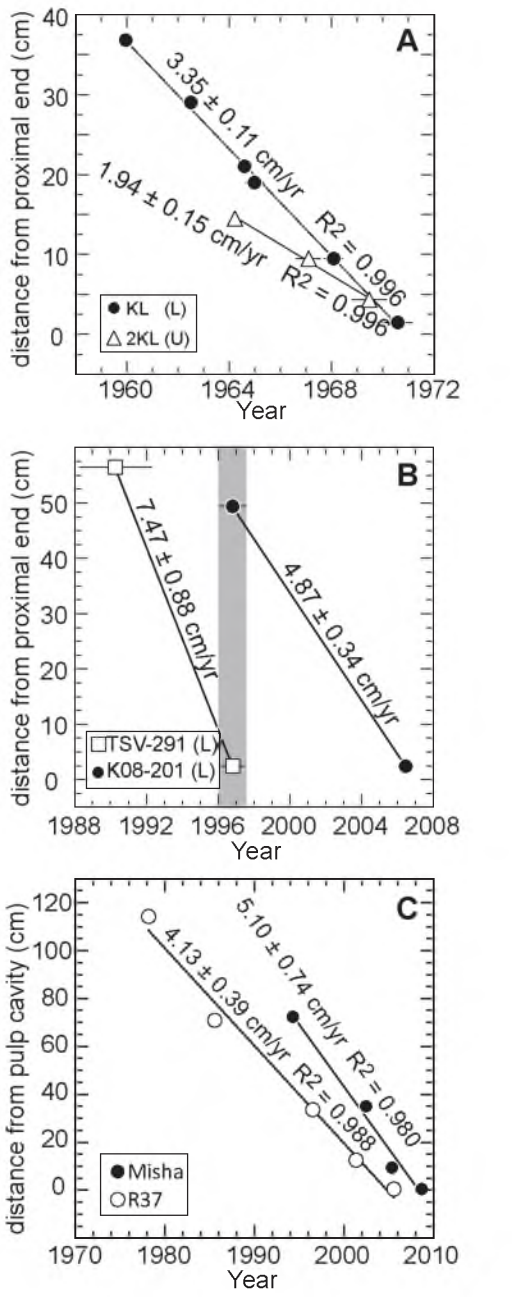

Figure 3.4. Calculated linear growth rates (cm/year) for A) upper (U) and lower (L) hippo canines from the same individual from Queen Elizabeth National Park, Uganda in 1971, B) lower canines from two hippos from Tsavo West National Park, Kenya, whose lives overlapped by ~1-2 years (shaded area), and C) two female African elephants. Growth rates are calculated from the slope of the regression lines. Error for ages is 2σ and if not shown is smaller than the symbol. Growth rates differ by ~20% between the two elephant tusks, which may reflect individual or ontogenetic variation. Misha's tusk represents growth during early adulthood (age 13 to 28), whereas R37's tusk represents growth from age 25 to 53 years old.

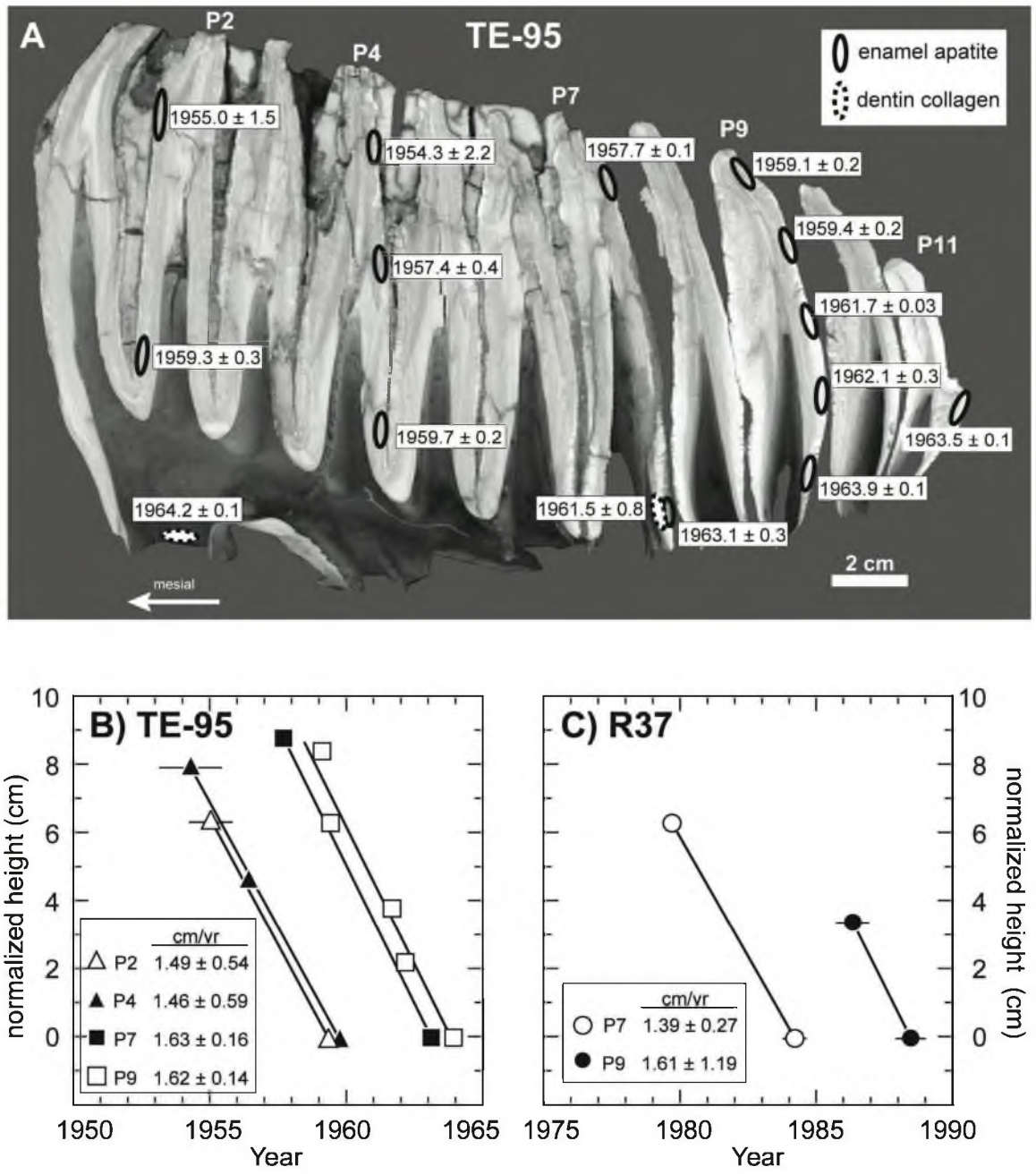

Figure 3.5. A) Longitudinally cut elephant molar (m3) from individual TE-95 showing ^{14}C ages (± 2σ) for thirteen enamel apatite and two dentin collagen samples. Sample locations are outlined as black ellipses. The molar consists of a series of eleven enamel-covered plates (P1 to P11). B) Vertical growth rates (cm/year) from four TE-95 molar plates shown in A) are calculated from ^{14}C ages. C) Vertical growth rates (cm/year) in two molar plates from a lower third molar belonging to R37 (see text). For B) and C) growth rates are calculated from slopes, height along a plate is normalized to the lowest sample location, and error is 2σ and if not shown, is smaller than the symbol.

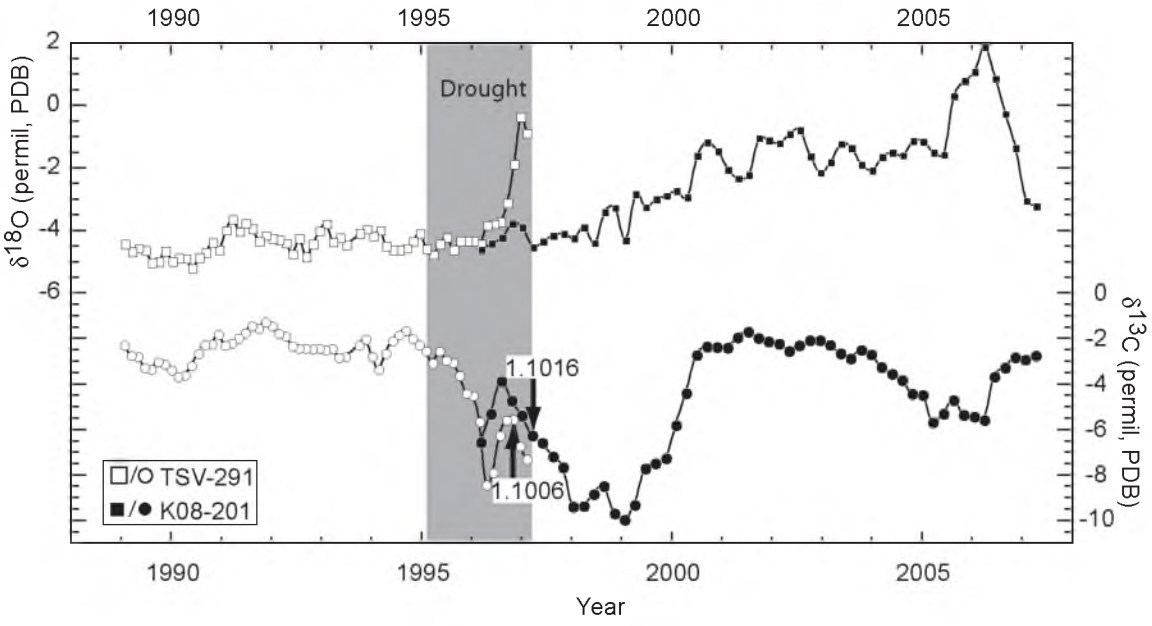

Figure 3.6. Intratooth stable isotope profiles from two hippo canines overlap to provide a continuous isotope record of 18.2 years. $F^{14}C$ values used as a tie-point between the two canines are labeled with arrows indicating sample location. Based on the shape of the $\delta^{13}C$ curves, the K08-201 profile has been shifted ~ +0.3 years, which is within the 2σ range of uncertainty. TSV-291 died in 1996, and the canine was collected near the town of Mtito Andei, Kenya. A steep rise in the $\delta^{18}O$ begins ~200 days before death and suggests physiological stress preceding death, a pattern observed in other serially sampled hippo canines. K08-201 was shot dead on 10 October 2007 as a (crop-raiding) nuisance animal near Mtito Andei.

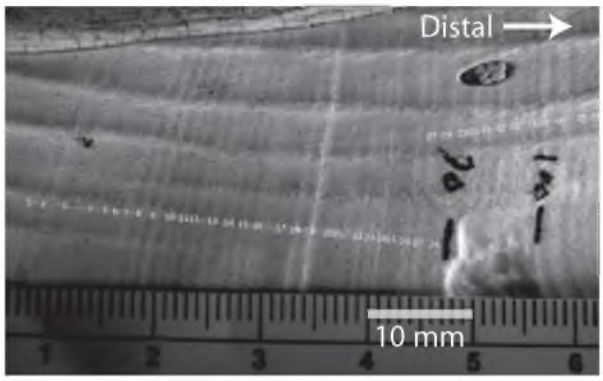

Figure 3.7. Photograph showing hippo canine (K11-KF) perikymata, which are periodic growth increments on the enamel surface of teeth. Each increment represents 10.3 ± 1.8 days. The original digital color photograph has been converted to an enhanced grayscale image to facilitate measurement of increments. Tick marks in scale at bottom of image are in millimeters.

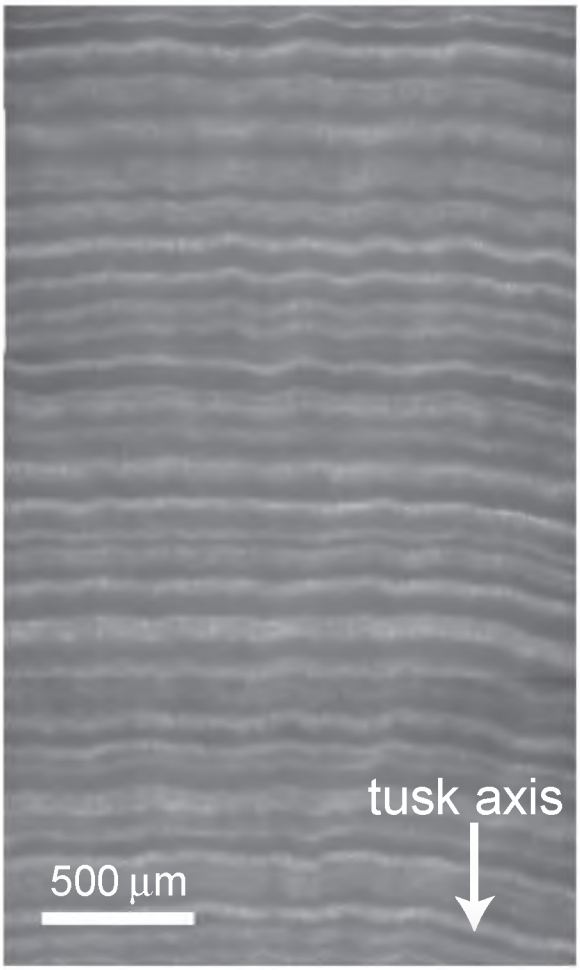

Figure 3.8 Photomicrograph of a transversely-cut ivory thin section (35x) from R37 showing second-order growth increments. Each increment is comprised of a dark-light couplet. The mean increment thickness measured along the ~34 mm thin section is 103 ± 28 μm (n=334). The growth rate calculated from ^{14}C data is 105 ± 11 μm/week, providing independent evidence for weekly periodicity of second-order increments in elephant tusks.

CHAPTER 4

HIGH-RESOLUTION STABLE ISOTOPE PROFILES FROM ELEPHANT (*LOXODONTA AFRICANA*) IVORY AND TAIL HAIR: MULTIYEAR RECORDS OF SEASONAL DIET AND CLIMATE VARIABILITY FROM 1982 TO 2006

4.1 Abstract

Stable isotope ratios in tissues of large mammalian herbivores record diet and climate information integrated over large spatial areas and can be used to study modern and fossil ecosystems. Sound interpretation of data requires that ecological and behavioral variables that determine the stable isotope ratios of tissues be measured and quantified through field observations, remote sensing data, and meteorological records—a nontrivial task when the cost of ecological monitoring of large herbivores is considered. We present multiyear, high-resolution (i.e., approximately weekly) stable isotope records from bioapatite in tusk ivory ($\delta^{13}C_{ivory}$ and $\delta^{18}O_{ivory}$) and tail hair ($\delta^{13}C_{hair}$ and $\delta^{15}N_{hair}$) of an African elephant (*Loxondonta africana*) from Kenya that was fitted with a GPS collar since 2001 and observed for nearly a decade. GPS and observational data provide behavioral, life history, and location information. NVDI, precipitation, and isotopic data from plants and water provide further constraints for interpreting isotope profiles.

Two profiles from micromilled tusk dentin span the periods 1982 to 1987 and 2000 to 2006 and record approximately weekly variability in $\delta^{13}C$ and $\delta^{18}O$. The $\delta^{13}C_{ivory}$ increases from baseline values by up to 4.5 ‰ due to diet switches from predominantly C_3 browsing to mixed C_3 browsing and C_4 grazing diet during the twice-yearly (biannual) wet seasons. The $\delta^{13}C_{hair}$ from 2000 to 2006 shows a similar trend with a slightly higher range (5 ‰). Thus, $\delta^{13}C$ serves as a proxy for diet and wet seasons. The $\delta^{18}O$ of tusk bioapatite is less tightly coupled to NDVI than $\delta^{13}C$, and varies approximately biannually up to 5 ‰. Using a matching filter, we show that NDVI can be used to predict $\delta^{13}C$ of ivory and vice versa. Methods for determining tusk growth rate include visual matching, measuring approximately weekly periodic growth increment thicknesses, and bomb-curve ^{14}C dating; the three methods yield virtually identical rates. Our results demonstrate that tusk isotope profiles at approximately weekly resolution serve as a proxy for seasonality of diet and precipitation, and thus can be used to reconstruct life history and climate information at unprecedented resolution in modern and fossil proboscidean tusks.

4.2 Introduction

The utility of stable isotopes in modern and paleoecological studies has been an area of active research since the pioneering work on stable isotopes as tracers in plant and herbivore ecosystems (e.g., DeNiro and Epstein, 1978, 1981; Park and Epstein, 1960; Tieszen et al., 1979). Later studies on carbon, nitrogen, and oxygen isotopes in different animal tissues such as collagen, bioapatite, and keratin provided greater insight into how animal tissues record dietary and climate information (Ambrose and Norr, 1993; Cerling

and Harris, 1999; Kohn, 1996; Lee-Thorp et al., 1989; Levin et al., 2006; Podlesak et al., 2008; Tieszen et al., 1983). These advances have led to (and in some cases been born from) the widespread use of isotopes to study animal diets and migration patterns as well as climate in modern and ancient ecosystems (e.g., Cerling et al., 2010; Gannes et al., 1998; Hobson, 1999; Secord et al., 2012; Zazzo et al., 2000).

Within the last 25 years or so, it was recognized that metabolically inert tissues could be serially sampled to provide a time series of stable isotope data. One of the first applications of this method in terrestrial ecosystems was oxygen isotope analysis of dentin bioapatite on late Pleistocene proboscidean tusks and bear canines (Koch et al., 1989). The study demonstrated that stable isotope profiles can be used to evaluate seasonality, and in that particular study, the results were used to determine season of death and to provide additional confirmation for circaseptan periodicities of growth increments in proboscidean tusk and molar dentin. Subsequent studies utilizing isotope profiles from proboscidean tusks and teeth have expanded to include carbon to evaluate diet (Codron et al., 2012; Fox and Fisher, 2004) and nitrogen to explore weaning and diet (Metcalfe et al., 2010; Rountrey et al., 2007), and thus give additional information on life history and the seasonality of diet and climate. Previously published isotope profiles from proboscidean tusks records have a resolution of approximately 2-5 samples per year, which is usually sufficient for detecting annual periodicities in diet and climate signals. However, for higher frequency changes in diet or climate, such as the twice-yearly (biannual) wet seasons that occur in parts of East Africa today, that scale of resolution will not sufficiently capture the range and nature of variability according to Nyquist sampling theory (Nyquist, 1928).

Recently, African elephant (*Loxodonta africana*) tail hair isotope profiles sampled at approximately weekly resolution captured dietary switches that are a result of biannual wet seasons in Kenya, and the results have implications for understanding elephant ecology and conservation (Cerling et al., 2004; Cerling et al., 2009; Cerling et al., 2006). Tail hair is limiting in that a single hair usually only represents a year's time, and certainly less than 3 years at best. Furthermore, most hair and other keratinous tissues studied to date are collected from an immobilized or recently deceased animal and are rarely preserved after death, which precludes obtaining high-resolution isotope profiles from the recent and geologic past.

High-resolution serial sampling of tusks offers a solution to the relatively short time represented in hair and its paucity in the recent and geologic past. Proboscidean tusks record decades of climate, diet, and life history information (Chapter 3). Stable isotope profiles from recent and unaltered fossil tusks can be serially sampled at high resolution to provide records of life history and seasonal changes in diet and climate in unprecedented detail and length of time. These profiles have the potential to elucidate the frequency and relative intensity of seasonal environmental variability (e.g., in vegetation or precipitation) in ancient ecosystems at a resolution that cannot be obtained from other isotopic proxies such as soil carbonates or plant biomarkers, or other environmental proxies such as pollen, phytoliths, paleosols, or charcoal.

Here we present two carbon and oxygen isotope profiles sampled at approximately weekly resolution from an African elephant (*Loxodonta africana*) tusk. The profiles span the periods 1982 to 1987 and 2000 to 2006. We also present carbon and nitrogen isotope profiles from tail hair from the same individual spanning most of the period from

2000-2006. Using the synchronous hair and tusk profiles, we show for the first time that carbon isotope ratios in hair and tusk provide nearly identical records of diet variability related to seasonal rains. The relationship between biannual wet seasons and diet change, whereby consumption of C_4 vegetation increases from a baseline of 10 to 20 % of total diet during the dry season to *ca.* 70% during the wet season, is supported by extensive NDVI, GPS, and precipitation data sets. We apply a matching filter to show that diet (as $\delta^{13}C$) can be predicted from NDVI and vice versa using tusk profile data from 1982 to 1987. Our results illustrate the potential use of high-resolution stable isotope profiles for studying the life history of proboscideans and the seasonality of climate variables in modern and ancient terrestrial ecosystems.

4.3 Background and Materials

4.3.1 Study area and sample collection

Tusk ivory and tail hair sampled for stable isotope analysis come from a single individual, Amina (R37), who was the matriarch of an elephant family unit called the Swahilis. The Swahilis inhabit the Samburu, Buffalo Springs, and Shaba National Reserves (the Reserves) and surrounding area in northern Kenya (Figure 4.1; Wittemyer, 2001). The Reserves, located at 0.5° N; 37.5° E, range in elevation from 800-1200 m, cover ~330 km^2 in the Samburu-Laikipia region, and provide a safe haven for the largest population of elephants living outside of protected areas in Kenya (Poole et al., 1992; Wittemyer, 2001). The primary source of water in the Reserves is the semipermanent Ewaso N'giro River and its tributaries; the vegetation communities vary from *Acacia*- and doum palm-dominated forests along the riparian corridors to *Acacia-Commiphora*

semiarid bushlands and *Acacia* wooded grasslands in the drier regions (Cerling et al., 2009; Wittemyer, 2001).

Using the tooth wear age criteria established by Laws (1966) and refined by Lee et al. (2012), the estimated age of R37 at death was 53 ± 5 years old. Five tail hairs were collected from R37 between January 2001 and September 26, 2006, when the elephant died. Tail hair was usually collected opportunistically: during immobilization events for fitting of a GPS collar or later, when changing the battery on the collar. Individual hairs were pulled from the tail with the root end intact so that the proximal end could be easily identified. Hairs ranged in length from 235 to 330 mm.

Within several days of death of the elephant on September 26, 2006, the tusks were removed by Kenya Wildlife Services (KWS) staff and transferred to a KWS ivory strong room in Isiolo, Kenya. The right tusk, the longer of the two and measuring 130 cm from the tip to the pulp cavity margin, was selected for study. In the summer of 2007, the tusk was prepared at a KWS facility in Nairobi for import to the United States (US). According to the terms in the import permit granted by the Convention on International Trade of Endangered Species (CITES) and the US Fish and Wildlife Service, the tusk was to be imported into the US in no more than 20 slabs measuring approximately 4x6x1 cm. The tusk was cross-cut (i.e., transversely) with a bow saw into several segments. Tusk segments were then cut longitudinally, approximately parallel to the structural axis of the tusk (Figure 4.2). A second longitudinal cut was made parallel to the first one on each cross-cut segment in order to isolate approximately 1-cm-thick pieces. Each piece was then cut into smaller slabs that were approximately 4 cm in

height, measured radially from the tusk axis to the outer margin, and 4 to 7 cm in length, measured along the tusk axis (Figure 4.3A).

4.3.2 Structure and composition of ivory

Elephant tusks are highly modified, continuously growing upper incisors comprised primarily of dentin with an outer layer of cementum (Figure 4.2). Initially at eruption, the cementum layer is several millimeters thick, but is usually missing at the distal end of the tusk due to normal wear. Enamel is present only on the bicuspid tip of a tusk when it initially erupts, and is rarely if ever present in tusks of adults. The boundary between the cementum and dentin in a tusk is called the cementum-dentin junction (CDJ) (Figure 4.3A). The composition of elephant tusk dentin is the same as tooth dentin in other mammals, and is made up of inorganic and organic components. These include the calcium phosphate mineral hydroxylapatite (~74%), type I collagen (~18%) and other proteins (~3%), and water (~5%) (Williams and Elliott, 1979). In biological hydroxylapatite ($Ca_{10}(PO_4)_6OH$, the carbonate anion (CO_3^{2-}) can substitute in the phosphate (PO_4) or the hydroxyl (OH) positions (Elliott, 2002; LeGeros et al., 1969). Tusk dentin is deposited throughout life along the conical pulp cavity surface, and incremental growth features representing annual, approximately weekly (or fortnightly), and daily intervals are present in proboscidean tusks. These increments are referred to as first-, second-, and third-order increments (Figure 4.2; Fisher, 1996). A geometric analogy for tusk growth is a stack of cones, where a new "cone" (or dentin layer), is added at the base of the stack. Detailed discussions of tusk growth processes, incremental growth features, and life history events recorded in tusks can be found in many of Fisher's works (e.g., Fisher, 1996, 2001; Fisher and Fox, 2003, 2007).

4.3.3 Observational, Meteorological, and Remote Sensing Data

Here we describe the observational, meteorological, and remote sensing data that provide the framework of behavioral, life history, climatic, and location information necessary to interpret the stable isotope profiles from tusks and tail hair.

The use of GPS collars to track the location and movement of elephants provides much greater information than traditional radio collar methods (Douglas-Hamilton, 1998; Douglas-Hamilton et al., 2005). R37 was fitted with a GPS collar that recorded her location at 1 to 3 hour intervals for a nearly continuous period from 2001 through September 2006.

Observational data come from work initiated by Iain Doulas-Hamilton through the organization Save-The-Elephants (STE), which has a field station in Samburu National Reserve. From November of 1997 to July 1999, George Wittemyer conducted daily observational transects, primarily along water courses in and near the Reserves, identifying 767 individual elephants in the area (Wittemyer, 2001), and observational transects continue to date with the support of STE staff.

Field observational data for R37 include known calving events on July 8, 1999 and April 27, 2004, inferred calving events (based on the age of existing calves) in the fall of 1996 and in 1992, and approximately 100 feeding observations of the Swahilis family between July 2001 and October 2002. Using data from GPS collars and field observations, Wittemyer and Getz (2007) determined the rank of 20 family unit matriarchs in and around the Reserves; R37's rank of 13th classified her as mid-low in the social hierarchy and as a result, she had a larger home range than higher ranking matriarchs (549 km^2, LoCoH method); spent less time in protected areas (i.e., the

Reserves) than individuals with higher social rank; and had no core area in the Reserves as defined by the area in which 50 % of GPS points lie (Wittemyer et al., 2007).

Daily precipitation records spanning 1957 through 2006 come from measurements made at Archer's Post, located near the east end of the Reserves (Figure 4.1). The biannual wet seasons are associated with the southward migration of the Intertropical Convergence Zone (ITCZ). The majority of annual precipitation occurs during these seasons, referred to as the "long rains" (March-May) and the "short rains" (October-December). From 2000 to 2005, the average rainfall in the Reserves during the "long rains" and the "short rains" was 143 mm (max.: 259 mm; min.: 63 mm) and 193 mm (max.: 356, min.: 55 mm), respectively (Cerling et al., 2009).

Normalized Difference Vegetation Index (NDVI) is a satellite measurement that can be used as a proxy for net primary productivity (NPP), where

$$NDVI = (NIR-RED)/(NIR+RED), \tag{4.1}$$

and NIR and RED are the amounts of near-infrared and red light, respectively, reflected by the vegetation as measured by the satellite sensors (Pettorelli et al., 2005). NDVI works as a proxy for NPP, measured on a scale from -1 to +1, because chlorophyll absorbs RED and mesophyll scatters NIR. An NDVI value <0 indicates an absence of vegetation. We use NDVI data from two different satellites in this study. NDVI data from 1982 through 1987 come from the National Oceanic and Atmospheric Administration Advanced Very High Resolution Radiometer (AVHRR) satellite and has a spatial resolution of 8-16 km, with data collection taking place on the 1st, 11th, and 21st day of each month. NDVI data spanning 2000 to 2006 come from the Satellite Pour

l'Observation de la Terre (SPOT). SPOT has spatial resolution of several meters and a semimonthly temporal resolution (Pettorelli et al., 2005). NDVI is summed over an area defined by a polygon that circumscribes nearly all GPS and observational location data for elephants using the Reserves (Figure 4.1).

4.4 Methods

4.4.1 Sample preparation for histological analysis

In order to develop spatially accurate serial sampling plans of tusk dentin and to conduct histological analysis for determining tusk growth rate, one longitudinal surface of each ivory slab was polished and thin sections were made from the transverse surface of the proximal end of every other slab from the pulp cavity margin to the tip of the tusk. For each thin section, the proximal ~5 mm was transversely cut, polished to ~1000 grit on one side, epoxied to a standard petrographic slide (27 x 46 mm), and cut to a thickness of *ca.* 250 microns with a Buehler® Isomet low speed saw. Ivory thin sections were polished to a thickness of 120 ± 30 microns using successively finer grits of emery paper ranging from 600 to 1200 grit, followed by 1.0 to 0.3 micron Buehler® aluminum oxide grit on a lap. Longitudinal surfaces of ivory slabs were polished by hand using successively finer grits of emery paper ranging from 320 to 1200 grit followed by high speed polish with 1.0 to 0.3 micron Buehler® aluminum oxide grit on a lap.

Photomicrographs of the ivory thin sections were taken using a Canon® Powershot A640 digital camera coupled to a petrographic microscope with an Alexis Scientific Clearshot Series 600 digital camera adapter. The camera shutter was controlled via computer using Canon® software. Images were taken at approximately 35x magnification under transmitted plain polarized light. A photomicrograph of a stage

micrometer with 10 μm graduations was included with each sequence of thin section photomicrographs for scale. Approximately 20 to 30 photomicrographs were taken to cover a vertical transect of an ivory thin section. Individual photomicrographs were stitched together in Adobe® Photoshop to produce a composite image from the pulp cavity margin or approximate structural axis of the tusk to the outer edge (Figure 4.3B).

Polished ivory slabs were scanned in color at 9600 dpi using an Epson® 4490 Photo flatbed scanner (Figure 4.3A). Images were converted to gray scale and levels were adjusted in Photoshop to enhance growth increments for measurement of thicknesses.

4.4.2 Sample preparation for stable isotope analysis

Tail hair was wiped with acetone to remove adhering contaminants (e.g., dust, oils, and dung). Elephant tail hair is quite thick, often on the order of 1-3 mm in diameter, and thus can be serially sampled for isotope analysis without cutting the hair into segments. Each hair was marked at 5 mm increments from the proximal (root) to the distal end and subsequently sampled at the midpoint between marked intervals (e.g., at 2.5, 7.5, and 12.5 mm). Approximately 500 μg was removed with a razor blade and transferred into a tin capsule for analyses. Wittemyer et al. (2009) determined an average tail hair growth rate of 0.81 ± 0.11 mm/day for female elephants (n=38), and thus a 5 mm sampling interval represents approximately six days.

Tusk dentin was sampled for stable isotope analyses by serial sampling parallel to second-order growth increments in an ivory slab (Figure 4.3B). This approach minimizes time averaging that results from sampling across growth increments, which represent

approximately weekly isochrons in the tusk. Sequential sampling was carried out using an end-milling technique on a high-precision milling device (Merchantek Micromill, now Electro Scientific Industries of Portland, Oregon, USA). The Micromill is equipped with a computer-controlled x-y-z stage, a vertically mounted variable-speed (1200-35000 RPM) drill, and a 40x binocular microscope with a camera that is connected to the computer. A 1-mm carbide endmill bit was used for all milling (Brasseler # H21.11.010). A total of 639 samples were milled from three ivory slabs (R37-DEN-1169, -1053, and -412). Ivory slabs were individually mounted to the Micromill stage using hot-melt glue with the polished longitudinal surface facing up and approximately parallel to the stage. Second-order growth increments are visible under 40x magnification of the binocular microscope (Figure 4.3B), and these were used as guides to map out drilling paths (scans) on the ivory surface. Using the Scan Tool in the Micromill software, a series of "master" scan lines were drawn along a growth increment every ~1500 μm from the initial starting point towards the CDJ. Next, a series of scans were interpolated at ~100 μm intervals between master scans using the Interpolate Tool. Scan lengths were approximately 4.5 cm (min: 4.2 cm; max.: 4.6 cm). The average milling depth was 1000 μm (min.: 500 μm; max.: 1120 μm. Optimum milling depth is limited by the curvature of the growth increments. For example, near the pulp cavity horn where curvature is high, a relatively shallow (~500 μm) milling depth is required to prevent significant time averaging resulting from milling through multiple growth increments. Average sample yields (for a 100 μm width, 1000 μm depth, and a 4.5 cm length scan) were 5.3 mg (min <1; max ~10 mg) of dentin powder. Sample powders were collected onto weighing paper and placed into 0.65 ml centrifuge tubes.

4.4.3 Stable isotope analysis

Tail hair segments were analyzed for stable carbon and nitrogen isotope ratios, reported as δ-values relative to the Pee Dee Belemnite (PDB) standard for carbon and atmospheric nitrogen (AIR) standard for nitrogen using permil (‰) notation where

$$\delta^{13}C\ (\delta^{15}N) = (R_{sample}/\ R_{standard} - 1) \times 1000 \qquad (4.2)$$

and R_{sample} and $R_{standard}$ are the $^{13}C/^{12}C$ ($^{15}N/^{14}N$) ratios in the sample and in the standard, respectively, and the $\delta^{13}C$ ($\delta^{15}N$) value of PDB (AIR) is defined as 0‰. Hair samples were combusted in a Costech 4010 Elemental Analyzer at 1650° C and inlet to a Finnigan MAT 252 Isotope Ratio Mass Spectrometer (IRMS) via continuous flow at the University of Utah's Stable Isotope Ratio Facility for Environmental Research (SIRFER). The carbon and nitrogen content of each sample was determined based on comparison of the sample mass and peak area to those of spinach and yeast standards. The average standard deviation of the primary standard, yeast, pooled from all runs for the five tail hairs is 0.15 ‰ for $\delta^{13}C$ and 0.13 ‰ for $\delta^{15}N$.

The carbonate component of hydroxylapatite in tusk dentin was analyzed for $\delta^{13}C$ and $\delta^{18}O$ values by IRMS. Stable isotope ratios are reported as δ-values relative to the Pee Dee Belemnite (PDB) standard using permil (‰) notation defined in equation 4.2. For oxygen, R_{sample} and $R_{standard}$ are the $^{18}O/^{16}O$ ratios in the sample and in the standard respectively, and the $\delta^{18}O$ value of PDB is defined as 0 ‰.

Prior to analysis, a majority of powdered dentin samples were pretreated with an oxidizer (hydrogen peroxide, H_2O_2) to remove the organic component of the dentin.

Pretreatment methods to remove organics (and exogenous carbonate, if present) from dentin vary by laboratory and there is no standard protocol. However, the most common is a two-step pretreatment with an oxidizer to remove organics followed by a weak acid to remove exogenous carbonate (e.g., Koch et al., 1997). Treatment of modern ivory with a weak acid may seem unnecessary, but using X-ray diffraction (XRD), Sakae et al. (1988) discovered calcite precipitation following pretreatment of bovine tooth dentin with 10 % NaOCl (bleach), an oxidizer.

To address the issue of potential calcite precipitation from pretreatment with an oxidizer, tusk dentin powders were subject to four different pretreatment methods and analyzed for the presence of calcite by XRD. About one gram of tusk dentin was ground with an agate mortar and pestle, split into five aliquots of ~150 mg each, and placed into 10 ml centrifuge tubes. Two aliquots were pretreated with 3% H_2O_2 (hydrogen peroxide) for 30 minutes. The other two were pretreated with 3% bleach for 30 minutes. Samples were occasionally agitated to keep the dentin suspended in the solution. Following the 30-minute pretreatment period, samples were centrifuged for 5 minutes at 5000 RPM. The supernatant was removed and the samples were rinsed with Milli-Q doubly distilled water. The rinse and centrifuge steps were repeated twice more. A pretreated peroxide and bleach sample were then subsequently pretreated with 0.1 M (Na-acetate) buffered acetic acid for 30 minutes. Samples were centrifuged and rinsed as above. The four pretreated samples were placed in a drying oven at 60°C overnight. Following discussion with Dr. William Parry, it was decided that the pretreated powders should be ground further with agate mortar and pestle again to ensure the samples were sufficiently powdered for XRD analysis.

Five powdered samples (four pretreated and one untreated) were mounted on glass slides with ethanol and allowed to air dry. Samples were analyzed on a Rigaku X-Ray powder diffractometer at 40Kv and 30mA using CuKα radiation and a Ni filter. The 2θ angle ranged from 20-55° at 2°/minute, which is common for X-ray work on apatite (Ayliffe et al., 1994; Koch et al., 1997; Sakae et al., 1988). After the XRD experiments were completed, it was determined that a higher concentration of hydrogen peroxide (10 to 30 %) was required to remove all organic matter from tusk dentin due to the relatively high organic content (~20 %) of dentin. XRD analysis was not conducted on dentin pretreated with 30 % hydrogen peroxide, but the results are still presented here for completeness.

Serially sampled tusk dentin powders were reacted with a 30 % hydrogen peroxide solution in 0.65 ml centrifuge tubes for 30 minutes, rinsed with DI water and centrifuged three times, and dried overnight at 60° C. Pretreatment results in a loss of *ca.* 40 % of initial sample mass. A subset of samples initially milled at 500 μm depths did not produce enough powdered dentin to be pretreated. That is, given the loss of powder during pretreatment, there would not have been enough powder for isotopic analyses, and therefore, the samples were analyzed untreated. Relatively low CO_2 yields were observed in the untreated (micromilled) powders during isotopic analysis that were attributed to low wettability during acid digestion. Dentin powder obtained from the same tusk slabs with a hand held drill (Dremel) produced CO_2 yields more consistent with, but slightly lower than, enamel. Thus, when sample mass was sufficient, pretreatment with H_2O_2 was used to remove the organics. This resulted in improved wettability of dentin powder during acid digestion that led to increased CO_2 yields.

Dentin powder was digested in 100 % H_3PO_4 (phosphoric acid) using a Finnigan CarboFlo coupled to the dual inlet on a Finnigan MAT 252 IRMS at SIRFER. The CarboFlo system is a hybrid positive pressure/vacuum system with a common acid bath (CAB). Approximately 800 to 1000 μg of tusk dentin was weighed out into a silver capsule, which was used as a precautionary measure to oxidize any SO_2 produced during digestion in phosphoric acid. Silver capsules containing powdered dentin were dropped from an autosampler carousel into the vigorously stirred CAB and reacted for 20 minutes at 90° C. A microcapillary tube submerged in the acid bath flushed it with 20 ml/minute of He and a 40 ml/minute He stream flushed the autosampler. The combined He streams swept the liberated H_2O and CO_2 through a dry ice/ethanol trap to remove water and then through a liquid nitrogen (LN) trap to collect the CO_2. Following the reaction period, the LN trap was isolated from positive pressure and evacuated with a rotary vacuum pump to ~10^{-3} Torr. The LN trap was removed and the CO_2 was cryogenically transferred to a microvolume held at -170°C. Once transferred to the microvolume, the CO_2 was analyzed through the dual inlet system on the IRMS. Internal laboratory standards of tusk dentin (R37-DEN), modern enamel (MCM), and calcite (UU Carrara) were used for data correction and had average standard deviations of ~0.1 ‰ for $\delta^{13}C$ and ~0.2 ‰ for $\delta^{18}O$ across all analytical runs.

4.4.4 Tusk and tail hair growth rates

The growth rate of serially sampled tissues must be known or determined in order to compare the stable isotope data to environmental or meteorological time series data such as NDVI or rainfall. Here we outline three methods used to determine growth rates of tail hair and tusks.

A commonly used method for determining the growth rate of hair is visual matching (VM), whereby isotope profiles from serially sampled hairs ($n \geq 2$) collected from the same individual are compared (Wittemyer et al., 2009). The growth rate of hair appears to be constant (West et al., 2004), but different hairs from the same individual may have different growth rates. The growth rate of tusks can be determined using ^{14}C bomb-curve dating (Chapter 3) or by histological methods whereby growth increments with a known periodicity are counted (e.g., Fisher, 1996, 2008; Fisher and Fox, 2003). Tusk growth rates are not likely constant throughout the life of an elephant (Fisher, 2001). Fisher and Fox (2003) have shown mammoths and mastodons exhibit intra-annual and long-term variation in tusk growth rates, and it follows that their extant relatives probably do, too.

We use the VM technique described by Wittemyer et al. (2009) to determine growth rates of individual hairs of R37. To determine a growth rate, we first calculate the time between two collection dates of tail hairs that have overlapping isotope profiles. We then select one or more match points between the profiles, such as a peak in the $\delta^{13}C$ profile, and align the overlapping profiles in Microsoft Excel by adjusting the relative position of the two profiles along a length scale (e.g., mm). Next, we calculate the distance from the proximal end of the more recent hair to the proximal end of the other

hair. Finally, we divide this distance by the time between collection dates to get a growth rate for the more recent hair. To determine the growth rate of the second hair, the growth rate of that hair can be adjusted so that the differences in multiple match points between the two hairs are minimized. This can also be done mathematically in several ways, but Wittemyer et al. (2009) find no difference between methods. The VM technique can be applied to various metabolically inert tissue types, including elephant tusks. For tusks, visual matching was used to determine a linear growth rate that best matched $\delta^{13}C$ peaks to NDVI peaks.

Bomb-curve ^{14}C dating is another method for determining the growth rate of a metabolically inert tissue (Chapter 3). Tissues that have been accurately dated include enamel, tusk dentin, hair, and horn. However, in Chapter 3, we show elephant tusks yielded more accurate growth rates than tail hair. This is in part because tusks often represent decades of time, whereas tail hairs generally represent about 1 years time. Tail hairs dated were also collected relatively recently (1998 to 2006), when the slope of the bomb-curve is shallower and resolving ages less than a year or two apart becomes challenging. Using the bomb-curve ^{14}C dating technique, a linear growth rate of 4.13 ± 0.39 cm/yr along the tusk axis was determined for the R37 tusk (Chapter 3). Although tusk growth rate appears to be linear over the last 30 years of life based on bomb-curve ^{14}C dating methods, the sampling resolution is too coarse to detect intra-annual variation. As for changes in long-term growth rates, we would expect the greatest variation to occur from the juvenile stage through early adulthood (~25 years of age), when overall growth rates are highest (Laws, 1966). This ontogenetic period is not present in the tusk of R37.

The large sample mass and sampling geometry required for determining growth rates by bomb-curve ^{14}C measurement yields an axial growth rate, and converting this to a radial growth rate (normal to the pulp cavity appositional surface) for comparison to the VM and histologically determined radial growth rates is a complicated task. It requires that the angle between the tusk axis and the pulp cavity be known, and this can only be done if the tusk axis is present or can be reasonably approximated. It was only possible to do this on sample 1053 (Chapter 3).

The third method to measure tusk growth rate is histological analysis of periodic growth increments, which provides evidence of intra-annual variations in growth rate. Growth rate was measured radially from the CDJ to the tusk axis. Using thin sections made from ivory slabs 412, 1053, and 1169, we measured the thickness of (approximately weekly) second-order growth increments normal to the pulp cavity surface, or the appositional surface. Increment thicknesses were measured using an ImageJ plug-in called IncMeas v1.2, written by Adam Rountrey. We smoothed the increment thickness data with a 10-point running mean.

For direct comparison to the VM method, we limit growth increment thickness data to the intervals that were serially sampled, rather than the entire transverse section of the slabs. We do this because in addition to intra-annual variation in radial growth rate, there is also variation in increment thickness along the pulp cavity from the horn of the pulp cavity to the pulp cavity margin. That is, there is not a uniformly thick layer of dentin deposited along the pulp cavity each day (or week). A transect normal to the pulp cavity from the tusk axis to the CDJ is spatially equivalent to moving from the horn to the margin of the pulp cavity (Figure 4.2). Incremental thickness is thinner at the horn and

the margin of the pulp cavity; therefore, sampling near the CDJ and near the intersection of a growth increment with the tusk axis, whose spatial equivalents are the pulp cavity margin and horn, respectively, was avoided when possible. One exception to this is in ivory slab 412. Due to geometric constraints imposed by preparation of adjacent slabs, slab 412 had to be sampled within 1.6 mm of the CDJ, and within 5.4 mm of the intersection of growth increments with the tusk axis.

4.4.5 Tuning growth rates

As a final step, we tune the stable isotope data based on the growth rates determined by methods described in Section 4.4.3 and by using the well-established relationship between the $\delta^{13}C$ and NDVI. In East Africa, NDVI is primarily controlled by rainfall: within days after the seasonal rains begin or any other significant rainfall event (~ >30 mm), NDVI begins to increase as grasses sprout and to a lesser extent, shrubs and trees increase photosynthetic activity above dry season baseline (Cerling et al., 2004; Cerling et al., 2006; Cerling et al., 2009; Wittemyer et al., 2009). Cerling et al. (2009) report peak NDVI occurs approximately 20 days after peak rainfall, and that the $\delta^{13}C$ peak in tail hair, which is a result of increasing C_4 vegetation in diet, occurs approximately 16 days after the NDVI peak. We use the software program AnalySeries (v 2.0.4.2), to tune $\delta^{13}C$ peaks to NDVI peaks. This involves aligning the $\delta^{13}C$ peaks with NDVI peaks by increasing or decreasing the tissue growth rate between two match points. After tuning, we shift each isotopic time series by +16 days to account for the lag between $\delta^{13}C$ and NDVI peaks.

4.4.6 Matching filter

If NDVI and $\delta^{13}C$ are considered as two related signals, a matching filter can be applied to predict $\delta^{13}C$ from NDVI and vice versa. Potential applications of the filter include using isotope profiles to reconstruct seasonality of vegetation in the past or given NDVI, predict the diet of elephants. Matching filters are commonly used in signal processing, whereby two signals, *a(t)* and *b(t)*, are related by convolution with the matching filter *f(t)*, such that convolution with signal *b(t)* (e.g., NDVI) will produce an impulse response signal *a(t)* (e.g., $\delta^{13}C_{ivory}$) as given by the following equation:

$$a(t) = f(t) * b(t) \tag{4.3}$$

which can be expressed in integral form as

$$a(t) = \int f(\tau)b(t-\tau)d\tau \tag{4.4}$$

where τ is a dummy integration variable (Menke, 1989). The method requires a tuning interval where the two signals are evaluated and the matching filter is constructed. The filter is only predictive if the tuning interval M is shorter than the signal interval N. Inverse methods require that the continuous functions in equation 4.3 be discretized and resampled at regular intervals. In discrete form, the functions can be expressed as vectors, and the convolution in equation 4.3 can be cast as

$$a(t) = \sum_{\tau=0}^{\infty} f(\tau)b(t-\tau) \quad (4.5)$$

where t is evaluated at the resampled intervals.

The matching filter code applied here was written in Matlab by Gerard Schuster and involves several steps. NDVI and tuned $\delta^{13}C$ data are discretized at 10-day intervals, smoothed through convolution with a center-weighted three-point mean, demeaned, and normalized. The filter is based on the least squares solution

$$f = [A^T A]^{-1} A^T d \quad (4.6)$$

where A is the convolution matrix of the input signal b(t) and the filter, and d is a damping factor (Menke, 1989).

A tuning interval of 600 days is used because it covers *ca.* three wet seasons. This is about one-third of the time represented in the 1982 to 1987 profile to which the matching filter is applied to predict both $\delta^{13}C$ from NDVI and NDVI from $\delta^{13}C$.

4.5 Results and Discussion

4.5.1 Tissue growth rates

4.5.1.1 Tail hair growth rates. Tuned growth rates from VM five R37 tail hairs have a mean value of 0.60 ± 0.03 mm/day and range from 0.55 to 0.62 mm/day (Table 4.1). Tuned growth rates vary little from the visually matched values. Isotope profiles from each hair were combined using VM to make a composite hair record, which was

then tuned to NDVI. Only one of five hairs had a tuned growth rate greater than one standard deviation away from the rate determined by the VM method. The average sampling frequency is 8.3 ± 0.5 days, and the time represented in an individual hair ranges from 379 to 533 days. Based on the growth rates, the combined isotope profiles span a 7.1-year (2579 days) period from September 4, 1999 to September 26, 2006. There is a 2.2-year gap (791 days) from November 1, 2002 to December 30, 2004 in the record due to a lack of sampling from November 2002 to June 2006. The date in the latter end of the gap, December 30, 2004, represents the distal end of the hair collected on June 17, 2006.

4.5.1.2 Tusk growth rates. Tusk growth rates are expressed in microns per day (μm/day) in the radial direction, approximately normal to the axis of the tusk, because this is the orientation of the thin section and of the serial sampling method (Figures 4.3 and 4.4). The growth rates determined by visual matching of $\delta^{13}C$ peaks with NDVI peaks range from 13.4 to 15.2 μm/day (Table 4.2). The single ^{14}C-based growth rate from slab 1053 is 14.9 ± 0.6 μm/day, which is nearly identical to the rate determined from the other two methods for this slab. Measurement of second-order growth increments yields similar rates, but importantly illustrates the variability of growth rates on an intra-annual basis (Table 4.2). The variation in increment thickness resulting from position along the pulp cavity surface is minimal except for near the horn (e.g., the tusk axis) and near the margin. There, growth rates appear to decrease, resulting in thinner increments, as demonstrated by the convex-up geometry of the growth curves in Figure 4.5. While the second-order growth increments are prominent in R37 ivory thin sections and polished slabs, the (annual) first-order increments observed in other proboscidean

tusks are not clearly resolvable in all parts of the tusk. This may be due to the lack of strong annual variability in temperature in tropical East Africa, which may be the primary cause for annual incremental features. This does not mean first-order increments are lacking in all *Loxodonta africana* tusks. Codron et al. (2012) report first-order increments in seven tusks from South Africa, where annual seasonality is present, and they have been documented in other polished transverse sections of African elephant tusks (plate 32, Sikes, 1971).

The three methods used to measure tusk growth rate yield nearly indistinguishable results for individual slabs, but the three slabs appear to have slightly different growth rates. The tuning process changes VM growth rates by < 5 %, INC rates by < 7 %, and the ^{14}C rate by *ca.* 2 %, and therefore has no significant effect on overall growth rates determined by the three methods (Figure 4.6 and Table 4.2). However, tuning corrects for short-term variability in the growth rate, so that mismatches of $\delta^{13}C$ peaks and NDVI peaks that result from assuming a linear growth rate are rectified.

Finally, tusk growth rate appears to be slower during the last several years of life than in younger animals. In slabs 412 and 1053, it ranges from 14.0 to 15.4 μm/day based on the different methods. These slabs represent periods from 1982 to 1987 and 1999 to 2004, respectively. The growth rate during the last three years of life (2004-2006), represented in slab 1169, ranges from 12.8 to 13.4 μm/day (Table 4.2). These data, albeit limited, suggest that growth through adulthood in this individual was relatively constant up until the last several years of life.

4.5.2 Stable isotope profiles

Stable isotope profiles from ivory for the periods 1982 to 1987 and 2000 to 2006 and the hair profile for the latter period provide information about elephant diet and the climate in which it lived. We present $\delta^{13}C$ and $\delta^{18}O$ results from ivory, followed by $\delta^{13}C$ and $\delta^{15}N$ from hair. We also compare hair and ivory $\delta^{13}C$ profiles from 2000 to 2006. Data from XRD analysis of pretreated tusk dentin showed no calcite precipitation (Figure C.1).

4.5.2.1 Stable isotope profiles in ivory. The tuned ivory $\delta^{13}C$ and $\delta^{18}O$ ($\delta^{13}C_{ivory}$ and $\delta^{18}O_{ivory}$, respectively) profiles from slab 412 (1982 to 1987) and the composite profile from slabs 1169 and 1053 (2000 to 2006) are shown in Figures 4.7 and 4.8, respectively, along with corresponding NDVI and rainfall records. Table 4.3 contains descriptive statistics for $\delta^{13}C_{ivory}$ from both profiles, and all isotope data (n = 597) are given in Table C.1. In the 1982 to 1987 profile, $\delta^{13}C_{ivory}$ values increase up to ~ 4 ‰ during and just after the wet seasons above the dry season "baseline" values of about -12.5 ‰ (Figure 4.7). The increase in $\delta^{13}C_{ivory}$ is associated with seasonally incorporating C_4 vegetation into diet following each rainy season and associated NDVI peak. Thus, $\delta^{13}C_{ivory}$ values function not only as a proxy for C_4 vegetation in diet, but also serve as a proxy for wet seasons. Plant surveys and observational data show nearly all C_4 vegetation in the area is grass, with one exception being the salt bush *Salsola dendroides*, which elephants are known to include in their diet. Thus, the increase in $\delta^{13}C_{ivory}$ values indicates a dietary switch to more grazing. Grazing peaks approximately five weeks after the initial rains of a wet season and two weeks after peak NDVI. Codron et al. (2012) show similar results for $\delta^{13}C$ and $\delta^{18}O$ in tusk bioapatite sampled every ~6

months using samples averaged over a 3.5 month period. The difference of more than an order of magnitude in sampling resolution and the lack of comparison to vegetation (NDVI) or rainfall limits the interpretation of the decades-long records from multiple elephants.

The 2000 to 2006 profile shows a similar trend to the 1982 to 1987 profile in that peak $\delta^{13}C_{ivory}$ values are associated with peak NDVI (Figure 4.8). However, high maximum NDVI values do not always result in high maximum $\delta^{13}C_{ivory}$ values for a given wet season in either profile. Figure 4.9 shows the relationship between the maximum $\delta^{13}C_{ivory}$ vs. the maximum NDVI value during 6-month intervals that bracket the "short" and "long" rains. We take the maximum values from the intervals March 1 through September 1 and September 1 through March 1 to delineate the wet seasons (Figure 4.9). The R^2 values (0.18) for both time periods represented by the isotope profiles suggest that other environmental factors influence the maximum $\delta^{13}C$ value. In a similar analysis, Cerling et al. (2009) showed, using $\delta^{13}C$ values from tail hair, that the 6-month maximum NDVI explained 61 % of the variance in the percent of C_4 vegetation ($\%C_4$) in diet.

To calculate the $\%C_4$ in diet using $\delta^{13}C_{ivory}$, $\delta^{13}C$ data of plants ($\delta^{13}C_{plant}$), and an enrichment factor between diet and bioapatite ($\varepsilon^*_{diet\text{-}apatite}$) must be determined. We use an enrichment factor of + 13.6 ‰ for $\varepsilon^*_{diet\text{-}apatite}$ based on preliminary data from sampling elephant breath from Utah's Hogle Zoo. The value is within the range (14.1 ± 0.5 ‰) determined for large ungulates (Cerling and Harris, 1999). The $\delta^{13}C_{plant}$ values for C_3 and C_4 plants comes from a large data set (n = 265) of plants collected in the Reserves between October 2004 and May 2006 during both wet and dry seasons. The average

$\delta^{13}C_{plant}$ from this data set is -27.4 ± 1.0 ‰ for C_3 plants and -13.4 ± 1.0 ‰ for C_4 plants. The range and mean $\%C_4$ in diet for the profiles is given in Table 4.3. The ranges of the 1982 to 1987 and 2000 to 2006 profiles are quite similar, but the mean $\%C_4$ in diet between the two periods differs by 4 % (Table 4.3). From 1982 to 1987, it is 14.5 ± 6.2 (1σ) %, whereas from 2000 to 2006, it is 18.5 ± 6.2%. Rainfall data from Archer's Post show that the latter period was wetter (353 mm/year) than the former (299 mm/yr). Given that C_4 grasses are more productive in warm, wet growing conditions, annual rainfall provides a simple explanation for the slightly higher contribution of C_4 vegetation to diet from 2000 to 2006. Elephant socio-ecology is a complex system, and many other variables may contribute to the small difference in mean $\%C_4$ in diet. For example, social rank of the Swahilis family, of which R37 became the matriarch, may have improved from the mid-1980s to the more recent period (2000-2006), providing better or more frequent access to C_4 vegetation at the beginning and end of the wet seasons when competition for C_4 vegetation is highest.

The $\delta^{18}O_{ivory}$ profiles show an oscillatory pattern similar to the $\delta^{13}C_{ivory}$ profiles (Figures 4.7 and 4.8). Overall, the $\delta^{18}O_{ivory}$ data exhibit greater variability over short time scales (e.g., weeks) and have slightly higher ranges than $\delta^{13}C_{ivory}$ data (Table 4.3). The most positive values coincide approximately with NDVI peaks, but in some cases precede or follow NDVI peaks by several weeks or occur entirely out of phase with NDVI and $\delta^{13}C$ peaks (Figures 4.7 and 4.8). Intervals where $\delta^{18}O_{ivory}$ and $\delta^{13}C_{ivory}$ are not in phase occur in the 1982 to 1987 and the 2000-2006 periods, and result in low R^2 values when the two isotopes are linearly regressed (0.027 and 0.070, respectively).

To understand the general trend of increasing $\delta^{18}O_{ivory}$ with increasing $\delta^{13}C_{ivory}$, it is useful to consider the sources of body water. For small mammals, drinking water, atmospheric oxygen, and metabolic water contribute 56%, ~30%, and 15%, respectively, where metabolic water in this case is derived from structurally bound oxygen (e.g., carbohydrates) rather than food-bound water (i.e., plant water) (Podlesak et al., 2008). However, the study by Podlesak et al. (2008) was done with dry laboratory feeds, and therefore, drinking water constitutes a higher proportion of water intake than in natural settings because there is almost no contribution from food-bound water. A study by Kohn (1996) suggests that plant water (*ca.* 50 %) is the primary source of oxygen in wild, large herbivores followed by oxygen that is in air (24 %), drinking water (< 20 %), and structurally bound in food (<10 %). Thus, variation in the $\delta^{18}O$ of plant water and drinking water will primarily control the $\delta^{18}O$ of body water ($\delta^{18}O_{bw}$), which determines $\delta^{18}O_{ivory}$.

Elephants are obligate drinkers, and during the dry season especially, elephants in and around SNR and BSNR drink daily from the Ewaso N'giro or one of its permanent tributaries. During the wet season, water availability away from permanent sources increases as does the water content in plants, the elephants become less reliant on the Ewaso N'giro River, and their range expands to areas where C_4 grasses are more abundant (Wittemyer et al., 2007). Plant water is often enriched with respect to meteoric water. Thus, one explanation for the more positive $\delta^{18}O_{ivory}$ values is that plant water (from grasses or browse) accounts for a greater fraction of body water during the wet season. Indeed, GPS data from July 11 to December 31, 2001 show that R37 visited

permanent water sources 83% of days during the dry season but only 34% of days during the wet season (Wittemyer et al., 2008).

Cerling et al. (2009) present δD tail hair (δD_{hair}) from the socially dominant family unit in the Reserves, the Royals, and δD water (δD_w) data from the Ewaso N'giro River and find the opposite trend in Royal's tail hair. During wet seasons, δD_{hair} becomes more negative as does the δD_w of the Ewaso N'giro. This trend can be explained by evaporative-enrichment of ^{18}O and D in river and plant water during the dry season, and depletion of the heavy isotopes during the wet season. As the dominant group in the Reserves, the Royals continue to utilize the Ewaso N'giro during the wet season, visiting the river on 84% of the days between July to December, 2001 (Wittemyer et al., 2008). GPS data allow us to determine that differences in water intake are most likely the cause for the opposite trends observed in R37's $\delta^{18}O_{ivory}$ and the δD_{hair} from the Royals, and may even be interpreted as rank-driven resource partitioning.

4.5.2.2 Stable isotope profiles in tail hair. Composite $\delta^{15}N$ and $\delta^{13}C$ profiles from five combined tail hairs (n =203) are shown in Figure 4.10, and all tail hair data (n =272) is given in Table C.2. Tail hair $\delta^{15}N$ ($\delta^{15}N_{hair}$) has a mean value of +11.0 ± 1.1‰ (1σ) and a range of 6.1 ‰ from +8.1 to +14.2 ‰. Tail hair $\delta^{13}C$ ($\delta^{13}C_{hair}$) has a mean value of -21.4 ± 0.9 ‰ and a range of 5.0 ‰ from -17.9 to -23.0 ‰ (Table 4.3). We use the reaction progress variable (RPV) model, originally applied by Ayliffe et al. (2004) to horse tail hair and described in greater detail by Cerling et al. (2007), to reconstruct the $\delta^{13}C$ of diet ($\delta^{13}C_{diet}$) and the $\%C_4$ vegetation in diet (Figure 4.10). The RPV model takes into account turnover time of dietary carbon using three pools that have different

fractional contributions to hair. Pool turnover times are described by first-order rate constants, expressed as half-lives ranging from several to ~150 days.

Isotopic data from plant samples collected in SNR and BSNR from October 2004 to July 2005 and in May 2006 provide an important framework for interpreting the hair data. Nearly 200 samples were collected during the former interval, which was drier than usual. About 70 samples come from the latter interval, which were collected towards the end of the "long rains". We use the same end-member values for C_3 and C_4 plants discussed in Section 4.5.2.1 for RPV model inputs. The plant $\delta^{15}N$ values ($\delta^{15}N_{plant}$) range from about 0 ‰ to + 12 ‰, with a majority of values lying between + 7 and + 12 ‰. Notable exceptions include a few C_4 grasses (*Andropogon* sp. and *Cynodon dactylon*) that had average $\delta^{15}N_{plant}$ values of + 4.7 and + 3.1 ‰, respectively, and the C_3 shrub *Indigofera*, which showed values ranging from + 0.4 to + 7.7 ‰. Values near 0 ‰ are indicative of nitrogen fixation, and this was primarily observed in *Indigofera schimperi* found in nonriparian zones.

Overall, during periods of increased $\delta^{13}C_{hair}$, $\delta^{15}N_{hair}$ generally increases (Figure 4.10). There are several trends in the hair profile that are of interest. The first is a period of anomalously low (~2σ from the mean) $\delta^{15}N_{hair}$ values that occurs from December 2005 through mid-March 2006. During this period, the "short" rains of 2005 failed, and the usual NDVI increase associated with rainy seasons is absent. In the hair, this is preceded by a rapid decrease in $\delta^{15}N$ from + 12 to less than + 9 ‰ beginning in September 2005. The $\delta^{13}C_{hair}$ also decreases and remains low during this period; it represents the longest interval of low $\%C_4$ in diet (10 to 15 %) in the hair profile (Figure 4.10). The $\delta^{13}C_{hair}$ and $\delta^{15}N_{hair}$ values remain low until arrival of the "long" rains in March of 2006, when both

increase rapidly as C_4 vegetation becomes a significant dietary component (>25 %) for the first time in nearly 9 months. The $\delta^{13}C_{hair}$ and $\delta^{15}N_{hair}$ data indicate that the diet of R37 during this period was comprised of ~90 % C_3 plants, all or some of which must have had relatively low $\delta^{15}N_{plant}$ values. Given that the trophic level enrichment is about +1 to +3 ‰ for $\delta^{15}N$ and the available isotopic data from plants, the diet during this period likely included significant quantities of *Indigofera schimperi*.

Another noteworthy trend is large-scale decoupling of the positive relationship between $\delta^{13}C_{hair}$ and $\delta^{15}N_{hair}$. This occurs twice in the hair profile, once in the middle of 2002 (May to August) and again from mid-June 2006 until death in September 2006. In the 2002 event, the $\delta^{13}C_{hair}$ decreases from -19 to -23 ‰ following the end of the "long" rains, which corresponds to a drop from 50 to ~0 % C_4 vegetation in diet, followed by a rebound to ~ 15-20 % C_4 (Figure 4.10). During this period, the $\delta^{15}N_{hair}$ remains constant (~ +12 ‰) when the $\delta^{13}C_{hair}$ decreases, and then increases by one permil as $\delta^{13}C_{hair}$ stabilizes. Decoupling of $\delta^{13}C_{hair}$ and $\delta^{15}N_{hair}$ occurs again at the end of May, 2006, when $\delta^{13}C_{hair}$ is decreasing following the end of the "long" rains and $\delta^{15}N_{hair}$ increases from + 10 to + 13 ‰ by mid-July, 2006. The decoupling of the $\delta^{13}C_{hair}$ and $\delta^{15}N_{hair}$ is either a result of diet, physiological processes, or a combination of the two. Even with the plant isotope data, it is difficult to ascribe the trend to any one of these possibilities.

4.5.2.3 Comparison of $\delta^{13}C$ profiles from tail hair and ivory. Tail hair and ivory $\delta^{13}C$ profiles from 2000 to 2006 are compared to evaluate the two different tissues and assess whether or not they are recording the same information. We convert ivory and hair $\delta^{13}C$ values to their respective $\delta^{13}C_{diet}$ values using + 13.6 ‰ (from unpublished data) and + 3.1 ‰ for $\varepsilon^*_{diet\text{-}apatite}$ and $\varepsilon^*_{diet\text{-}hair}$, respectively (Cerling and Harris, 1999). The $\delta^{13}C_{diet}$

profile from 2000 to 2006 calculated directly from $\delta^{13}C_{hair}$ values ($\delta^{13}C_{diet(hair)}$) differs significantly in range and shape from the $\delta^{13}C_{diet}$ calculated from the RPV model ($\delta^{13}C_{diet(RPV)}$). Since the parameters for describing a multiple-pool carbon turnover model are not known for bioapatite in ivory, we compare the $\delta^{13}C_{diet}$ data from ivory ($\delta^{13}C_{diet(ivory)}$) with $\delta^{13}C_{diet(hair)}$ rather than $\delta^{13}C_{diet(RPV)}$. Data from tuned hair and ivory profiles were fit with a cubic spline in Matlab and resampled weekly (Figure 4.11A). There is remarkable agreement between the two profiles in range (Table 4.3) and high-frequency variability, despite periods of offset of up to > 1 ‰ (Figure 4.11B). A linear regression yields the relationship $\delta^{13}C_{diet(ivory)} = 0.64 * \delta^{13}C_{diet(hair)} - 8.75$ ($R^2 = 0.49$). From examination of the residual of the two profiles (Figure 4.11B), it is evident that from 2000 to 2002, $\delta^{13}C_{diet(ivory)}$ is on average 0.5 ‰ more positive than $\delta^{13}C_{diet(hair)}$, and from 2005 through 2006, it is 0.4 ‰ more negative with respect to $\delta^{13}C_{diet(hair)}$. An important question to consider is: "What drives decoupling or differences in the two profiles?" The carbon isotope composition of hair and tusk bioapatite both ultimately derive from diet, but differences in formation and composition of the tissues result in variation between the calculated $\delta^{13}C_{diet}$ from each tissue.

Hair is made up of keratin, which consists mostly of proteins derived from amino acids. Amino acids used to construct hair are pulled from the blood stream at the follicle. The pool of available amino acids in the blood stream can come from an exogenous source (i.e., diet), or they can come from endogenous sources via the breakdown of existing proteins in tissues (e.g., muscle, organ, etc.) or bone collagen (e.g., Ayliffe et al., 2004 and references therein). Endogenous sources have different concentrations of hair-forming amino acids and they also have different turnover rates, which is largely a

function of metabolic activity. Ayliffe et al. (2004) determined that in horse tail hair, ~56 % of the carbon isotope ratio in hair is determined by current diet (e.g., in the past five days), whereas 44 % comes from diet over the past ~150 days, which is stored in tissues and skeletal material.

Carbon in the bioapatite of tusk dentin is derived from blood bicarbonate, which is the dominant carbonate species in the blood dissolved inorganic carbon (DIC) pool. Blood bicarbonate comes from cell-respired CO_2 produced through catabolism of carbohydrates and to a lesser extent, lipids and excess proteins. Previous studies on the $\delta^{13}C$ of bioapatite and CO_2 of breath suggest a constant enrichment between breath and bioapatite ($\varepsilon^*_{breath\text{-}apatite}$) of ~ +11 ‰ (Passey et al., 2005; Tieszen and Fagre, 1993). In the same study on horse tail hair by Ayliffe et al. (2004), the authors also found that 84 % of the carbon isotope ratio in blood bicarbonate in horses is determined by current diet (e.g., in the past 3 days), whereas only 16 % comes from diet over the past ~50 days, which is stored in tissues and skeletal material.

The faster turnover time of carbon in blood bicarbonate than in hair means there should be greater increases in the $\delta^{13}C$, and therefore a higher range in $\delta^{13}C_{ivory}$, associated with seasonal diet switching to C_4 vegetation. The data suggest otherwise; there is slightly greater range in the $\delta^{13}C_{hair}$ profile than in the $\delta^{13}C_{ivory}$ profile (Figure 4.11 and Table 4.3). Here we consider four potential factors, or combinations of them, that could lead to the lower amplitudes measured in the $\delta^{13}C_{ivory}$ profile.

The first is that dentin from different time periods may have been mixed by inadvertently milling across second-order features. This represents a source of physical mixing that results in time averaging. During serial sampling, the milling edge was

checked to ensure that it was parallel to growth increments every 10 samples (~1 mm). On several occasions, corrections of 50 to 100 μm were made to realign scan lines to be parallel with the growth increments.

A second factor that may contribute to the lower range in the $\delta^{13}C_{ivory}$ profile could be a result of time averaging through tissue formation, a physiological process. While the composition and formation of dentin differs from that of enamel, it may have an analogous maturation process whereby the initial and final densities of dentin differ. If this is the case, the maturation process is likely to be much less protracted and severe in tusk dentin than it is for enamel. Data that support a maturation process in tusk dentin include preliminary Fourier Transform Infrared (FTIR) spectroscopy data from a transect along the thin section for slab 1169. The data show increasing relative intensity in the phosphate peak and decreasing relative intensity in the primary amide peak, a proxy for protein content, moving from the pulp cavity towards the CDJ (Appendix C). A combination physical and physiological time-averaging is also plausible.

A third factor, albeit secondary to the previous two mentioned, could be a damping of the range in $\delta^{13}C_{ivory}$ during analysis on the IRMS. There are two important differences observed between enamel bioapatite and tusk dentin bioapatite. First, the CO_2 yields from H_2O_2-treated tusk bioapatite, measured as a voltage per unit mass of sample (mV/μg), were lower than for enamel bioapatite from R37 enamel by about 30%. This was compensated for by analyzing greater amounts of sample, but in some cases, where sample mass was limited, voltages were slightly lower (~1000 to 1300 mV) than for normal carbonate samples (≥1500 mV). All samples included in analyses were within the range of linearity on the IRMS (1000 to 8000 mV). The second difference is that

tusk bioapatite also took longer to digest in the CAB, which imparts a memory effect on subsequent samples. The memory effect would act to dampen the $\delta^{13}C_{ivory}$ values because when samples are run in sequence, the contribution of more negative $\delta^{13}C$ from the sample just before the $\delta^{13}C_{ivory}$ maximum would cause the maximum value to be more negative. To address the issue of a memory effect, the reaction time in the CAB was increased from 10 to 30 minutes, which reduced the memory effect to ~70 to 200 mV. In the case of low-voltage samples (~1000 mV) this would impart a 7 to 20 % memory effect, but for a majority of samples, the memory effect was smaller, on the order of 2 to 4 %.

Finally, differences in the protein content of C_3 vs. C_4 vegetation will result in different $\delta^{13}C$ values for hair and tusk bioapatite. The observed lower amplitudes in $\delta^{13}C_{ivory}$ could be explained if C_4 vegetation has higher protein content than the C_3 vegetation. This would result in a greater proportional contribution to the $\delta^{13}C_{hair}$ than to the $\delta^{13}C_{ivory}$, and could produce the higher amplitude observed in the $\delta^{13}C_{hair}$ profile. Weight percent nitrogen (%N) data from Samburu plants show the opposite; the average %N in C_3 vegetation is higher (3.3 ± 1.0 %, n = 139) than in C_4 grasses (1.6 ± 0.8 %, n = 53).

Given the four possibilities discussed above, the most likely causes of the lower amplitude in the $\delta^{13}C_{ivory}$ profile are due to time averaging introduced through milling and dentin maturation, but these are difficult to quantify and other factors that have not been identified may contribute to the observed pattern of lower than expected ranges in the $\delta^{13}C_{ivory}$ profile.

4.5.3 Matching filter

Profiles of actual and NDVI-predicted $\delta^{13}C$ show good agreement in location of peak maximum and peak width, and the predicted $\delta^{13}C$ profile maintains the similar overall structure of the actual profile (Figure 4.12A). In general, the "baseline" predicted $\delta^{13}C$ value is ~0.5 ‰ higher than the actual value, and maximum peak values differ by up to 1.5 ‰ (Figure 4.12B), which translates to a difference of 11 $\%C_4$. A linear regression of predicted and actual $\delta^{13}C$ values indicates the matching filter performs relatively well ($\delta^{13}C_{pred} = \delta^{13}C_{actual}$ (0.64) -3.9, R^2=0.563). The slope indicates that $\delta^{13}C_{pred}$ is more negative than $\delta^{13}C_{actual}$.

For NDVI, the predicted and actual profiles have the same peak frequency, but there are differences in peak shape and height, and a slight positive shift in location of peaks for predicted NDVI. When actual NDVI peaks are > 0.4, the predicted profile peaks underestimate the peak maxima, whereas they tend to match actual peak maximum in the range of 0.3 to 0.4, and overestimate peak heights <0.3 (Figure 4.13).

Overall, the matching filters accurately predict the frequency of seasonal changes using one environmental signal to predict the other, but differences in peak heights between predicted and actual peak height for both $\delta^{13}C$ and NDVI profiles seem to preclude the use of this technique for quantitatively evaluating seasonal change in vegetation or by proxy, rainfall.

4.5.4 Applications of tusk isotope profiles to modern and paleo-ecology

The results of this study have implications for modern ecology and terrestrial paleoecology. In C_3-C_4 ecosystems where tail hair or tusks can be collected, there is a

potential trove of information available regarding seasonal variations in vegetation, precipitation, and individual diet that can be determined from stable isotope profiles. For hair, these methods have been applied to numerous studies of other marine and terrestrial mammals. From a practical standpoint, stable isotope profiles are an efficient and less resource (i.e., time and money) intensive alternative for studying diet than traditional methods such as feces collection and feeding observations. Work that has yet to be done includes comparing multiyear isotope profiles from elephants of different social rank within a population to understand how hierarchal position affects access to resources during the dry season, when more limited access to available water sources and forage generates competition among family units (Wittemyer and Getz, 2007). Long-term tusk isotope profiles have the potential to elucidate changes in diet over multiyear (e.g., decadal) periods (Codron et al., 2012). These long-term isotope profiles can improve our understanding of the relationship between elephants, vegetation, and land-use change. They can also provide critical information to aid conservationists in developing strategies to manage the ever-increasing problem of elephant-human conflict in Asia and Africa.

Isotopic profiles from unaltered bioapatite in fossil proboscidean tusks have the potential to address long-standing questions related to seasonality of vegetation, precipitation, and proboscidean diet in terrestrial paleoenvironments throughout the recent past. The susceptibility of dentin bioapatite to diagenesis suggests isotope profiles from fossil tusks several hundred thousand years old or older may not be viable (Ayliffe et al., 1994). Primary isotope signatures have been recovered from numerous late Pleistocene tusks from North American and Eurasian localities on the order of 10^4 years old (Fox et al., 2007; Koch et al., 1989; Rountrey et al., 2012). The use of X-ray

diffraction on tusk dentin can be used on a case-by-case basis to evaluate recrystallization of dentin bioapatite before initiating stable isotope work.

To date, no stable isotope profiles on fossil tusks have been done at the approximately weekly resolution we used in this study, and this represents a potential avenue for future research for paleoenvironments where subannual seasonal environmental changes may have been present, such parts of the tropics where movement of the ITCZ results in biannual wet seasons. One especially important question with respect to hominid paleoenvironments in East Africa is whether the biannual wet seasons existed then as they do today. This frequency (and magnitude) of wet seasons would have had a significant effect on vegetation structure throughout the year in the hot ancient environments of the Omo-Turkana Basin (Passey et al., 2010). Whether or not Plio-Pliestocene fossil tusks from East African or other parts of the world are suitable for stable isotope profiles remains to be tested. If in fact diagenesis precludes the use of Plio-Pliestocene fossil tusks from East Africa, isotope profiles from the enamel proboscidean or other large herbivore molar teeth may provide alternative proxies for examining seasonal environmental variability.

4.6 Conclusions

The tusk and tail hair profiles from R37 offer a unique opportunity to "ground-truth" stable isotope data with NDVI, rainfall, GPS location, and observational data. Previous studies utilizing isotope profiles in fossil or modern tusks have all been in environments with annual seasonal cyclicity. We have demonstrated for the first time that diet and climatic information can be resolved at approximately weekly resolution from serially sampled tusk dentin and thus provide a record of subannual (seasonal)

changes in elephant diet and precipitation in Kenya. This frequency (~52 samples/year) is more than sufficient to resolve subannual seasonal signals according to Nyquist sampling theory. Tusk growth rates determined by visual matching, growth increment thicknesses, and bomb-curve ^{14}C dating show excellent agreement, varying by less than 10 %. Bomb-curve ^{14}C and VM methods are not feasible methods for fossil tusks. Unlike hair, tusk growth rate is variable over annual timescales and therefore, a final tuning step was added. However, tuned growth rates differed by < 7 % from untuned growth rates, and we therefore suggest tuning fossil tusk profiles is not necessary (nor possible in most cases). Combined, the isotope profile and growth rate results set the stage for using tusks from the recent geologic record as high-resolution archives of proboscidean life history and terrestrial paleoclimate. The matching filter data show that $\delta^{13}C$ can be used to predict NDVI given the appropriate tuning interval length. Further developed, this may be able to provide quantitative or relative estimates of seasonal vegetation or precipitation changes in ancient environments.

Tusk and hair isotope profile results have several implications for modern elephant ecology. The $\delta^{13}C_{ivory}$ and $\delta^{13}C_{hair}$ profiles from 2000 to 2006 are similar in their magnitude of variation and virtually identical in their ability to record high-frequency changes in diet. Subtle differences may provide insight into physiological processes or nutritional status; however, this could not be adequately addressed with our data due to the combined effects of potential time-averaging from sampling and physiological processes. The $\delta^{15}N_{hair}$ data, in combination with $\delta^{13}C_{hair}$, $\delta^{13}C_{plant,}$ and $\delta^{15}N_{plant}$ data, suggest that periods of decoupling in the usual positive relationship between $\delta^{15}N_{hair}$ and $\delta^{13}C_{hair}$ are indicative of diet or metabolic change.

R37 and her family, the Swahilis, held a relatively low social rank in the Reserves. R37 hair and tusk isotope profiles from 2000 to 2006 can be compared with hair isotope profiles from the Royals, the dominant family unit in the Reserves. R37's $\delta^{18}O_{ivory}$ and Royal's δD_{hair} data indicate different water-use strategies during the wet season that may be related to social rank, demonstrating that comparison of isotope profiles may be a powerful tool for studying social dynamics in ecosystems.

4.7 Acknowledgements

We thank the Office of the President of the Republic of Kenya, the Kenya Wildlife Service, and the Samburu and Buffalo Springs County Councils for permission to conduct this research. We thank David Daballen, Daniel Lentipo, and Chris Leadismo at Save The Elephants for sample collection and Dan Davis, Blake Hethmon, and Jared Singer for assistance with sample preparation and analyses; Gerard Schuster for furnishing the matching filter code written in Matlab; and Adam Rountrey for furnishing a copy of the ImageJ plug-in (IncMeas v1.2) used to measure growth increments. This project was supported by National Science Foundation grant EAR-0819611 awarded to Thure Cerling and by a University of Utah Graduate Research Fellowship (KTU). Neal Blair and Thea Wilson from Northwestern University performed FTIR analysis on thin section R37-DEN-1169 and generated Figures C.2 and C.3 in Appendix C. Stable isotope analyses were done at the SIRFER facility at the University of Utah. This work was carried out under CITES permits US831854/9, 02US053837/9, and 07US159997/9.

4.8 References

Ambrose, S. H., and Norr, L., 1993, Experimental evidence for the relationship of the carbon isotope ratios of whole diet and dietary protein to those of bone collagen and carbonate, *in* Lambert, J. B., and G., G., eds., Prehistoric Human Bone: Archeology at the Molecular Level: New York, Springer-Verlag, p. 1-37

Ayliffe, L., Cerling, T., Robinson, T., West, A., Sponheimer, M., Passey, B., Hammer, J., Roeder, B., Dearing, M., and Ehleringer, J., 2004, Turnover of carbon isotopes in tail hair and breath CO_2 of horses fed an isotopically varied diet: Oecologia, v. 139, no. 1, p. 11-22.

Ayliffe, L., Chivas, A., and Leakey, M., 1994, The retention of primary oxygen isotope compositions of fossil elephant skeletal phosphate: Geochimica et Cosmochimica Acta, v. 58, no. 23, p. 5291-5298.

Cerling, T., and Harris, J., 1999, Carbon isotope fractionation between diet and bioapatite in ungulate mammals and implications for ecological and paleoecological studies: Oecologia, v. 120, no. 3, p. 347-363.

Cerling, T. E., Ayliffe, L. K., Dearing, M. D., Ehleringer, J. R., Passey, B. H., Podlesak, D. W., Torregrossa, A. M., and West, A. G., 2007, Determining biological tissue turnover using stable isotopes: The reaction progress variable: Oecologia, v. 151, no. 2, p. 175-189.

Cerling, T. E., Harris, J. M., Leakey, M. G., Passey, B. H., and Levin, N. E., 2010, Stable carbon and oxygen isotopes in East African mammals: Modern and fossil, *in* Werdelin, L., and Sanders, W., eds., Cenozoic Mammals of Africa: Berkeley, University of California Press, p. 941-952.

Cerling, T. E., Passey, B. H., Ayliffe, L. K., Cook, C. S., Ehleringer, J. R., Harris, J. M., Dhidha, M. B., and Kasiki, S. M., 2004, Orphans' tales: Seasonal dietary changes in elephants from Tsavo National Park, Kenya: Palaeogeography, Palaeoclimatology, Palaeoecology, v. 206, no. 3-4, p. 367-376.

Cerling, T. E., Wittemyer, G., Ehleringer, J. R., Remien, C. H., and Douglas-Hamilton, I., 2009, History of Animals using Isotope Records (HAIR): A 6-year dietary history of one family of African elephants: Proceedings of the National Academy of Sciences, v. 106, no. 20, p. 8093-8100.

Cerling, T. E., Wittemyer, G., Rasmussen, H. B., Vollrath, F., Cerling, C. E., Robinson, T. J., and Douglas-Hamilton, I., 2006, Stable isotopes in elephant hair document migration patterns and diet changes: Proceedings of the National Academy of Sciences, v. 103, no. 2, p. 371-373.

Codron, J., Codron, D., Sponheimer, M., Kirkman, K., Duffy, K. J., Raubenheimer, E. J., Mélice, J. L., Grant, R., Clauss, M., and Lee-Thorp, J. A., 2012, Stable isotope series from elephant ivory reveal lifetime histories of a true dietary generalist: Proceedings of the Royal Society B: Biological Sciences, v. published online February 15, 2012, p. 1-9.

DeNiro, M. J., and Epstein, S., 1978, Influence of diet on the distribution of carbon isotopes in animals: Geochimica et Cosmochimica Acta, v. 42, no. 5, p. 495-506.

-, 1981, Influence of diet on the distribution of nitrogen isotopes in animals: Geochimica et Cosmochimica Acta, v. 45, no. 3, p. 341-351.

Douglas-Hamilton, I., 1998, Tracking elephants using GPS technology: Pachyderm, v. 25, p. 81-92.

Douglas-Hamilton, I., Krink, T., and Vollrath, F., 2005, Movements and corridors of African elephants in relation to protected areas: Naturwissenschaften, v. 92, no. 4, p. 158-163.

Elliott, J. C., 2002, Calcium Phosphate Biominerals, *in* Kohn, M. J., Rakovan, J., and Hughes, J., eds., Phosphates- Geochemical, Geobiological, and Materials Importance, Volume 48: Chantilly, The Mineralogical Society of America, p. 427-453.

Fisher, D. C., 1996, Extinction of Proboscideans in North America, *in* Shoshani, J., and Tassy, P., eds., The Proboscidea: Evolution and Palaeoecology of Elephants and Their Relatives: Oxford, Oxford University Press, p. 296-315.

-, 2001, Season of death, growth rates, and life history of North American mammoths: Proceedings of the International Conference on Mammoth Site Studies., p. 121-135.

-, 2008, Taphonomy and paleobiology of the Hyde Park mastodon: Palaeontographica Americana, v. 61, p. 197-289.

Fisher, D. C., and Fox, D. L., 2003, Season of death and terminal growth histories of Hiscock mastodons: Bulletin of the Buffalo Society of Natural Sciences, v. 37, p. 83-101.

-, 2007, Season of Death of the Dent Mammoths, *in* Brunswig, R. H., and Pitblado, B. L., eds., From the Dent Prairie to the Peaks of the Rockies: Recent Paleoindian Research in Colorado: Boulder, University of Colorado Press, p. 123-153.

Fox, D. L., and Fisher, D. C., 2004, Dietary reconstruction of Miocene Gomphotherium (Mammalia, Proboscidea) from the Great Plains region, USA, based on the carbon isotope composition of tusk and molar enamel: Palaeogeography Palaeoclimatology Palaeoecology, v. 206, no. 3-4, p. 311-335.

Fox, D. L., Fisher, D. C., Vartanyan, S., Tikhonov, A. N., Mol, D., and Buigues, B., 2007, Paleoclimatic implications of oxygen isotopic variation in late Pleistocene and Holocene tusks of Mammuthus primigenius from northern Eurasia: Quaternary International, v. 169, p. 154-165.

Gannes, L. Z., Del Rio, C. M., and Koch, P., 1998, Natural abundance variations in stable isotopes and their potential uses in animal physiological ecology: Comparative Biochemistry and Physiology-Part A: Molecular & Integrative Physiology, v. 119, no. 3, p. 725-737.

Hobson, K. A., 1999, Tracing origins and migration of wildlife using stable isotopes: A review: Oecologia, v. 120, no. 3, p. 314-326.

Koch, P. L., Fisher, D. C., and Dettman, D., 1989, Oxygen isotope variation in the tusks of extinct proboscideans: A measure of season of death and seasonality: Geology, v. 17, no. 6, p. 515-519.

Koch, P. L., Tuross, N., and Fogel, M. L., 1997, The effects of sample treatment and diagenesis on the isotopic integrity of carbonate in biogenic hydroxylapatite: Journal of Archaeological Science, v. 24, p. 417-430.

Kohn, M. J., 1996, Predicting animal $\delta^{18}O$: Accounting for diet and physiological adaptation: Geochimica et Cosmochimica Acta, v. 60, no. 23, p. 4811-4829.

Laws, R., 1966, Age criteria for the African elephant, Loxodonta a. africana: East African Wildlife Journal, v. 4, p. 1-37.

Lee, P. C., Sayialel, S., Lindsay, W. K., and Moss, C. J., 2012, African elephant age determination from teeth: Validation from known individuals: African Journal of Ecology, v. 50, no. 1, p. 9-20.

Lee-Thorp, J. A., Sealy, J. C., and Van Der Merwe, N. J., 1989, Stable carbon isotope ratio differences between bone collagen and bone apatite, and their relationship to diet: Journal of archaeological science, v. 16, no. 6, p. 585-599.

LeGeros, R., Trautz, O., Klein, E., and LeGeros, J., 1969, Two types of carbonate substitution in the apatite structure: Cellular and Molecular Life Sciences, v. 25, no. 1, p. 5-7.

Levin, N. E., Cerling, T. E., Passey, B. H., Harris, J. M., and Ehleringer, J. R., 2006, A stable isotope aridity index for terrestrial environments: Proceedings of the National Academy of Sciences, v. 93, no. 30, p. 11201-11205.

Menke, W., 1989, Geophysical Data Analysis: Discrete Inverse Theory, San Diego, Academic Press, International Geophysics Series, 289 p.

Metcalfe, J. Z., Longstaffe, F. J., and Zazula, G. D., 2010, Nursing, weaning, and tooth development in woolly mammoths from Old Crow, Yukon, Canada: Implications for Pleistocene extinctions: Palaeogeography, Palaeoclimatology, Palaeoecology, v. 298, no. 3, p. 257-270.

Nyquist, H., 1928, Certain topics in telegraph transmission theory: Transactions of the American Institute of Electrical Engineers, v. 47, no. 2, p. 617-644.

Park, R., and Epstein, S., 1960, Carbon isotope fractionation during photosynthesis: Geochim. et Cosmochim. Acta, v. 21, p. 110-126.

Passey, B., Robinson, T., Ayliffe, L., Cerling, T., Sponheimer, M., Dearing, M., Roeder, B., and Ehleringer, J., 2005, Carbon isotope fractionation between diet, breath CO2, and bioapatite in different mammals: Journal of Archaeological Science, v. 32, no. 10, p. 1459-1470.

Passey, B. H., Levin, N. E., Cerling, T. E., Brown, F. H., and Eiler, J. M., 2010, High-temperature environments of human evolution in East Africa based on bond ordering in paleosol carbonates: Proceedings of the National Academy of Sciences, v. 107, no. 25, p. 11245-11250.

Pettorelli, N., Vik, J. O., Mysterud, A., Gaillard, J.-M., Tucker, C. J., and Stenseth, N. C., 2005, Using the satellite-derived NDVI to assess ecological responses to environmental change: Trends in Ecology & Evolution, v. 20, no. 9, p. 503-510.

Podlesak, D. W., Torregrossa, A.-M., Ehleringer, J. R., Dearing, M. D., Passey, B. H., and Cerling, T. E., 2008, Turnover of oxygen and hydrogen isotopes in the body water, CO_2, hair, and enamel of a small mammal: Geochimica et Cosmochimica Acta, v. 72, no. 1, p. 19-35.

Poole, J. K., Aggarwal, N., Sinange, R., Nganga, S., Broten, M., and Douglas-Hamilton, I., 1992, The Status of Kenya's Elephants: Kenya Wildlife Service Department of Resource Surveys and Remote Sensing Report, 114 p.

Rountrey, A. N., Fisher, D. C., Tikhonov, A. N., Kosintsev, P. A., Lazarev, P. A., Boeskorov, G., and Buigues, B., 2012, Early tooth development, gestation, and season of birth in mammoths: Quaternary International, v. 255, p. 196-205.

Rountrey, A. N., Fisher, D. C., Vartanyan, S., and Fox, D. L., 2007, Carbon and nitrogen isotope analyses of a juvenile woolly mammoth tusk: Evidence of weaning: Quaternary International, v. 169, p. 166-173.

Sakae, T., Mishima, H., and Kozawa, Y., 1988, Changes in bovine dentin mineral with sodium hypochlorite treatment: Journal of Dental Research, v. 67, no. 9, p. 1229-1233.

Secord, R., Bloch, J. I., Chester, S. G. B., Boyer, D. M., Wood, A. R., Wing, S. L., Kraus, M. J., McInerney, F. A., and Krigbaum, J., 2012, Evolution of the earliest horses driven by climate change in the Paleocene-Eocene thermal maximum: Science, v. 335, no. 6071, p. 959-962.

Sikes, S. K., 1971, The Natural History of the African Elephant, Cambridge Univ Press. 397 p.

Tieszen, L., and Fagre, T., 1993, Effect of diet quality and composition on the isotopic composition of respiratory CO2, bone collagen, bioapatite, and soft tissues, *in* Lambert, J. B., and Grupe, G., eds., Prehistoric Human Bone: Archaeology at the Molecular Level: New York, Springer-Verlag, p. 121-155.

Tieszen, L. L., Boutton, T. W., Tesdahl, K., and Slade, N. A., 1983, Fractionation and turnover of stable carbon isotopes in animal tissues: Implications for $\delta^{13}C$ analysis of diet: Oecologia, v. 57, no. 1, p. 32-37.

Tieszen, L. L., Senyimba, M. M., Imbamba, S. K., and Troughton, J. H., 1979, The distribution of C3 and C4 grasses and carbon isotope discrimination along an altitudinal and moisture gradient in Kenya: Oecologia, v. 37, no. 3, p. 337-350.

West, A. G., Ayliffe, L. K., Cerling, T. E., Robinson, T. F., Karren, B., Dearing, M. D., and Ehleringer, J. R., 2004, Short-term diet changes revealed using stable carbon isotopes in horse tail-hair: Functional Ecology, v. 18, no. 4, p. 616-624.

Williams, R. A. D., and Elliott, J. C., 1979, Basic and Applied Dental Biochemistry, Edinburgh, Churchill Livingstone, 311 p.

Wittemyer, G., 2001, The elephant population of Samburu and Buffalo Springs National Reserves, Kenya: African Journal of Ecology, v. 39, no. 4, p. 357-365.

Wittemyer, G., Cerling, T. E., and Douglas-Hamilton, I., 2009, Establishing chronologies from isotopic profiles in serially collected animal tissues: An example using tail hairs from African elephants: Chemical Geology, v. 267, no. 1-2, p. 3-11.

Wittemyer, G., Getz, W., Vollrath, F., and Douglas-Hamilton, I., 2007, Social dominance, seasonal movements, and spatial segregation in African elephants: A contribution to conservation behavior: Behavioral Ecology and Sociobiology, v. 61, no. 12, p. 1919-1931.

Wittemyer, G., and Getz, W. M., 2007, Hierarchical dominance structure and social organization in African elephants, *Loxodonta africana*: Animal Behaviour, v. 73, no. 4, p. 671-681.

Wittemyer, G., Polansky, L., Douglas-Hamilton, I., and Getz, W. M., 2008, Disentangling the effects of forage, social rank, and risk on movement autocorrelation of elephants using Fourier and wavelet analyses: Proceedings of the National Academy of Sciences, v. 105, no. 49, p. 19108-19113.

Zazzo, A., Bocherens, H., Brunet, M., Beauvilain, A., Billiou, D., Mackaye, H. T., Vignaud, P., and Mariotti, A., 2000, Herbivore paleodiet and paleoenvironmental changes in Chad during the Pliocene using stable isotope ratios of tooth enamel carbonate: Paleobiology, v. 26, no. 2, p. 294-309.

Table 4.1. Tail hair lengths and growth rates based on visual matching of isotope profiles

Tail hair Sample ID	Sample Date	Length (mm)	Growth rate (mm/day)		days/sample[a]	Time in hair[a]	
			VM	Tuned	avg ± sd	days	years
R37-010125	25-Jan-01	310	0.69 ± 0.03	0.61 ± 0.03	8.2 ± 0.4	508	1.39
R37-020204	4-Feb-02	330	0.63 ± 0.03	0.60 ± 0.03	7.9 ± 0.4	524	1.43
R37-021101	1-Nov-02	235	0.59 ± 0.03	0.62 ± 0.03	8.1± 0.4	379	1.04
R37-060617	17-Jun-06	320	0.60 ± 0.03	0.60 ± 0.03	8.3± 0.4	533	1.46
R37-060627	27-Sep-06	290	0.55 ± 0.03	0.55 ± 0.03	9.1± 0.5	527	1.44

Note: VM is visual matching. a) Calculated from tuned growth rates

Table 4.2. Growth rates, sample thickness, and time represented in sampled interval of ivory slabs.

Sample ID	No. of samples	sample width avg ± sd (μm)	dist. milled (μm)	Radial growth rate (um/day)				days/sample[b] avg ± sd	Time in milled[b] ivory slab (yrs)
				VM	INC[a]	^{14}C	Tuned		
R37-DEN-412	249	102 ± 24	25400	14.0	15.4 ± 4.7	—	14.3	7.1 ± 1.7	4.9
R37-DEN-1053	225	100 ± 23	22470	15.2	14.7 ± 4.1	14.9 ± 0.6	14.6	6.9 ± 1.6	4.2
R37-DEN-1169	150	91 ± 12	14457	13.4	12.8 ± 3.6	—	13.3	6.8 ± 0.9	3.0

Note: VM and INC are visual matching and 2nd-order growth increments. VM and ^{14}C growth rates are linear. a) INC growth rate was calculated only from increments in the sampled interval. Growth rate data for the entire slab is shown in Figure 4.5 b) Calculated from tuned growth rates.

Table 4.3. Descriptive statistics from ivory and hair profiles

Profile		(‰) $\delta^{13}C^{a}$	$\delta^{18}O^{a}$	$\delta^{15}N^{b}$	$\delta^{13}C_{diet}{}^{c}$	$\%C_4{}^{d}$
Ivory (412)	min.	-13.1	-7.1	—	-26.7	5.0
(n = 241)	max.	-8.9	-2.1	—	-22.5	35.1
	range	4.2	5.0	—	4.2	30.1
	avg.	-11.8	-4.7	—	-25.4	14.5
	sd	0.9	0.8	—	0.9	6.2
Ivory (1169 & 1053)	min.	-12.9	-6.6	—	-26.5	6.6
(n = 331)	max.	-8.4	-1.2	—	-22.0	38.5
	range	4.5	5.4	—	4.5	32.0
	avg.	-11.2	-3.9	—	-24.8	18.5
	sd	0.8	0.9	—	0.8	6.0
Hair	min.	-23.0	—	8.1	-26.1	9.6
(n = 203)	max.	-17.9	—	14.2	-21.0	45.6
	range	5.0	—	6.1	5.0	36.0
	avg.	-21.4	—	11.0	-24.5	20.5
	sd	0.9	—	1.1	0.9	6.3
					$\delta^{13}C_{diet}{}^{d,e}$	$\%C_4{}^{d,e}$
Hair (RPV)	min.	—	—	—	-27.4	0.0
(n = 203)	max.	—	—	—	-17.9	67.7
	range	—	—	—	9.5	67.7
	avg.	—	—	—	-24.5	21.0
	sd	—	—	—	1.5	10.8

a) vs.VPDB; b) vs. AIR; c) diet calculations based on $\varepsilon_{diet\text{-}apatite}$ and $\varepsilon_{diet\text{-}keratin}$ of +13.6 and +3.1, respectively; d) %C4 calculations based on end-member values for C3 and C4 plants given in text; e) diet calculated using the RPV model from Cerling et al. (2007).

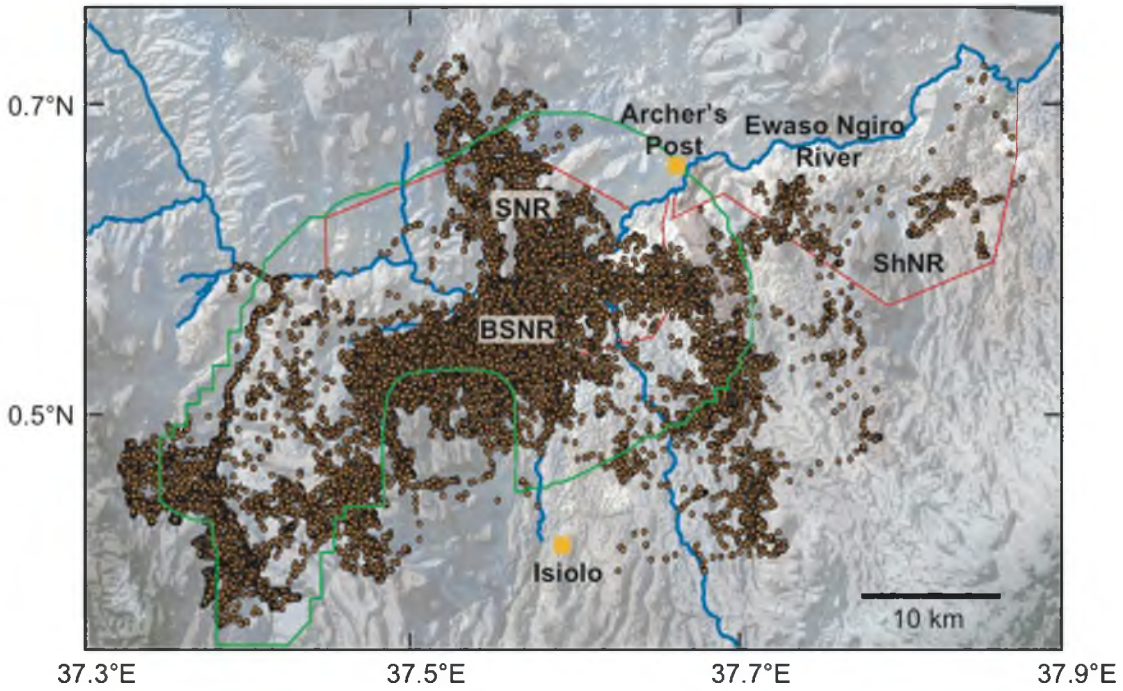

Figure 4.1: Schematic map of area occupied by R37. Dots indicate hourly locations of R37 between 2001 and 2006. NDVI data come from the area within the green polygon. SNR= Samburu National Reserve; BSNR= Buffalo Springs National Reserve; ShNR= Shaba National Reserve. The border between SNR and BSNR is the Ewaso Ngiro River.

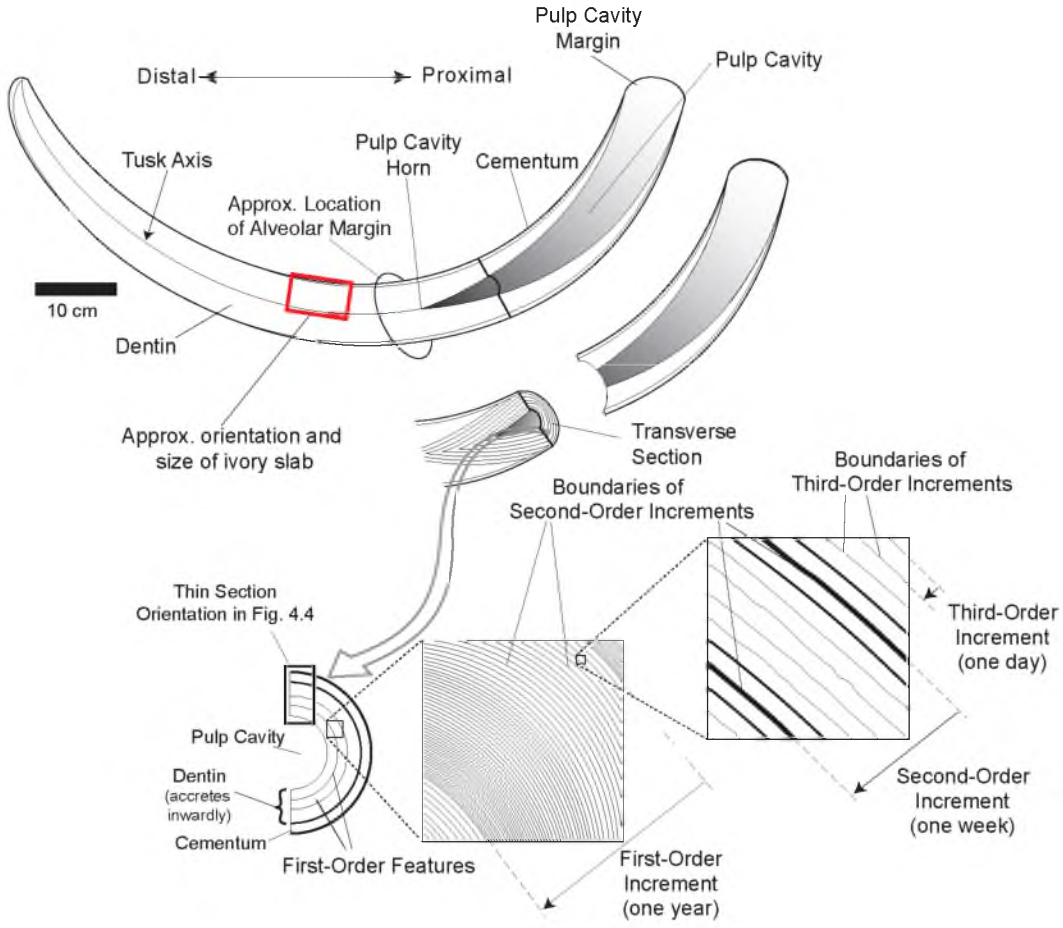

Figure 4.2. Schematic illustrating structural features and periodic growth increments in a tusk. Upper: longitudinally-cut elephant tusk showing structural features and approximate size and orientation of ivory slabs (red outline); Lower: transverse view illustrating first-, second-, and third-order growth increments. Modified from (Fisher and Fox, 2007)

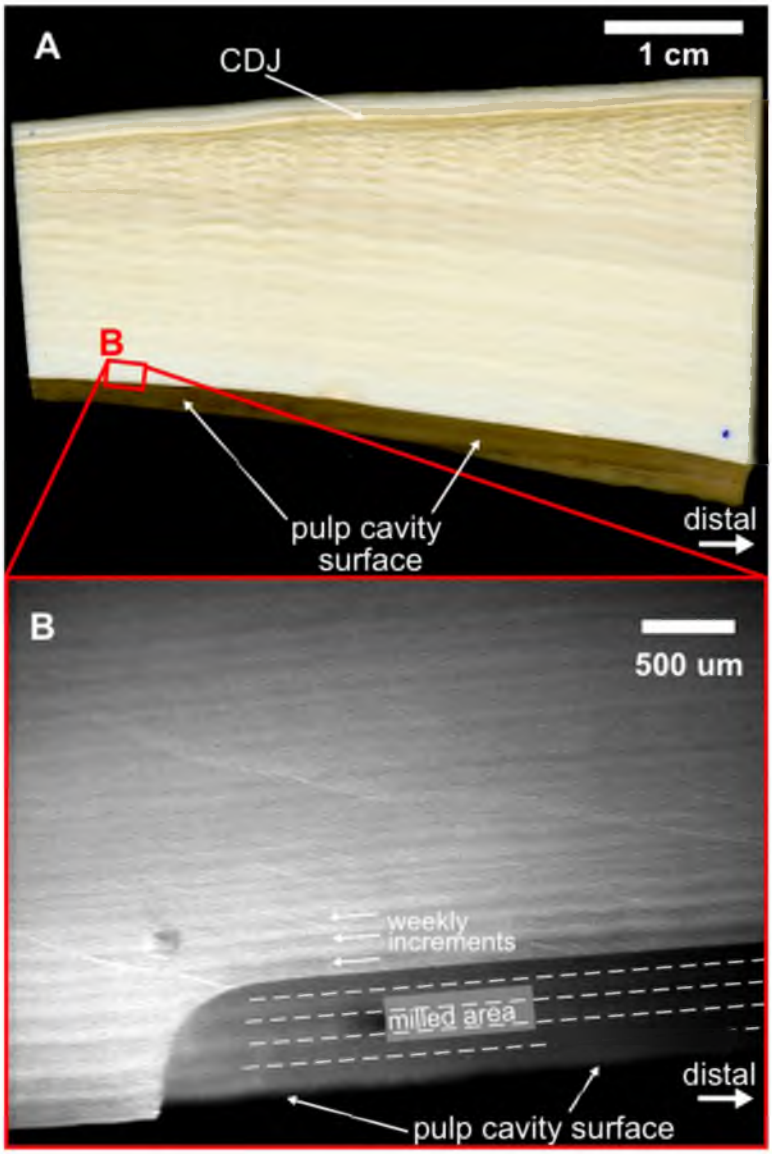

Figure 4.3. A) Color photograph of the polished longitudinal surface of ivory slab 1169 prior to serial sampling. B) Photomicrograph of the polished longitudinal surface of slab 1169 under reflected light at 40x magnification. Five samples have been milled to a depth of 1000 μm and ~100 μm thickness each, and boundaries are shown with dashed white lines. Approximately weekly increments are indicated by white arrows on the polished ivory surface.

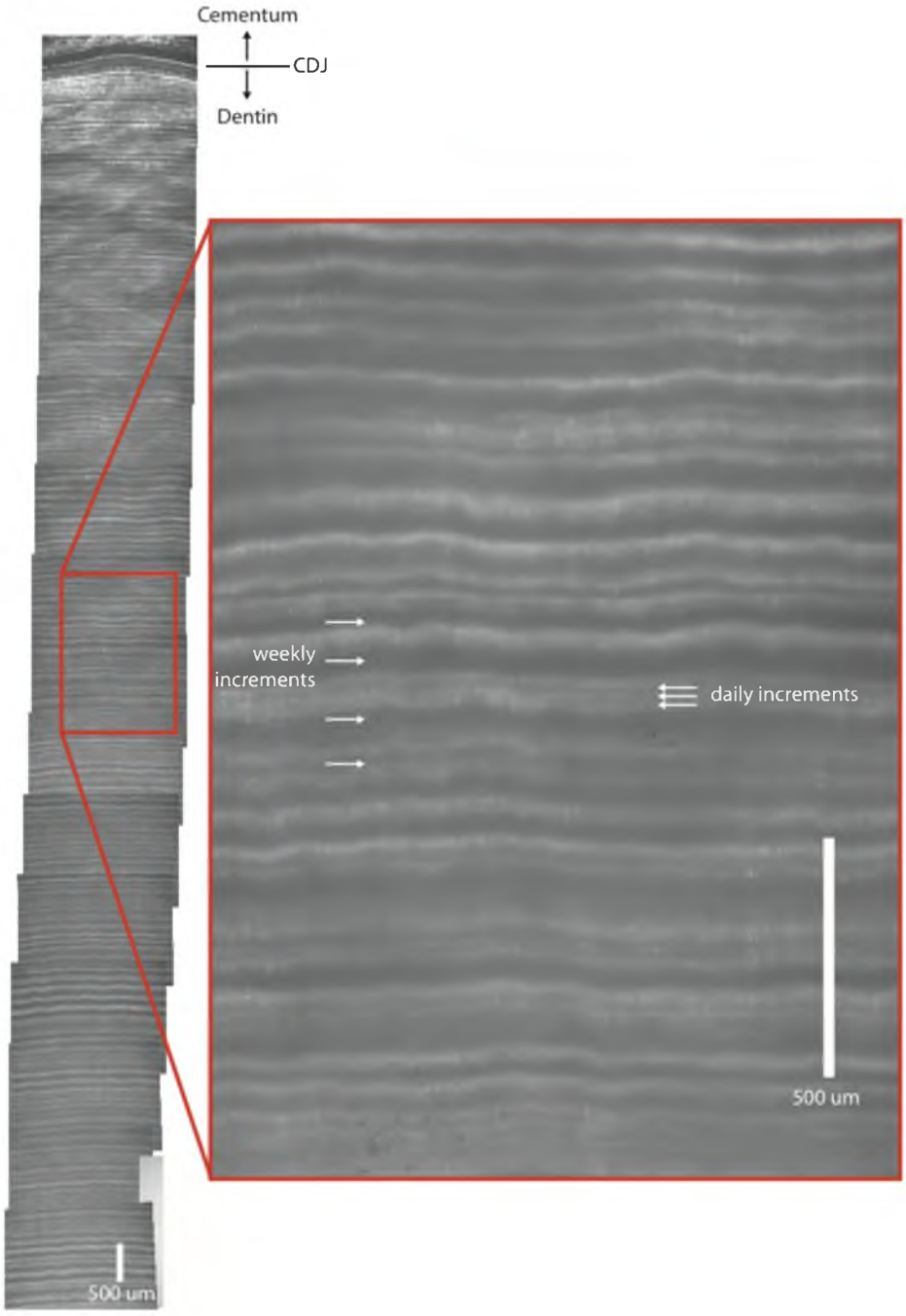

Figure 4.4. Left: Mosaic of stitched photomicrographs from a thin section of sample1169 at 35x magnification under transmitted plain polarized light. Right: inset of composite thin section. Approximately weekly (second-order) and daily (third-order) increments are shown with arrows.

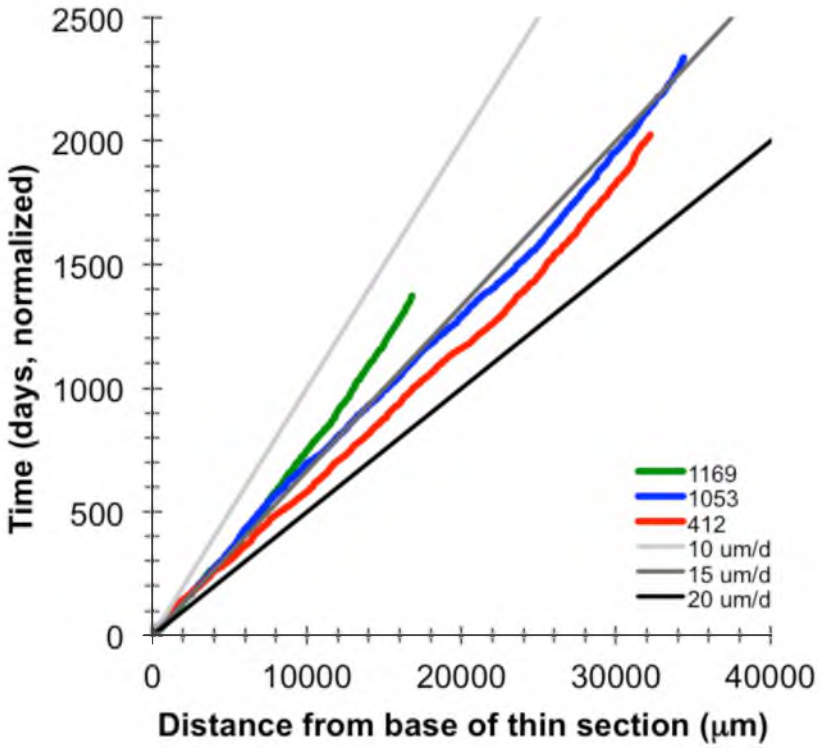

Figure 4.5. Tusk growth rates calculated from second-order growth increment thicknesses for three ivory slabs. Three modeled linear growth rates (10, 15, and 20 μm/day) are plotted as a reference.

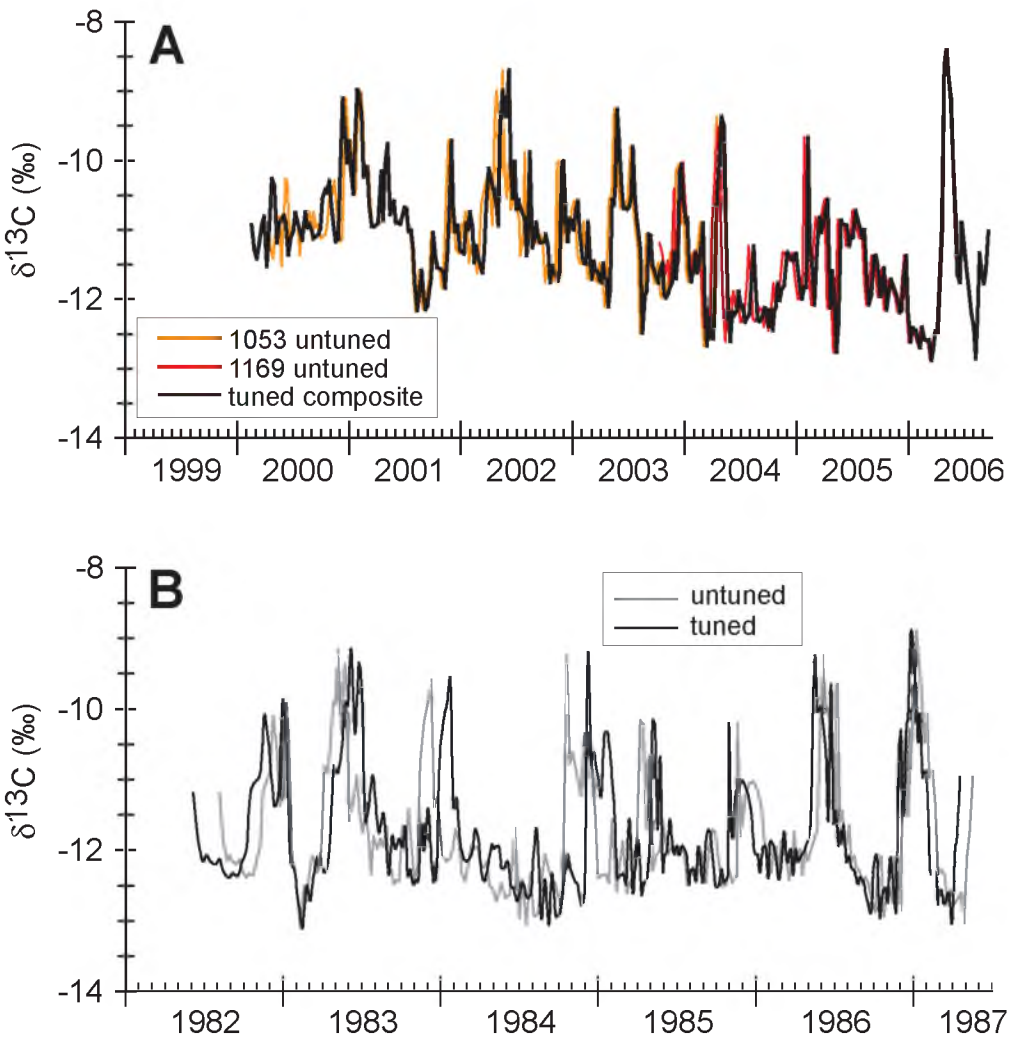

Figure 4.6. Tuned vs. untuned $\delta^{13}C$ values for ivory slabs A) 1169 and 1053 and B) 412. Tuned data from A) are a composite record from 1169 and 1053 based on 0.7 years overlap.

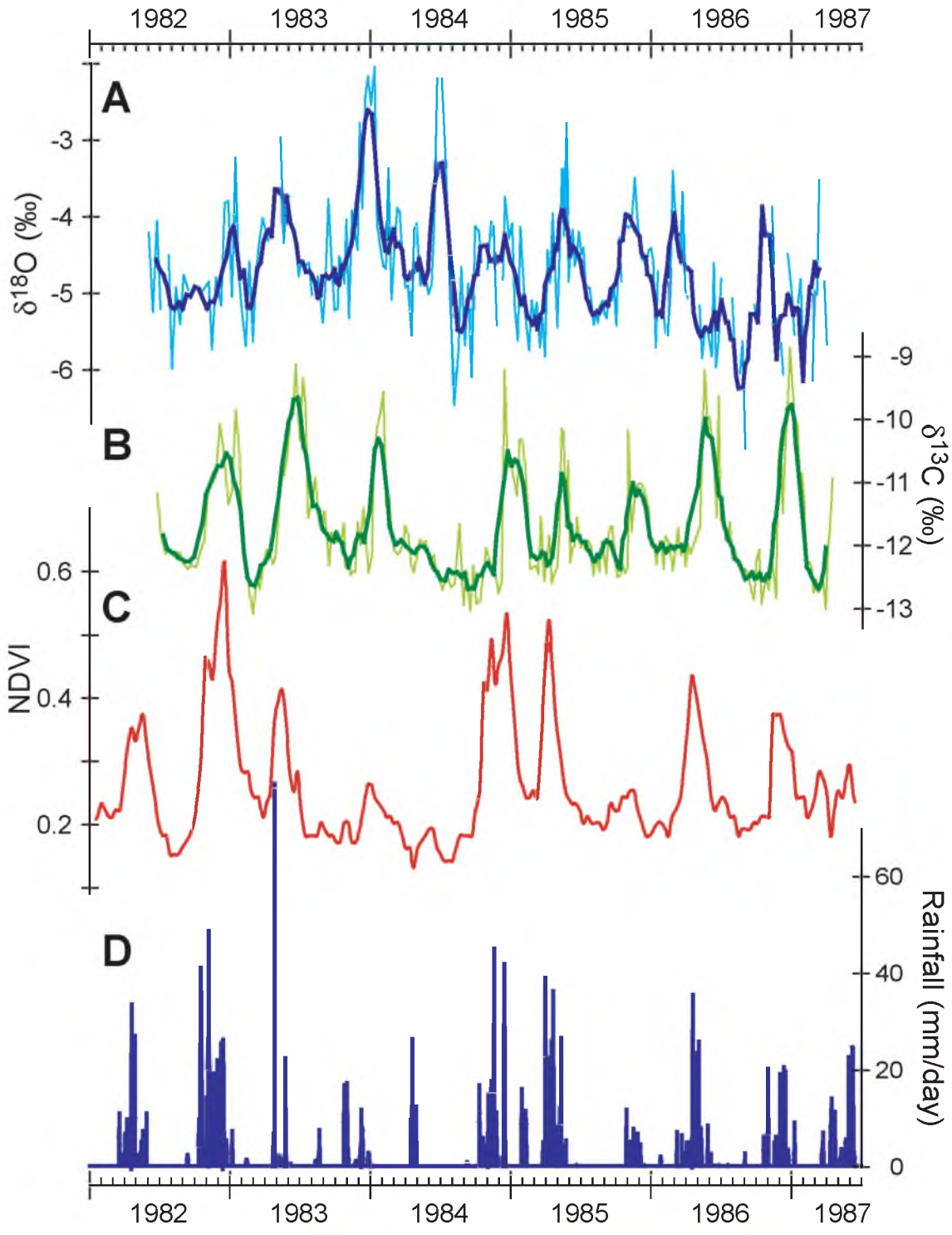

Figure 4.7. Stacked rainfall, NDVI, $\delta^{13}C$, and $\delta^{18}O$ plots of tuned composite ivory profiles from slab 412. Bold lines in the $\delta^{13}C$ and $\delta^{18}O$ profiles are 5-point running means.

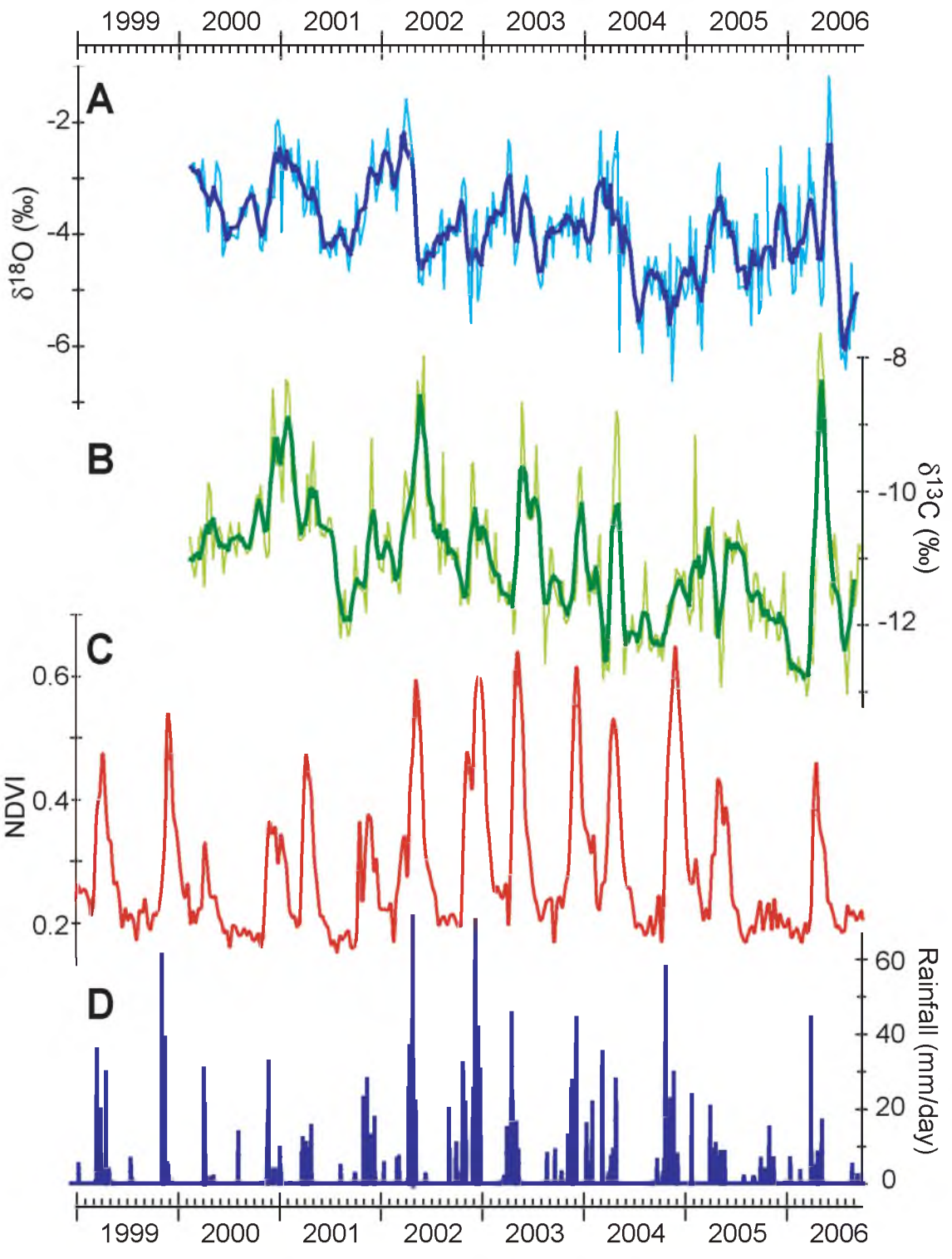

Figure 4.8. Stacked rainfall, NDVI, $\delta^{13}C$, and $\delta^{18}O$ plots of tuned composite ivory profiles from slabs 1169 and 1053. Bold lines in the $\delta^{13}C$ and $\delta^{18}O$ profiles are 5-point running means.

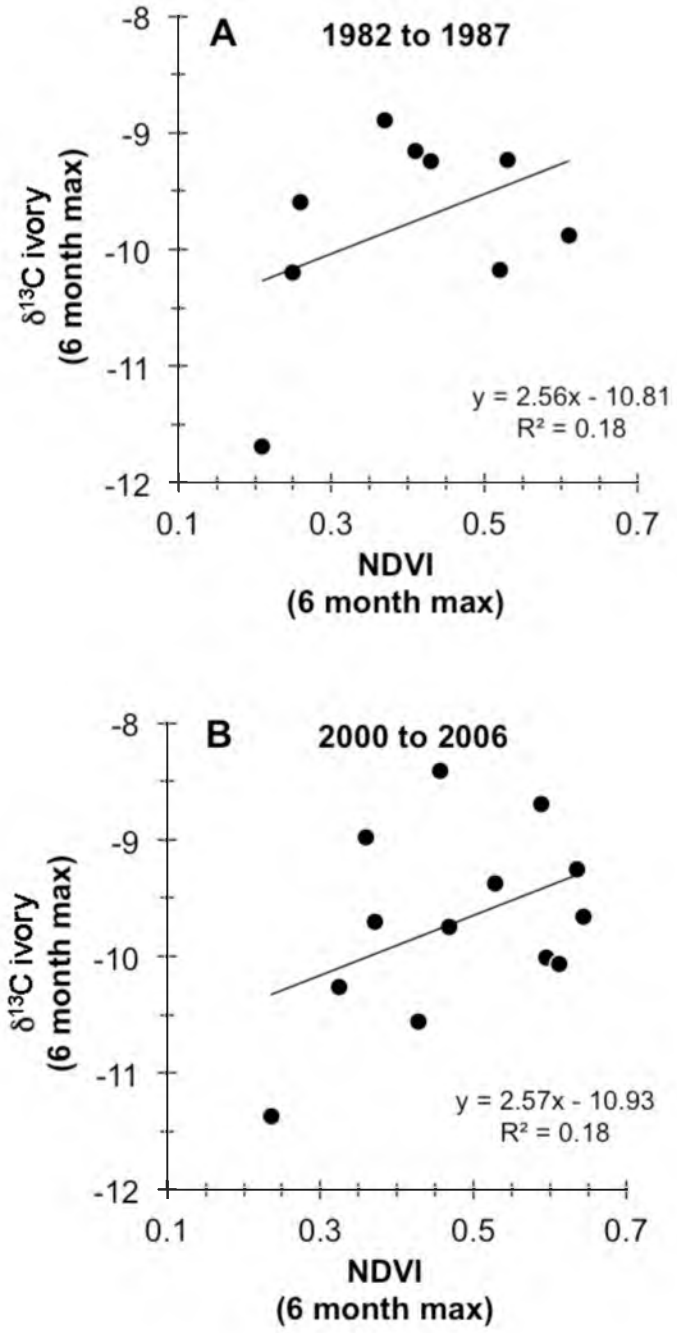

Figure 4.9. 6 month maximum NDVI vs. $\delta^{13}C_{ivory}$ profiles from A) 1982 to 1987 and B) 2000-2006. 6-month intervals are from March 1 to September 1 and from September 1 to March 1, which bracket the two wet seasons.

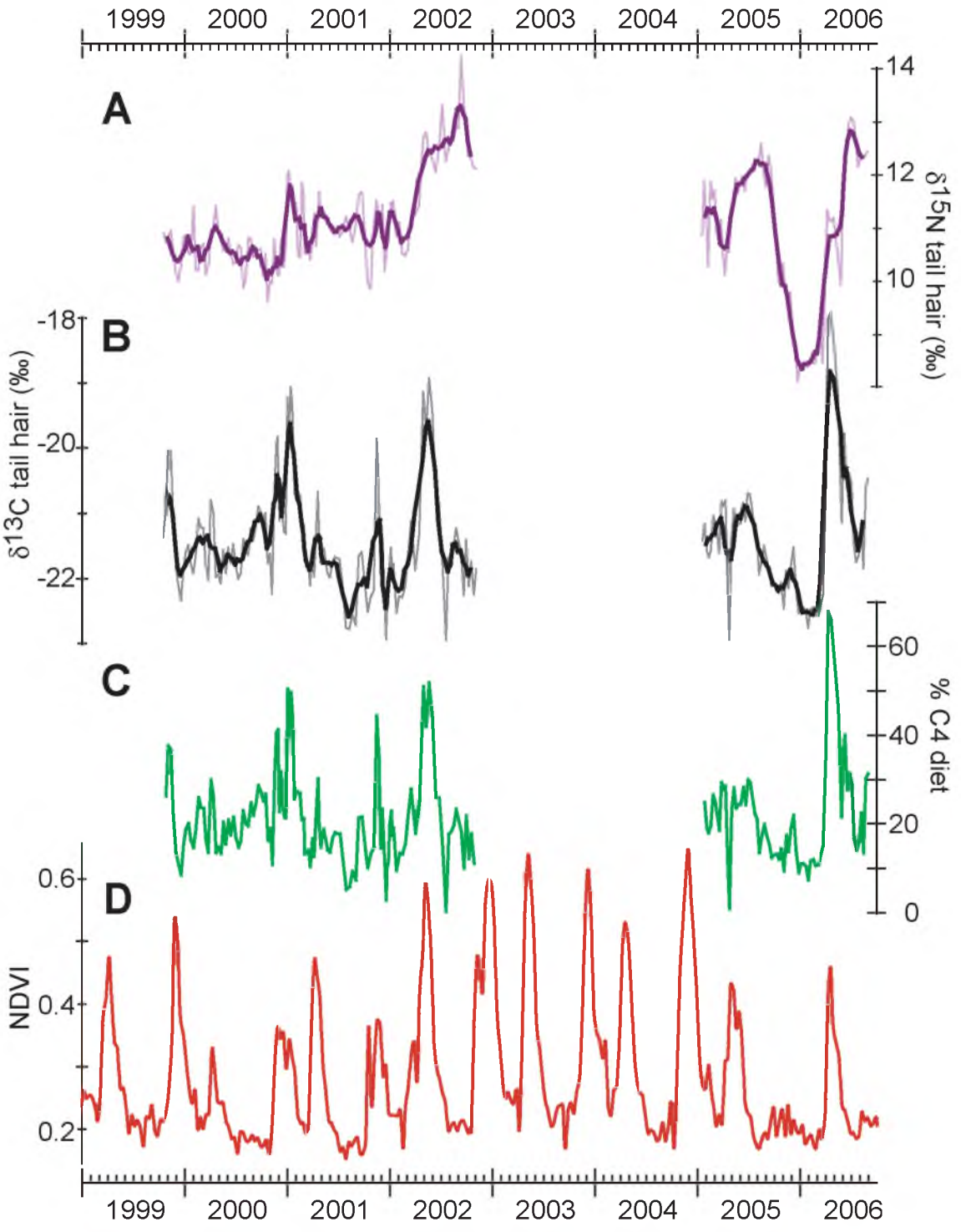

Figure 4.10. Tail hair isotope and diet profiles. A) and B) are $\delta^{15}N$ and $\delta^{13}C$ values of tuned composite tail hair profiles, respectively. Bold lines in A) and B) are 5-point running means. C) Calculated $\%C_4$ in diet using the RPV model (Cerling et al., 2007); D) is NDVI.

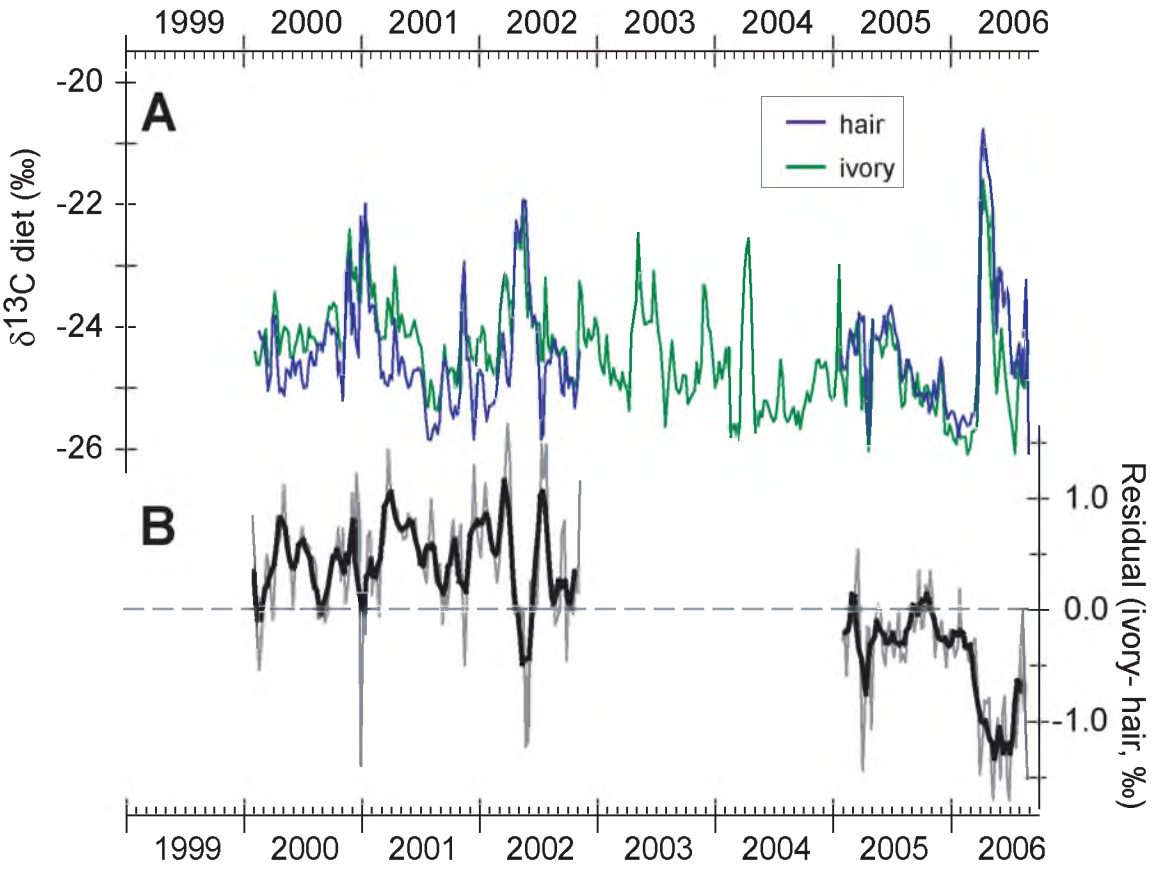

Figure 4.11. A) The $\delta^{13}C_{diet}$ calculated from ivory (green line) and hair (blue line) using enrichment factors of + 13.6 ‰ and + 3.1 ‰ for diet-apatite and diet-keratin, respectively. B) Residual plot of $\delta^{13}C_{diet(ivory)} - \delta^{13}C_{diet\ (hair)}$. Bold line is 5-point running mean.

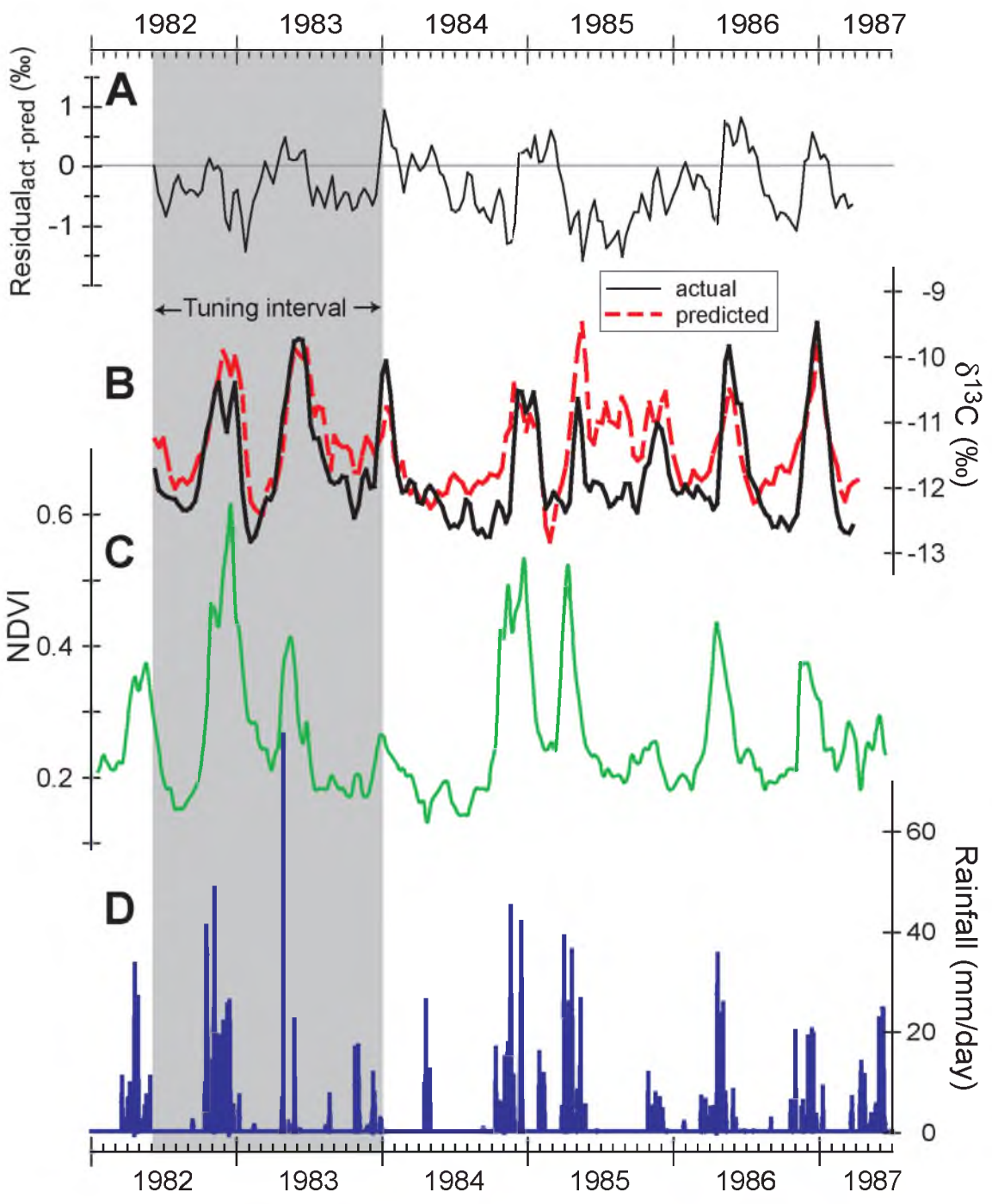

Figure 4.12. Matching filter results for predicted $\delta^{13}C$ based on NDVI data compared to actual $\delta^{13}C_{ivory}$ data from 1982 to 1987. A) Residual between actual and predicted $\delta^{13}C$, B) actual (black) vs. predicted (red dashed) $\delta^{13}C$, C) NDVI that served as matching filter input, and D) rainfall. The shaded box represents the 600-day tuning interval.

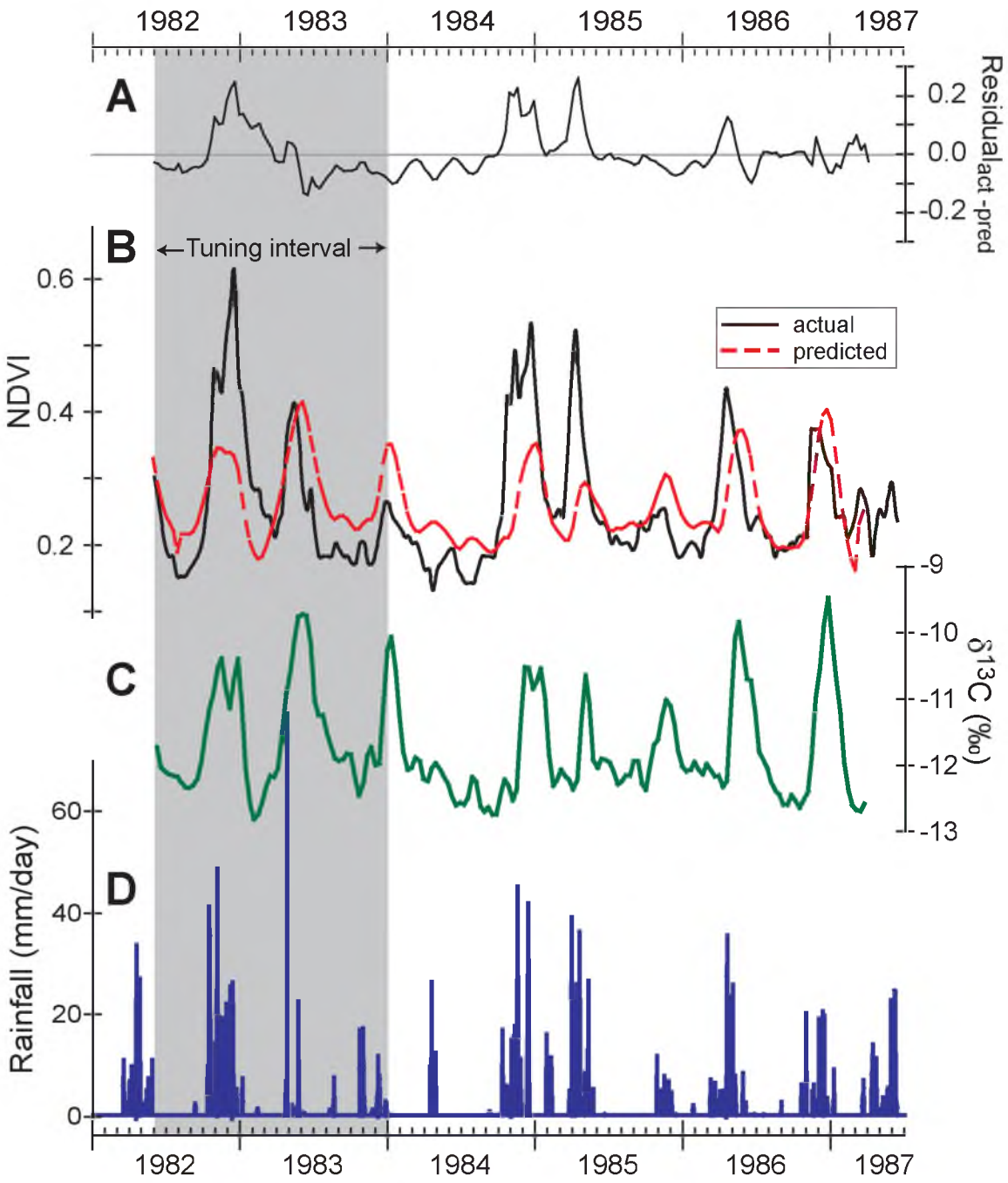

Figure 4.13. Matching filter results for predicted NDVI based on $\delta^{13}C$ data compared to actual NDVI data from 1982 to 1987. A) Residual between actual and predicted NDVI , B) actual (black) vs. predicted (red dashed) NDVI, C) $\delta^{13}C$ that served as matching filter input, and D) rainfall. The shaded box represents the 600-day tuning interval.

CHAPTER 5

FORWARD AND INVERSE METHODS FOR EXTRACTING CLIMATE AND DIET INFORMATION FROM STABLE ISOTOPE PROFILES IN PROBOSCIDEAN MOLARS

5.1 Abstract

Intratooth stable isotope profiles in enamel provide a time series of dietary and environmental information that if correctly interpreted, serve as archives of seasonal variability in past environments. The challenge in interpreting these profiles correctly is due to time averaging imparted by enamel mineralization and developmental geometry, whereby the primary ($\delta^{13}C$ or $\delta^{18}O$) input signal is attenuated and shifted, which can potentially lead to incorrect interpretations of the magnitude or frequency of seasonal variability. Existing forward and inverse models were developed to reconstruct the primary input signal from intratooth profiles in continuously growing teeth. Here the models are extended to molar plates of *Loxodonta*, *Elephas*, and *Mammuthus* (LEM) clade proboscideans, which grow over a long but finite interval of time. Proboscidean molars are particularly attractive for intratooth profiles because they may contain up to a decade or more of information and they are often well preserved in the fossil records because of their thick enamel and large size.

Forward model parameters are established using histological analysis of molar thin sections of extant elephants (*Loxodonta africana*) and a mammoth (*Mammuthus columbi*) and micro-CT analysis of elephant molar plates. The density of immature enamel is about 65 % of the final density of mature enamel. The appositional length varies from approximately 35 to 55 mm, and the maturation length is about 70 mm. Histological methods are used to determine crown formation time (CFT) in elephant and mammoth molar plates. CFT for the elephant and mammoth molar plates studied in thin section are about 5 to 6 years and 11 years, which translate to mean growth rates of about 21 mm/year and 16 mm/year, respectively. The growth rate for elephant plates appears to be linear, whereas the longer-forming mammoth plates follow a logarithmic growth curve.

Coeval molar and tusk profiles from a zoo elephant are compared. The tusk isotope profile serves as a proxy for the primary input signal, and thus provides an opportunity to evaluate the forward and inverse models. The results from the zoo elephant profiles demonstrate that the inverse model accurately reconstructs the amplitude and overall structure of the primary input signal. Inverse results from two mammoth molar profiles are presented, one of which reveals more than double the range in $\delta^{13}C$ of diet than the model input from the enamel profile. Inversion model results illustrate that improved reconstruction of the primary input signal can lead to more accurate interpretations of the seasonal variability of diet and body water and by extension, vegetation and precipitation in past environments.

5.2 Introduction

Carbon and oxygen stable isotope ratios in mammalian herbivore teeth record information about an organism's diet, life history, and physiology, as well as the climate in which it lived. A tooth sampled serially along its growth axis provides a stable isotope profile that serves as an isotopic time-series over the period in which it formed, as was first shown in dentin by Koch et al. (1989) and in enamel by Fricke and O'Neil (1996). Since these pioneering studies on intratooth stable isotope profiles, numerous other studies have employed this method to study a wide variety of aspects of seasonality in herbivore ecology that include seasonal diet change (Metcalfe et al., 2011), migration patterns (Koch et al., 1998), prehistoric herding strategies (Balasse et al., 2002), and seasons of birth (Balasse et al., 2003; Frémondeau et al., 2012) and death (e.g., Koch et al., 1989). Oxygen isotope profiles in tooth enamel have been used to investigate changes in seasonality of climate (Fricke et al., 1998; Koch et al., 1989) and changes in paleoelevation over tectonic timescales (Dettman et al., 2001; Kohn et al., 2002).

With the exception of a handful of studies on late Pleistocene proboscidean tusks and molar dentin (e.g., Koch et al., 1989; Rountrey et al., 2012; Rountrey et al., 2007), nearly all intratooth isotope profiles come from fossil enamel rather than dentin due to the resistance of the former and susceptibility of the latter to diagenetic alteration of the primary isotope signature (Lee-Thorp and dan der Merwe, 1987; Schoeninger and DeNiro, 1982; Wang and Cerling, 1994). Enamel apatite is less susceptible to diagenesis due to its larger crystal size and its lower organic content (<1%) compared to dentin (~20%). Although enamel is generally the only fossil material suitable for stable isotope analysis, there is a significant drawback to choosing it over tooth dentin for generating

isotope profiles. The prolonged enamel maturation phase and the sampling geometry both lead to attenuation and shifting of the primary input signal recorded in the tooth (Balasse, 2003; Passey and Cerling, 2002).

Enamel formation can broadly be described as occurring in two phases, secretion and maturation, and it proceeds from the apex toward the cervix of the tooth crown (e.g., Hiller et al., 1975; Moss-Salentijn et al., 1997; Suga, 1982). New enamel is deposited on the appositional surface, which is oriented at a low oblique angle to the enamel dentin junction (EDJ). The length of the appositional surface, or appositional length (l_a), is relatively constant in teeth such as hippo canines and rodent incisors, but histological and radiographic data indicate variable l_a in caprine (Zazzo et al., 2010; Zazzo et al., 2012), bovine (Balasse, 2002; Zazzo et al., 2005), and equine (Hoppe et al., 2004) molars. The addition of each new enamel layer to a developing tooth can be viewed as occurring in a discrete time interval during the secretory phase of enamel formation. In this phase, apatite crystallites are seeded in an organic-rich matrix. As a result, initial enamel density is only a fraction of its final density (e.g., Passey and Cerling, 2002). The organic matter and water are required during matrix deposition and maturation of enamel. Ameloblast cells and the protein amelogenin facilitate mineralization of hydroxylapatite and body water provides essential ions (Ca^{2+}, PO_4^{3-}, OH^-, and CO_3^{2-}) in solution. During the maturation phase, enamel becomes progressively denser as organic material and body water are replaced with apatite. The maturation process leads to damping of the primary isotopic input signal recorded during the secretory phase as successive incremental addition of carbon and oxygen (as carbonate ions) occurs throughout the maturation phase.

Sampling also leads to attenuation and temporal shifting in isotope profiles. The conventional sampling method involves drilling a ~1mm wide path normal to the growth axis of the tooth. The more deeply the drilling path penetrates the enamel, the more time averaging there is as more layers of enamel (e.g., time slices) are integrated into the sample. Thus, the main challenge of generating isotope profiles and interpreting the data is that the combined effects of maturation and sampling geometry can attenuate and shift the primary input signal so that the true magnitude of the isotopic variation and the shape of the curve can give misleading patterns of variability and seasonality (Passey and Cerling, 2002; Passey and Cerling, 2004; Zazzo et al., 2005).

Changes to sampling protocol (e.g., size, geometry, and location) and mathematical modeling are the two main approaches that have been developed in an effort to reconstruct the primary isotopic input signal from measured profile data. The first approach, modification of sampling geometry, principally addresses the time-averaging effects due to sampling. Zazzo et al. (2005) present modeled results from bovine enamel using the forward model of Passey and Cerling (2002) where conventional sampling, sampling parallel to the appositional surface, and sampling the innermost enamel layer are explored. An important result of the modeling was that conventional sampling could produce a sinusoidal profile from nonsinusoidal inputs (Figure 7b of Zazzo et al., 2005), which in fossil teeth would lead to incorrect interpretations of seasonality in past environments. Passey and Cerling (Figure 6, 2002) show that varying drilling depth using conventional sampling geometry induces temporal shift, but has no effect on isotopic variation.

Several studies have proposed sampling the innermost (10 to 20 μm) enamel (Balasse, 2003; Metcalfe et al., 2011; Tafforeau et al., 2007; Zazzo et al., 2005) because the initial enamel density as a proportion of the density of fully mature enamel is thought to be higher at the EDJ than in the rest of the enamel (Suga, 1989; Tafforeau et al., 2007)). Given the extremely narrow width of this enamel, the method presents limited options for sampling and analysis. Zazzo et al. (2005) demonstrate that isotope profiles can be micromilled at ~20 μm thicknesses from the outer enamel surface to the EDJ, but the overall precision (± 100 μm) in drill bit location is five to ten times lower than the desired sample interval. This means there is a high probability that the micromilling method would result in either incorporating adjacent dentin (i.e., over drilling) or not completely drilling through the entire layer of inner enamel (i.e., under drilling). An alternative method for targeting the innermost enamel is to drill from the underside of the enamel (Metcalfe et al., 2011), but this is a particularly invasive method that requires completely separating enamel from dentin at the EDJ, which may be quite labor intensive (or unfeasible) for many types of teeth.

Another option for obtaining stable isotope profiles from the inner enamel layer is secondary ion mass spectrometry (SIMS). SIMS can achieve the spatial resolution required (< 20 μm), but the number of SIMS instruments available represents only a small fraction of the isotope ratio mass spectrometers (IRMS) available, and thus is currently time and cost prohibitive. SIMS also requires a polished cross section of the enamel, and this may not be feasible for all specimens, especially those belonging to museum collections.

Another issue that arises when solely targeting the innermost enamel is that the initial density of the immature enamel must be determined for accurate interpretation of profile data. To date, the only method capable of measuring density at this scale is X-ray synchrotron microtomography (Tafforeau et al., 2007). Accessibility to X-ray synchrotron microtomography facilities is very limited and can be cost prohibitive.

The second approach to recovering the primary carbon or oxygen input signal is through the development of forward and inverse models that consider how stable isotopes are incorporated into developing enamel. Passey and Cerling (2002) proposed a forward model that accounts for the maturation period, geometry of enamel formation, and sampling depth. The main parameters input into the model are initial density as a fraction of the final enamel density (f_i), the length of apposition (l_a), maturation length (l_m), sampling length (Δx), and sampling depth (Δz) (Figure 5.1). The two length parameters (l_m and l_a) are treated as constant, as the model was developed for continuously growing teeth. Using the forward model equations developed in Passey and Cerling (2002) as an operator term **A**, Passey et al. (2005) developed an inverse model whereby inversion of the linear system $\mathbf{Am} = \mathbf{d}$, where **d** is measured profile data, yields **m**, the estimated primary input signal.

Stable isotope profiles from teeth that form over multiple years provide an opportunity to investigate terrestrial paleoenvironments at unprecedented resolution and can give insight into seasonal variations in diet and climate. Combined use of forward and inverse models is currently the only method that accounts for time averaging from both the enamel mineralization process and sampling. If the input parameters f_i, l_a, and l_m, can be determined, then inversion of the measured data **d** can provide a reliable

estimate of the primary isotopic input signals, which in turn give information about an animal's diet and physiology and about the environment in which it lived. Application of inverse methods to isotope profiles from hypsodont proboscidean molars is an unexplored proxy of seasonality of diet and climate in terrestrial ecosystems throughout the late Neogene. Proboscidean molars are attractive because a single plate (Figure 5.3) may contain up to a decade of information (Dirks et al., 2012), and due to their large size and thick enamel, they are often well preserved in the fossil record.

In this study, forward model parameters (f_i, l_a, and l_m) are determined to describe enamel formation in elephant molars. Parameters f_i and l_m are determined using micro-computed tomography (micro-CT) and l_a is measured on developing plates and in thin sections. Growth rates of individual plates are evaluated using bomb-curve ^{14}C data and histological data from molar thin sections. The forward model is tested by comparing coeval high-resolution tusk and molar isotope profiles. The forward model was developed using an indeterminate tooth (i.e., a hippopotamus canine) as a model for enamel growth and geometry, and it treats l_a and l_m as constant. It also assumes that mineralization proceeds at a constant (linear) rate over the maturation phase. Evaluation of the forward model suggests it works satisfactorily for elephant molar plates. Application of the inversion methods developed by Passey et al. (2005) yield an estimated primary input signal that is similar in amplitude and structure to the known input signal. The inverse model is also applied to isotope profiles from molars of a wild African elephant and two Pleistocene fossil mammoths.

5.3 Background and Materials

Molars and tusks from four extant African elephants and two *Mammuthus columbi* molars were used in the study. For two of the elephants, Misha and R37, tusk and molar material was analyzed. The background and tusk isotope profiles from R37 were presented in Chapter 4. A lower left third molar (m3) from R37 was bomb-curve ^{14}C-dated in Chapter 3. Misha was captured in South Africa at an estimated age of 1 year old in 1982 and later transferred to the Happy Hollow Zoo in San Jose, California. She was transferred again in August of 1983 to Marine World Africa in nearby Redwood Shores, CA and then sometime in 1986 moved once more to Six Flags Discovery Kingdom in Vallejo, CA where she remained for nearly 20 years. On April 22, 2005, Misha made her final move, from California to Utah's Hogle Zoo in Salt Lake City. On September 9, 2009 Misha was euthanized due to rapidly declining health at an age of approximately 27 years old. The Hogle Zoo agreed to loan one tusk and several molars to the University of Utah for study. Data come from Misha's tusk dentin and lower right m3, although additional molars (lower left m3) and additional loose plates that were not able to be assigned to specific molars were also loaned for study.

Other molars come from elephants that lived in and around Tsavo National Park (TNP) and Samburu National Reserve (SNR), Kenya. For the individual from TNP, TE-95, there are two molars, a lower right m2 (or possibly an m1) and a lower right m3 (or possibly an m2). Based on the molar size, I presume TE-95 was a male. Bomb-curve ^{14}C dating of the m3 indicates 1964 as the year of death (Chapter 3). The molar from the SNR elephant is K07-M53.95A (hereafter K07-M53), which is an unerupted lower m1

(or possibly m2) that was removed from the mandibular crypt. 2006 is the estimated year of death of K07-M53.

Each molar or tusk from the four different elephants possesses unique attributes that contribute to the study. As discussed in Chapter 4 (Section 4.3.1), extensive background information on R37 and the ability to work on both the tusk and molar provide an opportunity to compare how diet and climate signals are recorded in the two tissues, tusk dentin and molar enamel. Misha's tusk and molar provide a similar opportunity to compare isotope profiles from the two tissues, but with greater constraint on the isotope ratios in the tissues formed during her time in Utah. A section of her developing molar is used for studying enamel formation. Cutting of Misha's tusk in preparation for various methods of research described below deserves brief mention here, as it varied slightly from the preparation of R37's tusk (Chapter 4, Section 4.3.1).

The left tusk of Misha was selected for study because it was the longer of her tusks (96.2 cm). The tusk was transversely cut at the proximal end during the necropsy, and approximately 5 to 20 cm of the pulp cavity is missing from the proximal end. The tusk was cut longitudinally down the growth axis using a slow-speed (~220 feet per minute) band saw at the University of Michigan under the guidance of Dan Fisher. A second longitudinal cut was made parallel to the first to isolate a 1 cm thick research slice. The research slice was then cut normal to the longitudinal cut but along the tusk axis to separate the upper and lower halves of the tusk. The upper half was cut into nine 8 x 4 x 1 cm slabs and the proximal part of the slab was left intact as a single 17 cm long piece. The lower half of the research slice was left entirely intact.

The molars from TE-95 formed from the mid-1950s to the mid-1960s when the pulse of anthropogenic ^{14}C was produced in the atmosphere, providing an excellent opportunity to determine growth rates using bomb-curve ^{14}C age-dating techniques developed in Chapter 3. The developing molar from K07-M53 is used to study enamel maturation using micro-CT.

Two late Pleistocene mammoth (*Mammuthus columbi*) molars are also used in this study. Specimen LACM-47129 is from the Rancholabrean locality of Costeau Pit in Orange County, CA (Miller, 1971). The fragmentary specimen consists of the three most mesial plates of an unerupted molar. The other specimen, IMNH-40368, is a ~10 cm long fragment of an enamel plate spalled off from the posterior side of a molar plate. The specimen comes from layer "E" at the American Falls fossil site in Idaho, and is also of Rancholabrean age. Based on a K/Ar age date on the overlying Cedar Butte basalt of 72 ± 14 ka, the age of layer E is approximately 125 ka (Pinsof, 1992; Scott et al., 1982).

5.4 Methods

Methods used to determine input parameters for the forward and inverse models include micro-CT, histological analysis of tusk and molar thin sections, bomb-curve ^{14}C-dating, and stable isotope and elemental profiles on molars and tusks (Table 5.1). Here I describe the methods used to prepare samples for and to acquire micro-CT, histological, isotope, and elemental data. Three sampling methods are used to generate stable carbon and oxygen intratooth profiles in order to evaluate which profile best resembles the primary input signal. ^{14}C bomb-curve data are discussed here and the method is described in Chapter 3 (Section 3.3). Stable isotope data from conventionally drilled

profiles are input into forward (Passey et al., 2002) and inverse (Passey et al., 2005) models, which are reviewed in this section.

5.4.1 Micro-CT of molars

Micro-CT was used to determine 1) initial enamel density (f_i) as a function of final enamel density and 2) maturation length (l_m). These parameters are included in both the forward and inverse models. Two developing molars were selected for micro-CT analysis. Misha's lower right m3 (Misha_Rm3) consisted of four plates that were in the incipient stage of being joined together by cementum and a fifth loose plate (Misha_Rm3.5), which was chosen for micro-CT analysis. Photos taken during the necropsy show two pulp cavity tissues posterior to the fifth plate, but they could not be identified with certainty during sample selection. The lower m1 (or m2) from K07-M53 consists of 9 plates, 5 of which were in the incipient stage of being joined together by cementum and four additional loose plates. The posterior loose plate (K07-M53_m1.9) was chosen for micro-CT analysis. This is the most diminutive plate at 6.5 cm in length. Longitudinal sections measuring 5 mm in width were cut from near the center of each molar plate using a Buehler Isomet® slow speed saw. For Misha_Rm3.5, the section ran the full length of the tooth (~10 cm). Dentin was cut away in some places, but at least some dentin and the full thickness of enamel were present in the prepared section. The molar plate section was then cut into thirds, with each piece ranging from 3 to 4 cm in length. The molar section from K07-M53_m1.9 was cut from the lower ~3.8 cm of the plate.

Micro-CT scans were done near the top and bottom of the K07-M53_m1.9 section, and at the top and bottom of each of the three pieces of the Misha_Rm3.5 molar

section, for a total of eight scans. A piece of elephant tusk dentin and an isolated fragment of mature elephant molar enamel were also scanned to develop a calibration curve used to convert grayscale values to absolute densities. Densities of the enamel chip, tusk dentin fragment, and a marble of known density were determined using a pycnometer.

All scans were done on an Xradia® Micro XCT-400 at 60kV/10W and 4x magnification. The instrument and analytical method are described in detail in Hsieh (2012). Scan volumes were 5 mm^3 with resolution of 5.05 μm/voxel, resulting in ~1000 stacks per scan. Unsigned 16-bit (U16) data files (~2GB) were reduced to unsigned 8-bit (U8) files (~1GB) using the software program MIPAV in order to facilitate data processing. During conversion from U16 to U8 files, the maximum U16 grayscale value was set at 255 on the U8 grayscale (0 to 255).

Stacks were analyzed in ImageJ (version 10.2) by taking a series of linear grayscale profiles normal to the EDJ using a 10 to 25 pixel-width line. Within each 5 mm^3 scan volume, profiles were taken in two to five stacks across the entire thickness of the dentin and enamel. Profiles were smoothed with a 10-point running mean and converted from grayscale to percent of maximum enamel density based on the density calibration data.

5.4.2. Histological sample preparation and analysis

5.4.2.1 Molar thin sections and flatbed scans. Thin sections were made from Misha molar plate Misha_Rm3.5, TE-95 m3 molar plate 7 (TE-95_Rm3.7), and the isolated enamel plate from the American Falls mammoth (IMNH-40368). Thin section

preparation was similar to that of the tusk dentin (Section 4.4.1, Chapter 4). Briefly, plates were cut longitudinally on a Buehler Isomet® slow speed saw to a thickness of several millimeters. Due to their length (~10 cm), plates were cut transversely into smaller pieces to fit onto oversized or standard petrographic slides. Misha_Rm3.5 was already cut into three pieces for micro-CT analysis (a, b, and c; Figure 5.4), and TE-95_rm3.7 (Figure 5.5) and IMNH-40368 (Figure 5.6) were each cut into two pieces (a and b). When making transverse cuts, plates were partially cross-cut with the Isomet saw, but the final portion of enamel to be in contact with the slide was broken by hand in an attempt to eliminate loss of material from saw blade kerf (~0.5 mm). Longitudinal sections were polished to 600 grit and epoxied to frosted oversized or petrographic slides. Molar plate thick sections were then cut to a thickness of ~500 μm, polished by hand on emery paper using successively finer grits from 600 to 2500 grit followed by 1.0- to 0.3-micron Buehler® aluminum oxide grit on a lap. Finished thicknesses ranged from 80 to 150 μm.

Photomicrographs of the three molar thin sections were taken using a Canon® Powershot SD750 digital camera coupled to a petrographic microscope with a custom-fabricated digital camera adapter. Images were taken at 25 to 400x magnification under transmitted plane polarized light. Images were also taken at 25x magnification of the Misha_Rm3.5 thin section under crossed polars. A photomicrograph of a stage micrometer with 10-μm graduations was included with each sequence of thin section photomicrographs for scale. Magnification was selected so that the field of view of a photomicrograph captured the full enamel thickness in each image. Individual photomicrographs from the cervical margin to the apex of the molar plates Misha_Rm3.5

(Figure 5.4), TE-95_rm3.7 (Figure 5.5), and IMNH-40368 (Figure 5.6) were stitched together in Adobe® Photoshop to produce composite images of the enamel on the posterior side of each molar plate.

5.4.2.2 Tusk thin sections and flatbed scans. One longitudinal surface of each ivory slab was polished in order to develop spatially accurate serial sampling plans for tusk dentin. Thin sections were made from the transverse surface of the proximal end of every other slab from the pulp cavity margin to the tip of the tusk to enable histological analysis for determining tusk growth rate. Methods for slab polishing and thin section preparation are described in Chapter 4 (Section 4.4.1). Flatbed scans of polished longitudinal surfaces and photomicrographs of thin sections were made; methods of producing these are also described in Chapter 4 (Section 4.4.1)

A thin section was not prepared from slab M640, so instead, the transverse face was polished and scanned in color at 9600 dpi using an Epson® 4490 Photo flatbed scanner. The image was converted to gray scale and levels were adjusted in Photoshop to enhance growth increments for histological analysis (Figure 5.7).

5.4.2.3 Histological analyses of tusk and molars. ImageJ was used for histological analysis of enamel thin sections and flatbed scans of ivory slab M640. Second-order growth increments in M640 were measured in ImageJ using the method described in Section 4.4.4 of Chapter 4. The base of slab M640 was cut along the tusk axis, and therefore, the angle θ between the tusk axis and the growth increments on the longitudinal surface was measured in multiple places in order to compare axial ^{14}C- and radial increment-based growth rates (Figure 5.8).

Recently, crown formation time (CFT) in proboscidean teeth was measured using histological features observed in thin section (Dirks et al., 2012). To determine CFT, the appositional angle α must be measured, where α is defined as the angle between striae of Retzius and the EDJ. The daily secretion rate (DSR) must also be measured. DSR is the thickness of enamel secreted daily by ameloblast cells along enamel prisms. Given α and DSR, one can calculate using trigonometry the daily extension rate (DER), which represents the daily length of crown extension from the apex to the cervix. The angle α was measured from Misha, TE-95, and IMNH-40368 thin sections (Figures 5.4, 5.5, and 5.6, respectively) and DSR was measured or estimated to calculate CFT.

5.4.3 Sampling tusks and molars for C and O stable isotope analysis

5.4.3.1 Tusk dentin sampling and pretreatment. Ivory slab M640 was selected for sampling based on ^{14}C-derived growth rates that indicate the dentin in M640 captures the move from California to Utah. 175 samples were end-milled from ivory slab M640 at 100 to 200 μm resolution using the method described in Section 4.4.2 of Chapter 4. The 100 to 200 μm sampling resolution corresponds to approximately one and two week's time, respectively. A flatbed scan of slab M640 after micromilling is shown in Figure 5.8. The tusk profile serves as the primary $\delta^{13}C$ and $\delta^{18}O$ input signals.

Tusk profile data from ivory slab R37-DEN-412 is also used in this study as a primary input signal for molar plate R37_Rm3.8, and the profile data are presented in Chapter 4 (Figure 4.7). This slab was selected because based on bomb-curve ^{14}C growth rates, the tusk dentin in it formed over the same time interval as the posterior section of the R37 left m3. All serially sampled tusk dentin powders were reacted with a 30 %

hydrogen peroxide solution in 0.65 ml centrifuge tubes for 30 minutes, rinsed with DI water and centrifuged three times, and then dried overnight at 60° C. Pretreatment resulted in a loss of *ca.* 40 % of initial sample mass.

5.4.3.2 Molar enamel sampling. All molar plates sampled for intratooth profiles were sampled using the conventional method. Each tooth was measured along the outer enamel surface of the plate from the cervix to the apex and marked every centimeter with a pencil. After the first series of marks were made, a second set of marks was added every 2 mm. Using a Dremel tool with a 1 mm diameter carbide steel bit (Brasseler # H21.11.010), samples were drilled every ~2 mm from the outer enamel surface to a depth ranging from 0.5 to 1.2 mm deep for the Misha (Figure 5.9), R37 (Figure 5.10), and LACM molars. Sampling depth for the isolated enamel plate IMNH-40368 ranged from ~1.5 to ~3 mm, the latter of which represents the full thickness of the enamel. After drilling, samples were scanned on a flatbed scanner and the sample lengths (Δx) and depths (Δz) were measured in ImageJ for accurate values to input into the inverse model.

Two other serial sampling methods were applied to sample Misha_Rm3.5b to generate intratooth profiles that captured isotopic shifts in $\delta^{13}C$ and $\delta^{18}O$ associated with the move from CA to UT. The two additional profiles allow comparison of profiles generated from high resolution sampling methods with the $\mathbf{m}_{est}$ generated by running conventionally sampled profile data in the inverse model.

The first high-resolution sampling method was micromilling 50 μm thick samples of enamel parallel to the appositional surface using the same end-milling technique for tusk dentin described in Section 4.4.2 of Chapter 4. The appositional angle, α, was measured in multiple places along the EDJ on the thin section. Scan lines were then

mapped onto the molar sample using the micromill software, and 36 samples were milled from the outer enamel surface to the EDJ (Figure 5.11). The outermost nine scans were milled at 100 μm thickness in order to produce enough powder for analyses because of shorter effective scan lengths. All sample powders generated by conventional and micromilling methods were analyzed without pretreatment. Samples from immature portions of enamel likely still contained organics associated with the secretory phase of enamel formation.

The second high-resolution sampling technique is laser ablation gas chromatography IRMS (LA-GC-IRMS). Thermal ablation of enamel using a CO_2 laser has been primarily used on rodent teeth. The method is minimally invasive as a single laser pit is ~250 μm in diameter and 100 μm depth (Passey and Cerling, 2006). Three profiles, each consisting of 13 or 14 scans, were done across the entire enamel thickness (2.8 to 3.0 mm) from the EDJ to the outer enamel surface. Profiles were done 54, 71, and 80 mm above the cervical margin (Figure 5.12). Each scan consisted of CO_2 cryogenically pooled from five laser shots (8.5 milliseconds at 7.5 Watts) taken along a path parallel to the EDJ.

5.4.4 Stable isotope carbon and oxygen isotope analysis

The carbonate component of hydroxylapatite in powdered tusk dentin and molar enamel samples was analyzed for stable carbon and oxygen isotope ratios, reported as δ-values relative to the Pee Dee Belemnite (PDB) using permil (‰) notation where

$$\delta^{13}C\ (\delta^{18}O) = (R_{sample}/\ R_{standard} - 1) \times 1000 \qquad (5.1)$$

and R_{sample} and $R_{standard}$ are the $^{13}C/^{12}C$ ($^{18}O/^{16}O$) ratios in the sample and in the standard, respectively, and the $\delta^{13}C$ ($\delta^{18}O$) value of PDB is defined as 0‰. Sample powders were digested in 100 % H_3PO_4 (phosphoric acid) using a Finnigan CarboFlo coupled to the dual inlet on a Finnigan MAT 252 IRMS at the University of Utah's Stable Isotope Ratio Facility for Environmental Research (SIRFER).

The CarboFlo system is a hybrid positive pressure/vacuum system with a common acid bath (CAB). Approximately 800 to 1000 μg of dentin (350 to 600 μg of enamel) was weighed out into a silver capsule, which was used as a precautionary measure to oxidize any SO_2 produced during digestion in phosphoric acid. Silver capsules containing powdered samples were dropped from an autosampler carousel into the vigorously stirred CAB and reacted for 10 (enamel) to 20 minutes (dentin) at 90 ± 2° C. A microcapillary tube submersed in the acid bath flushed it with 20 ml/minute of He and a 40 ml/minute He stream flushed the autosampler. The combined He streams swept the liberated H_2O and CO_2 through a dry ice/ethanol trap to remove water and then through a liquid nitrogen (LN) trap to collect the CO_2. Following the reaction period, the LN trap was isolated from positive pressure and evacuated with a rotary vacuum pump to ~10^{-3} Torr. The LN trap was removed and the CO_2 was cryogenically transferred to a microvolume held at -170°C. Once transferred to the microvolume, the CO_2 was analyzed through the dual inlet system on the IRMS. Internal laboratory standards of tusk dentin (R37-DEN), modern enamel (MCM, MRS), and calcite (UU Carrara) were used for data correction of samples and had average standard deviations of ~0.1 ‰ for $\delta^{13}C$ and ~0.2 ‰ for $\delta^{18}O$ across all analytical runs.

CO_2 liberated from enamel by LA-GC-IRMS was inlet via GC interfaced to a Finnigan MAT 252 IRMS in continuous flow. A correction of + 0.7 ‰ was applied to $\delta^{13}C$ laser values based on the average offset between laser and conventional $\delta^{13}C$ values from the portion of the molar that formed exclusively in Utah. A correction of + 7.4 ‰ was applied to $\delta^{18}O$ laser values. The + 7.4 ‰ offset is a result of liberating phosphate bound oxygen, which is 8 to 9 ‰ enriched in ^{18}O compared to carbonate. Passey and Cerling (2006) report similar offsets of + 0.3 ± 1.1 ‰ for $\delta^{13}C$ and + 6.4 ± 0.7 ‰ for $\delta^{18}O$ in modern enamel.

5.4.5 Tusk dentin sampling and analysis of Sr isotope ratios and elemental abundance

Strontium isotope ratios and relative elemental abundance for a suite of metals were measured by laser ablation inductively coupled plasma mass spectrometry (LA-ICP-MS). Since a thin section was lacking for M640, sample preparation of M640 for LA-ICP-MS required embedding a transversely-cut section in a standard 25 mm diameter epoxy mount (probe mount). A probe mount was selected because it fits a wide range of sample holders for various instruments, including Cameca® electron microprobe, nanoSIMS, SIMS, and the Photon Machines® 193 nm laser ablation system. The overall length of the M640 transverse section is ~37 mm, and therefore, the section was cut diagonally into two ~22 mm long pieces and embedded in separate epoxy mounts. Only the proximal M640 sample (M640b) was analyzed (Figure 5.13).

Elemental abundances were measured along scan lines radial to the pulp cavity ranging from 5 to 12 mm. Elements analyzed include Mg, P, Ca, Ti, Mn, Cu, Zn, Sr, Ba,

Pb, and U. Laser beam spot size was 86.5 x 5 μm, laser power was set at 8 mJ, and the scan rate was 2 μm/second. Ablated material was transferred to an Agilent 7500ce quadrupole ICP-MS via a 1.0 L/minute He stream. Data are reported in counts. A synthetic calcium carbonate standard (MACS-3) was also analyzed (Jochum et al., 2012).

The strontium isotope ratio ($^{87}Sr/^{86}Sr$) was measured along scans parallel to the elemental scans described above. Laser beam spot size was 65 μm in diameter, laser power was set at 8 mJ, and the scan rate was 2 μm/second. Ablated material was transferred to a Thermo Scientific Neptune multicollector ICP-MS via a 1.0 L/minute He stream. Data for each scan are blank corrected and corrected for ^{87}Rb based on ^{88}Rb. The data have not been corrected to the standard (USGS MACS-3: $^{87}Sr/^{86}Sr = 0.70759$), but this should not affect the relative change in the ratio.

5.4.6 Forward and inverse models

5.4.6.1. Forward model. I apply the forward model developed by Passey and Cerling (2002) to describe the effects of tooth enamel mineralization on $\delta^{13}C$ and $\delta^{18}O$ values. The three principal equations of the forward model that describe time averaging of the isotopic signal base on enamel maturation and sampling geometry are reviewed here. The first equation describes the isotopic composition of enamel in a volume parallel to the appositional surface *i* (see Figure 5.1) based on the mineralization parameters:

$$\delta_{ei} = (f_i * \delta_{mi}) + (1 - f_i) * \frac{\sum_{n=i+1}^{i+1+l_m} \delta_{m_n}}{l_m} \quad (5.2)$$

where δ_{ei} is the isotope ratio of the fully mineralized enamel, f_i is the initial density of the enamel as a fraction of the fully mineralized enamel, δ_{mi} is the isotope ratio of the input signal (diet or body water) during the secretory phase, and l_m is the maturation length (Figure 5.1). The model accounts for different sampling depths by casting the drilling depth as a function of l_a, where

$$\delta_{ci} = \frac{1}{l_a} \sum_{n=i-l_a}^{i} \delta_{e_n} \tag{5.3}$$

and δ_{ci} is the isotope ratio of the column of enamel drilled normal to the enamel surface and δ_{en} is the isotope ratio of each volume of enamel *i* deposited along the appositional surface through time (Figure 5.1). If the drilling depth is half or one-third of the way through the entire enamel thickness, then l_a in the first term of equation 5.3 is $0.5*l_a$, or $1/3*l_a$, respectively.

Finally, to account for the distance between samples along the growth axis of the tooth, the term sampling length (l_s) is introduced, which represents the distance between samples. If the sampling path is only 1 mm wide (parallel to the growth axis), but the distance between each sample path is 5 mm, then l_s is 5 mm. The isotope ratio of that portion of the enamel is modeled by averaging the number of columns in a sampling path such that

$$\delta_{di} = \frac{1}{l_s} \sum_{n=i-\frac{1}{2}l_s}^{i-1+\frac{1}{2}l_s} \delta_{c_n} \tag{5.4}$$

where δ_{di} is the isotope ratio over the sampling interval l_s.

5.4.6.2. Inverse model. In the inverse model developed by Passey et al. (2005), measured profile data **d** are related to the primary input signal **m** by the linear system

$$\mathbf{Am}=\mathbf{d} \tag{5.5}$$

where **A** is an averaging matrix of dimensions *M x N*. The system of equations is underdetermined because there are more unknown parameters *M* than measured data *N*, and thus is considered an ill-posed problem. Menke (1989) and Zhdanov (2002) both provide an excellent background on discrete inverse theory from a geophysical perspective, and Passey et al. (2005) provides a more detailed description of the model, including code for running the inversion (mSolve1_1) and error measurement (Emeas1_1) in Matlab.

Input parameters include f_i, l_a, l_m, sample length along the growth axis (Δx, or l_s in the forward model), and sample depth (Δz). These *a priori* inputs constrain the system, which is solved by determining a minimum length solution by the following equation:

$$\mathbf{m}_{est} = \langle\mathbf{m}\rangle + \mathbf{A}^T[\mathbf{A}\mathbf{A}^T + \varepsilon^2\mathbf{I}]^{-1}[\mathbf{d} - \mathbf{A}\langle\mathbf{m}\rangle] \tag{5.6}$$

where $\mathbf{m}_{est}$ is the estimated primary input signal, $\langle\mathbf{m}\rangle$ is an *a priori M* x 1 reference vector, and the term $\varepsilon^2\mathbf{I}$ is a regularization parameter, where ε is the damping factor and **I** is an *N x N* identity matrix.

Primary constraints to the family of solutions generated by equation 5.6 are the regularization parameter, which is controlled by the damping factor (ε); the input

parameters (and associated uncertainties); and a reference vector, which is constrained by the ecological range of $\delta^{13}C$ values or the $\delta^{18}O$ values of body water measured from an intratooth profile. An appropriate ε is essential for narrowing down the family of solutions to those that are realistic for the system. Smaller ε values return a longer (or more oscillatory) solution than larger ε values. To determine the appropriate ε, the model utilizes the Morozov discrepancy principle, whereby the predicted error (E_{pred}) calculated from ε is compared to the measured error (E_{meas}). E_{meas} is calculated (using the code in Emeas1_1) based on uncertainties in measured isotopic profile data, Δx, and Δz. These three variables are called r1, r2, and r3 in the model code and in subsequent figures. An appropriate ε value returns an E_{pred} that is similar to the E_{meas} (Passey et al., 2005). Additional sensitivity tests used to evaluate inverse model results include changing the parameters f_i, l_a, l_m, as well as the reference vector range, value, and standard deviation.

5.5 Results

5.5.1. Micro-CT

Densities of tusk dentin and fully mature molar enamel measured by pycnometry yield values of 1.84 and 3.34 g/cm^3, respectively. The value for tusk dentin is lower than the value of ~2.2 g/cm^3 observed by Weatherell (1974) in human teeth. The value for elephant enamel is slightly higher but within ~15% of the density reported for human enamel (Weatherell et al., 1974), and it is close to the value for pure apatite (3.15 to 3.2 g/cm^3). From this point forward, density results are presented as a percent of final enamel density (%FD). A total of 23 density profiles normal to the EDJ were measured

in two molar segments, and 22 of these are shown in Figure 5.14. Four density profiles from within 0.1 to 1.25 mm of the base of K07-M93 yield a mean f_i of 64.5 ± 1.8 %FD (± 1σ) (Figure 5.14B). The f_i of enamel from within the interval of 150 to 100 μm from EDJ from the same four K07-M93 profiles is essentially the same (63.6 ± 1.7 %FD). However, moving several millimeters up towards the apex of the tooth, enamel at the EDJ increases to 70 and 77 %FD at 2.5 and 3.75 mm above the cervix. A maximum of 91 %FD was measured in a profile 36.25 mm above the base of K07-M53. In general, the five profiles from the uppermost 5 mm (~33 to 38 mm) of K07-M53 are ~90 % final density near the EDJ, which decreases to ~55% at the outer enamel surface (Figure 5.14B). Total enamel thickness along molar plate K07-M53_1.9 ranges from ~0.1 mm to ~2 mm.

Twelve density profiles were taken along molar segment Misha_Rm3.5 from 3.5 to 94.6 mm above the base of the plate (Figure 5.14A). In general, the density profiles from 0 to ~40 mm are very similar to those from K07-M53. For example, the two profiles near the base of the plate, at 3.5 and 7.5 mm, have mean densities of 79.6 and 79.9 %FD, respectively, whereas the density from K07-M53 taken from 3.75 mm is 77 %FD (Figure 5.4). Density profiles from 33 to 38 mm in both profiles are also similar, with densities near the EDJ of ~90 %FD. One exception is the profile at 34.5 mm from K07-M53, which has a density of 80 %FD. In the upper half of Misha_Rm3.5 from 54 to 95 mm above the cervix, the enamel near the EDJ is or is nearly fully mature (100 %FD). The profile at 94.6 mm is an exception. The density at the EDJ is 80 %FD at the EDJ and increases to full density by about 1.8 mm from the EDJ. This profile was taken within about a millimeter of the dentin horn, where the tooth germ originates and

therefore is not considered representative of typical enamel density at the EDJ. In nearly all profiles with ≥1 mm of enamel thickness, the outermost enamel has a density of 55 to 65 %FD, suggesting that outer enamel f_i is equal to or slightly less than the f_i near the EDJ.

Density profiles ~35 mm above the cervix or higher show a sharp decrease from nearly 100 %FD to *ca.* 60 %FD moving from the EDJ to the outer enamel surface (Figure 5.14). The break in slope in the density profile moving from the EDJ towards the outer enamel surface marks the location of the maturation front in each profile. Maturation length, l_m, is determined by plotting the distance from the EDJ where the break in slope occurs versus the position of the profile above the cervix (Figure 5.15). Dividing the enamel thickness by the slope of this line yields l_m, which is 69.8 ± 4.8 mm, where the uncertainty is calculated from the slope error. The maturation angle is 2.49 ± 0.17 °. Density profiles from 83.6 and 86.5 mm are omitted from the l_m calculation because the full enamel thickness was not captured in the micro-CT scan.

5.5.2. Histological analyses

5.5.2.1 Tusk thin sections. The thickness of 246 second-order growth increments are plotted for Misha ivory slab 640 in Figure 5.16A. Mean thickness is 139 ± 38 μm, with a range of 67 to 240 μm. If weekly (i.e., exactly 7 days) periodicity is assumed, then the mean daily (radial) growth rate is 19.9 ± 5.4 μm/day with a range of 9.6 to 34.2 μm/day, and the total time in slab M640 is 1722 days (4.71 years) (Figure 15.5B). This is similar to a mean growth rate of 18 ± 8.2 μm/day determined from counting third-order increments (n=336) in Misha thin section M720. Although the daily growth rate varies

from about 10 to 34 μm/day, it appears generally linear over the 4.7 years represented in slab M640 (Figure 5.16B).

Measurement of the angle θ between the tusk axis and growth increments (Figure 5.8) yields a mean value of 7.7 ± 0.4° (n =7) (Appendix D). The overall axial growth rate of Misha's tusk determined by bomb-curve ^{14}C age dating can be converted to a radial growth rate by taking the tangent of θ. The axial growth rate of 51.0 ± 7.4 mm/year (Chapter 3) yields a radial growth rate of 19.0 ± 3.0 μm/day, which is within 5 % of the value determined by histological methods.

A third method for determining the growth rate comes from using the stable isotope data as a time marker for the date of Misha's move to Utah on April 22, 2005. The date of death (Sept. 9, 2008) is represented by the pulp cavity surface. The distance between the two points on slab M640 (18.14 mm) divided by the total time she lived in Utah (1236 days) yields a growth rate of 14.7 ± 0.8 μm/day, which is ~25 % less than the ^{14}C and histological results.

5.5.2.2 Molar thin sections. The appositional angle, α, was measured along the three molar thin sections where possible. Misha's fifth molar plate was still developing at death and had a relatively high organic content in the immature enamel in the lower half of the plate. The presence of organic matter interferes with the optics of transmitted light microscopy so that much of the immature or partially mature enamel appears opaque or blurred in thin section. Mature enamel on the other hand, has clearly discernable histological features that include enamel prisms, daily growth increments, and striae of Retzius (Figures 5.4, 5.5, and 5.6). Four measurements of α were made along

Misha_Rm3.5, and have a mean value of 3.3 ± 0.5 ° (Figure 5.17A). The measurements from the TE-95 thin section (n=16) yield a mean value of 3.4 ± 0.4° with a range of 2.8 to 4.8 ° (Figure 5.17B). In both molars, there is an increase in α towards the cervix that is best described by a logarithmic curve (Figure 5.17, Appendix D). A single logarithmic regression for all elephant data (Misha and TE-95) may be appropriate as well. The combined mean angle of apposition from both elephants (α_{LFN}), except in the lower 25 mm where α increases rapidly, is 3.2 ± 0.2°. A linear regression of α_{LFN} from 25 mm yields a shallow slope of -0.0034°/mm ($R^2 = 0.18$), indicating that α_{LFN} is essentially constant from the apex of the plate down to about 25 mm above the cervix.

The appositional angle in mammoth molars ($\alpha_{mammoth}$) is greater than in elephants, and there is a relatively greater increase in $\alpha_{mammoth}$ at the base of the plate than observed in elephants (Figure 5.17B, Appendix D). The mean $\alpha_{mammoth}$ value is 6.9 ± 2.0° (n=24) with a range of 11.8 to 4.2°. If the high angles observed in the lower 25 mm of the plate are excluded, then the mean $\alpha_{mammoth}$ decreases to 5.8 ± 0.7°. As with the elephant molars, the angle of apposition is best described by a logarithmic function.

Appositional length, l_a, can be calculated from enamel thickness and α, where l_a = enamel thickness/tan α. Using this approach on the two elephant molar thin sections and limiting the region of interest to 25 mm or higher above the cervix, the mean l_a for elephant molar plates is 55.6 ± 4.3 mm (n=14). Due to the rapid decrease of enamel thickness and the steepening of α near the cervix, l_a diminishes to 14 mm and 9 mm at 3.6 and 1.3 mm above the cervix. The l_a calculated with this method from mammoth molar IMNH-40368 is 29.4 ± 3.5 mm using an enamel thickness of 3 mm and an α of 5.8 ± 0.7°.

An alternative method for determining l_a is through measurement on the surface of developing molar plates. The appositional surface is smooth, whereas enamel in the maturation phase is rugose. Measurements of l_a from plates of developing molars K07-M53 and TE-95 ranged from 31.8 to 48.9 mm. Both molars had a diminutive posterior plate that indicated molar formation was nearing completion. Thus, l_a values determined by this method may represent minimum values as the plates may have completed (or nearly completed) crown extension.

A third method for measuring l_a is to trace prominent striae of Retzius from the EDJ to the outer enamel surface. The distance along the outer enamel surface of the plate from the point on the outer enamel surface above where the striae intersect the EDJ to the intersection of the striae with the enamel surface gives the l_a. This was done on the Misha and TE-95 thin sections and yielded a mean l_a value of 45.5 ± 2.0 mm (n=4) with a range of 43.5 to 48.3 mm. In several cases, the outermost 200 to 500 microns of enamel had spalled off, probably while preparing the thin section, and thus, the intersection with the outer enamel surface had to be estimated.

CFT was calculated from α and DSR values. The DSR was measured in thin section TE-95 (at 100x) in a single transect at ~80 mm above the cervix. Mean DSR is 3.0 ± 0.4 μm (n=24) with a range of 2.20 to 3.83 μm. The α value is calculated as a function of distance from the cervix using the logarithmic regression equations in Figure 5.17. Although DSR likely varies throughout formation of a plate, a value of 3 μm is used as a basis for calculating CFT in the two elephant molars, and a DSR of 3.5 μm is used to calculate CFT of the mammoth molar based on data from Dirks (2012). CFT represents the time required for the crown of a molar plate to grow to its full length, but

this is different from the total formation time of a molar plate because it does not account for enamel maturation that continues after the secretory phase. CFTs are modeled using constant DSRs of 2, 3, and 4 μm/day for the two elephant molars (Figures 5.18A and 5.18B) and DSRs of 3, 3.5, and 4 μm/day for the mammoth molar (Figure 5.18C).

The mammoth plate is worn to a height of ~103 mm. An initial crown height of 180 mm is assumed based on published data for a mammoth molar plate (Dirks et al., 2012), although this is a gross approximation. CFT for the three molars are shown in Table 5.2, and range from 3.6 to 9.0 years for the Misha and TE-95 plates and 9.7 to 12.9 years for the IMNH-40368 plate. A linear growth rate appears to be appropriate for profiles in elephant molar plates, but not for a full profile in a mammoth plate. For the elephant plates, a linear growth rate of *ca.* 22 mm/year fits the modeled CFT using DSR = 3 μm/day (Figure 5.18A). An l_m of 70 ± 5 mm and a growth rate of 22 mm/year yield a maturation time of 3.2 ± 0.2 years.

5.5.3. C and O stable isotope profiles in tusks and molars

5.5.3.1 Micromill sampling of tusks. The $\delta^{13}C$ and $\delta^{18}O$ values from Misha ivory slab M640 are plotted in Figure 5.19, and all data (n= 97) are presented in Appendix D. A radial growth rate of 14.7 μm/day is applied to the data based on the location of isotope shift in the tusk ivory and the date of the transfer from CA to UT. The mean $\delta^{18}O$ values during the CA and UT portions of the tusk are -9.3 ± 0.8 ‰ and -12.9 ± 0.8 ‰, respectively. Taking $\delta^{18}O$ values just before and after the move yields a shift of -5.0 ‰ between CA and UT.

The $\delta^{13}C$ data indicate that Misha had a C_3-dominated diet in UT during the time interval represented in M640, but had a highly variable diet during the last 2 years in CA (Figure 5.19). Mean $\delta^{13}C$ values for CA and UT are -7.7 ± 2.5 and -13.3 ± 0.6 ‰. The $\delta^{13}C$ values from just before and after the move yield a shift of -8.3 ‰ between CA and UT. The magnitude of the $\delta^{13}C$ and $\delta^{18}O$ shifts recorded in the ivory will be used as a baseline for comparison to the magnitude of isotopic shifts recorded in the molar profiles using the laser, micromill, and conventional sampling methods.

The $\delta^{13}C$ and $\delta^{18}O$ values from R37 ivory slab 412 were presented and discussed in Chapter 4 (Figure 4.7 and Appendix C), and will be used in the modeling component of the study as the primary input signal for modeling intratooth profile data from R37_Rm3.8 (Figure 5.10).

5.5.3.2 Micromill sampling of molar enamel. The $\delta^{13}C$ and $\delta^{18}O$ values (n=36) of enamel micromilled from Misha_Rm3.5b are plotted in Figure 5.20A and listed in Appendix D. Stable isotope data from micromill sampling of portions of the molar that formed in Utah are compared to laser and conventional data, as well as the ivory isotope data (Table 5.3). The isotopic shift is -3.1 ‰ and -2.2 ‰ for $\delta^{13}C$ and $\delta^{18}O$, respectively. Sample yield, measured as millivolts per microgram (mV/μg) of sample digested, is plotted as a function of distance from the EDJ (Figure 5.20B). The decrease in yield from the EDJ towards the outer enamel surface suggests a linear maturation phase.

5.5.3.3 Laser sampling of molar enamel. The $\delta^{13}C$ and $\delta^{18}O$ values from the three laser profiles are plotted in Figure 5.21 and listed in Appendix D. Scans that produced charred ablation pits indicate the presence of organic matter and resulted in anomalous isotope values. These data are not plotted or considered in evaluation of profile data. A

temporal shift between profiles (Figure 5.12) is evident in the isotope data (Figure 5.21). The enamel at 80 mm above the cervix formed earliest, and the isotopic shift associated with the move is not present in the plotted data (Figure 5.21A), although scans removed due to charred pits suggest the shift may occur near the outer enamel surface (~2600 μm). The diet shift from C_4 to C_3 and back to C_4 that occurred in mid–2004 (Figure 5.18) is recorded in the 80 mm profile. Although it does not have the temporal resolution of the ivory profile, the magnitude of the shift is similar (~8 ‰), but the corrected $\delta^{13}C$ values during the interval of C_3 diet (1300 to 1800 μm from the EDJ) are anomalously negative at -16.6 ‰ (Figure 5.21A). The lack of charred ablation pits and the normal yields from this interval (Figure 5.22) suggest no contamination from organics.

The profile from 71 mm above the cervix also records the diet switch in 2004, although the profile shape and $\delta^{13}C$ values differ from the 80 mm profile. With a resolution ~250 μm, time averaging is most likely the cause of the differences in the structure of isotope profiles from similar time intervals but different locations (e.g., 71 vs. 80 mm). In the 71mm profile, the isotopic shift associated with the move occurs 1700 μm above the EDJ (Figure 5.21B). The shifts in $\delta^{13}C$ and $\delta^{18}O$ are -6.1 ‰ and -3.3 ‰, respectively. The profile from 54 mm has the simplest structure of the three profiles with the shift associated with the move at 700 μm (Figure 5.21C). The shifts in $\delta^{13}C$ and $\delta^{18}O$ are -5.9 ‰ and -3.1 ‰, respectively, which are nearly identical to those from the 71 mm profile.

The yields for each laser scan are plotted as a function of distance from the EDJ (Figure 5.22). Yield is a function of the carbonate mineral content, and thus serves as a proxy for apatite mineral density per unit volume ablated. The decrease in yield from the

EDJ towards the outer enamel surface suggests a linear maturation phase, which is in agreement with the micromill yield data (Figure 5.20B).

5.5.3.4 Conventional sampling of molar enamel. The $\delta^{13}C$ and $\delta^{18}O$ values (n=42) from conventional drilling of Misha_Rm3.5 are plotted in Figure 5.23 and listed in Appendix D. Overall, the conventionally drilled profiles have similar structure to the M640 ivory profiles, and the enamel and ivory profiles overlap from early 2004 through January 2007 (Figures 5.19 and 5.23). The isotopic shift associated with the move occurs 72.2 mm above the EDJ (Figure 5.21B). The shifts in $\delta^{13}C$ and $\delta^{18}O$ are -4.0 ‰ and -3.4 ‰, respectively. Other similar features include the diet switch that occurs during 2004, although the return to $\delta^{13}C$ values associated with a C_4-dominated diet (*ca.* -5 ‰) are not present in the enamel profile. Similar features in the $\delta^{18}O$ profiles include two periods where $\delta^{18}O$ values increase 2 to 3 ‰ while Misha was in UT (Figures 5.19 and 5.23).

There is an offset between enamel and tusk isotope data ($\delta_{enamel} - \delta_{tusk}$) that formed after the move to UT (Table 5.3). This long-term offset observed over a period of ~1.5 years should not be influenced by isotope turnover associated with the move, and therefore may be a result of pretreatment of tusk dentin (and/or lack thereof for enamel). A correction factor of + 0.7 ‰ for $\delta^{13}C$ and -1.3 ‰ $\delta^{18}O$ is applied to the tusk profile used in the models so that isotope ratios from the tusk and tooth are in agreement based on the long-term Utah values.

The $\delta^{13}C$ and $\delta^{18}O$ values (n=39) from conventional drilling of R37_Rm3.8 are listed in Appendix D, and discussed in greater detail in Section 5.5.4. The conventionally drilled profiles from R37 show relatively low variability. The mean $\delta^{13}C$ value is -10.8 ±

0.3 ‰ with a range of 1.2 ‰, and mean $\delta^{18}O$ is -1.3 ± 0.3 ‰ with a range of 1.3 ‰. As with the Misha tusk and enamel data, there is an offset between the two profiles, and corrections were applied so that the isotope values in both profiles were in agreement.

5.5.4. Modeling results

5.5.4.1 Forward model. The micro-CT, histological, and stable isotope data from the molars and tusks provide data necessary to test whether the forward model of Passey and Cerling (2002) is applicable to elephant molar plates. Forward model parameters are f_i = 0.65, l_a = (35, 45, and 55 mm), and l_m = 70 mm. Isotope data from enamel profiles values are smoothed with a three-point weighted mean (0.25, 0.5, 0.25) for all modeling work. Since each method for measuring l_a yielded different results (37 mm by visual methods, 45 mm by tracing striae of Retzius, and 56 mm by thin section trigonometric calculations), forward model results using 3 different l_a values (35, 45 and 55 mm) are shown for Misha_Rm3.5 (Figure 5.24). Forward model results using tusk profile data (Figure 5.19, Appendix D) as the primary input signal are generally in good agreement with measured enamel values (Figure 5.24). For carbon, there is a temporal offset in the beginning of the record and the modeled enamel curves lag the measured data across the move by up to four months. Another region of misfit is just before the move, where modeled $\delta^{13}C$ values are up to 1 ‰ greater than measured enamel values. For oxygen, modeled curves are close to the measured curve in overall structure, but underpredict the $\delta^{18}O$ value by ~1 ‰ prior to the move. A temporal offset is present and most pronounced at the beginning and end of the modeled interval.

Model results from R37 are presented in Figure 5.25. The primary input signal for the model is isotope profile data from ivory slab R37-DEN-412 (Figure 4.7). An l_a of 35 mm was selected for plate R37_Rm3.8 for two reasons. First, plate height (76 mm) is approximately 75% of the height of the Misha and TE-95 plates from which the longer l_a values were derived, and it follows that l_a might scale with overall plate height. Second, using an l_a of 45 mm or greater removed nearly all amplitude from the modeled isotope profiles. The approximate period over which molar plate R37_Rm3.8 formed is estimated as 1981 to 1987 (see ^{14}C data from plate R37_Rm3.7 in Chapter 3). Visual matching of $\delta^{13}C$ profiles was used to align the forward model results to the measured enamel data (Figure 5.25A). The modeled and measured data overlap for a period of *ca.* 3 years, and there is good agreement between the two. Agreement is fairly poor, however, for much of the $\delta^{18}O$ forward model with the measured data (Figure 5.25B). Measured $\delta^{18}O$ data show a peak with amplitude of ~0.7 ‰ that occurs in late 1985, which is not present in the model results.

In evaluating forward model results, it is important to keep in mind that temporal offset between model and measured data can have two sources: error in growth rates from the tusk or from the molar. The differences observed between the modeled and measured isotope values can be a result of incorrect model parameters or they can arise from incorrect assumptions about the tusk profile being representative of the primary input signal. This will be addressed in greater detail in the discussion below.

5.5.4.2 Inverse model. Inverse model results ($\mathbf{m}_{est}$) from two elephant and two fossil mammoth molar profiles are given as the mean of 100 solutions ($\pm 1\sigma$). Results from elephant molars are presented first because they include a known primary input

signal from the tusk profile data and thus offer a way in which the inversion results can directly be evaluated. All plots showing inversion results ($\mathbf{m_{est}}$) and measured enamel profiles also include boxplots comparing measured error (E_{meas}) and prediction error (E_{pred}) (see Passey et al., 2005 for equations).

Misha_Rm3.5 profile results are shown in Figure 5.26. The primary input signal is the M640 isotope profile smoothed with a five-point median. A median filter was selected because it preserves edges better than a moving average filter. The estimated $\delta^{13}C$ profile, $\mathbf{m_{est\_C}}$, is shifted + 80 days for comparison to the primary input signal. The profile nearly reaches the -4 to -5 $\delta^{13}C$ values associated with the 2004-2005 diet change in CA, but overpredicts the $\delta^{13}C$ values when diet changes from C_4- to C_3-dominated. The rapid shift in the primary input signal associated with the move occurs over a longer period (5 months) in $\mathbf{m_{est\_C}}$ than in the tusk profile (~3-4 weeks). There is oscillation in $\mathbf{m_{est\_C}}$ after the isotope shift associated with the move that first underpredicts and then overpredicts the $\delta^{13}C$ value of enamel. The $\delta^{13}C$ value of Misha's diet was relatively constant in UT, and $\mathbf{m_{est\_C}}$ matches this value in the latter part of the enamel and primary input signals.

The estimated $\delta^{18}O$ profile, $\mathbf{m_{est\_O}}$, does a better job than $\mathbf{m_{est\_C}}$ at recovering the primary input signal. $\mathbf{M_{est\_O}}$ recovers the main features of the primary input signal, which include the shift associated with the move and periods of variability in the primary input signal that occurred before and after the move. In particular, $\mathbf{m_{est\_O}}$ shows the period of increased $\delta^{18}O$ values just after the move to UT, around late summer of 2005. There are minor offsets ($\leq$ 1 ‰) between the measured (primary input signal) and modeled ($\mathbf{m_{est\_O}}$) $\delta^{18}O$ values and in the temporal scale.

Inverse model results from the R37_Rm3.8 profile are plotted in Figure 5.27. The five-point median smoothed R37-DEN-412 profile serves as the primary input signal. No temporal shift of $\mathbf{m}_{est\_C}$ is required for comparison to the primary input signal. $\mathbf{M}_{est\_C}$ tracks the periodicity and amplitude of the primary input signal quite well for the first two years of the record, but the two signals differ in the latter portion of the record. $\mathbf{M}_{est\_O}$ and primary $\delta^{18}O$ input signals show little agreement. This is to be expected considering the similar poor fit observed in the forward model. Results from the R37_Rm3.8 should be interpreted with caution as there remains uncertainty as to whether or not visual matching of the tusk and molar profiles is correct.

Model parameters for mammoth molar profiles are based on histological results (l_a= 30 mm) and micro-CT results from elephant molars (f_i= 0.65 and l_m=70 mm). The mammoth molars were sampled opportunistically (e.g., they were found in the lab) without any prior knowledge of the specimens, and in this regard, the results are fortuitous because the resulting profiles are quite different. The enamel profiles from LACM-47129 (Figure 5.28), particularly for $\delta^{13}C$, have a periodic structure, whereas the profiles from IMNH-40368 are nearly constant throughout their entirety with the exception of several samples near the cervix (Figure 5.29). Although the true primary input signals are unknown, the contrasting profiles offer an opportunity to test the inverse model on profiles that suggest two very different dietary and, to a lesser degree, climatic scenarios.

The $\delta^{13}C$ range in the measured LACM-47129 enamel profile is 3.7 ‰ (-4.7 to -8.4 ‰), whereas $\mathbf{m}_{est\_C}$ has a range of 8.1 ‰ (-2.7 to -10.8 ‰). $\delta^{18}O$ from enamel and $\mathbf{m}_{est\_O}$ have similar ranges of 1.5 ‰ and 1.9 ‰, respectively. The entire profile (45 mm)

appears to contain one period of oscillation in carbon and possibly slightly more than one full period in oxygen. While it is tempting to suggest the profiles have the same periodicity, the record is not long enough to say this with confidence. Moreover, approximately one third of the record was sampled from enamel within 25 mm of the cervix where changes in α, l_a, and possibly growth and maturation rates occur. Even with the limited profile length, dietary interpretations of the $\mathbf{m}_{\mathbf{est\_C}}$ and the enamel data yield two different results. With enamel data alone, one would infer a mixed diet throughout the year comprised of up to ~60% C_3 plants and up to 65 % C_4 vegetation. The $\mathbf{m}_{\mathbf{est\_C}}$ values tell a different story, suggesting greater reliance on a single vegetation type (of up to ~80% C_3 or C_4) throughout the year. The data further suggest a larger seasonal change in vegetation than one would infer from the enamel data alone. Mammoths are thought to have been primarily grazers, and therefore, the data may indicate seasonal variation in grass type or conversely, a flexible diet that included C_3 browse and C_4 grasses. $\mathbf{M}_{\mathbf{est\_C}}$ and $\mathbf{m}_{\mathbf{est\_O}}$ from LACM-47129 highlight the potential utility of the model for longer periodic profiles that encompass 2 or more years.

The IMNH-40368 enamel profiles exhibit a very small range of values over a ~55 mm interval from 92 to 36 mm that represents more than half of the time contained in the molar plate. In the interval from 25 mm to the cervix, the profiles show greater variability. Opacity of thin section IMNH-40368 under plane polarized transmitted light throughout most of this interval suggests the region was still in the maturation phase (Figure 5.6), whereby the higher organic content and smaller apatite crystal size may have made it more susceptible to diagenesis (c.f., bone or tooth dentin). This is also the region of the plate where appositional geometry changes dramatically. For these reasons,

enamel profile data below 25 mm were excluded from the inverted data set, and are not discussed further here.

The $\delta^{13}C$ range in the enamel profile from 92 to 36 mm is 0.4 ‰ and the $\delta^{18}O$ range is 0.8 ‰. Model solutions over this same range for $\mathbf{m}_{est\_C}$ and $\mathbf{m}_{est\_O}$ are 1.2 ‰ and 1.5 ‰, respectively. Both $\mathbf{m}_{est}$ and enamel profiles indicate that throughout most of the period of record, the individual had an isotopically constant (C_3-dominated) diet and body water composition. Given that the fossil was found in or near lacustrine sediments, it is likely the mammoth relied on drinking water from a lake large enough to buffer variation in the $\delta^{18}O$ of the water throughout the year. Although the enamel profiles, especially carbon, are essentially constant, model solutions for both isotopes show in-phase, low amplitude, quasi-sinusoidal periodicity that could be interpreted as weak (and possibly annual) seasonal variability. This sort of tantalizing interpretation is tenuous and a rigorous test for a seasonal signal at the American Falls site would ideally include multiple enamel profiles from proboscideans and other coeval hypsodont taxa whose enamel mineralization and geometry is understood.

5.5.5. Sr isotope and elemental data from tusk profiles

Strontium isotope data are presented with $\delta^{18}O$ data from M640 in Figure 5.30A. The baseline $^{87}Sr/^{86}Sr$ ratio from the CA portion of Misha's tusk is *ca.* 0.707 ± 0.0005. Upon the move to UT, the $^{87}Sr/^{86}Sr$ ratio changes to *ca.* 0.711 ± 0.0007. During the isotopic shift associated with the move, the $^{87}Sr/^{86}Sr$ ratio has two short periods in which it spikes sharply back towards, but never completely to, the CA value (Figure 5.30A). The larger of the two spikes coincides with a brief drop in $\delta^{18}O$ of about 0.7 ‰. Tusk

$^{87}Sr/^{86}Sr$ ratios are near the higher range of published values for water from the Sacramento-San Joaquin delta (*ca.* 0.7061 to 0.7073) (Ingram and Weber, 1999), and they are also slightly higher than the values measured at the Hogle Zoo between August 2009 and May 2012 (0.70859 ± 0.0001 to 0.71062 ± 0.0001; n= 8). No food was measured, and the proportional contribution from water vs. food is not known. However, the difference between CA and Hogle Zoo (UT) water values of *ca.* 0.003 is on the same order as the difference observed in the CA and UT portions of the tusk, *ca.* 0.004. Elemental abundance data for ^{88}Sr and ^{138}Ba show changes associated with the move (Figure 5.30B and C). ^{138}Ba shows a greater range of variation in the CA portion of the tusk. Nearly all other elemental profiles lacked significant structure or variability and are therefore not included. There is some periodicity and covariation in profiles of elements associated with apatite (Mg, P, and Ca) that warrants future study.

5.6 Discussion

5.6.1 Stable isotope turnover in elephants

The results from the M640 tusk profile provide a unique opportunity to evaluate the turnover time of carbon and oxygen in tusk dentin, and by extension elephant body water and blood bicarbonate. Evidence from stable isotope profiles in tusk dentin from R37 (Chapter 4) suggest some damping of the primary input signal (e.g., dietary $\delta^{13}C$) that may be due to a relatively short maturation period of dentin or the turnover of carbon in the blood bicarbonate pool from which carbon and oxygen in apatite-bound carbonate is derived. This issue is addressed in greater detail in Section 5.6.4. Aside from collecting breath samples before, during, and after the move from CA to UT to measure

the isotope ratios of respired CO_2, which was not done with Misha, the tusk profile serves as the best record of turnover of carbon and oxygen in the body. The tusk profile shows turnover of carbon and oxygen isotopes occurs at indistinguishable rates over a 293 μm interval. If the radial growth rate of ~19 μm/day is assumed, turnover occurs in 15 days, or if the growth rate is ~15 μm/day, then turnover is complete in 20 days. Thus, estimated turnover rates are 5 to 7 %/day for carbon and oxygen in elephant blood bicarbonate and body water.

5.6.2. Comparison of sampling methods for intratooth profiles

Conventional drilling, micromilling, and laser ablation were used to generate isotope profiles from Misha_Rm3.5 in order to determine which method produces a profile that best resembles the primary input signal. Other considerations include sample preparation, time required to complete the sampling, and accessibility to necessary instrumentation. The magnitude of the isotopic shift associated with the move from each profile, expressed as Δδ, is given in Table 5.4. The isotopic shift in tusk profile M640 is also included in Table 5.4, and it is assumed to represent the primary input signal. A convenient way to evaluate the extent to which the enamel profiles are damped is to calculate the percent of the total amplitude (% $\Delta\delta_{tusk}$) they capture with respect to that observed in the tusk profile. For carbon, the micromill and conventional drilling methods both capture <50 % of the true amplitude, whereas the laser captures 72 %. Oxygen results show that conventional and laser methods both recover *ca.* 65 % of the true amplitude and the micromill captures 44 %. When $\mathbf{m}_{est}$ values are included in the comparison to the primary input signals, they perform the best of all methods, essentially

capturing the true input signal, albeit slightly over-predicted at 110 % of the true amplitude for both isotopes (Table 5.4). These data suggest that conventional sampling, which is the fastest sampling method, coupled with inverse modeling, is the best method for producing isotope profiles that match the amplitude of the primary input signal.

The laser profiles captured *ca.* 70 % of the amplitude of the shift, but there are several limitations to this method. The laser system only accommodates samples on the order of millimeters, which makes analysis of proboscidean molar plates impossible unless they can be cut into small segments. Furthermore, interpretation of $\delta^{18}O$ data is complicated by the inclusion of phosphate oxygen, and there is a paucity of labs that currently have LA-GC-IRMS systems ($n \approx 2$). The micromill is more widely available than the laser system, but the micromilled profile yielded lower amplitudes than the conventional method. A potential source of damping in the case of Misha_Rm3.5 is error in the angle at which scans are drilled. Minor variations from the true α angle when setting the scans, variability in α throughout the enamel profile, or undulation of the EDJ can all lead to mismatch between micromill scans and the true appositional surface. Micromilling of molar enamel differs from tusk dentin because in the latter case, second-order increments serve as a "road map" to keep scans parallel to growth increments, whereas with the former, one is left to drill scans by "dead reckoning" as increments in enamel are not visible in thick sections (Figure 5.11).

5.6.3. Histological analyses

The histological data from molar thin sections contribute a tremendous amount of information to this study in providing two ways to measure l_a and by allowing for

measurement of α and DSR values required to calculate CFT. Another critical finding from all three thin sections is that the angle of apposition, α, increases significantly within 25 mm of the cervix. It is also noteworthy that in fully mature plates, enamel thickness begins to decrease at height of ~20 mm above the cervix. Both the Misha and R37 molar profiles lacked tusk profile data corresponding to the lowest 25 mm of the studied plates because these portions of their tusks were not sampled. Without data to evaluate the behavior of the isotope profiles during that interval, the most parsimonious recommendation is to avoid inverse modeling of isotope profile data from this interval until additional studies are done. The IMNH-40368 enamel profile was truncated at 26 mm above the cervix (Figure 5.29), but the entire LACM-47129 profile was input into the model because one-third of the profile was sampled below 25 mm.

5.6.4. Forward and inverse model parameters

The overall performance of the forward and inverse models for the Misha and R37 molar data is discussed here with an emphasis on evaluating the potential application to fossil proboscidean molars. For elephant molars, forward model parameters f_i= 0.65, l_m= 70 mm, and l_a= 35 mm (the shortest length) applied to the tusk profiles fit the measured enamel signal best; however, the intermediate l_a (45 mm) was used in inversions. In the Misha forward models (Figures 5.24), the modeled enamel data show a better overall fit to the measured data after the move to Utah, but overall, both perform sufficiently well over the 3+ year period at reconstructing the amplitude and frequency recorded in the measured enamel profile.

A series of sensitivity tests on the three main parameters, f_i, l_a, and l_m was done in the inverse model with the Misha $\delta^{18}O$ profile. The test consisted of changing a single parameter at a time within a range of plausible values. For f_i, the values ranged from 0.25 to 0.75. The lower value of 0.25 was chosen because this value has been measured in teeth of several mammals (e.g., *Hippopotamus amphibius*, *Bos taurus*, *Bison bison*) and suggested for a variety of other taxa including rodents (incisors) and ungulates. Results indicate the f_i value of 0.65 determined by micro-CT is accurate and relatively robust: values of 0.55 and 0.75 result in minor differences for the Misha $\delta^{18}O$ profile (Figure 5.31A). Thus, the differences observed between f_i values of inner enamel (0.65 to 0.7) versus those of other enamel (0.55 to 0.65) may not have a significant effect on inversion results. A difference of this magnitude (~0.10) would, however, have a larger effect if f_i were 0.25 as is the case for some mammal teeth. The results also show that an f_i value of 0.25 is not appropriate for elephant molars.

The maturation length was evaluated at lengths of 50, 75, and 100 mm, and shows very little change with different l_m lengths (Figure 5.31B). The small effect of changes in l_m is to be expected since ~65% of the signal is recorded in the secretory phase of enamel formation. Changes in l_m will have a greater damping effect for teeth with a lower f_i.

The model showed the greatest sensitivity to the parameter l_a (Figure 5.31C). In the case of elephant molars, where f_i is relatively high, the appositional length is responsible for a significant amount of time averaging, which increases with sampling depth z. Appositional lengths tested ranged from 20 to 100 mm and although the shortest length produced the best results, it is an unrealistic value for elephant molars.

In summary, sensitivity tests on the Misha $\delta^{18}O$ profile suggest the f_i value determined in this study is accurate and exhibits low sensitivity to changes of *ca.* ± 0.1. There is little variation with changes in l_m, which is due to the relatively high f_i. The model is most sensitive to l_a because it imparts a significant damping effect on the primary input signal.

The large shift in the Misha $\delta^{18}O$ profile made it an obvious candidate for the sensitivity tests. It may be possible that the uniqueness of the profile, the one-way shift, may not be representative of seasonal (e.g., annual or biannual) changes in the primary input signal. Due to uncertainty in chronology and growth rates, there is still some uncertainty in matching of the profiles from the R37 molar and tusk. This precludes meaningful results from sensitivity tests on the R37 profiles, but generating profiles from adjacent molar plates or ivory slabs would address this issue.

Both forward and inverse model results from Misha_Rm3.5 show regions of misfit to the measured profile. The misfit can be decomposed into offset in the y-axis (isotopic) or in the x-axis (temporal). Uncertainty in both variables warrants discussion because it may impart significant effects that could also be attributed to inadequate parameterization.

The principal source of isotopic uncertainty arises from the assumption that the tusk profile is representative of the primary input signal. Two R37 tusk profiles presented in Chapter 4 and the Misha M640 profile presented in this chapter convincingly show that tusk profiles record high resolution changes in stable isotope ratios at approximately weekly resolution, but do they record the full range of isotope variation? Comparison of the $\delta^{13}C$ of diet ($\delta^{13}C_{diet}$) based on R37 hair and tusk dentin during 2006

shows ranges that are very similar, (4.8 and 4.5 ‰, respectively; Figure 4.11). Yet when $\delta^{13}C_{diet}$ is calculated from hair data with the Reaction Progress Variable model, the modeled $\delta^{13}C_{diet}$ range for hair becomes 8.5 ‰, or nearly twice the range observed in the tusk dentin. So while tusk profiles provide high-resolution isotopic records, it is important to keep in mind that they may not represent the true primary input signal that is being sought through the forward and inverse modeling.

Growth rate must be assigned to molars and tusks in order to convert isotope profiles from two different length domains into the time domain for comparison. Chapters 3 and 4 show that bomb-curve ^{14}C dating or histological methods can be used to calculate tusk growth rates and the ^{14}C method is also applicable to proboscidean molars. In this chapter, I add histological analysis of molar thin sections as another method for determining growth rates in teeth. Measurement of perikymata is not applicable to elephant molars because they have a rough enamel surface that obscures this feature, the time period in the increment is unknown, and they are eventually covered with cementum. Tusk and molar growth rates were determined using all methods available and although the histological and ^{14}C methods both yielded a radial growth rate of *ca.* 19 μm/day for M640, the isotope data indicate a growth rate of *ca.* 15 μm/day. Misha's ^{14}C-derived growth rate is based on data from along the entire length of the tusk, which may not be representative of the last 5 years of her life. Reconciling the difference between the histological-based growth rate and the isotope-based is more difficult. It may be that the "weekly" value assumed is not 7.0 days, or varies between individuals. A shorter time period of about 5 days for second-order increments would bring the two growth rates into

agreement. Although there is no basis for arguing for such a period, it can be argued that for this zoo elephant, a period of 7 days may not be correct.

Molar growth rates also show differences based on the method used. In Chapter 3, growth rates for six plates from two molars range from 14 to 16 mm/year, and from one of these plates (TE-95_Rm3.7), a thin section was made in order to directly compare 14C- and histologically-derived growth rates. The histological data from TE-95_Rm3.7 suggest a growth rate of about 22 mm/year. The histologically determined growth rates assume a constant DSR along the growth axis of the tooth, but this has not been verified.

In summary, growth rates for tusks and teeth have been determined through a variety of methods and are in general agreement, but for the task at hand, which is to compare high-resolution isotope profiles from the two tissues on a temporal scale, non-linear growth rates or uncertainties of even 10% in each tissue limit the ability to determine whether temporal offsets in the measured and modeled profiles are a result of erroneous model parameters or growth rates. The observed misfit is likely due to some combination of both.

5.6.5. Application of the inverse model to fossil proboscidean molars

An important question to address is how meaningful are inversion results from fossil proboscidean molars? The mammoth profiles indicate that inverse models produce realistic estimated input signals, but there are considerations and caveats for other extinct proboscidean molars. Molar morphology of proboscideans outside of the *Loxodonta*, *Elephas*, and *Mammuthus* (LEM) clade is significantly different from those evaluated in this study, and therefore should not be evaluated with inverse methods using the

parameters determined here. Even for species within the LEM clade, similarity of tooth morphology to *L. africana* and *M. columbi* should be considered before applying the inverse model to enamel profiles. Model parameters f_i and l_m determined for African elephants are likely appropriate for most fossil taxa within the LEM clade. This may remain an untested assumption, as fossilized developing molars may not retain their original density gradients, which renders micro-CT and other methods for measuring density (e.g., phosphorus content) useless. Molars of extinct mammoths preserved in permafrost are an exception, and represent a unique opportunity to establish f_i and l_m in extinct mammoths. It will also be necessary to determine crown formation times in fossil molars to transform profile data from length to time domains, keeping in mind that the CFT metric does not include the period of enamel maturation that occurs after crown formation is complete.

The 30 mm range of l_a values observed in African elephants is rather large, especially considering the sensitivity of inversion results to l_a (Figure 5.31C), and more developing molars of elephants should be characterized to determine the amount of variation that exists based on plate number (anterior to posterior), molar number, upper vs. lower dentition, and sex. These data will provide a framework for evaluating l_a values of fossil proboscidean plates, which must be determined histologically or in the case of fossil molars that were developing when the animal died, this may be possible through measurement along the outer enamel surface.

Application of the inverse model with parameters determined in this study should be restricted to molars from LEM clade proboscideans. While these clades comprise only a small fraction of all clades in the order Proboscidea, they were the dominant clades over

the past *ca.* 6 Ma across most continents and therefore offer ample opportunity for studying the diet and life history of late Neogene proboscideans and the seasonality of vegetation and precipitation of their paleoenvironments. Careful morphological and histological study of molars from other similar taxa such as *Primelephas* may extend the method beyond the LEM clade. These considerations apply to the general application of the inverse model to all mammalian teeth. Calculating an estimated input signal from an enamel profile using inverse methods is by definition an ill-posed problem as it is an under determined system. Thus, it is critical that the three key model parameters (f_i, l_a, and l_m) be determined on a case-by-case basis to the extent possible. Failure to do so increases the chance of producing erroneous and misleading model results.

5.6.6. Recommended profile and modeling scheme

The results of this study illustrate the potential use of inverse methods for recovering estimated primary input signals of dietary carbon or body water oxygen from intratooth profiles from proboscidean molars. Here I recommend how one might pursue the use of inverse modeling of intratooth profiles in other mammalian teeth. The most important step is generating a robust forward model, which requires characterizing the parameters f_i, l_a, and l_m. This entails spatial analysis of enamel density to determine f_i and l_m, which in this study was done by micro-CT, but other methods such as measuring phosphorus content or using backscattered electron imaging are also available. Histological analysis via thin section is important for establishing growth rates and also provides a means for determining l_a.

Misha provided a unique case for testing the forward model in that a tusk profile was available to serve as a primary input signal. Experiments on small mammals where a

diet or water switch can be done are invaluable for developing a forward model, but not entirely necessary (cf., Passey and Cerling, 2002). For larger animals, translocations between zoos or parks around the country can serve as unintended diet and water switches, as was the case with Misha. Collaborating with the Hogle Zoo in Salt Lake City has provided (and continues to provide) amazing opportunities to study isotopes in animal tissues and breath.

With regard to sampling protocols for enamel profiles, these will vary by tooth size, model parameters, and the frequency of the primary input signal (if known). For elephant molars, which grow ~15 to 22 mm/year, sampling every 2-3 millimeters was sufficient. In the case of East African elephants, where biannual rains lead to changes in the $\delta^{13}C$ of diet and the $\delta^{18}O$ of body water on timescales of 3-4 months, 2mm represents a minimum sampling interval. Linearity of growth rate is also an important variable that should be determined. The model assumes linear growth and deviations from this will impart temporal error on model results and subsequent interpretations.

When conventionally drilling profiles, it is not critical to keep the sampling interval (Δx) and depth (Δz) constant since each of these variables is input with the corresponding **d** value into the model. These parameters ultimately affect uncertainty in the model solutions, so it is critical to minimize Δx and Δz uncertainty. This can be accomplished through careful measurement after a profile is drilled using either a micrometer or via digital measurement from a scanned image of the molar profile. I found the latter method to be faster, and scanning also leaves you with a digital image of the profile. Finally, as discussed previously, in the lowest 25 mm of molar plates, l_a decreases as α increases. This change in the geometry of the appositional surface is not

accounted for in the models used here, and the profile samples from this interval should not be included in the model input unless the model is adapted to account for this. This may be problematic for isotope profiles in smaller teeth. For example, Zazzo et al. (2012) found α increases in sheep teeth around 20 mm above the cervix, but since sheep molar crowns are only 40 to 50 mm in length, this means only 50-60 % of the profile can be used in the inverse model. Adjustment to the model that accounts for changes in l_a as a function of length may permit inversion of profile data from the entire crown length, which would benefit those working on shorter molar crowns or well-worn proboscidean molar plates.

5.7 Conclusions

This study extends the use of the inverse model developed by Passey et al. (2005) for reconstructing the estimated primary input signal for continuously growing teeth to molars of proboscideans in the *Loxodonta*, *Elephas*, and *Mammuthus* clades. Using coeval tusk and enamel profiles from a translocated zoo elephant, I evaluated how well the inverse model could reconstruct the primary input signal from the enamel profile. Inverted conventionally sampled profiles have $\delta^{13}C$ and $\delta^{18}O$ amplitudes that are within 10 % of tusk values, which represent the primary input signal. Profiles generated by micromilling and laser ablation methods yield amplitudes ranging from 32 to 72 % of the tusk amplitudes. Inversion results from conventionally drilled profiles successfully reconstruct the dominant structural features of the primary ($\delta^{13}C$ or $\delta^{18}O$) input signal, although some blurring still occurs. The structure of both the raw and inverted conventionally drilled profiles more closely resembles that of the tusk profile than the

micromill and laser ablation profiles. Results clearly demonstrate that the inverse model produces estimated primary input signals that more accurately reflect the true primary input signal than high-resolution sampling methods such as micromill or laser ablation scans.

Inversion of a molar profile from R37 suggests the record of seasonal diet change associated with the biannual rains in Kenya is preserved in elephant enamel, but uncertainty in the time interval represented by this profile precludes confident temporal placement and direct comparison to tusk profile data from R37. Inversion of a mammoth molar profile from a late Pleistocene site in southern coastal California indicates a highly variable seasonal diet that ranged from 28 to 82% C_4 vegetation. Inversion of a seemingly flat molar profile from a late Pleistocene site in Idaho produced estimated primary input signals that suggest weak (annual?) seasonality.

The ability of the inverse model to reliably reconstruct estimated primary input signals hinges upon development of a robust forward model that accurately describes enamel formation and geometry. To this end, histological and micro-CT methods were employed to characterize forward model parameters f_i, l_a, and l_m. Elephant molar f_i is 65 ± 2%FD, which is about a factor of 2.5 higher than has been observed in other mammalian teeth. Elephant molar l_m is 70 ± 5 mm, which is similar but slightly longer than that measured in hippopotamus canines, and l_a measurements based on three methods range from about 35 to 55 mm. Future work should be directed towards determining the optimal method for measuring l_a, and characterizing the variability among extant (and fossil) proboscideans. The results from the sensitivity test further demonstrate the significance of the parameter l_a in enamel formation.

Histological data suggest the CFT for elephant molar plates is 4.8 to 6 years based on measured appositional angles (α) and a constant DSR of 3 μm/day. This implies growth rates of 20 to 22 mm/year. ^{14}C-based growth rates are lower than those determined by CFT, ranging from 13 to 16 mm/year. CFT does not include the time required for enamel maturation after crown extension is complete. Mammoth molar growth rates are not linear over the entire CFT, which is estimated at ~11 years assuming a constant DSR of 3.5 μm/day. This should be considered when applying the inverse model to profiles greater than approximately 10 cm in length, where effects of a non-linear growth rate become pronounced. Histological data also reveal a changing enamel structure in the lower 25 mm of elephant and mammoth molars that will affect inverse model results. Therefore, enamel profile data from this interval should not be included in the inverse model unless the forward and inverse models are adapted to account for this. Extension of the inverse model to LEM clade proboscidean teeth in the fossil record provides a new proxy for estimating the timing and magnitude of seasonality in ancient ecosystems spanning the last 6 million years and most of the continents.

5.8 Acknowledgements

I thank the Office of the President of the Republic of Kenya, the Kenya Wildlife Service, the Samburu and Buffalo Springs County Councils, and Utah's Hogle Zoo for permission to conduct this research. I thank Dr. Nancy Carpenter and Doug Thompkins at Utah's Hogle Zoo for furnishing Misha's molar and tusk; David Daballen, Iain Douglas-Hamilton, Daniel Lentipo, Chris Leadismo, and George Wittemyer, at Save The Elephants for sample collection; Scott Beld, Dan Davis, and Jared Singer for assistance

with sample preparation, photomicroscopy, and isotope analyses; Adam Rountrey for furnishing a copy of the ImageJ plug-in (IncMeas v1.2) used to measure growth increments; CL Lin and Ching Hoa Hsieh for assistance with micro-CT work at the University of Utah; Fernando Medina for access to and assistance with the pycnometer in Jan Miller's laboratory; Diego Fernandez, Glen Mackey, and Chris Anderson for assistance with LA-ICP-MS sampling and analyses; and Scott Hynek for Sr isotope analyses of zoo water samples. I thank John M. Harris at the Los Angeles County Museum and the Mary Thompson at the Idaho Museum of Natural History for information on fossil proboscidean material. Research was supported by National Science Foundation grants EAR-0819611 and BCS-0621542, a University of Utah Graduate Research Fellowship, and the Department of Geology and Geophysics Graduate Research Fund. This work was carried out under CITES permits US831854/9, 02US053837/9, and 07US159997/9.

5.9 References

Balasse, M., 2002, Reconstructing dietary and environmental history from enamel isotopic analysis: Time resolution of intra-tooth sequential sampling: International Journal of Osteoarchaeology, v. 12, no. 3, p. 155-165.

-, 2003, Potential biases in sampling design and interpretation of intra-tooth isotope analysis: International Journal of Osteoarchaeology, v. 13, no. 1-2, p. 3-10.

Balasse, M., Ambrose, S. H., Smith, A. B., and Price, T. D., 2002, The seasonal mobility model for prehistoric herders in the south-western Cape of South Africa assessed by isotopic analysis of sheep tooth enamel: Journal of Archaeological Science, v. 29, no. 9, p. 917-932.

Balasse, M., Smith, A. B., Ambrose, S. H., and Leigh, S. R., 2003, Determining sheep birth seasonality by analysis of tooth enamel oxygen isotope ratios: The Late Stone Age site of Kasteelberg (South Africa): Journal of Archaeological Science, v. 30, no. 2, p. 205-215.

Dettman, D. L., Kohn, M. J., Quade, J., Ryerson, F., Ojha, T. P., and Hamidullah, S., 2001, Seasonal stable isotope evidence for a strong Asian monsoon throughout the past 10.7 my: Geology, v. 29, no. 1, p. 31.

Dirks, W., Bromage, T. G., and Agenbroad, L. D., 2012, The duration and rate of molar plate formation in *Palaeoloxodon cypriotes* and *Mammuthus columbi* from dental histology: Quaternary International, v. 255, p. 79-85.

Fisher, D. C., and Fox, D. L., 2007, Season of Death of the Dent Mammoths, *in* Brunswig, R. H., and Pitblado, B. L., eds., From the Dent Prairie to the Peaks of the Rockies: Recent Paleoindian Research in Colorado: Boulder, University of Colorado Press, p. 123-153.

Fricke, H. C., Clyde, W. C., O'Neil, J. R., and Gingerich, P. D., 1998, Evidence for rapid climate change in North America during the latest Paleocene thermal maximum: Oxygen isotope compositions of biogenic phosphate from the Bighorn Basin (Wyoming): Earth and Planetary Science Letters, v. 160, no. 1, p. 193-208.

Fricke, H. C., and O'Neil, J. R., 1996, Inter-and intra-tooth variation in the oxygen isotope composition of mammalian tooth enamel phosphate: Implications for palaeoclimatological and palaeobiological research: Palaeogeography, Palaeoclimatology, Palaeoecology, v. 126, no. 1, p. 91-99.

Frémondeau, D., Cucchi, T., Casabianca, F., Ughetto-Monfrin, J., Horard Herbin, M., and Balasse, M., 2012, Seasonality of birth and diet of pigs from stable isotope analyses of tooth enamel (δ18O, δ13C): A modern reference data set from Corsica, France: Journal of Archaeological Science.

Hiller, C. R., Robinson, C., and Weatherell, J. A., 1975, Variations in the composition of developing rat incisor enamel: Calcified Tissue International, v. 18, no. 1, p. 1-12.

Hoppe, K. A., Stover, S. M., Pascoe, J. R., and Amundson, R., 2004, Tooth enamel biomineralization in extant horses: Implications for isotopic microsampling: Palaeogeography, Palaeoclimatology, Palaeoecology, v. 206, no. 3, p. 355-365.

Hsieh, C. H., 2012, Procedure and analysis of mineral samples using high resolution X-ray micro tomography: Master of Science, University of Utah, 151 p.

Ingram, L. B., and Weber, P. K., 1999, Salmon origin in California's Sacramento–San Joaquin river system as determined by otolith strontium isotopic composition: Geology, v. 27, no. 9, p. 851-854.

Jochum, K. P., Scholz, D., Stoll, B., Weis, U., Wilson, S. A., Yang, Q., Schwalb, A., Börner, N., Jacob, D. E., and Andreae, M. O., 2012, Accurate trace element analysis of speleothems and biogenic calcium carbonates by LA-ICP-MS: Chemical Geology, v. 318, p. 31-44.

Koch, P. L., Fisher, D. C., and Dettman, D., 1989, Oxygen isotope variation in the tusks of extinct proboscideans: A measure of season of death and seasonality: Geology, v. 17, no. 6, p. 515-519.

Koch, P. L., Hoppe, K. A., and Webb, S. D., 1998, The isotopic ecology of late Pleistocene mammals in North America: Part 1. Florida: Chemical Geology, v. 152, no. 1-2, p. 119-138.

Kohn, M. J., Miselis, J. L., and Fremd, T. J., 2002, Oxygen isotope evidence for progressive uplift of the Cascade Range, Oregon: Earth and Planetary Science Letters, v. 204, no. 1, p. 151-165.

Lee-Thorp, J. A., and dan der Merwe, N. J., 1987, Carbon isotope analysis of fossil bone apatite: South African Journal of Science, v. 83, no. 11, p. 712-715.

Menke, W., 1989, Geophysical Data Analysis: Discrete Inverse Theory, San Diego, Academic Press, International Geophysics Series, 289 p.

Metcalfe, J. Z., Longstaffe, F. J., Ballenger, J. A. M., and Haynes Jr, C. V., 2011, Isotopic paleoecology of Clovis mammoths from Arizona: Proceedings of the National Academy of Sciences, v. 108, no. 44, p. 17916-17920.

Miller, W. E., 1971, Pleistocene vertebrates of the Los Angeles Basin and vicinity (exclusive of Rancho La Brea): Bulletin of the Los Angeles County Museum of Natural History, v. 10, 124 p.

Moss-Salentijn, L., Moss, M., and Yuan, M. S., 1997, The ontogeny of mammalian enamel, *in* Von Koenigswald, W., and Sander, P., eds., Tooth Enamel Microstructure: Rotterdam, AA Balkema, p. 5-30.

Passey, B. H., and Cerling, T. E., 2002, Tooth enamel mineralization in ungulates; implications for recovering a primary isotopic time-series: Geochimica et Cosmochimica Acta, v. 66, no. 18, p. 3225-3234.

-, 2004, Response to the comment by MJ Kohn on "Tooth enamel mineralization in ungulates: Implications for recovering a primary isotopic time-series" by BH Passey and TE Cerling (2002): Geochimica et Cosmochimica Acta, v. 68, no. 2, p. 407-410.

-, 2006, In situ stable isotope analysis ($\delta^{13}C$,$\delta^{18}O$) of very small teeth using laser ablation GC/IRMS: Chemical Geology, v. 235, no. 3-4, p. 238-249.

Passey, B. H., Cerling, T. E., Perkins, M. E., Voorhies, M. R., Harris, J. M., and Tucker, S. T., 2002, Environmental change in the Great Plains; an isotopic record from fossil horses: Journal of Geology, v. 110, no. 2, p. 123-140.

Passey, B. H., Cerling, T. E., Schuster, G. T., Robinson, T. F., Roeder, B. L., and Krueger, S. K., 2005, Inverse methods for estimating primary input signals from time-averaged isotope profiles: Geochimica et Cosmochimica Acta, v. 69, no. 16, p. 4101-4116.

Pinsof, J. D., 1992, The late Pleistocene vertebrate fauna from the American Falls area, southeastern Idaho: Dissertation, Idaho State University, 232 p.

Rountrey, A. N., Fisher, D. C., Tikhonov, A. N., Kosintsev, P. A., Lazarev, P. A., Boeskorov, G., and Buigues, B., 2012, Early tooth development, gestation, and season of birth in mammoths: Quaternary International, v. 255, p. 196-205.

Rountrey, A. N., Fisher, D. C., Vartanyan, S., and Fox, D. L., 2007, Carbon and nitrogen isotope analyses of a juvenile woolly mammoth tusk: Evidence of weaning: Quaternary International, v. 169, p. 166-173.

Schoeninger, M. J., and DeNiro, M. J., 1982, Carbon isotope ratios of apatite from fossil bone cannot be used to reconstruct diets of animals: Nature, v. 297, p 577-578.

Scott, W., Pierce, K., Bradbury, J. P., and Forester, R., 1982, Revised Quaternary stratigraphy and chronology in the American Falls area, southeastern Idaho: Cenozoic Geology of Idaho: Idaho Bureau of Mines and Geology Bulletin, v. 26, p. 581-595.

Suga, S., 1982, Progressive mineralization pattern of developing enamel during the maturation stage: Journal of Dental Research, v. 61, p. 1532-1542.

-, 1989, Enamel hypomineralization viewed from the pattern of progressive mineralization of human and monkey developing enamel: Advances in Dental Research, v. 3, no. 2, p. 188-198.

Tafforeau, P., Bentaleb, I., Jaeger, J. J., and Martin, C., 2007, Nature of laminations and mineralization in rhinoceros enamel using histology and X-ray synchrotron microtomography: Potential implications for palaeoenvironmental isotopic studies: Palaeogeography, Palaeoclimatology, Palaeoecology, v. 246, no. 2, p. 206-227.

Wang, Y., and Cerling, T. E., 1994, A model of fossil tooth and bone diagenesis: Implications for paleodiet reconstruction from stable isotopes: Palaeogeography, Palaeoclimatology, Palaeoecology, v. 107, no. 3-4, p. 281-289.

Weatherell, J., Robinson, C., and Hallsworth, A., 1974, Variations in the chemical composition of human enamel: Journal of Dental Research, v. 53, no. 2, p. 180-192.

Zazzo, A., Balasse, M., Passey, B., Moloney, A., Monahan, F., and Schmidt, O., 2010, The isotope record of short-and long-term dietary changes in sheep tooth enamel: Implications for quantitative reconstruction of paleodiets: Geochimica et Cosmochimica Acta, v. 74, no. 12, p. 3571-3586.

Zazzo, A., Balasse, M., and Patterson, W. P., 2005, High-resolution $\delta^{13}C$ intratooth profiles in bovine enamel: Implications for mineralization pattern and isotopic attenuation: Geochimica et Cosmochimica Acta, v. 69, no. 14, p. 3631-3642.

Zazzo, A., Bendrey, R., Vella, D., Moloney, A., Monahan, F., and Schmidt, O., 2012, A refined sampling strategy for intra-tooth stable isotope analysis of mammalian enamel: Geochimica et Cosmochimica Acta, v. 84, 1-13.

Zhdanov, M. S., 2002, Geophysical Inverse Theory and Regularization Problems, Netherlands, Elsevier Science Ltd, Methods in Geochemistry and Geophysics, 609 p.

Table 5.1. List of analyses performed by sample ID and element on fossil and modern proboscidean molars and tusks. Conv.= conventional

Sample ID and element	Isotope profile			Thin section	μCT	Histological analyses	14C
	Conv.	Laser	μmill				
R37 molar	X						X
R37 tusk			X	X		X	X
Misha molar	X	X	X	X	X	X	
Misha tusk (M640)			X			X	X
K95-M53 molar					X		
TE-95 molar				X		X	X
IMNH-40368 molar	X						
LACM-47129 molar	X						

Table 5.2. Modeled crown formation time (CFT) in years for three proboscidean molar plates. Misha_Rm3.5 and TE-95_Rm3.7 are Loxodonta africana and IMNH-40368 is a Mammuthus columbi. Modeled results assume constant daily secretion rates (DSR). DSR values in microns.

	CFT (years)		
Thin section	DSR=2	DSR=3	DSR=4
Misha_Rm3.5	7.26	4.84	3.63
TE-95_Rm3.7	9.00	6.00	4.50
	DSR=3	**DSR=3.5**	**DSR=4**
IMNH-40368	12.89	11.05	9.67

Table 5.3. Mean $\delta^{13}C$ and $\delta^{18}O$ values for all Misha enamel and tusk apatite that formed during her time in Utah (2005–2009). All enamel values are in agreement, whereas tusk dentin is ~ + 1 ‰ depleted in $\delta^{13}C$ and enriched in ~ + 1.3 ‰ in $\delta^{18}O$ compared to enamel. Laser values are corrected to conventional (acid digestion) values using $\varepsilon^*_{laser\text{-}acid}$ values of -0.7 ‰ for carbon and -7.4 ‰ for oxygen.

		‰				
Sample ID	**Sampling method**	**$\delta^{13}C$**	**1σ**	**$\delta^{18}O$**	**1σ**	**n**
Enamel						
Misha _Rm3.5	conventional	-12.7	0.3	-14.3	0.5	26
Misha _Rm3.5	micromill	-12.4	0.3	-14.2	0.4	17
Misha _Rm3.5	laser	-12.6	0.5	-14.2	0.6	7
Ivory						
Misha_M640	micromill	-13.3	0.6	-12.9	0.8	45

Table 5.4. Comparison of the magnitude of isotopic shift (Δδ) associated with the move from CA to UT by sampling method. The magnitude of the shift in the enamel is also shown as a % of the shift in the M640 tusk dentin profile, which is assumed to represent the primary input signal. Enamel maturation and sample geometry lead to damping of the full magnitude of the shift. Conv. = conventional, and modeled conv. is the result of running the conventional data in the inversion model.

Sample ID	**Sampling method**	**Δ $\delta^{13}C$ (‰)**	**%Δ $\delta^{13}C_{tusk}$**	**Δ $\delta^{18}O$ (‰)**	**%Δ $\delta^{18}O_{tusk}$**
Tusk dentin					
Misha_M640	micromill	-8.3	—	-5.0	—
Enamel					
Misha _Rm3.5	micromill	-3.1	37%	-2.2	44%
Misha _Rm3.5	laser	-6.0	72%	-3.2	64%
Misha _Rm3.5	conv.	-4.0	48%	-3.4	68%
Misha _Rm3.5	modeled conv.	-9.1	110%	-5.5	110%

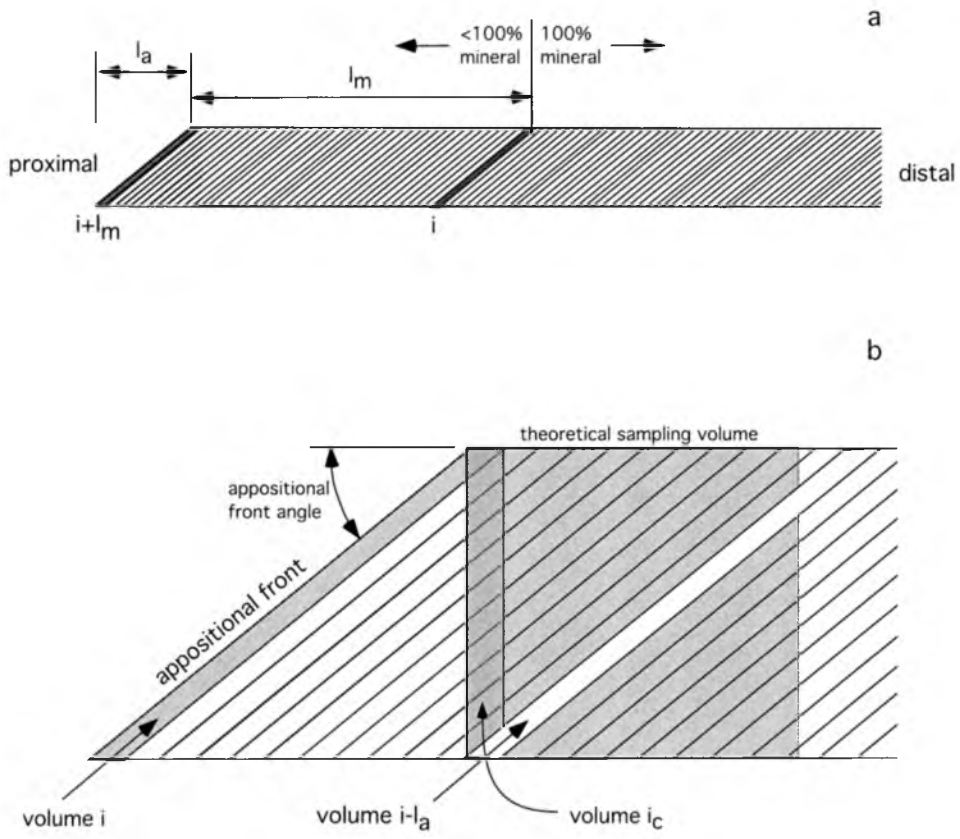

Figure 5.1. Schematic of an enamel cross-section illustrating enamel formation and model parameters describes in equations 5.2 to 5.4. Only enamel is shown, the EDJ is at the bottom of each schematic, and the enamel is forming from right to left. a) Model parameters l_a and l_m are shown. Volume *i* is in the final stage of maturation whereas volume $i+l_m$ is the most recently formed volume in the secretory phase with density f_i. b) Volume *i* is also shown here, as is volume i_c, a column described in equation 5.3. A theoretical sampling volume described in equation 5.4 is comprised of n columns of dimension i_c, and is shown here with a width (Δx) and depth (Δz) through the full enamel thickness by the shaded square. From Passey and Cerling (2002).

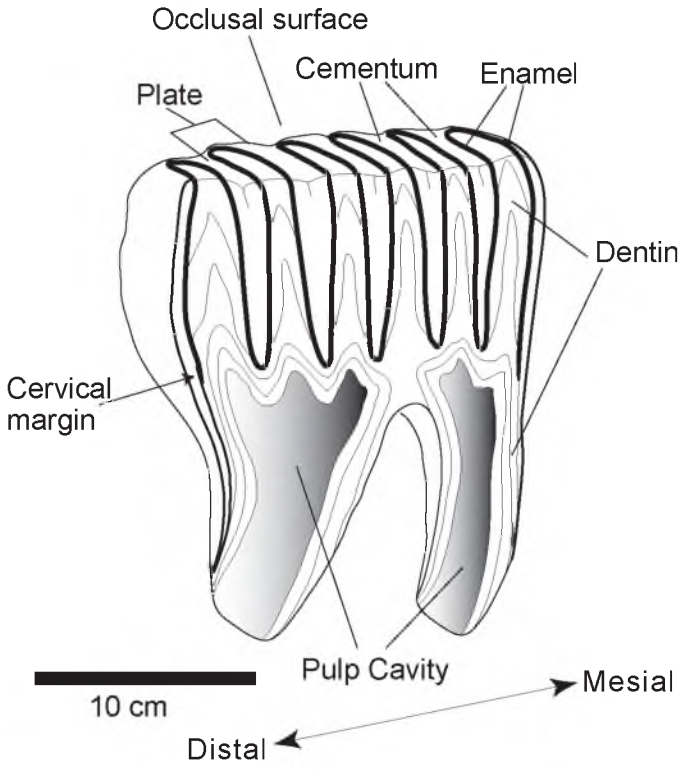

Figure 5.2. Schematic drawing of a fully-formed proboscidean molar with a worn occlusal surface. The molar comprises six plates cemented together. Each enamel-covered plate has a dentin interior and is joined to adjacent plates by cementum. Modified from Fisher and Fox (2007).

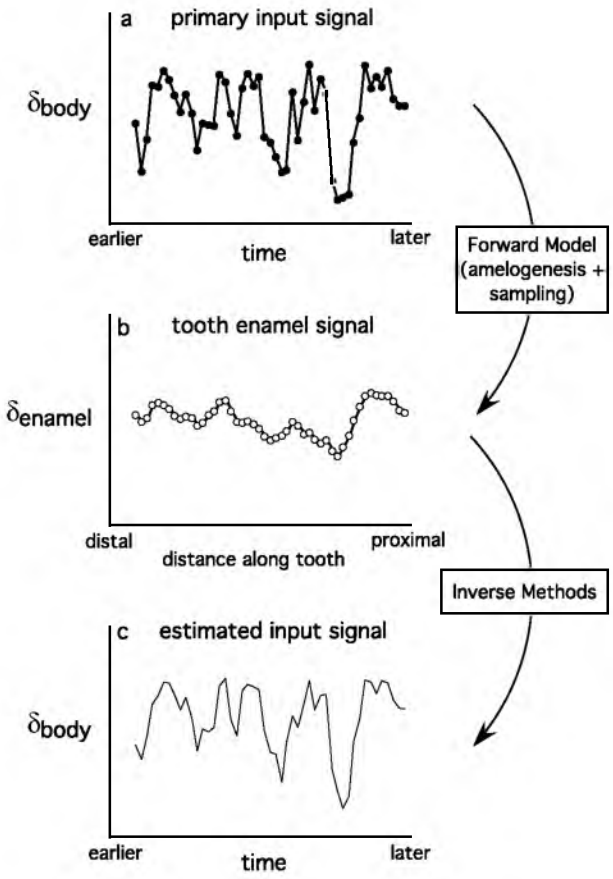

Figure 5.3: Schematic representation of forward and inverse models. From Passey et al., 2005.

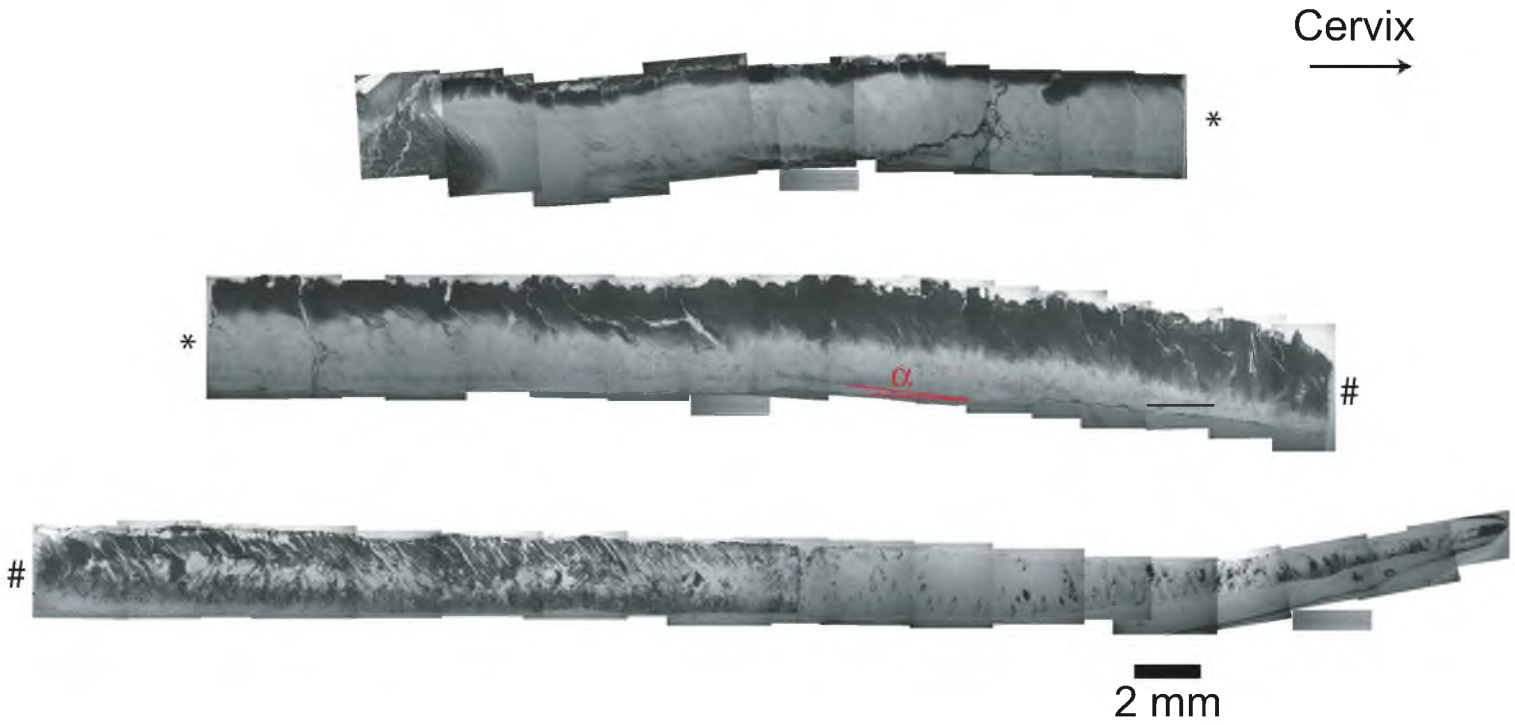

Figure 5.4. Composite photomicrograph from elephant molar thin section Misha_Rm3.5 at 40x magnification. The upper, middle, and lower images represent the top, middle, and bottom of the posterior side of the molar plate from the crown apex to the cervix, which is towards the right in all three images. Image tie points are indicated by symbols (*,#). The entire enamel thickness is shown throughout most of the images, and the EDJ is at the base of each image.

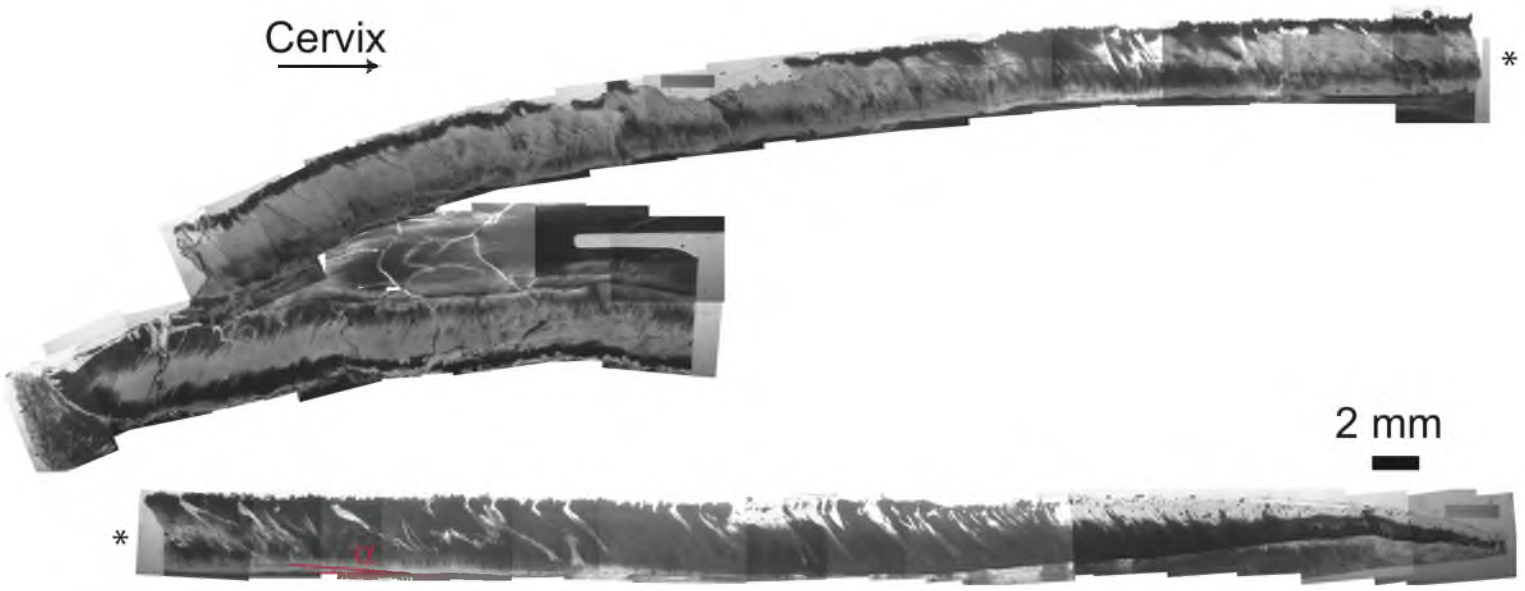

Figure 5.5. Composite photomicrograph from elephant molar thin section TE-95_Rm3.7 at 25x magnification. The upper and lower images comprise the posterior side of the molar plate from the crown apex to the cervix, which is towards the right in both images. Image tie points are indicated by asterisks. The entire enamel thickness (~3 mm) is shown throughout most of the images, and the EDJ is at the base of each image.

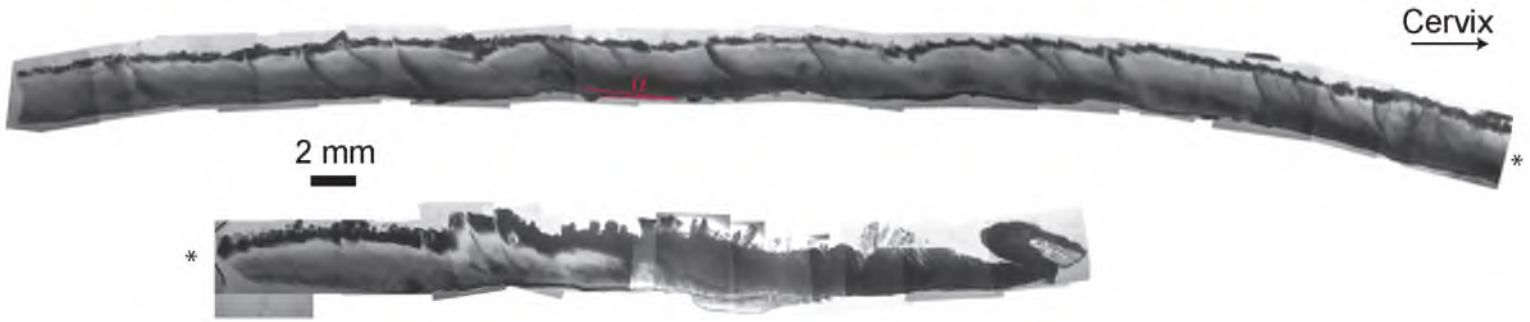

Figure 5.6. Composite photomicrograph from mammoth molar thin section IMNH-40368 at 25x magnification. The upper and lower images comprise the posterior side of the molar plate from the crown apex to the cervix, which is towards the right in both images. Image tie points are indicated by asterisks. The entire enamel thickness (~2.8 mm) is shown throughout all images, and the EDJ is at the base of each image.

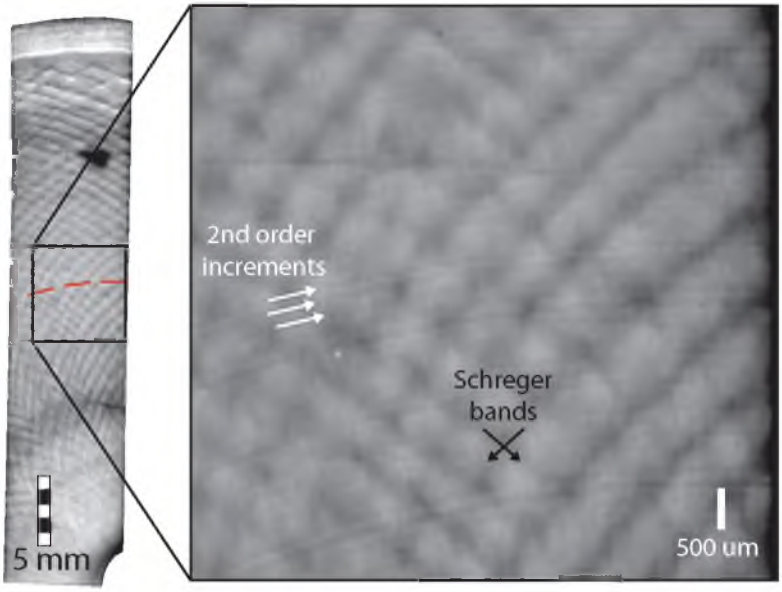

Figure 5.7. Flatbed scan of the proximal transverse side of Misha ivory slab M640. The tip of the pulp cavity is shown in the lower right corner of the full scan (at left). A red dashed line marks the position where the isotopic shift associated with the move from CA to UT occurs. Scale bar is 5 mm in length. Inset (at right) illustrates the second-order growth increments, indicated by white arrows. Increment thicknesses were measured to determine radial growth rate.

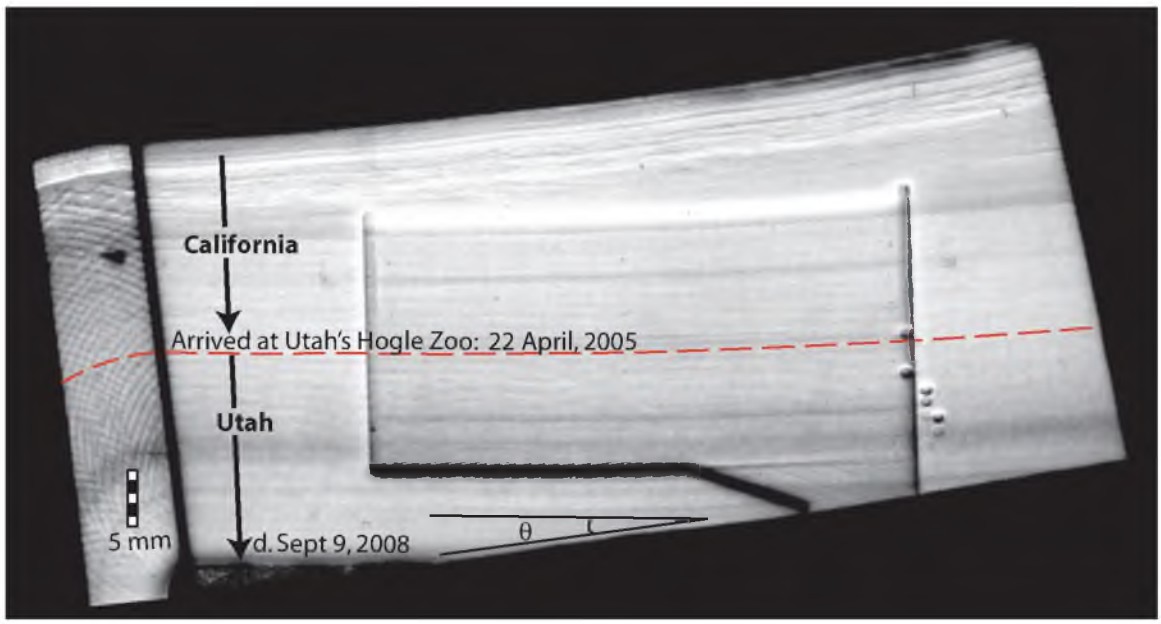

Figure 5.8. Flatbed scan of micromilled sample M640, with the proximal end to the left. On the left of the image is a transversely-cut piece reflected 90° about the vertical axis to show the tree-ring like structure. To the right is the polished longitudinally-cut slab after micromilling. The tip of the pulp cavity can be seen in the lower left part of the image. The red line is an isochron indicating the location of the isotopic shift associated with the move from CA to UT. The angle θ was measured at multiple places along the base of the slab to convert axial growth rate to radial growth rate, which enables comparison of axial ^{14}C-derived and radial histologically-derived growth rates.

Figure 5.9. Flatbed scan of conventionally drilled sample Misha_Rm3.5. Samples were drilled on the posterior side of the plate at intervals of 5 mm from 0 to 30 mm from the cervix and ~2 mm from 30 mm to the apex of the tooth (~103mm).

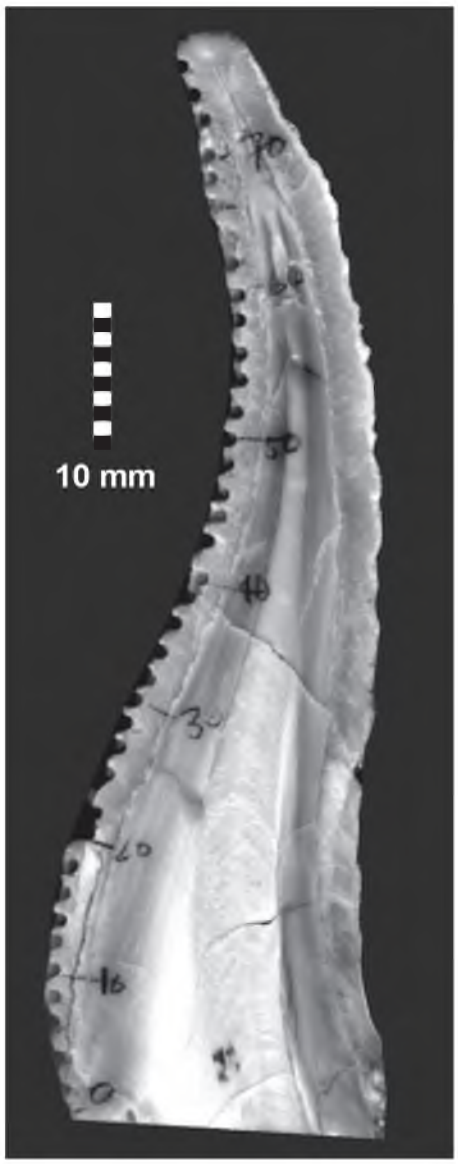

Figure 5.10. Flatbed scan of conventionally drilled sample R37_Rm3.8. Samples were drilled on the side of the plate at ~2 mm interval.

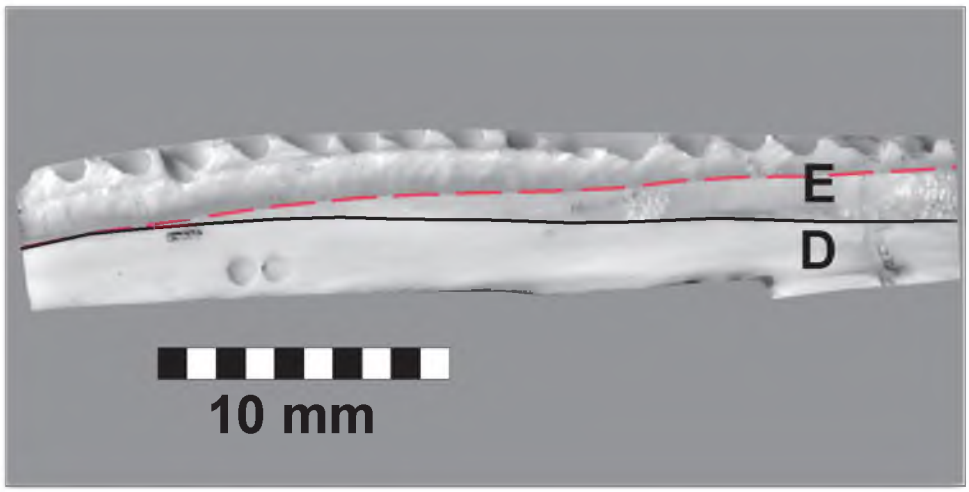

Figure 5.11. Image of sample Misha_Rm3.5b after micromill, laser, and conventional sampling. The black line marks the EDJ and the red dashed line marks the last micromilled scan. The angle of the micromill scans is approximately parallel to the appositional surface, which is ~3.2° offset from EDJ. Width of scale bar is 10 mm.

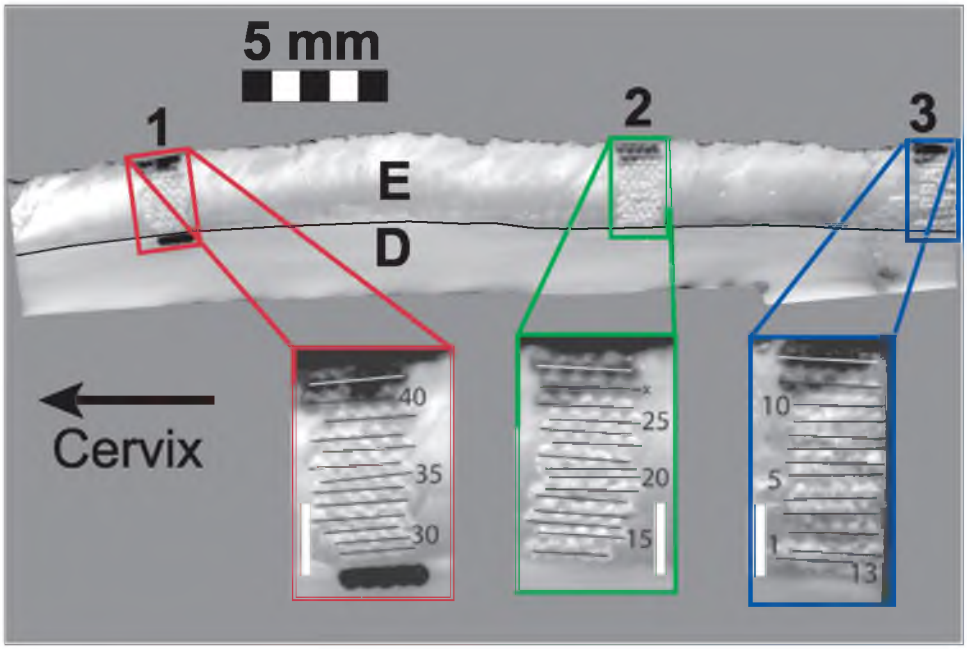

Figure 5.12. Image of sample Misha_Rm3.5b after sampling by LA-GC-IRMS. Profiles 1, 2, and 3, are 54, 71, and 80 mm above the cervix. The inset boxes show individual scans as black lines parallel to the EDJ. There are 5 laser pits per scan. In profile 1, one scan was done in dentin and is shown by the charred area at the base of the image. Charred scans near the outer enamel surface indicate immature enamel that contains a higher concentration of organic material than mature enamel. Width of scale bars is 5 mm in upper image and 1 mm in inset boxes.

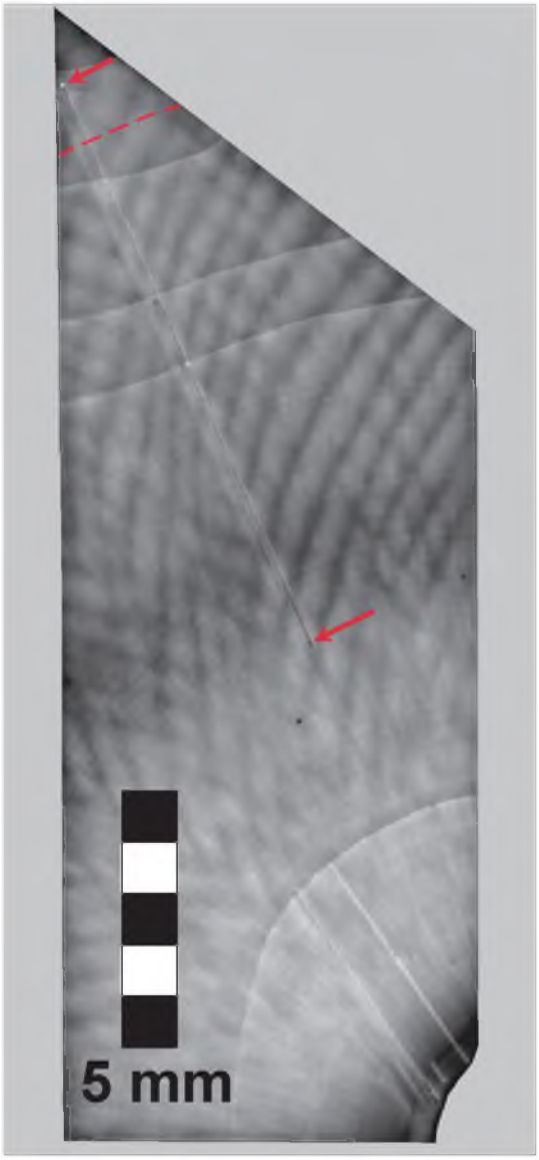

Figure 5.13. Flatbed scan of sample M640b after sampling by LA-ICP-MS. The beginning and end of two parallel scans is shown with two red arrows, with time progressing from the upper left to lower right. Scan lengths are 12 mm each. The right scan was done for elemental abundance with an 86 μm wide x 5 μm high beam, and the left scan was done for $^{87}Sr/^{86}Sr$ with a 65 μm diameter beam. The red dashed line marks the approximate position where the move from CA to UT is recorded in the elemental and Sr isotope data. Scale bar is 5mm in length.

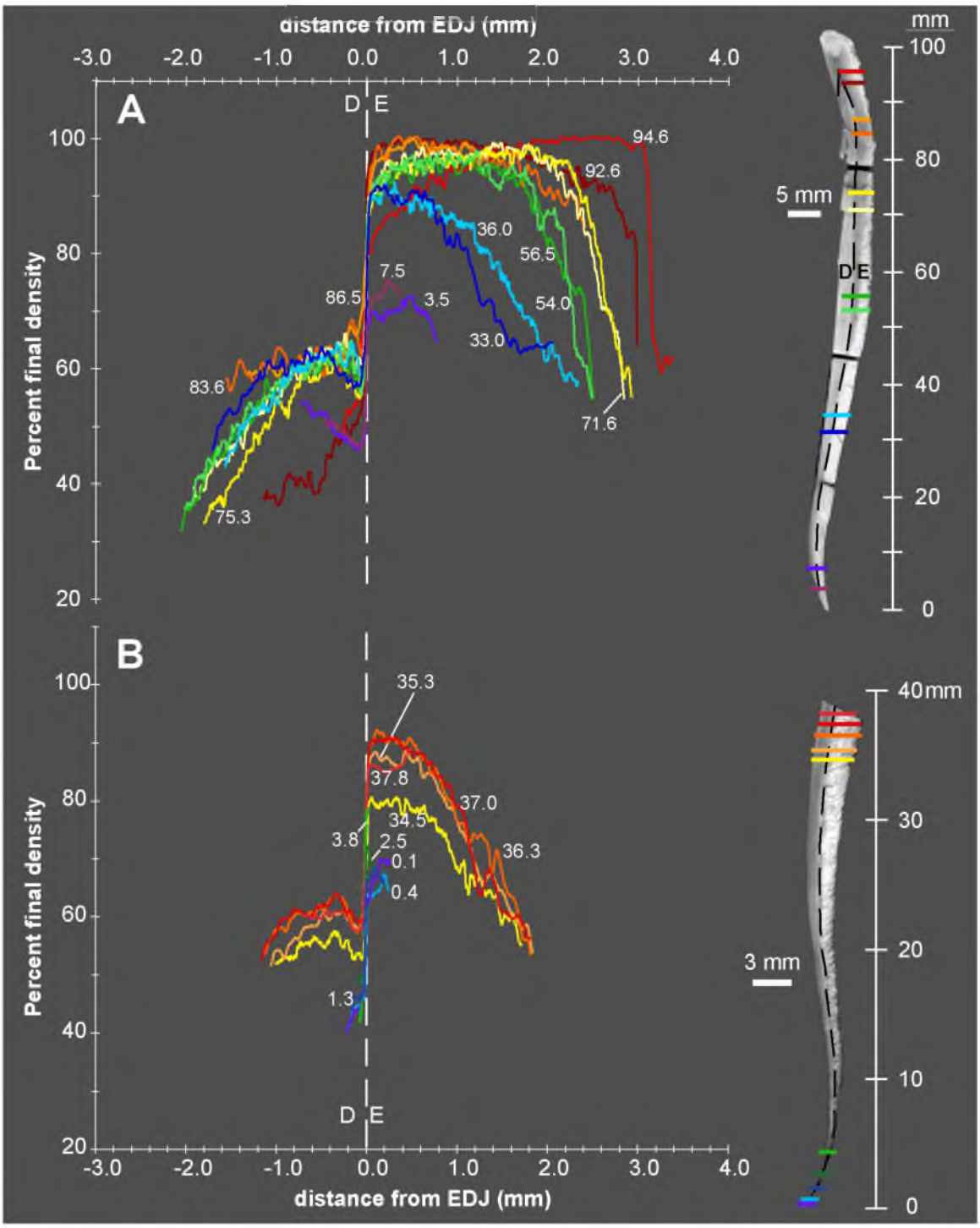

Figure 5.14. Micro-CT transects normal to the EDJ in two molar sections from A) Misha_Rm3.5 and B) K07-M53_m1.9. Grayscale images of specimens are shown at right, each with different length and width scales. Colored lines correspond to distance from the base of the plate. Dentin (D) is to the left and enamel (E) to the right in the plots and images.

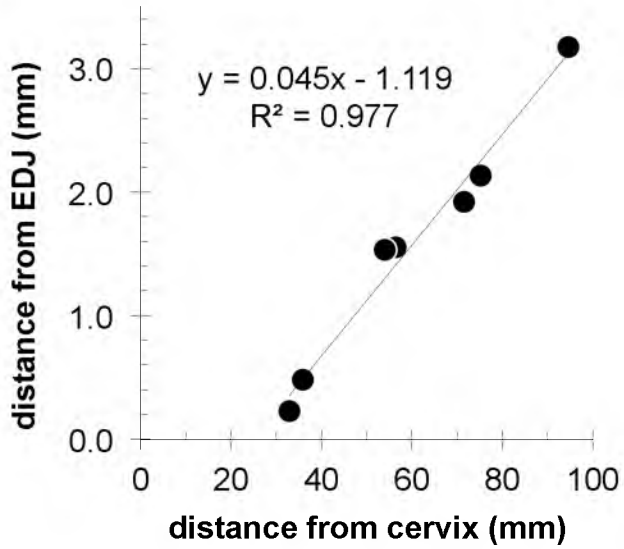

Figure 5.15. The break in slope in a density profile normal to the EDJ indicates the position of the maturation front. Plotted here is the location of the break in slope (mm from the EDJ) vs. the position of the density profile above the cervix (mm). The maturation length (l_m) is 69.8 ± 4.8 mm.

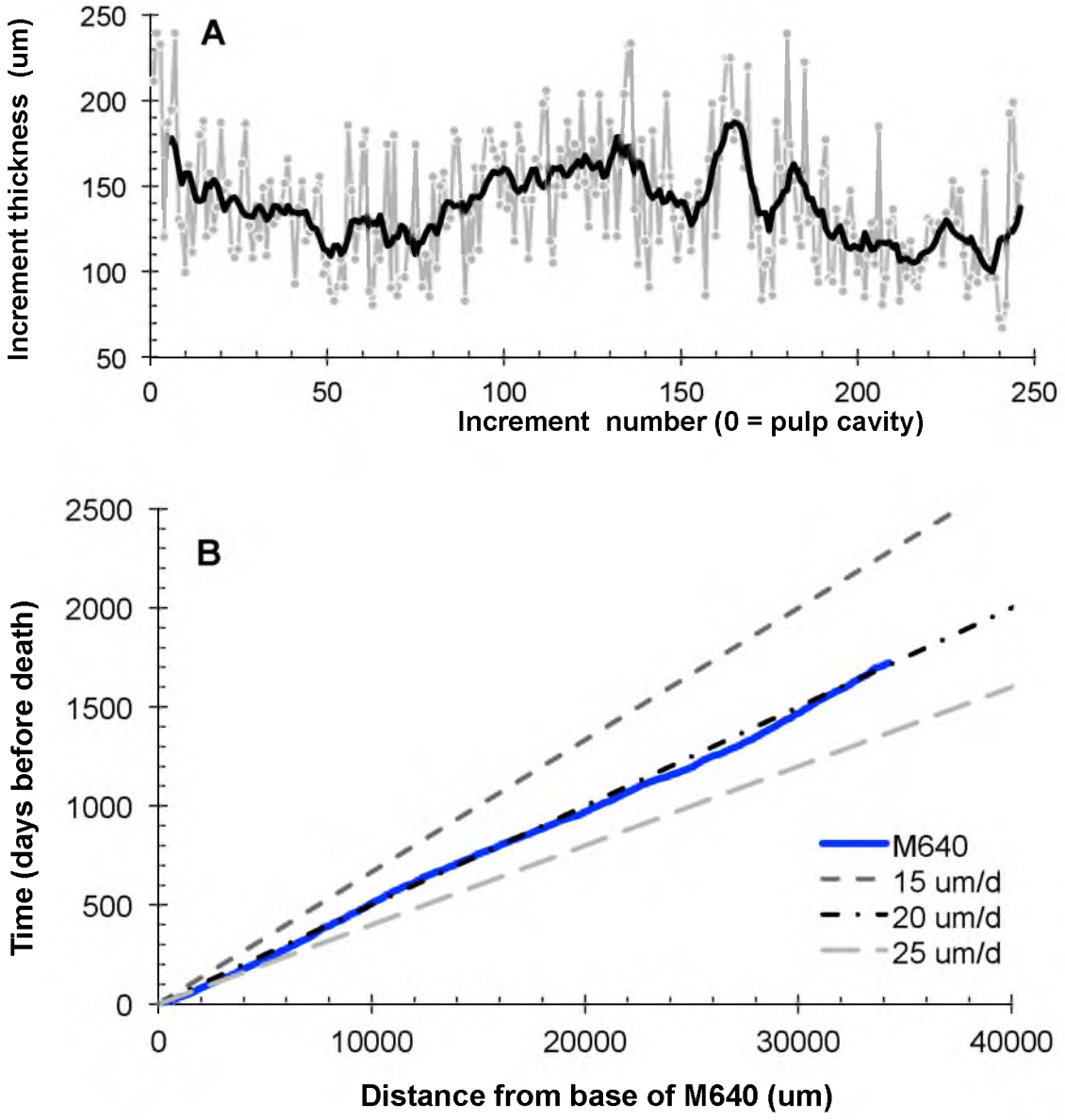

Figure 5.16. Histological data from ivory slab M640. A) Second-order increment thickness vs. increment number with raw data in gray and a 10-point running average in black. B) Sum of increments from the base of M640 vs. number of days since death, assuming each second-order increment represents seven days. Given this assumption, the growth rate is approximately linear (20 μm/day). Modeled linear growth rates (15,20, and 25μm/day) are shown for comparison.

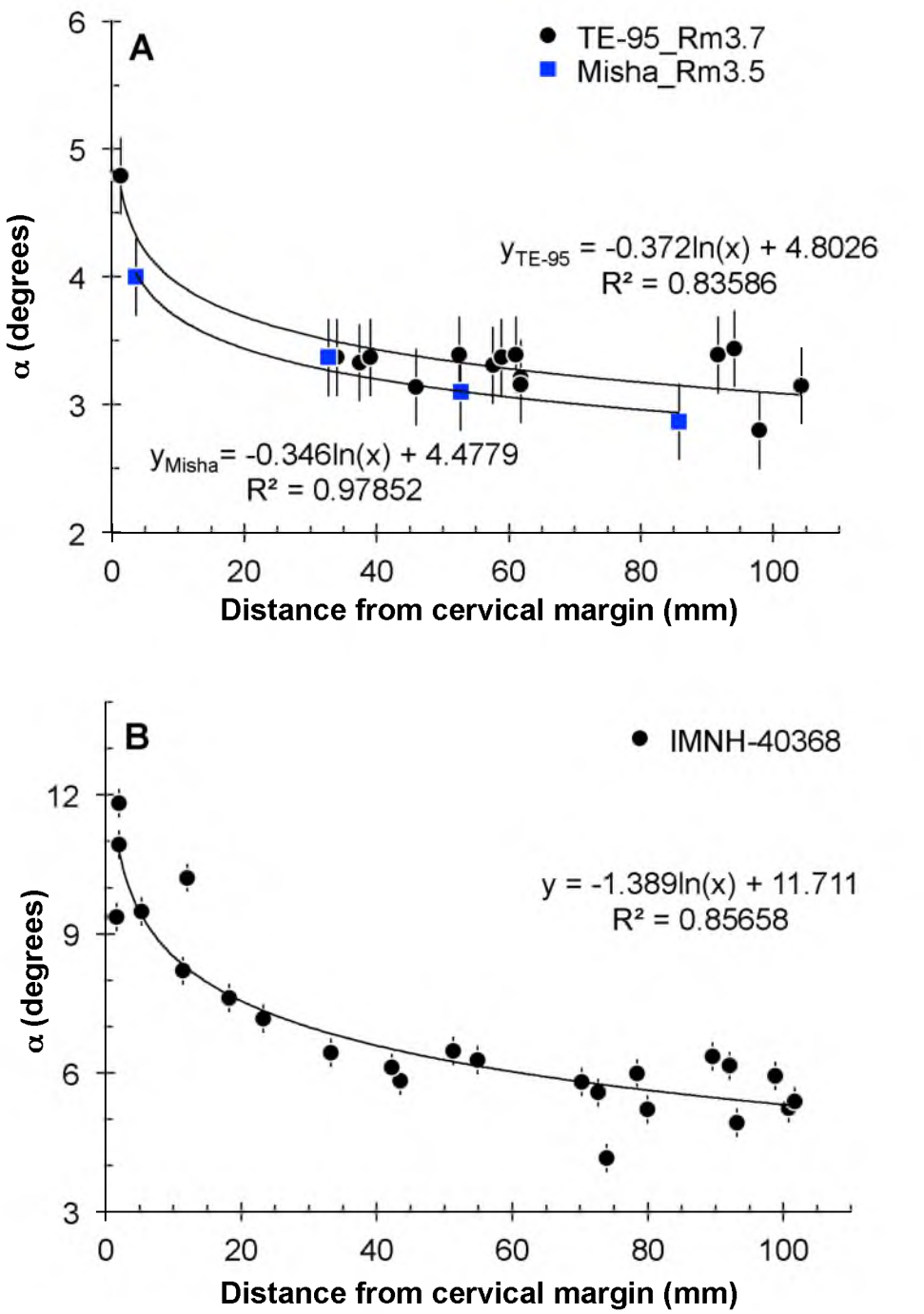

Figure 5.17. Plots of α vs. distance from the cervical margin for two proboscidean species, A) *Loxodonta africana* and B) *Mammuthus columbi*, where α is the angle of apposition measured between the striae of Retzius and the EDJ.

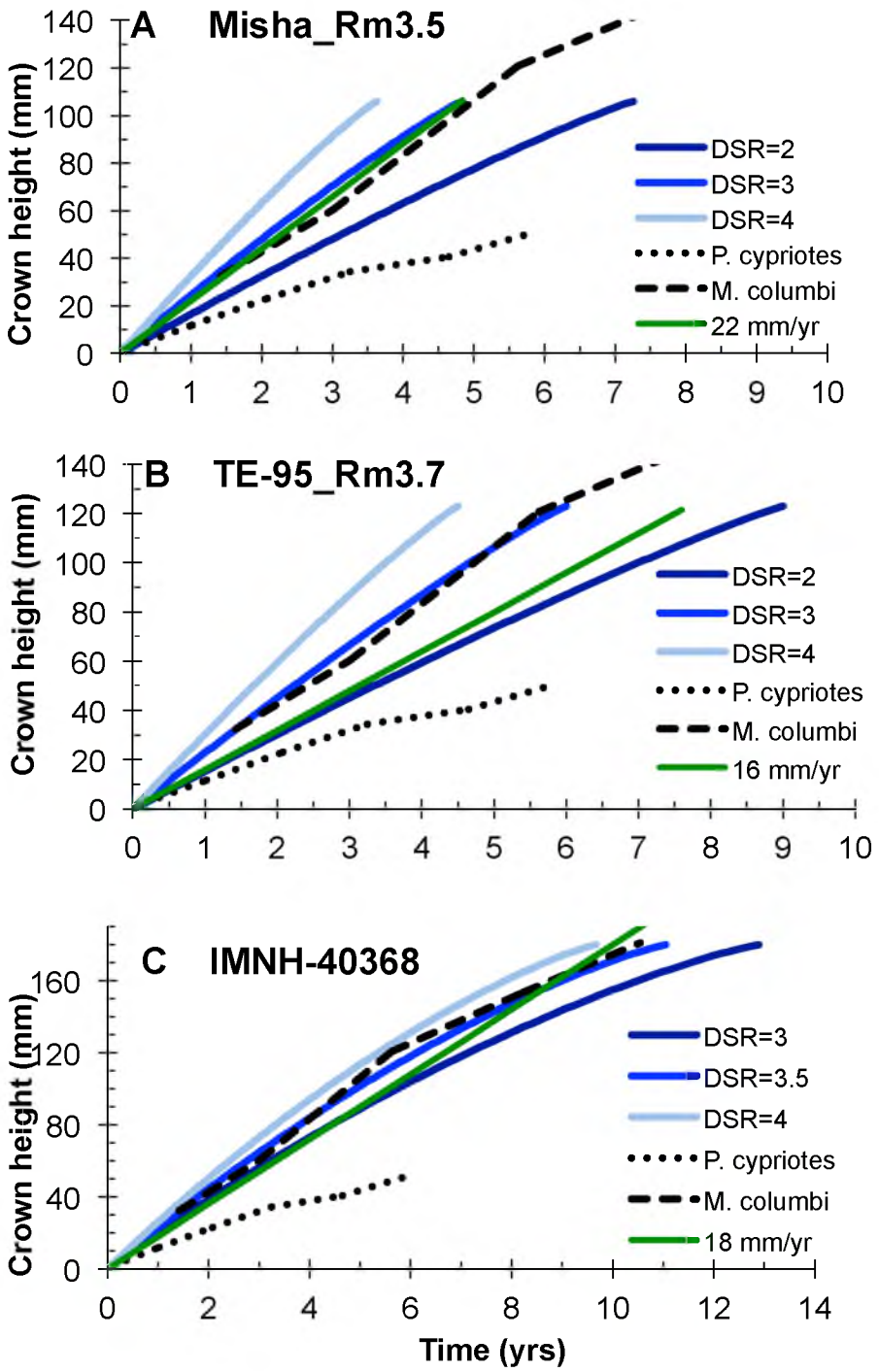

Figure 5.18. Modeled crown formation time (years) for two *L. africana* molar plates (A and B) and *M. columbi* using constant daily secretion rates (DSRs). Appositional angles (α) are from the logarithmic regressions in Figure 5.17. Data from *P. cypriotes* and *M. columbi* (in black) are from Dirks (2012). Green lines represent modeled linear growth rates; for TE-95, the ^{14}C-based growth rate of 16mm/year is modeled.

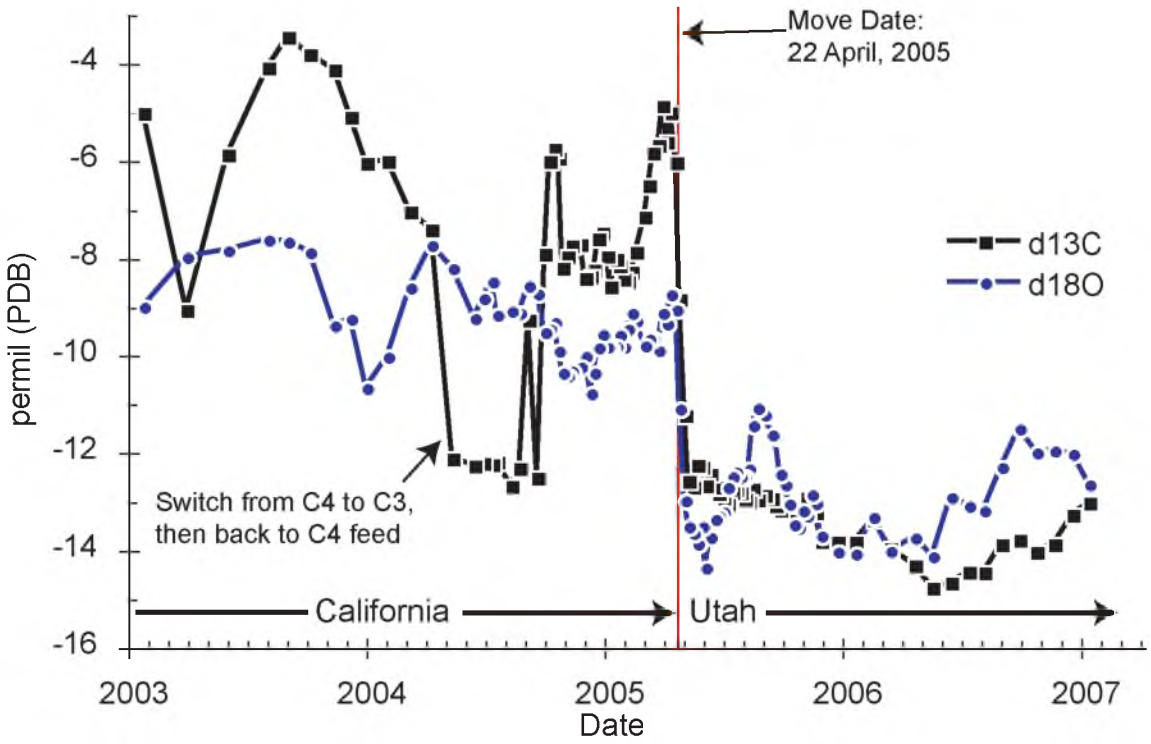

Figure 5.19. $\delta^{13}C$ and $\delta^{18}O$ values from Misha ivory slab M640 (n=97). The time interval is from January 2003 to January 2007. The move from CA to UT occurs in late April 2005 (red line) and results in a sharp decrease in both $\delta^{13}C$ and $\delta^{18}O$ values.

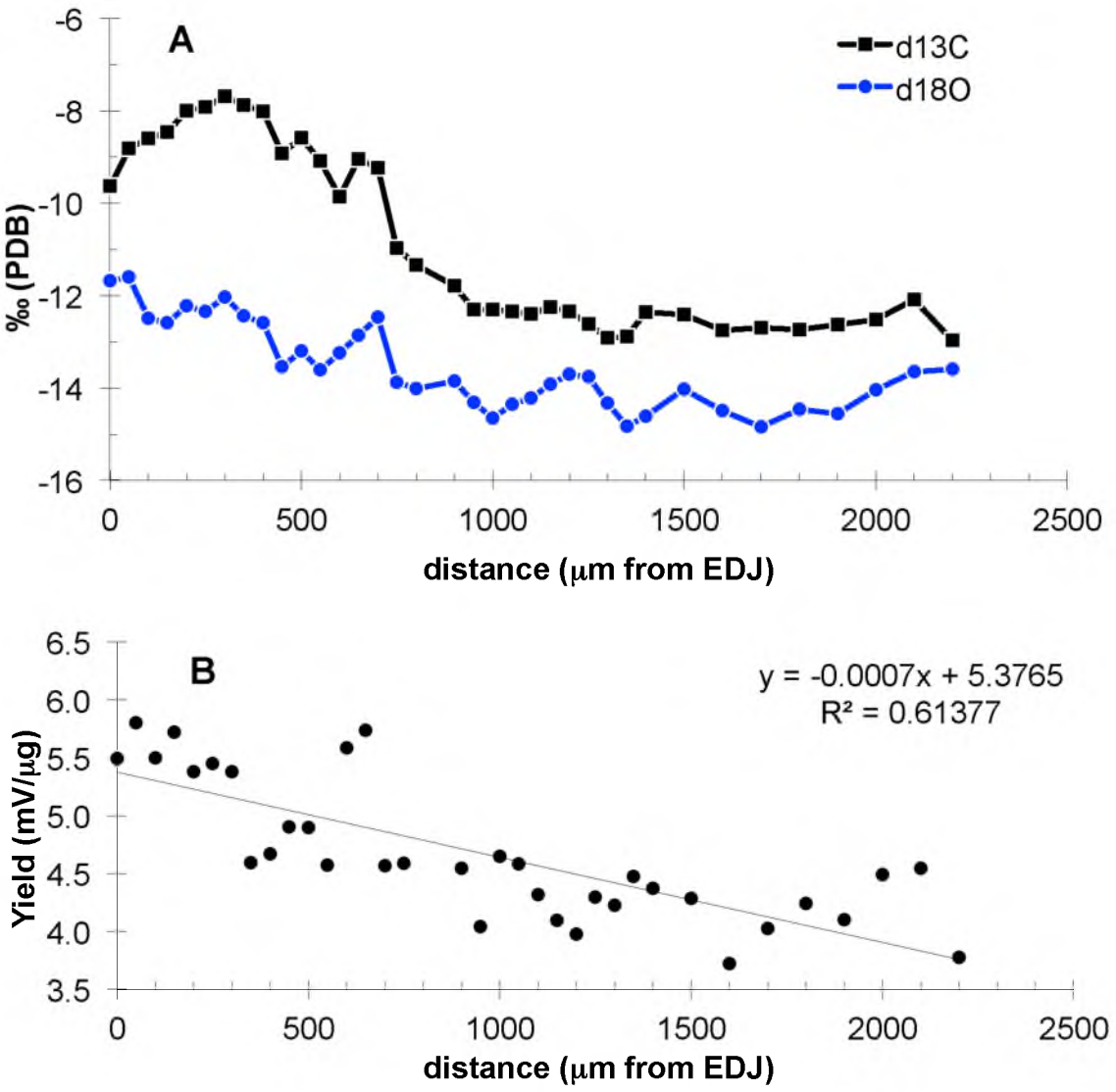

Figure 5.20. A) $\delta^{13}C$ and $\delta^{18}O$ values of samples micromilled at 50μm intervals from Misha_Rm3.5b. The isotopic shift associated with the move from CA to UT occurs 750 μm from the EDJ. B) The decrease in CO_2 yield, measured on the mass spectrometer in millivolts per microgram of sample reacted, from the EDJ to the outer enamel surface illustrates the gradient from mature (5.5 to 5.0 mV/μg) to immature enamel (<5 mV/μg).

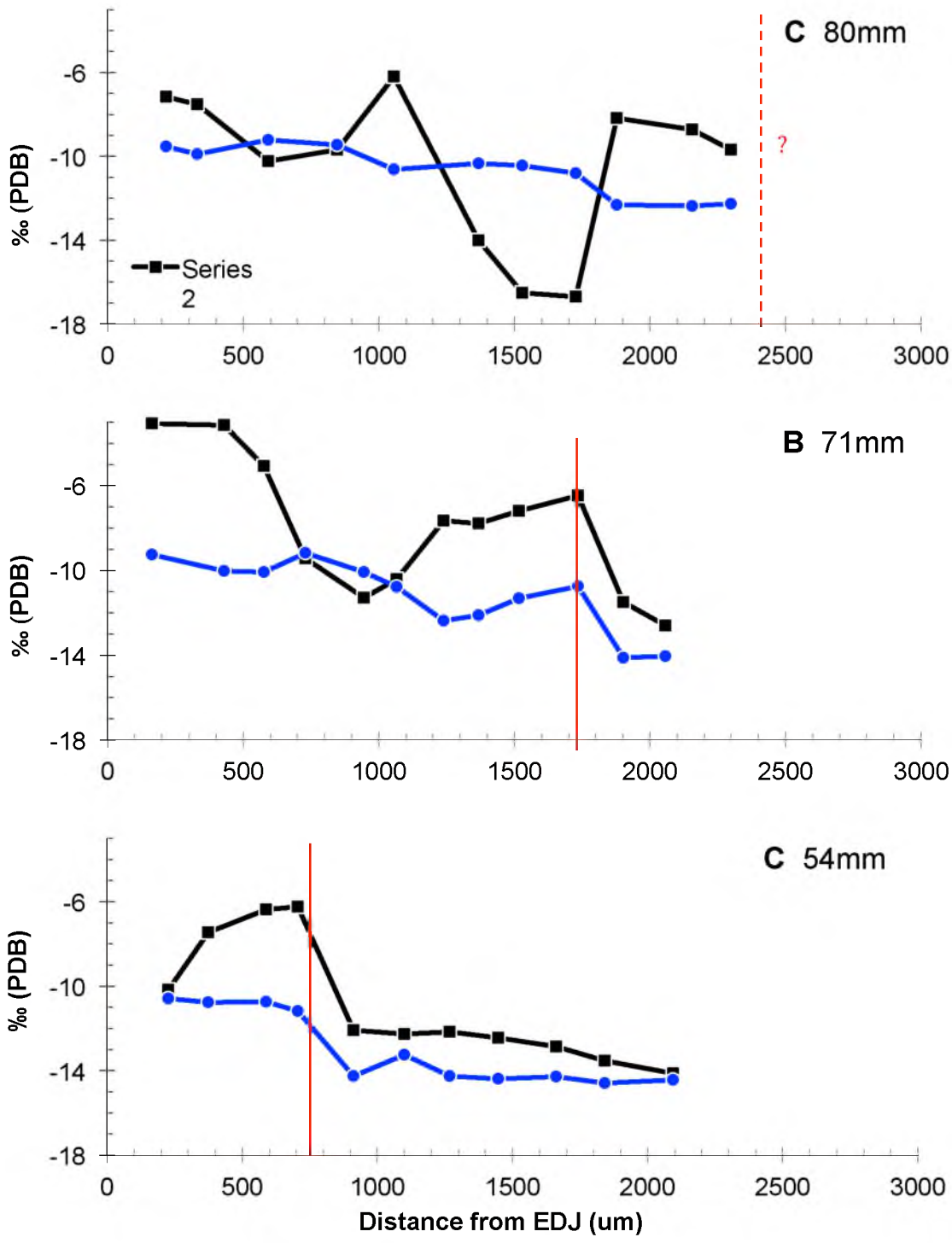

Figure 5.21. $\delta^{13}C$ and $\delta^{18}O$ values from LA-GC-IRMS of Misha_Rm3.5b enamel. Laser scans are approximately parallel to the EDJ. The isotopic shift associated with the move from CA to UT is marked with a red line. Scan regions are A) 80 mm, B) 71 mm, and C) 54 mm above the cervix. The shift occurs closer to the EDJ as the scan region moves closer to the cervix (A to C).

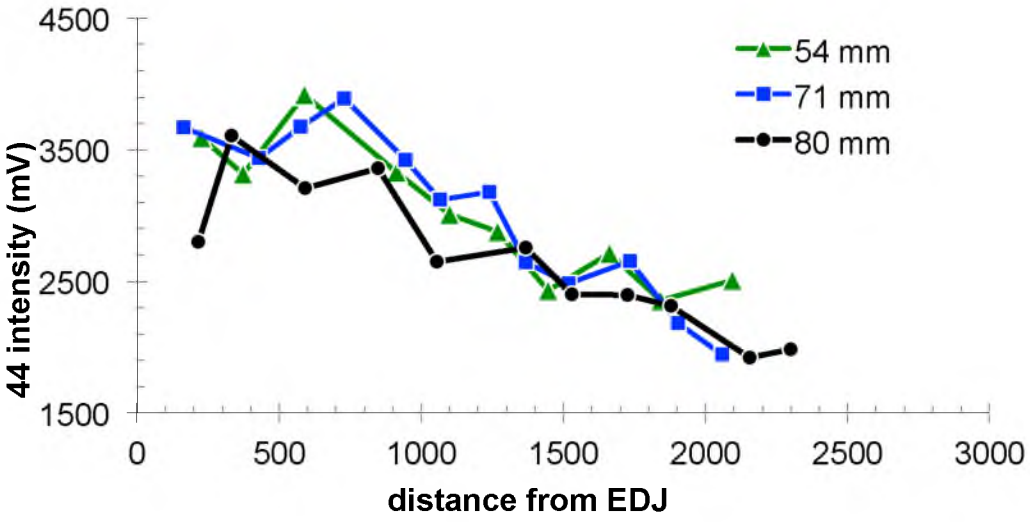

Figure 5.22. LA-GC-IRMS yields versus distance from the EDJ from three profiles at 54, 71, and 80 mm above the cervix. The decrease in CO_2 yield from the EDJ to the outer enamel surface suggests a linear gradient from mature to immature enamel, similar to that observed in Figure 5.20B. All scans were done at the same laser settings, and yield is measured in millivolts on the major mass (44) detector of the IRMS.

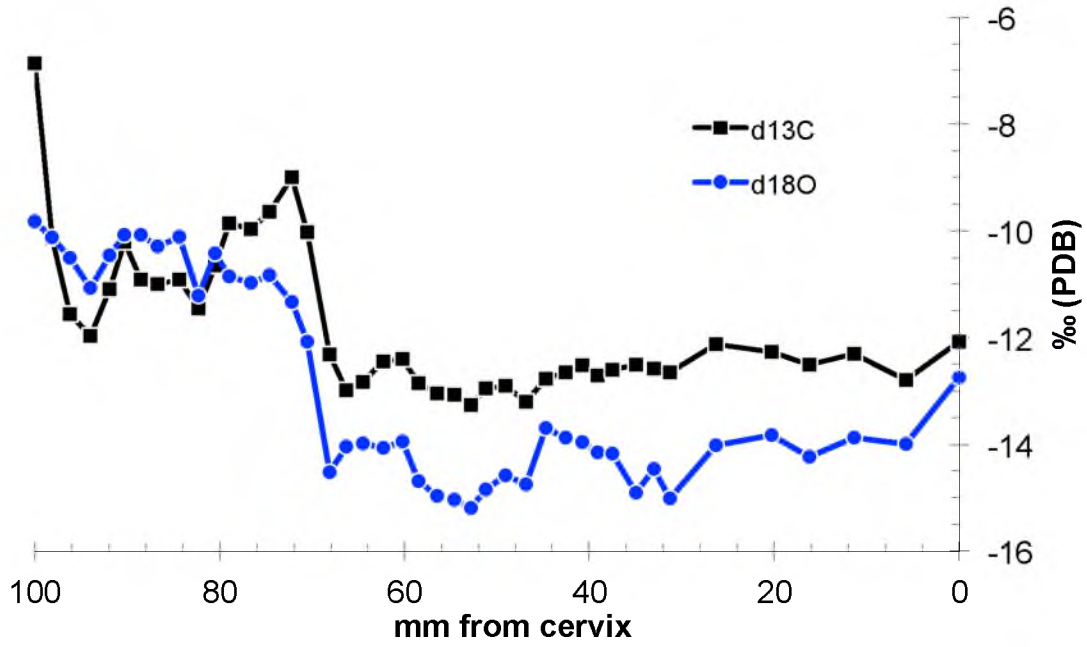

Figure 5.23. $\delta^{13}C$ and $\delta^{18}O$ values of samples conventionally drilled at 2 to 5mm intervals along Misha_Rm3.5. The isotopic shift associated with the move from CA to UT occurs 72 mm above the cervix.

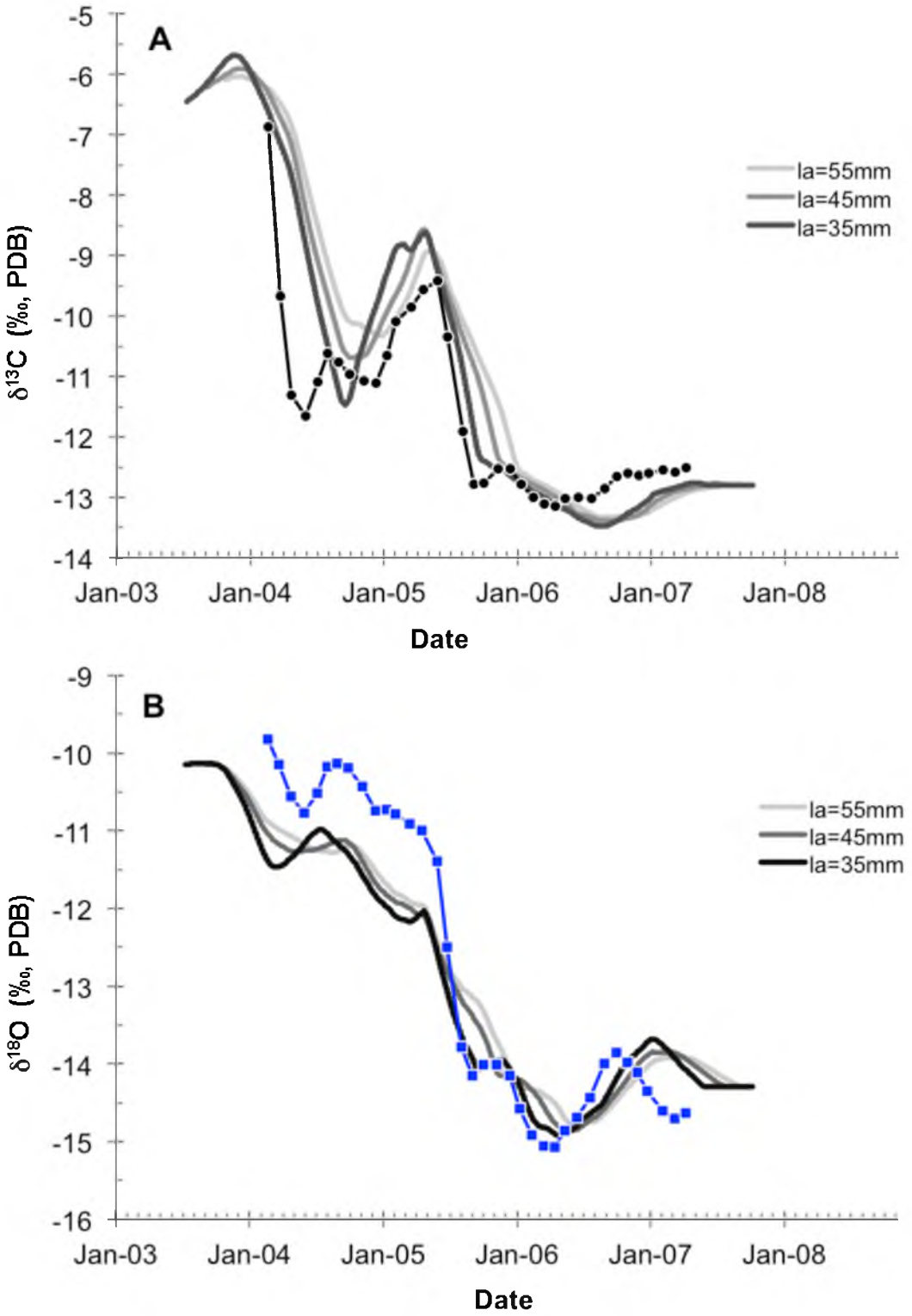

Figure 5.24. Forward model results for A) $\delta^{13}C$ and B) $\delta^{18}O$ from molar Misha_Rm3.5. The three grey lines represent l_a values of 35, 45, and 55 mm. Measured enamel data have been smoothed with a 3-point weighted average and are shown in A) as black circles and in B) as blue squares.

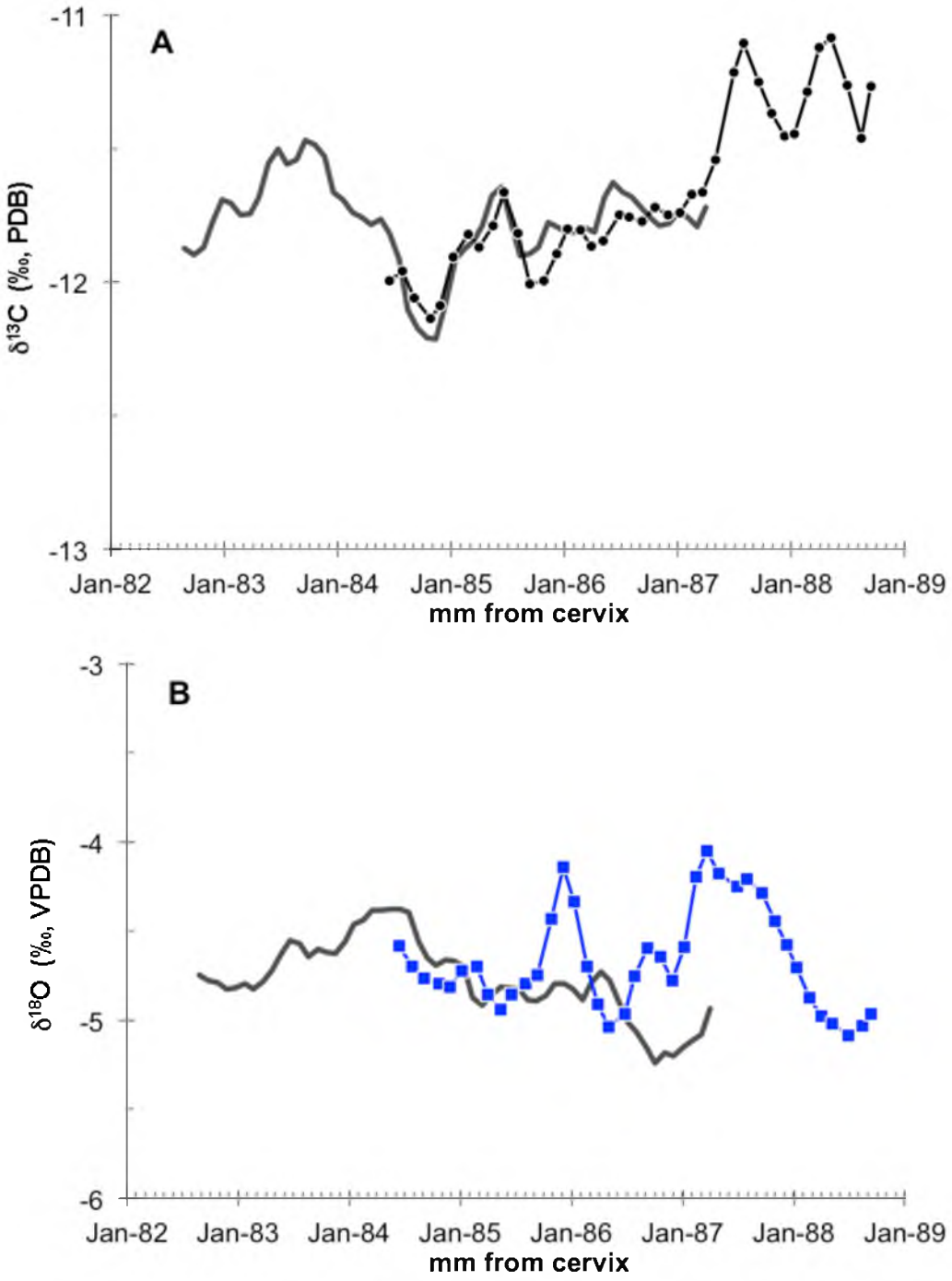

Figure 5.25. Forward model results (l_a=35mm) for A) $\delta^{13}C$ and B) $\delta^{18}O$ from molar R37_Rm3.8. Measured enamel data have been smoothed with a 3-point weighted average and are shown in A) as black circles and in B) as blue squares.

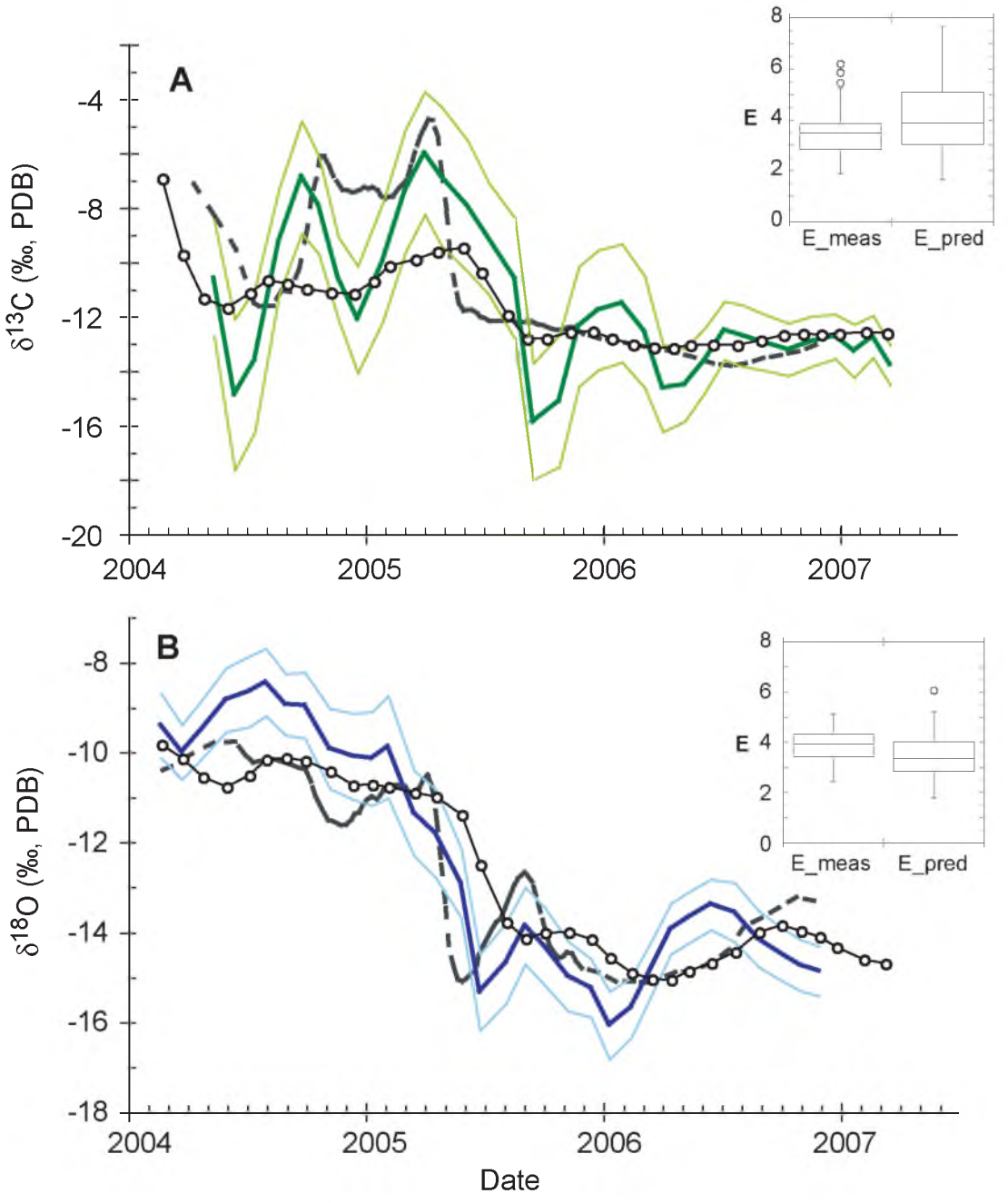

Figure 5.26. Inverse model results for A) $\delta^{13}C$ and B) $\delta^{18}O$ from molar Misha_Rm3.5. Bold colored line is the mean $\mathbf{m}_{est}$ from 100 solutions ($\pm 1\sigma$). Dashed grey line is the primary input, and circles are measured data. In both models l_a= 45 mm, l_m= 70 mm, openindx= 0.65*l_a, r2($\sigma_{\Delta x}$) = 0.2 mm, and r3($\sigma_{\Delta z}$) = 0.3 mm. A) r1(σ_{ms}) =0.12 ‰ ,ε^2 =0.005, and a reference vector (RV) of -6 to -10 ‰; B) r1(σ_{ms}) =0.22 ‰, ε^2 =0.024, and RV of -11 to -14 ‰.

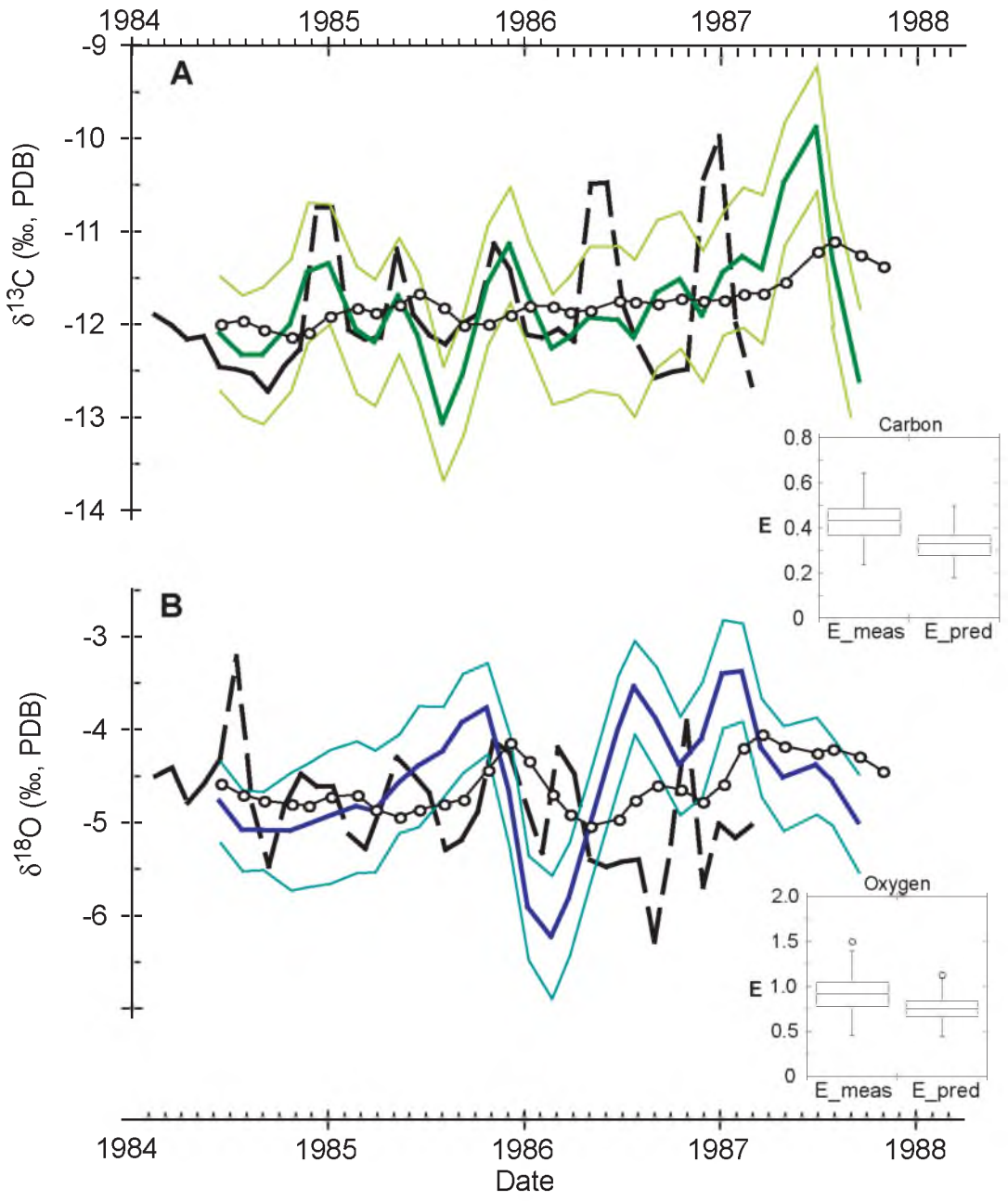

Figure 5.27. Inverse model results from molar R37_Rm3.8 for A) $\delta^{13}C$ and B) $\delta^{18}O$. Bold colored line is the mean $\mathbf{m}_{est}$ from 100 solutions ($\pm 1\sigma$). Dashed grey line is the primary input, and circles are measured data. In both models l_a= 45 mm, l_m= 70 mm, openindx= 1, r2($\sigma_{\Delta x}$) = 0.2 mm, and r3($\sigma_{\Delta z}$) = 0.3 mm. For A) r1(σ_{ms}) =0.1 ‰, ε^2 =0.0035, and the reference vector (RV) is -11 to -12 ‰ and for B) r1(σ_{ms}) =0.15 ‰, ε^2 =0.012, and RV is -3 to -6 ‰.

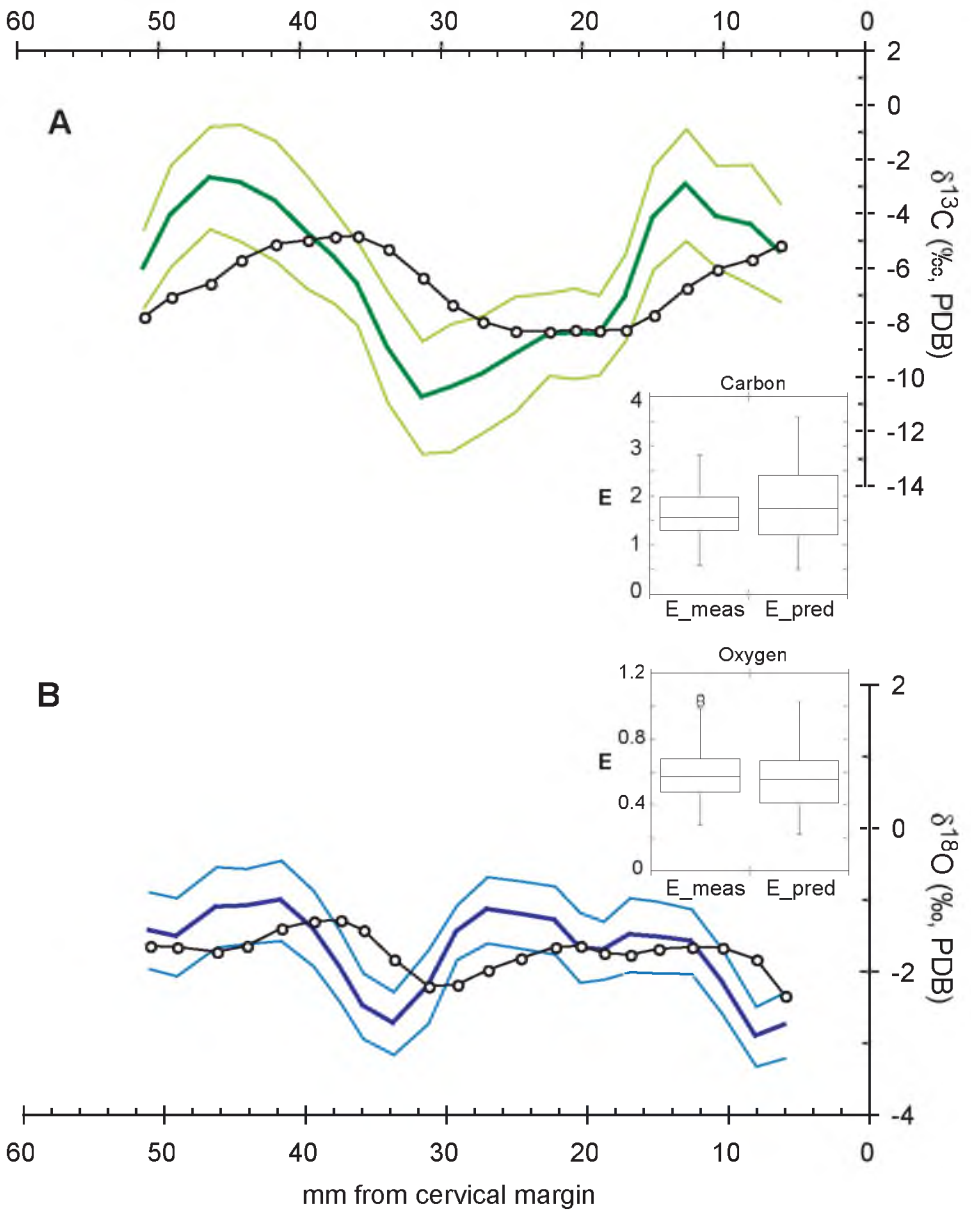

Figure 5.28. Inverse model results from mammoth molar LACM-47129 for A) $\delta^{13}C$ and B) $\delta^{18}O$. Bold colored line is the mean $\mathbf{m}_{est}$ from 100 solutions ($\pm 1\sigma$) and circles are measured data. In both models l_a= 30 mm, l_m= 60 mm, openindx= 0.75*la, r2($\sigma_{\Delta x}$) = 0.5 mm, and r3($\sigma_{\Delta z}$) = 0.5 mm. For A) r1(σ_{ms}) =0.1 ‰, ε^2 =0.006, and the reference vector (RV) is -5 to -8 ‰ and for B) r1(σ_{ms}) =0.15 ‰, ε^2 =0.02, and RV is -1 to -4 ‰.

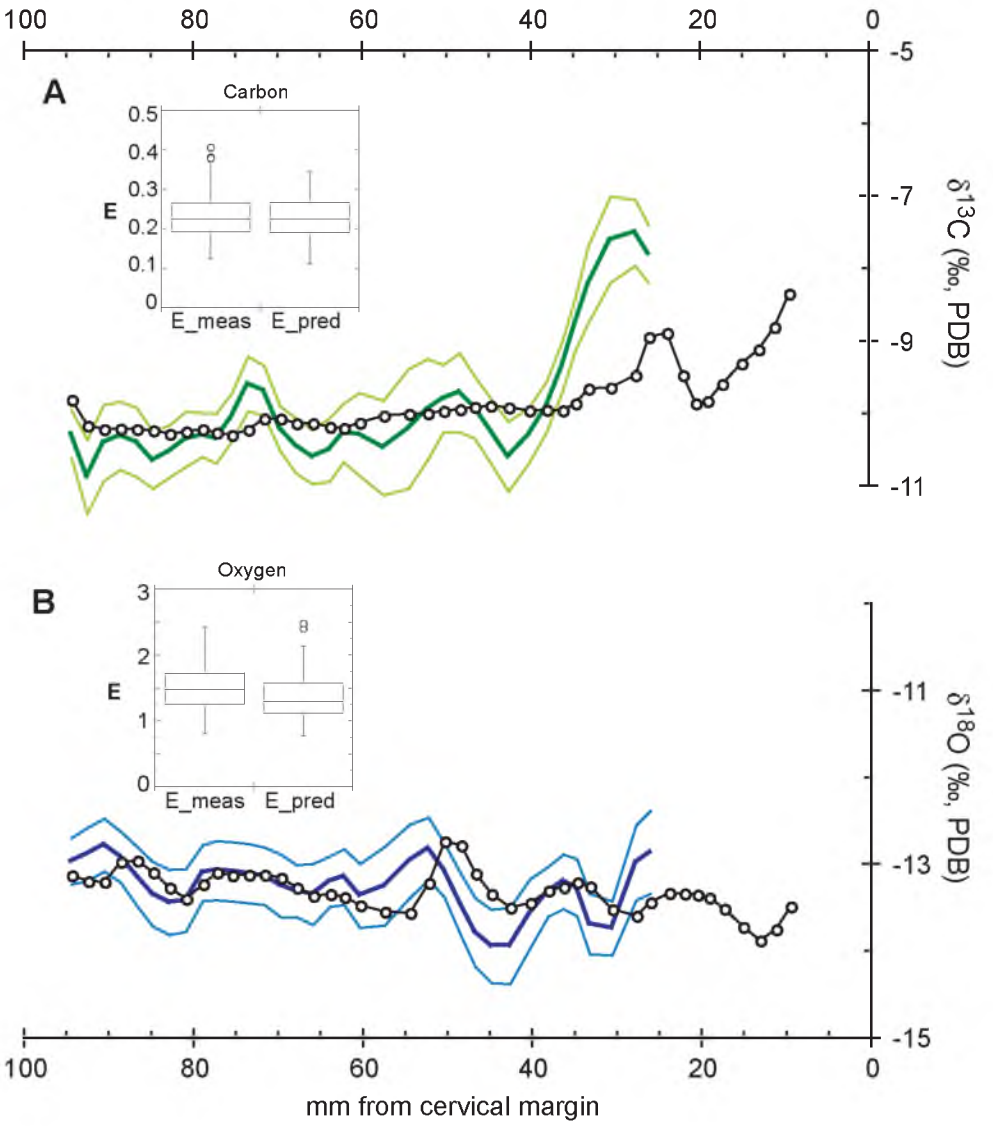

Figure 5.29. Inverse model results from mammoth molar IMNH-40368 for A) $\delta^{13}C$ and B) $\delta^{18}O$. Bold colored line is the mean $\mathbf{m}_{est}$ from 100 solutions ($\pm 1\sigma$) and circles are measured data. In both models l_a= 30 mm, l_m= 60 mm, openindx= 1, r2($\sigma_{\Delta x}$) = 0.5 mm, and r3($\sigma_{\Delta z}$) = 0.5 mm. For A) r1(σ_{ms}) =0.1 ‰, ε^2 =0.005, and the reference vector (RV) is -8 to -11 ‰ and for B) r1(σ_{ms}) =0.2 ‰, ε^2 =0.05, and RV is -11 to -14 ‰. Profile data from within 25 mm of the cervix were omitted from the inversion (see text for explanation).

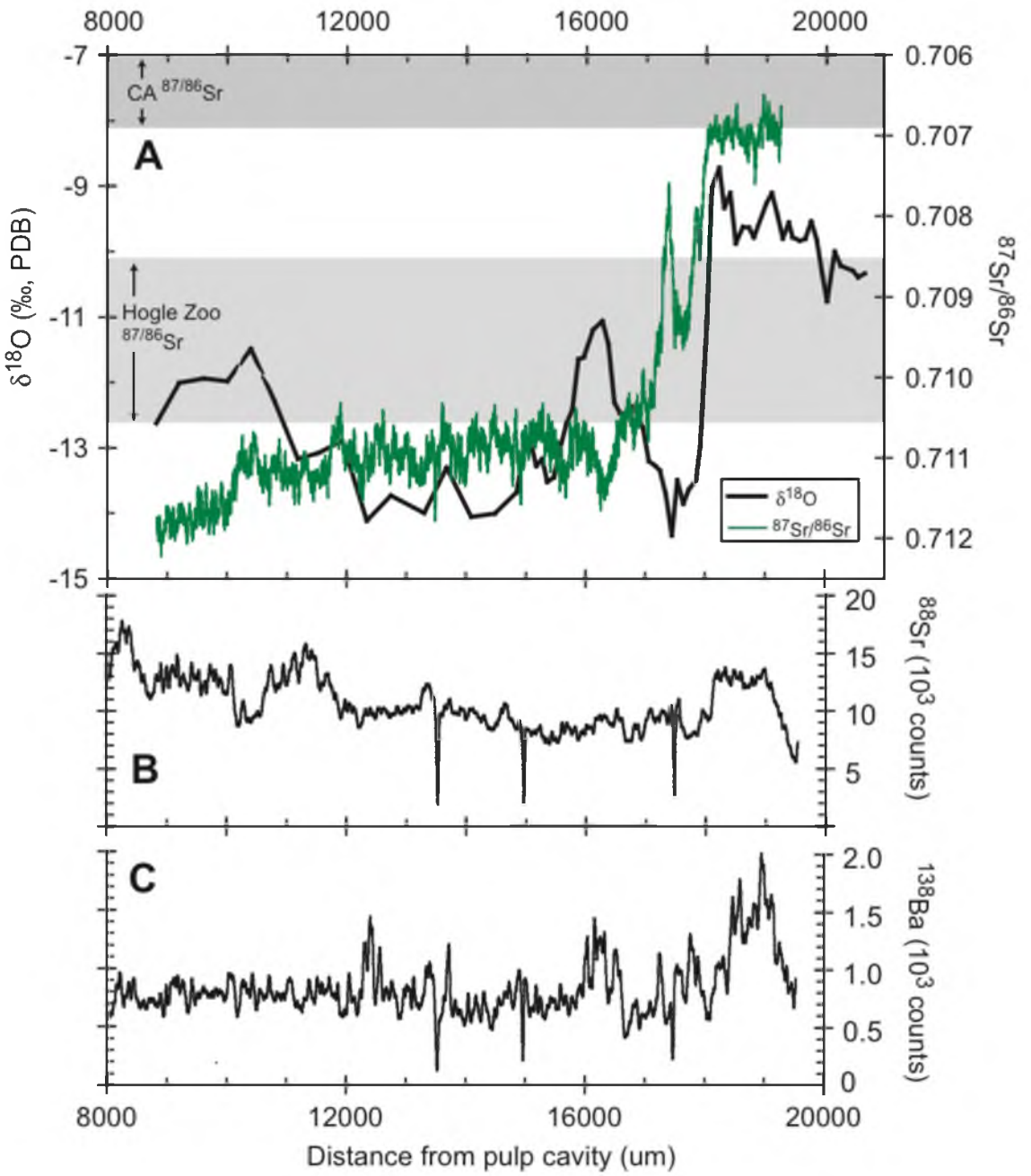

Figure 5.30. A) $^{87}Sr/^{86}Sr$ ratio and $\delta^{18}O$, B) ^{88}Sr, and C) ^{138}Ba data from Misha ivory slab M640. Ranges of $^{87}Sr/^{86}Sr$ ratios in water from CA (from Ingram and Weber, 1999) and the Hogle Zoo (n=8) are shown in gray boxes. The three distinct drops in counts (in B and C and to a lesser extent the $^{87}Sr/^{86}Sr$ ratio in A) are from cracks in the ivory and are used to align profiles. Overall turnover of the $^{87}Sr/^{86}Sr$ ratio in Misha appears to lag that of $\delta^{18}O$. However, the two "spikes" associated with the move may contribute to the delayed $^{87}Sr/^{86}Sr$ ratio turnover.

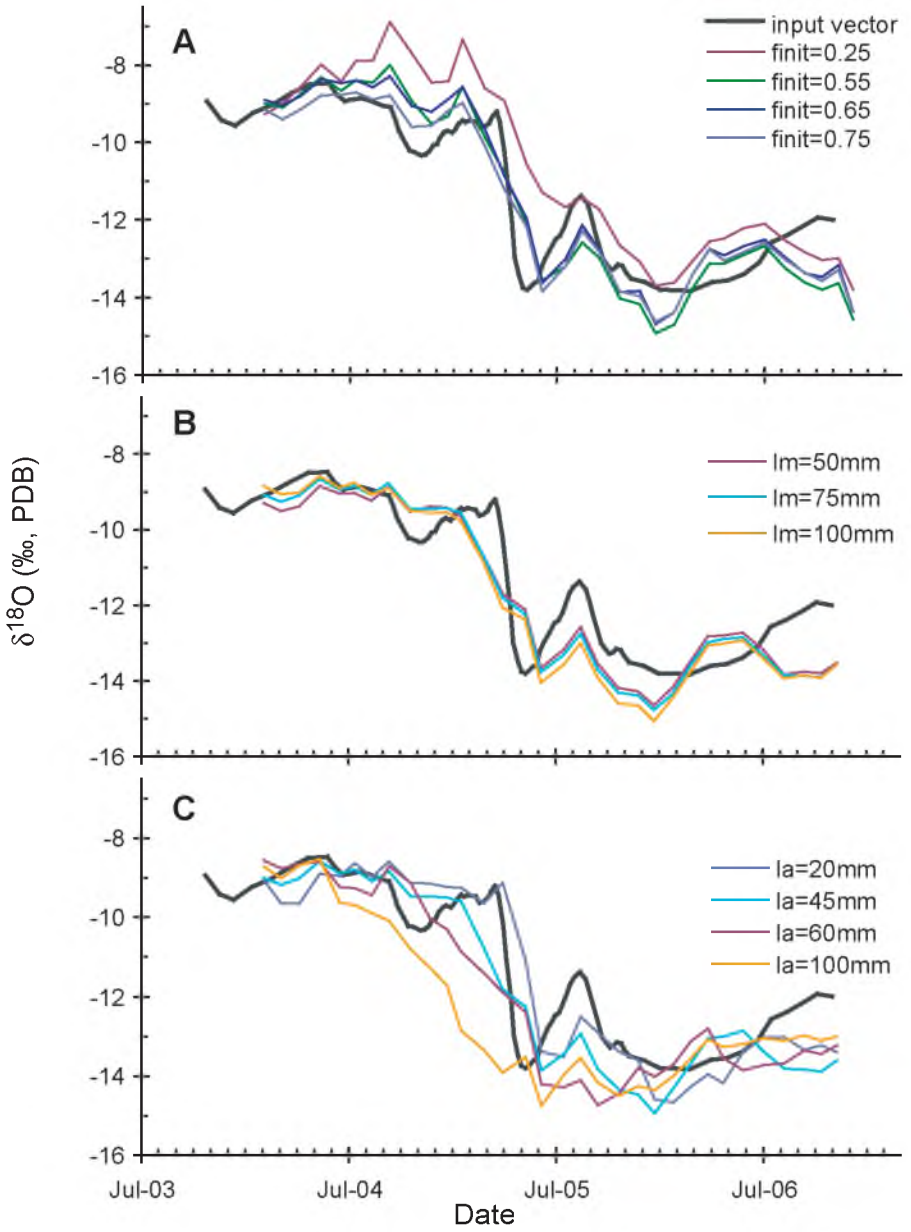

Figure 5.31. Sensitivity test results for A) f_i, B) l_m, and C) l_a using Misha_Rm3.5 $\delta^{18}O$ profile data. In each plot, the gray line represents the primary input signal from the M640 ivory profile.

APPENDIX A

DATA TABLES ASSOCIATED

WITH CHAPTER 3

Table A.1
Background information for [1]

Sample ID	Known Age	Taxon	Part	Tissue
FMNH-20754	Nov, 1905	*Taurotragus oryx*	tail hair	keratin
MAM-3528	Dec, 1930	*Gazella granti*	body hair	keratin
MAM-3559	1932	*T. scriptus*	body hair	keratin
LP878	Aug, 1953	*Colobus badius*	body hair	keratin
LP2989	Dec, 1956	*Cercocebus albigena*	body hair	keratin
L10335	Aug, 1960	*Cercopithecus mitis*	body hair	keratin
L10830	1962	*C. mitis*	body hair	keratin
L13873	Jul, 1964	*C. mitis*	body hair	keratin
L15346	Mar, 1966	*C. mitis*	body hair	keratin
L16286	Feb, 1967	*Cephalophus niger*	body hair	keratin
OHORN-1974	1974	*Oryx beisa*	basal horn	keratin
L3791	Jun, 1982	*Colobus angolensis*	body hair	keratin
MAM-8759	1988	*Sylvicapra grimmia*	body hair	keratin
TSV-171-Prox-K	July, 1998	*Loxodonta africana*	tail hair	keratin
R37-Dist-K	May, 2005	*L. africana*	tail hair	keratin
R37-Prox-K	Sep, 2006	*L. africana*	tail hair	keratin
TSV-171-Dist-K	unknown	*L. africana*	tail hair	keratin
R37-PC-C	Sep, 2006	*L. africana*	tusk dentin	collagen
Misha-PC-C	Sep, 2008	*L. africana*	tusk dentin	collagen
Misha-MID1-C	unknown	*L. africana*	tusk dentin	collagen
Misha-MID2-C	unknown	*L. africana*	tusk dentin	collagen
Misha-TIP-C	unknown	*L. africana*	tusk dentin	collagen
R37-MID1-C	unknown	*L. africana*	tusk dentin	collagen
R37-MID2-C	unknown	*L. africana*	tusk dentin	collagen
R37-MID3-C	unknown	*L. africana*	tusk dentin	collagen
R37-TIP-C	unknown	*L. africana*	tusk dentin	collagen
TE-95 Rm6-ROOT-C	unknown	*L. africana*	molar dentin	collagen
TE-95 Rm6.7-1.3-C	unknown	*L. africana*	molar dentin	collagen
TE-95 Rm6.7-10.1-2C	unknown	*L. africana*	molar dentin	collagen
TE-95 Rm6.7-10.1-C	unknown	*L. africana*	molar dentin	collagen

^{4}C samples

Geographic Location	Lat/Long.	Collector/Collection
Tana River District, Kenya	-2.53, 40.52	C.E. Akeley/FMNH
S of Lake Turkana, Kenya	2.0 , long. unkn	T. Cerling/KNM-MAM
Elburgon, Kenya	-0.26, 36.39	T. Cerling/KNM-MAM
Shabunda, DRC	-2.70, 27.34	T. Cerling/CRNS-Lwiro
Iraugi, DRC	unknown	T. Cerling/CRNS-Lwiro
Iraugi, DRC	unknown	T. Cerling/CRNS-Lwiro
Kuwinka, Rwanda	-2.49, 29.21	T. Cerling/CRNS-Lwiro
Butare, Rwanda	-2.60, 29.74	T. Cerling/CRNS-Lwiro
Musenge/Idambo DRC	unknown	T. Cerling/CRNS-Lwiro
Bwaniba/Kahuzi, DRC	unknown	T. Cerling/CRNS-Lwiro
Northern Kenya	unknown	T. Cerling
Bunyakiri, DRC	-2.15, 28.65	T. Cerling/CRNS-Lwiro
40km S of Nairobi, Kenya	-1.65, long. unkn	T. Cerling/KNM-MAM
TWNP, Kenya	-2.99, 38.47	T. Cerling
SNR, Kenya	0.61, 37.64	T. Cerling
SNR, Kenya	0.61, 37.64	T. Cerling
TWNP, Kenya	-2.99, 38.47	T. Cerling
SNR, Kenya	0.61, 37.64	T. Cerling
Salt Lake City, UT	40.75, -111.81	K. Uno/ Hogle Zoo
Salt Lake City, UT	40.75, -111.81	K. Uno/ Hogle Zoo
Salt Lake City, UT	40.75, -111.81	K. Uno/ Hogle Zoo
Salt Lake City, UT	40.75, -111.81	K. Uno/ Hogle Zoo
SNR, Kenya	0.61, 37.64	T. Cerling
SNR, Kenya	0.61, 37.64	T. Cerling
SNR, Kenya	0.61, 37.64	T. Cerling
SNR, Kenya	0.61, 37.64	T. Cerling
TWNP, Kenya	-2.99, 38.47	T. Cerling
TWNP, Kenya	-2.99, 38.47	T. Cerling
TWNP, Kenya	-2.99, 38.47	T. Cerling
TWNP, Kenya	-2.99, 38.47	T. Cerling

Table A.1 Continued

Sample ID	Known Age	Taxon	Part	Tissue	Geographic Location	Lat/Long.	Collector/Collection
R37-PC-tissue	Sep, 2006	*Loxodonta africana*	soft tissue	PC tissue	SNR, Kenya	0.61, 37.64	T. Cerling
KL-1-E	1971	*Hippopotamus amphibius*	canine enamel	bioapatite	Lake Edward, Uganda	-0.20, 29.90	H. Klingel
TSV-291-(2-3)	1996	*H. amphibius*	canine enamel	bioapatite	TWNP, Kenya	-2.98, 38.02	T. Cerling
R37-PC-DEN	Sep, 2006	*L. africana*	tusk dentin	bioapatite	SNR, Kenya	0.61, 37.64	T. Cerling
R37-PC-DEN(T)	Sep, 2006	*L. africana*	tusk dentin	bioapatite §	SNR, Kenya	0.61, 37.64	T. Cerling
K08-201 2-3 cm	Oct, 2007	*H. amphibius*	canine enamel	bioapatite	TWNP, Kenya	-2.98, 38.02	T. Cerling
Misha-PC-DEN	Sep, 2008	*L. africana*	tusk dentin	bioapatite	Salt Lake City, UT	40.75, -111.81	K. Uno/ Hogle Zoo
Misha-PC-DEN(T)	Sep, 2008	*L. africana*	tusk dentin	bioapatite §	Salt Lake City, UT	40.75, -111.81	K. Uno/ Hogle Zoo
KL-8-E	unknown	*H. amphibius*	canine enamel	bioapatite	Lake Edward, Uganda	-0.20, 29.90	H. Klingel
KL-15.5-E	unknown	*H. amphibius*	canine enamel	bioapatite	Lake Edward, Uganda	-0.20, 29.90	H. Klingel
KL-17-E	unknown	*H. amphibius*	canine enamel	bioapatite	Lake Edward, Uganda	-0.20, 29.90	H. Klingel
KL-24-E	unknown	*H. amphibius*	canine enamel	bioapatite	Lake Edward, Uganda	-0.20, 29.90	H. Klingel
KL-31.5-E	unknown	*H. amphibius*	canine enamel	bioapatite	Lake Edward, Uganda	-0.20, 29.90	H. Klingel
2KL-43-E	unknown	*H. amphibius*	canine enamel	bioapatite	Lake Edward, Uganda	-0.20, 29.90	H. Klingel
2KL-95-E	unknown	*H. amphibius*	canine enamel	bioapatite	Lake Edward, Uganda	-0.20, 29.90	H. Klingel
2KL-145-E	unknown	*H. amphibius*	canine enamel	bioapatite	Lake Edward, Uganda	-0.20, 29.90	H. Klingel
K11-KF-340/350	unknown	*H. amphibius*	canine enamel	bioapatite	Koobi Fora, Kenya	3.95, 36.18	T. Cerling
K11-KF-40/50	unknown	*H. amphibius*	canine enamel	bioapatite	Koobi Fora, Kenya	3.95, 36.18	T. Cerling
K08-201-(49-50)	unknown	*H. amphibius*	canine enamel	bioapatite	TWNP, Kenya	-2.98, 38.02	T. Cerling
TSV-291-(56-57)	unknown	*H. amphibius*	canine enamel	bioapatite	TWNP, Kenya	-2.98, 38.03	T. Cerling
TE-95 Rm5.7-1.7	unknown	*L. africana*	molar enamel	bioapatite	TENP, Kenya	-2.99, 38.47	T. Cerling
TE-95 Rm6.2-1.1	unknown	*L. africana*	molar enamel	bioapatite	TENP, Kenya	-2.99, 38.47	T. Cerling
TE-95 Rm6.2-7.5	unknown	*L. africana*	molar enamel	bioapatite	TENP, Kenya	-2.99, 38.47	T. Cerling
TE-95 Rm6.7-1.3	unknown	*L. africana*	molar enamel	bioapatite	TENP, Kenya	-2.99, 38.47	T. Cerling
TE-95 Rm6.7-10.1	unknown	*L. africana*	molar enamel	bioapatite	TENP, Kenya	-2.99, 38.47	T. Cerling
TE-95 Rm6.4-1.5	unknown	*L. africana*	molar enamel	bioapatite	TENP, Kenya	-2.99, 38.47	T. Cerling
TE-95 Rm6.4-6.2	unknown	*L. africana*	molar enamel	bioapatite	TENP, Kenya	-2.99, 38.47	T. Cerling
TE-95 Rm6.4-9.5	unknown	*L. africana*	molar enamel	bioapatite	TENP, Kenya	-2.99, 38.47	T. Cerling
TE-95 Rm6.9-2.0	unknown	*L. africana*	molar enamel	bioapatite	TENP, Kenya	-2.99, 38.47	T. Cerling
TE-95 Rm6.9-4.2	unknown	*L. africana*	molar enamel	bioapatite	TENP, Kenya	-2.99, 38.47	T. Cerling
TE-95 Rm6.9-5.8	unknown	*L. africana*	molar enamel	bioapatite	TENP, Kenya	-2.99, 38.47	T. Cerling
TE-95 Rm6.9-8.3	unknown	*L. africana*	molar enamel	bioapatite	TENP, Kenya	-2.99, 38.47	T. Cerling

Table A.1 Continued

Sample ID	Known Age	Taxon	Part	Tissue	Geographic Location	Lat/Long.	Collector/Collection
TE-95 Rm6.9-10.4	unknown	*L. africana*	molar enamel	bioapatite	TENP, Kenya	-2.99, 38.47	T. Cerling
TE-95 Rm6.11-2.3	unknown	*L. africana*	molar enamel	bioapatite	TENP, Kenya	-2.99, 38.47	T. Cerling
R37 Lm6.3-0.7	unknown	*L. africana*	molar enamel	bioapatite	SNR, Kenya	0.61, 37.64	T. Cerling
R37 Lm6.7-1.0	unknown	*L. africana*	molar enamel	bioapatite	SNR, Kenya	0.61, 37.64	T. Cerling
R37 Lm6.7-7.3	unknown	*L. africana*	molar enamel	bioapatite	SNR, Kenya	0.61, 37.64	T. Cerling
R37 Lm6.10-5.0	unknown	*L. africana*	molar enamel	bioapatite	SNR, Kenya	0.61, 37.64	T. Cerling
R37 Lm6.10-1.6	unknown	*L. africana*	molar enamel	bioapatite	SNR, Kenya	0.61, 37.64	T. Cerling
T.triandra_051964	May, 1964	*T .triandra*	grass	bulk tissue	TWNP, Kenya	-2.99, 38.47	T. Cerling/KNM-H
T.triandra_071962	July, 1962	*T .triandra*	grass	bulk tissue	near Narok, Kenya	-1.09, 35.87	T. Cerling/KNM-H
H.nyassae_011964	Jan, 1964	*Hyparrhenia nyassae*	grass	bulk tissue	Thika, Kenya	-1.13, 37.24	T. Cerling/KNM-H

Abbreviations and symbols: CRNS-Lwiro: Centre de Recherche en Sciences Naturelles, Lwiro, Democratic Republic of Congo DRC: Democratic Republic of Congo; FMNH: Field Museum of Natural History; KNM-H: Kenya National Museums Herbarium; KNM-OM: Kenya National Museums Mammalogy Collection; PC: pulp cavity; SNR: Samburu National Reserve; TWNP: Tsavo West National Park; TENP: Tsavo East National Park §: treated with 3% NaOCl.

Table A.2

K11-KF hippo canine increment measurements

interval (mm from prox. end)	inc #	inc thickness mm	cum dist mm
20 to 60	1	0.80	0.80
	2	0.68	1.48
	3	0.78	2.26
	4	0.66	2.92
	5	0.69	3.61
	6	0.69	4.30
	7	0.80	5.10
	8	1.15	6.25
	9	0.89	7.14
	10	1.40	8.55
	11	0.89	9.43
	12	1.18	10.61
	13	1.52	12.13
	14	1.41	13.53
	15	0.90	14.43
	16	1.23	15.66
	17	1.20	16.86
	18	1.61	18.47
	19	1.16	19.63
	20	1.32	20.94
	21	0.95	21.90
	22	1.48	23.37
	23	1.22	24.59
	24	1.14	25.73
	25	1.39	27.12
	26	0.98	28.10
	27	0.83	28.93
	28	1.13	30.06
	29	0.84	30.90
	30	0.90	31.79
	31	0.87	32.66
	32	1.37	34.04
	33	1.30	35.34
	34	1.27	36.61
	35	0.72	37.34
	36	1.13	38.46
20 to 60 (cont.)	37	0.70	39.16
	38	0.67	39.83
	39	1.19	41.01
	40	1.39	42.40
50 to 100	1	1.38	1.55
	2	1.99	3.04
	3	1.44	4.51
	4	1.00	5.96
	5	1.05	7.38
	6	1.16	8.77
	7	1.33	10.07
	8	1.44	11.37
	9	1.27	12.70
	10	1.00	14.15
	11	1.83	15.62
	12	1.49	17.10
	13	1.38	18.62
	14	1.38	20.10
	15	2.21	21.67
	16	1.38	23.16
	17	1.38	24.62
	18	1.83	26.04
	19	0.94	27.45
	20	1.83	28.76
	21	1.13	30.09
	22	1.15	31.44
	23	0.94	32.71
	24	1.31	34.01
	25	1.24	35.25
	26	1.55	36.52
	27	1.57	37.84
	28	1.05	39.18
	29	1.22	40.54
	30	1.28	41.98
	31	1.39	43.42

Table A.2 Continued

interval (mm from prox. end)	inc #	inc thickness mm	cum dist mm
50 to 100 (cont.)	32	1.72	44.83
	33	1.05	46.30
	34	1.50	47.80
	35	2.11	49.33
	36	1.44	50.89
	1	0.90	1.29
90 to 160	2	1.12	2.41
	3	1.35	3.76
	4	1.40	5.16
	5	1.40	6.57
	6	1.59	8.16
	7	1.83	9.99
	8	1.36	11.35
	9	2.06	13.41
	10	1.35	14.76
	11	1.33	16.09
	12	1.11	17.20
	13	1.28	18.48
	14	1.39	19.87
	15	1.00	20.87
	16	1.22	22.10
	17	1.33	23.43
	18	2.00	25.43
	19	2.34	27.77
	20	1.78	29.55
140 to 210	1	1.30	1.30
	2	1.17	2.72
	3	0.75	1.35
	4	1.64	2.72
	5	1.49	1.32
	6	1.73	2.64
	7	1.85	1.34
	8	0.89	2.74

interval (mm from prox. End)	inc #	inc thickness mm	cum dist mm
140 to 210 (cont.)	9	1.37	1.37
	10	1.03	2.67
	11	1.23	1.24
	12	1.37	2.38
	13	0.89	1.34
	14	1.30	2.64
	15	1.05	1.22
	16	1.55	2.44
	17	1.44	1.24
	18	1.92	2.59
	19	0.82	1.35
	20	0.75	2.68
	21	1.27	1.26
	22	1.41	2.48
	23	1.95	1.15
	24	1.37	2.34
	25	0.78	1.30
	26	0.85	2.60
	27	1.18	1.29
	28	1.08	2.48
	29	1.37	1.16
	30	1.74	2.41
190 to 260	1	0.82	1.12
	2	1.13	2.25
	3	0.98	3.23
	4	1.38	4.61
	5	1.28	5.89
	6	1.13	7.01
	7	1.57	8.58
	8	1.07	9.65
	9	1.32	10.97
	10	1.76	12.72
	11	1.55	14.27
	12	0.96	15.23
	13	1.01	16.24

Table A.2 Continued

interval (mm from prox. end)	inc #	inc thickness mm	cum dist mm
190 to 260 (cont.)	14	1.57	17.81
	15	1.49	19.29
	16	1.47	20.76
	17	1.51	22.26
	18	1.67	23.93
	19	1.47	25.40
	20	1.76	27.16
	21	1.63	28.79
	22	1.15	29.94
	23	0.69	30.63
	24	1.23	31.86
	25	1.07	32.93
	26	1.04	33.97
	27	0.90	34.88
	28	0.96	35.84
	29	0.99	36.82
	30	0.78	37.60
	31	0.67	38.27
	32	0.82	39.08
	33	0.97	40.05
	34	1.36	41.41
	35	2.07	43.48
	36	0.86	44.33
	37	0.90	45.23
	38	0.56	45.80
	39	1.32	47.12
	40	1.51	48.62
	41	1.51	50.13

interval (mm from prox. End)	inc #	inc thickness mm	cum dist mm

SUMMARY by photographed interval				
interval	**# incs**	**mean (mm)**	**days/inc**	**2σ**
20 to 60	40	1.06	8.6	1.2
50 to 100	37	1.42	11.5	0.9
140 to 210	34	1.28	10.4	0.8
190 to 260	41	1.22	9.9	1.5
ALL	**158**	**1.27**	**10.3**	**1.8**

Table A.3

Tusk increment measurements from thin section R37-1053

inc #	inc thickness µm	cumulative distance µm	inc #	inc thickness µm	cumulative distance µm
1	0	0	37	79	3716
2	96	96	38	104	3820
3	87	183	39	84	3904
4	107	290	40	90	3994
5	53	343	41	104	4098
6	65	408	42	76	4174
7	84	492	43	93	4267
8	96	588	44	194	4461
9	104	692	45	79	4540
10	96	788	46	121	4661
11	62	850	47	87	4748
12	90	940	48	65	4813
13	124	1063	49	96	4909
14	79	1142	50	73	4982
15	113	1255	51	107	5089
16	105	1360	52	120	5208
17	107	1467	53	82	5290
18	87	1554	54	76	5366
19	93	1647	55	70	5436
20	113	1759	56	48	5484
21	129	1889	57	70	5554
22	155	2044	58	118	5672
23	149	2193	59	73	5745
24	115	2308	60	59	5805
25	146	2454	61	73	5878
26	124	2578	62	68	5945
27	98	2677	63	104	6049
28	82	2758	64	84	6134
29	124	2882	65	115	6249
30	115	2997	66	111	6360
31	96	3093	67	107	6467
32	93	3186	68	90	6557
33	134	3319	69	87	6644
34	146	3466	70	87	6731
35	96	3561	71	101	6833
36	76	3637	72	84	6917

Table A.3 Continued

inc #	inc thickness µm	cumulative distance µm	inc #	inc thickness µm	cumulative distance µm
73	149	7066	109	84	11238
74	62	7128	110	121	11359
75	73	7201	111	129	11488
76	90	7291	112	84	11572
77	82	7373	113	127	11699
78	101	7474	114	79	11778
79	163	7637	115	98	11876
80	104	7741	116	121	11997
81	104	7845	117	110	12107
82	79	7924	118	113	12219
83	113	8037	119	152	12371
84	127	8163	120	128	12499
85	101	8264	121	82	12581
86	143	8408	122	70	12651
87	107	8515	123	113	12764
88	84	8599	124	149	12913
89	98	8698	125	76	12989
90	93	8790	126	87	13076
91	121	8911	127	118	13194
92	118	9030	128	83	13277
93	146	9176	129	118	13395
94	127	9302	130	158	13553
95	149	9451	131	110	13662
96	121	9572	132	138	13800
97	70	9643	133	83	13883
98	59	9702	134	98	13982
99	115	9817	135	180	14162
100	141	9958	136	124	14286
101	135	10093	137	129	14415
102	172	10264	138	129	14544
103	143	10408	139	104	14648
104	172	10579	140	93	14741
105	166	10745	141	76	14817
106	160	10906	142	124	14941
107	107	11013	143	158	15098
108	141	11153	144	118	15217

Table A.3 Continued

inc #	inc thickness μm	cumulative distance μm	inc #	inc thickness μm	cumulative distance μm
145	115	15332	181	138	19529
146	121	15453	182	132	19661
147	146	15599	183	79	19740
148	104	15703	184	101	19841
149	110	15813	185	135	19976
150	135	15948	186	113	20089
151	90	16038	187	142	20231
152	96	16134	188	87	20318
153	73	16207	189	96	20414
154	73	16280	190	68	20481
155	93	16373	191	96	20577
156	110	16482	192	163	20740
157	129	16612	193	107	20847
158	107	16719	194	82	20928
159	82	16800	195	110	21038
160	118	16918	196	143	21181
161	124	17042	197	113	21294
162	113	17155	198	155	21449
163	59	17214	199	139	21588
164	90	17304	200	177	21765
165	135	17439	201	166	21931
166	87	17526	202	172	22103
167	113	17639	203	104	22207
168	149	17788	204	107	22314
169	143	17931	205	135	22449
170	143	18075	206	104	22553
171	146	18221	207	166	22719
172	121	18342	208	107	22826
173	149	18491	209	129	22955
174	138	18629	210	141	23096
175	158	18786	211	149	23245
176	110	18896	212	82	23326
177	104	19000	213	132	23459
178	113	19113	214	96	23554
179	146	19259	215	76	23630
180	132	19391	216	115	23745

Table A.3 Continued

inc #	inc thickness µm	cumulative distance µm	inc #	inc thickness µm	cumulative distance µm
217	138	23883	253	101	27454
218	142	24025	254	96	27550
219	90	24115	255	104	27654
220	115	24231	256	93	27747
221	110	24340	257	76	27823
222	118	24459	258	90	27913
223	98	24557	259	101	28014
224	169	24726	260	101	28115
225	129	24855	261	93	28208
226	90	24945	262	113	28321
227	115	25060	263	118	28439
228	90	25150	264	110	28549
229	90	25241	265	70	28619
230	84	25325	266	87	28706
231	101	25426	267	65	28771
232	82	25508	268	65	28835
233	56	25564	269	68	28903
234	101	25665	270	79	28982
235	56	25722	271	98	29080
236	107	25828	272	113	29193
237	129	25958	273	90	29283
238	101	26059	274	90	29373
239	101	26160	275	82	29454
240	84	26245	276	79	29533
241	73	26318	277	79	29612
242	87	26405	278	84	29696
243	82	26487	279	68	29764
244	93	26579	280	115	29879
245	124	26703	281	155	30034
246	98	26802	282	103	30136
247	84	26886	283	84	30221
248	90	26976	284	101	30322
249	107	27083	285	101	30423
250	96	27179	286	93	30516
251	113	27291	287	107	30623
252	62	27353	288	96	30719

Table A.3 Continued

inc #	inc thickness µm	cumulative distance µm	inc #	inc thickness µm	cumulative distance µm
289	82	30800	325	63	33821
290	96	30896	326	59	33880
291	135	31031	327	82	33962
292	76	31107	328	68	34030
293	93	31200	329	59	34089
294	68	31267	330	51	34139
295	73	31340	331	46	34186
296	59	31399	332	42	34228
297	56	31456	333	51	34278
298	76	31532	334	51	34329
299	62	31594	335	76	34405
300	118	31712			
301	87	31799			
302	82	31880			
303	87	31968			
304	93	32060			
305	98	32159			
306	70	32229			
307	87	32316			
308	98	32415			
309	73	32488			
310	72	32560			
311	84	32644			
312	104	32748			
313	96	32844			
314	160	33004			
315	73	33077			
316	65	33142			
317	113	33255			
318	62	33316			
319	62	33378			
320	82	33460			
321	107	33567			
322	73	33640			
323	65	33705			
324	53	33758			

SUMMARY	
Growth Rate (µm/week)	
103	**mean**
29	**1σ**

Table A.4

Measurements of angle (θ) between tusk axis and growth increments and calculated radial growth rate in μm/week from ivory slab R37-1053

Slab	θ (°)	μm/day	μm/week
1053	7.41	14.7	102.9
1053	7.97	15.8	110.7
1053	7.22	14.3	100.2
1053	7.57	15.0	105.1
1053	7.88	15.6	109.5
1053	7.56	15.0	105.0
1053	7.62	15.1	105.8
1053	7.02	13.9	97.4
average	**7.53**	**14.94**	**104.6**
stdev	**0.3**	**0.6**	**4.4**

Growth rate (μm/day) =(TAN(RADIANS(angle))*axial growth rate)/365.25*1000

APPENDIX B

FIGURES AND DATA TABLES ASSOCIATED

WITH CHAPTER 4

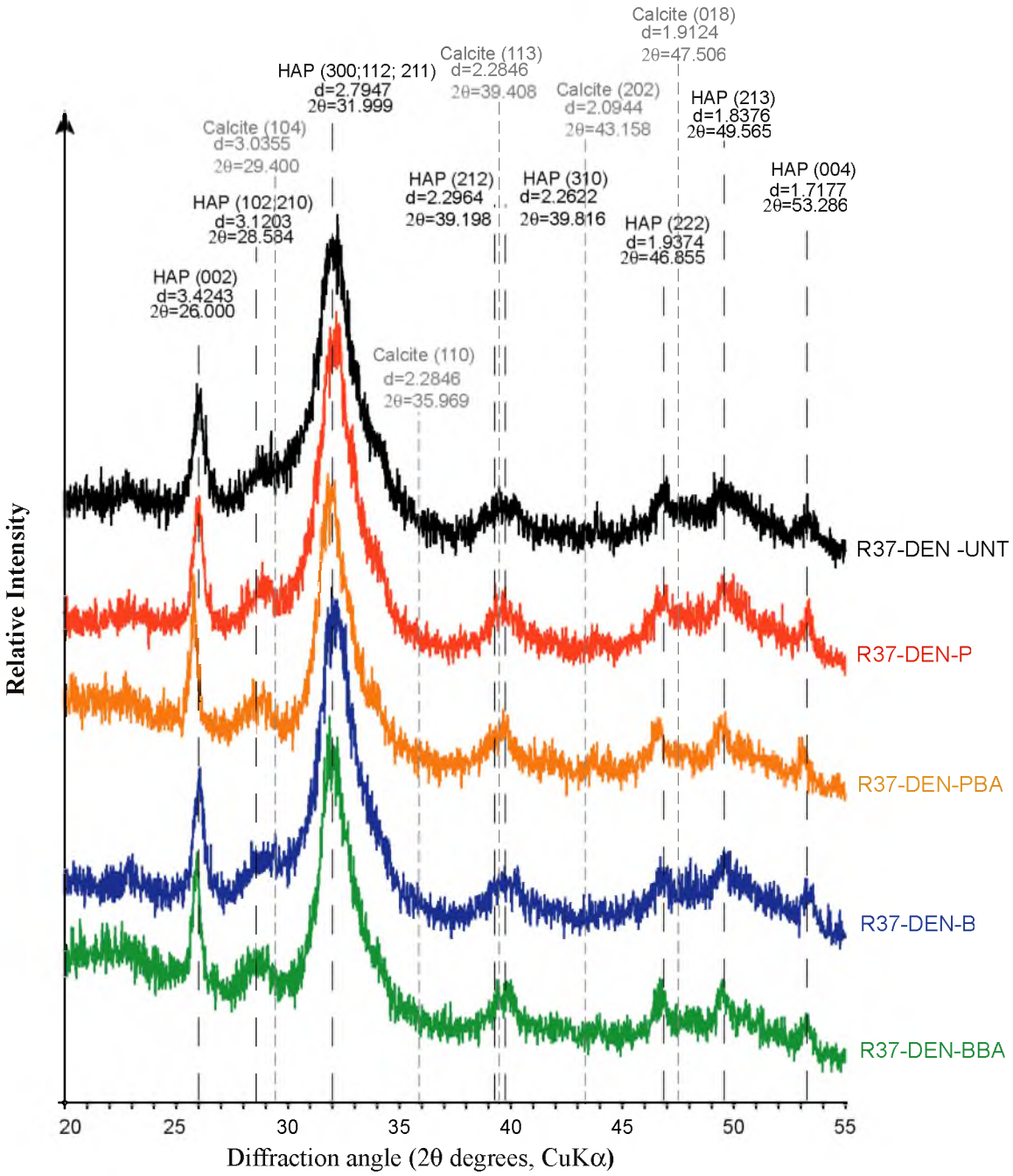

Figure B.1. X-ray diffraction patterns for untreated and pretreated dentin powders. HAP, hydroxylapatite; UNT, untreated; P, 3% hydrogen peroxide; B, 3% bleach (NaOCl); PBA, peroxide followed by buffered acetic acid; BBA, bleach followed by buffered acetic acid. All peaks from pretreated samples (P, PBA, B, and BBA) are sharper than peaks from the untreated dentin. Samples treated with buffered acetic acid (PBA and BBA) are slightly sharper than those pretreated with only the oxidizers (P and B). There are no peaks at prominent calcite positions (29.400°, 39.408°, or 43.158°).

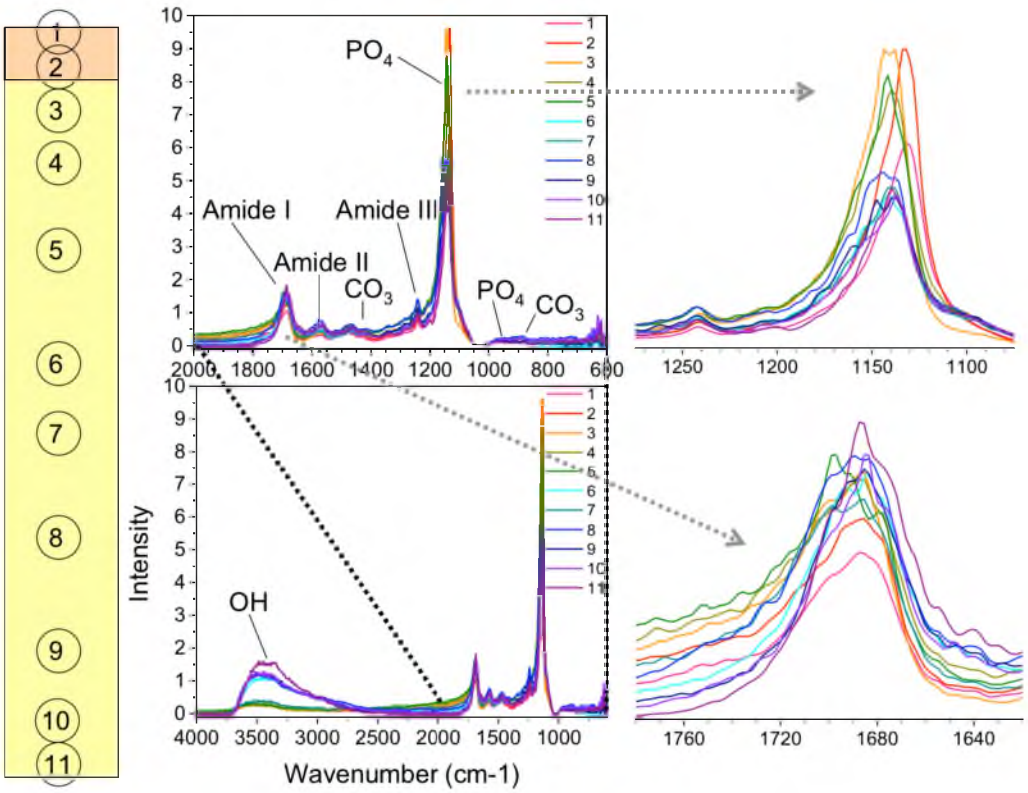

Figure B.2. FTIR spectra from eleven scans of thin section R37-DEN-1169 show differences in relative intensities moving from cementum (1 and 2) to dentin (3 through 11). Scan 11 is near the pulp cavity. Phosphate (PO_4^{3-}) peaks (top right) from dentin taken closer to the pulp cavity (scans 6 to 11) have lower intensity than those closer to the cementum-dentin junction (CDJ), suggesting they are less mineralized. The Amide I peak (lower right), a proxy for organic content, is highest in scan 11 near the pulp cavity.

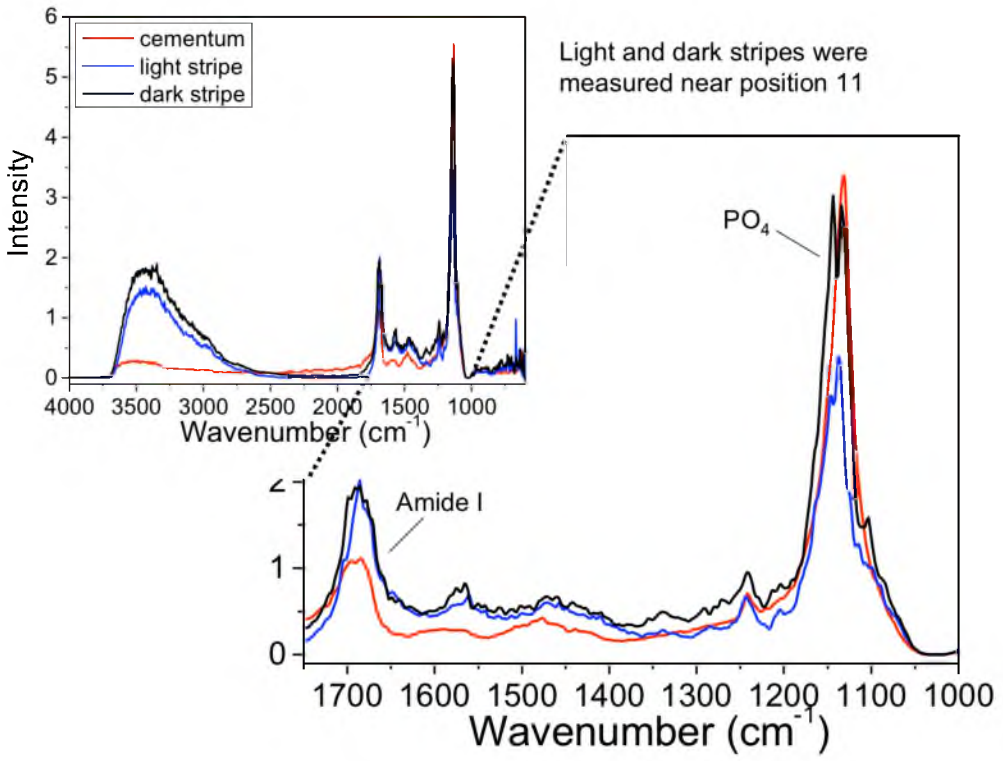

Figure B.3. FTIR spectra from R37-DEN-1169 thin section showing differences in relative intensities between light and dark growth increments. Peaks in the spectra include hydroxyl (OH^-) at wavenumber ~3400, Amide I, and phosphate (PO_4^{3-}). The light band has a lower intensity in phosphate and hydroxyl, suggesting it is less mineralized than the dark band. Location of the bands are indicated as Position 11, which is shown in Figure B.1.

Table B.1

Stable carbon and oxygen isotope profile data from R37 tusk dentin with tuned and untuned dates

Sample ID	$\delta^{13}C$ (‰, VPDB)	$\delta^{18}O$ (‰, VPDB)	dist. from base (μm)	untuned date	tuned date
R37-1169-000	-11.0	—	78	21-Sep-06	21-Sep-06
R37-1169-001	-11.6	-5.1	191	12-Sep-06	13-Sep-06
R37-1169-002	-11.8	-5.3	277	6-Sep-06	7-Sep-06
R37-1169-003	-11.6	-5.7	377	29-Aug-06	30-Aug-06
R37-1169-004	-11.3	-4.6	474	22-Aug-06	23-Aug-06
R37-1169-005	-12.2	-6.1	564	15-Aug-06	17-Aug-06
R37-1169-006	-12.9	-5.5	651	9-Aug-06	10-Aug-06
R37-1169-007	-12.4	-6.4	747	2-Aug-06	3-Aug-06
R37-1169-008	-12.2	-6.2	858	24-Jul-06	26-Jul-06
R37-1169-009	-11.9	-6.3	971	16-Jul-06	18-Jul-06
R37-1169-010	-11.5	-5.8	1071	9-Jul-06	10-Jul-06
R37-1169-012	-10.9	-3.1	1265	24-Jun-06	26-Jun-06
R37-1169-013	-11.8	-3.2	1367	16-Jun-06	19-Jun-06
R37-1169-014	-11.6	-2.0	1467	9-Jun-06	11-Jun-06
R37-1169-015	-10.8	-1.2	1571	1-Jun-06	4-Jun-06
R37-1169-016	-10.0	-2.7	1671	25-May-06	28-May-06
R37-1169-017	-9.1	-3.2	1765	18-May-06	21-May-06
R37-1169-018	-8.8	-5.1	1863	10-May-06	13-May-06
R37-1169-019	-8.4	-5.3	1958	3-May-06	6-May-06
R37-1169-020	-8.6	-4.7	2057	26-Apr-06	29-Apr-06
R37-1169-021	-11.0	-4.1	2156	19-Apr-06	22-Apr-06
R37-1169-023	-12.5	-3.1	2353	4-Apr-06	8-Apr-06
R37-1169-024	-12.5	-3.3	2449	28-Mar-06	1-Apr-06
R37-1169-025	-12.7	-2.5	2547	20-Mar-06	24-Mar-06
R37-1169-026	-12.9	-4.2	2642	13-Mar-06	17-Mar-06
R37-1169-027	-12.6	-4.5	2742	6-Mar-06	10-Mar-06
R37-1169-028	-12.6	-4.3	2849	26-Feb-06	2-Mar-06
R37-1169-029	-12.6	-4.8	2951	18-Feb-06	23-Feb-06
R37-1169-030	-12.4	-3.2	3045	11-Feb-06	16-Feb-06
R37-1169-031	-12.7	-4.0	3140	4-Feb-06	9-Feb-06
R37-1169-032	-12.6	-5.0	3242	28-Jan-06	1-Feb-06
R37-1169-033	-12.5	-5.1	3347	20-Jan-06	25-Jan-06
R37-1169-034	-12.4	-4.2	3462	11-Jan-06	16-Jan-06
R37-1169-035	-12.6	-4.3	3567	3-Jan-06	9-Jan-06
R37-1169-036	-12.2	-3.8	3660	27-Dec-05	2-Jan-06
R37-1169-037	-11.4	-3.2	3757	20-Dec-05	26-Dec-05
R37-1169-038	-11.7	-4.5	3857	13-Dec-05	18-Dec-05

Table B.1 Continued

Sample ID	$\delta^{13}C$ (‰, VPDB)	$\delta^{18}O$ (‰, VPDB)	dist. from base (μm)	untuned date	tuned date
R37-1169-039	-12.2	-2.5	3956	5-Dec-05	11-Dec-05
R37-1169-040	-12.2	-3.9	4044	29-Nov-05	5-Dec-05
R37-1169-041	-12.0	—	4143	21-Nov-05	28-Nov-05
R37-1169-042	-11.9	—	4252	13-Nov-05	20-Nov-05
R37-1169-044	-11.7	-5.1	4446	30-Oct-05	5-Nov-05
R37-1169-045	-12.0	-4.8	4543	22-Oct-05	29-Oct-05
R37-1169-046	-12.2	-2.9	4637	15-Oct-05	22-Oct-05
R37-1169-047	-11.6	—	4735	8-Oct-05	15-Oct-05
R37-1169-048	-11.8	-4.3	4829	1-Oct-05	8-Oct-05
R37-1169-049	-12.0	-5.3	4923	24-Sep-05	1-Oct-05
R37-1169-050	-11.5	-5.4	5024	17-Sep-05	24-Sep-05
R37-1169-051	-11.4	-3.7	5113	10-Sep-05	18-Sep-05
R37-1169-052	-11.4	-3.7	5207	3-Sep-05	11-Sep-05
R37-1169-053	-11.9	-4.4	5310	26-Aug-05	3-Sep-05
R37-1169-054	-12.1	-5.7	5414	18-Aug-05	26-Aug-05
R37-1169-055	-11.8	-4.3	5514	11-Aug-05	19-Aug-05
R37-1169-056	-11.0	-5.1	5610	4-Aug-05	12-Aug-05
R37-1169-057	-11.1	-5.0	5714	27-Jul-05	5-Aug-05
R37-1169-060	-10.7	-5.0	6024	4-Jul-05	13-Jul-05
R37-1169-061	-11.1	-3.8	6112	27-Jun-05	6-Jul-05
R37-1169-062	-11.1	-4.6	6207	20-Jun-05	29-Jun-05
R37-1169-063	-11.2	-3.8	6304	13-Jun-05	22-Jun-05
R37-1169-064	-10.9	-3.9	6397	6-Jun-05	16-Jun-05
R37-1169-065	-10.9	-4.0	6485	31-May-05	9-Jun-05
R37-1169-066	-10.9	-4.1	6579	24-May-05	2-Jun-05
R37-1169-067	-10.9	-3.4	6675	16-May-05	26-May-05
R37-1169-068	-12.4	-3.7	6771	9-May-05	19-May-05
R37-1169-069	-12.8	-4.1	6870	2-May-05	12-May-05
R37-1169-070	-11.9	-2.8	6966	25-Apr-05	5-May-05
R37-1169-071	-11.6	-2.9	7054	18-Apr-05	28-Apr-05
R37-1169-072	-12.1	-3.6	7148	11-Apr-05	22-Apr-05
R37-1169-073	-10.6	-4.7	7256	3-Apr-05	14-Apr-05
R37-1169-074	-10.7	-4.2	7354	27-Mar-05	7-Apr-05
R37-1169-075	-10.9	-3.7	7445	20-Mar-05	31-Mar-05
R37-1169-076	-11.0	-3.8	7539	13-Mar-05	24-Mar-05
R37-1169-077	-10.8	-4.9	7633	6-Mar-05	17-Mar-05
R37-1169-078	-11.3	-4.7	7734	26-Feb-05	10-Mar-05
R37-1169-079	-12.1	-6.1	7832	19-Feb-05	2-Mar-05

Table B.1 Continued

Sample ID	$\delta^{13}C$ (‰, VPDB)	$\delta^{18}O$ (‰, VPDB)	dist. from base (μm)	untuned date	tuned date
R37-1169-080	-11.6	-4.8	7928	12-Feb-05	23-Feb-05
R37-1169-081	-11.3	-5.6	8030	4-Feb-05	16-Feb-05
R37-1169-082	-9.7	-3.9	8129	28-Jan-05	9-Feb-05
R37-1169-083	-11.8	-4.6	8218	21-Jan-05	2-Feb-05
R37-1169-084	-11.8	-5.1	8309	14-Jan-05	27-Jan-05
R37-1169-085	-12.0	-3.7	8405	7-Jan-05	20-Jan-05
R37-1169-086	-11.8	-5.0	8504	31-Dec-04	12-Jan-05
R37-1169-087/088	-11.3	-5.2	8651	20-Dec-04	2-Jan-05
R37-1169-089	-11.5	-4.9	8809	8-Dec-04	21-Dec-04
R37-1169-090	-11.4	-4.5	8905	1-Dec-04	14-Dec-04
R37-1169-091/092	-11.3	-4.4	9061	19-Nov-04	3-Dec-04
R37-1169-093	-11.8	-6.0	9212	8-Nov-04	21-Nov-04
R37-1169-094	-11.9	-6.6	9302	1-Nov-04	15-Nov-04
R37-1169-095	-12.0	-4.2	9395	25-Oct-04	8-Nov-04
R37-1169-096	-11.8	-5.9	9491	18-Oct-04	1-Nov-04
R37-1169-097	-12.1	-5.5	9559	13-Oct-04	27-Oct-04
R37-1169-098	-12.2	-4.7	9630	8-Oct-04	22-Oct-04
R37-1169-099	-12.5	-5.1	9718	1-Oct-04	15-Oct-04
R37-1169-100	-12.2	-4.7	9811	24-Sep-04	9-Oct-04
R37-1169-101	-12.4	-5.2	9903	17-Sep-04	2-Oct-04
R37-1169-102	-12.1	-4.8	9990	11-Sep-04	26-Sep-04
R37-1169-103	-12.1	-4.4	10086	4-Sep-04	18-Sep-04
R37-1169-104	-12.3	-4.6	10187	27-Aug-04	11-Sep-04
R37-1169-105	-12.3	-5.1	10285	20-Aug-04	4-Sep-04
R37-1169-106	-12.3	-4.9	10379	13-Aug-04	28-Aug-04
R37-1169-107	-11.8	-4.4	10466	6-Aug-04	22-Aug-04
R37-1169-108	-11.2	-4.7	10560	30-Jul-04	15-Aug-04
R37-1169-109	-11.8	-4.6	10662	23-Jul-04	7-Aug-04
R37-1169-110	-12.2	-6.1	10753	16-Jul-04	1-Aug-04
R37-1169-111	-12.3	-5.5	10843	9-Jul-04	25-Jul-04
R37-1169-112	-12.3	-5.7	10937	2-Jul-04	18-Jul-04
R37-1169-113	-12.1	-5.5	11020	26-Jun-04	12-Jul-04
R37-1169-114	-12.1	-5.0	11113	19-Jun-04	5-Jul-04
R37-1169-115	-11.9	-4.7	11220	11-Jun-04	27-Jun-04
R37-1169-116	-12.2	-4.7	11319	4-Jun-04	20-Jun-04
R37-1169-117	-12.2	-3.9	11418	27-May-04	13-Jun-04
R37-1169-118	-12.2	-3.5	11508	21-May-04	6-Jun-04
R37-1169-119	-12.6	-4.2	11601	14-May-04	31-May-04

Table B.1 Continued

Sample ID	$\delta^{13}C$ (‰, VPDB)	$\delta^{18}O$ (‰, VPDB)	dist. from base (μm)	untuned date	tuned date
R37-1169-120	-12.0	-4.6	11701	6-May-04	23-May-04
R37-1169-121	-11.0	-3.4	11796	29-Apr-04	16-May-04
R37-1169-122	-9.5	-6.1	11888	22-Apr-04	10-May-04
R37-1169-123	-9.8	-4.2	11981	15-Apr-04	—
R37-1169-124	-10.3	-4.4	12065	9-Apr-04	—
R37-1169-125	-10.9	-4.0	12159	2-Apr-04	—
R37-1169-126	-12.4	-3.9	12256	26-Mar-04	—
R37-1169-127	-12.4	-3.9	12342	19-Mar-04	—
R37-1169-128	-12.4	-3.9	12437	12-Mar-04	—
R37-1169-129	-12.4	-3.6	12536	5-Mar-04	—
R37-1169-130	-11.6	-3.4	12642	26-Feb-04	—
R37-1169-131	-11.5	-3.4	12738	19-Feb-04	—
R37-1169-132	-11.4	-3.4	12824	13-Feb-04	—
R37-1169-133	-11.3	-3.3	12909	6-Feb-04	—
R37-1169-134	-11.4	-4.2	12994	31-Jan-04	—
R37-1169-135	-11.8	-5.0	13085	24-Jan-04	—
R37-1169-136	-11.4	-5.2	13179	17-Jan-04	—
R37-1169-137	-10.9	-4.5	13269	10-Jan-04	—
R37-1169-138	-10.5	-4.6	13363	3-Jan-04	—
R37-1169-139	-10.0	-4.2	13455	27-Dec-03	—
R37-1169-140	-10.7	-3.8	13549	20-Dec-03	—
R37-1169-141	-11.5	-3.9	13647	13-Dec-03	—
R37-1169-142	-11.3	-4.1	13747	6-Dec-03	—
R37-1169-143	-10.4	-4.2	13836	29-Nov-03	—
R37-1169-144	-11.3	-4.7	13919	23-Nov-03	—
R37-1169-145	-11.8	-5.3	14010	16-Nov-03	—
R37-1169-146	-11.5	-5.1	14107	9-Nov-03	—
R37-1169-147	-11.6	-5.4	14207	1-Nov-03	—
R37-1169-149	-11.3	—	14361	21-Oct-03	—
R37-1169-150	-11.2	—	14457	14-Oct-03	—
R37-1053-002	-9.4	-2.2	12029	15-Apr-04	3-May-04
R37-1053-003	-10.7	-2.8	12143	31-Mar-04	16-Apr-04
R37-1053-004	-12.1	-3.7	12240	25-Mar-04	10-Apr-04
R37-1053-005	-12.6	-4.4	12329	20-Mar-04	4-Apr-04
R37-1053-006	-12.6	-2.7	12437	13-Mar-04	28-Mar-04
R37-1053-007	-12.3	-3.6	12531	7-Mar-04	22-Mar-04
R37-1053-008	-12.7	-3.4	12639	1-Mar-04	15-Mar-04

Table B.1 Continued

Sample ID	$\delta^{13}C$ (‰, VPDB)	$\delta^{18}O$ (‰, VPDB)	dist. from base (μm)	untuned date	tuned date
R37-1053-009	-12.2	-3.5	12740	23-Feb-04	9-Mar-04
R37-1053-010	-10.9	-2.2	12830	18-Feb-04	3-Mar-04
R37-1053-011	-11.2	-3.1	12937	11-Feb-04	25-Feb-04
R37-1053-012	-11.4	-3.4	13037	5-Feb-04	19-Feb-04
R37-1053-013	-11.6	-3.6	13124	31-Jan-04	13-Feb-04
R37-1053-014	-11.3	-4.0	13224	25-Jan-04	7-Feb-04
R37-1053-015	-11.6	-3.8	13328	19-Jan-04	31-Jan-04
R37-1053-016	-11.8	-4.5	13431	12-Jan-04	25-Jan-04
R37-1053-017	-11.6	-4.5	13528	6-Jan-04	18-Jan-04
R37-1053-018	-10.8	-4.1	13629	31-Dec-03	12-Jan-04
R37-1053-019	-10.9	-4.0	13714	26-Dec-03	7-Jan-04
R37-1053-020	-10.6	-3.4	13826	19-Dec-03	30-Dec-03
R37-1053-021	-10.1	-3.6	13920	14-Dec-03	24-Dec-03
R37-1053-022	-10.2	-3.9	14026	7-Dec-03	18-Dec-03
R37-1053-023	-11.4	-4.5	14125	1-Dec-03	11-Dec-03
R37-1053-024	-11.7	-3.7	14222	25-Nov-03	5-Dec-03
R37-1053-025	-11.3	-4.2	14327	19-Nov-03	28-Nov-03
R37-1053-026	-11.7	-3.7	14424	13-Nov-03	22-Nov-03
R37-1053-027	-11.8	-3.4	14511	8-Nov-03	16-Nov-03
R37-1053-028	-11.9	-4.1	14619	1-Nov-03	10-Nov-03
R37-1053-029	-12.0	-3.5	14723	26-Oct-03	3-Nov-03
R37-1053-030	-11.9	-3.9	14827	19-Oct-03	27-Oct-03
R37-1053-031	-11.5	-3.7	14907	14-Oct-03	22-Oct-03
R37-1053-032	-11.6	-4.1	15006	8-Oct-03	16-Oct-03
R37-1053-033	-11.8	-3.8	15106	2-Oct-03	9-Oct-03
R37-1053-035	-11.5	-3.9	15296	14-Sep-03	20-Sep-03
R37-1053-036	-11.1	-4.5	15410	8-Sep-03	13-Sep-03
R37-1053-037	-11.1	-3.8	15509	2-Sep-03	7-Sep-03
R37-1053-038	-11.9	-3.7	15603	27-Aug-03	1-Sep-03
R37-1053-039	-11.9	-3.9	15699	21-Aug-03	26-Aug-03
R37-1053-040	-12.5	-4.6	15804	14-Aug-03	19-Aug-03
R37-1053-041	-11.3	-4.1	15909	8-Aug-03	13-Aug-03
R37-1053-037	-11.1	-4.9	16008	2-Aug-03	6-Aug-03
R37-1053-043	-10.8	-5.0	16109	27-Jul-03	31-Jul-03
R37-1053-044	-10.5	-4.8	16206	21-Jul-03	25-Jul-03
R37-1053-045	-9.8	-4.7	16302	15-Jul-03	18-Jul-03
R37-1053-046	-10.5	-4.1	16404	9-Jul-03	12-Jul-03
R37-1053-047	-10.7	-3.7	16498	3-Jul-03	6-Jul-03

Table B.1 Continued

Sample ID	$\delta^{13}C$ (‰, VPDB)	$\delta^{18}O$ (‰, VPDB)	dist. from base (μm)	untuned date	tuned date
R37-1053-048	-10.7	-3.8	16596	27-Jun-03	29-Jun-03
R37-1053-049	-10.7	-4.0	16702	22-Jun-03	24-Jun-03
R37-1053-050	-10.7	-3.4	16783	15-Jun-03	17-Jun-03
R37-1053-051	-10.4	-3.0	16893	9-Jun-03	10-Jun-03
R37-1053-052	-9.7	-3.2	16992	3-Jun-03	4-Jun-03
R37-1053-053	-9.3	-3.4	17099	28-May-03	28-May-03
R37-1053-051	-10.4	-3.7	17200	22-May-03	22-May-03
R37-1053-055	-10.6	-3.9	17291	17-May-03	17-May-03
R37-1053-056	-10.6	-4.2	17370	11-May-03	10-May-03
R37-1053-057	-11.9	-4.5	17477	5-May-03	4-May-03
R37-1053-058	-12.1	-4.6	17578	29-Apr-03	28-Apr-03
R37-1053-059	-11.7	-3.7	17668	25-Apr-03	23-Apr-03
R37-1053-060	-11.7	-3.1	17741	19-Apr-03	18-Apr-03
R37-1053-061	-11.5	-2.4	17832	14-Apr-03	12-Apr-03
R37-1053-062	-11.8	-2.4	17913	8-Apr-03	6-Apr-03
R37-1053-063	-11.7	-3.4	18016	2-Apr-03	31-Mar-03
R37-1053-064	-11.6	-4.0	18113	27-Mar-03	24-Mar-03
R37-1053-065	-11.6	-3.6	18212	22-Mar-03	19-Mar-03
R37-1053-066	-11.5	-3.4	18299	15-Mar-03	12-Mar-03
R37-1053-067	-11.7	-3.7	18399	9-Mar-03	6-Mar-03
R37-1053-068	-11.4	-3.7	18498	3-Mar-03	27-Feb-03
R37-1053-069	-10.9	-3.9	18597	25-Feb-03	21-Feb-03
R37-1053-071	-11.5	-3.6	18698	19-Feb-03	15-Feb-03
R37-1053-072	-11.5	-3.3	18797	14-Feb-03	9-Feb-03
R37-1053-073	-11.4	-4.3	18890	7-Feb-03	2-Feb-03
R37-1053-074	-11.0	-4.1	18989	1-Feb-03	27-Jan-03
R37-1053-075	-10.6	-3.6	19095	26-Jan-03	20-Jan-03
R37-1053-076	-10.7	-4.0	19197	20-Jan-03	14-Jan-03
R37-1053-077	-11.0	-4.2	19293	12-Jan-03	5-Jan-03
R37-1053-078	-10.9	-4.6	19427	6-Jan-03	30-Dec-02
R37-1053-079	-10.8	-5.0	19522	31-Dec-02	24-Dec-02
R37-1053-080	-11.2	-5.2	19625	24-Dec-02	17-Dec-02
R37-1053-081	-10.8	-3.6	19733	19-Dec-02	11-Dec-02
R37-1053-082	-10.0	-3.7	19818	12-Dec-02	4-Dec-02
R37-1053-083	-10.0	-4.2	19931	7-Dec-02	28-Nov-02
R37-1053-084	-11.6	-5.6	20020	30-Nov-02	21-Nov-02
R37-1053-085	-11.7	-5.0	20126	24-Nov-02	15-Nov-02
R37-1053-086	-11.6	-4.4	20234	18-Nov-02	9-Nov-02

Table B.1 Continued

Sample ID	$\delta^{13}C$ (‰, VPDB)	$\delta^{18}O$ (‰, VPDB)	dist. from base (μm)	untuned date	tuned date
R37-1053-087	-11.6	-3.2	20326	11-Nov-02	2-Nov-02
R37-1053-088	-11.5	-3.0	20433	5-Nov-02	26-Oct-02
R37-1053-089	-11.8	-3.2	20533	30-Oct-02	20-Oct-02
R37-1053-090	-11.3	-4.0	20634	24-Oct-02	14-Oct-02
R37-1053-091	-11.1	-3.9	20731	18-Oct-02	7-Oct-02
R37-1053-092	-11.2	-4.1	20832	12-Oct-02	1-Oct-02
R37-1053-094	-11.2	-4.0	20924	30-Sep-02	18-Sep-02
R37-1053-095	-11.1	-3.9	21131	24-Sep-02	12-Sep-02
R37-1053-096	-10.9	-3.8	21230	18-Sep-02	5-Sep-02
R37-1053-097	-11.1	-4.0	21333	12-Sep-02	30-Aug-02
R37-1053-098	-11.3	-3.9	21432	6-Sep-02	24-Aug-02
R37-1053-099	-9.9	-5.0	21527	30-Aug-02	17-Aug-02
R37-1053-100	-11.1	-3.6	21639	24-Aug-02	10-Aug-02
R37-1053-101	-11.4	-3.7	21741	19-Aug-02	5-Aug-02
R37-1053-102	-10.8	-4.3	21821	12-Aug-02	29-Jul-02
R37-1053-104	-10.7	-4.4	21926	30-Jul-02	15-Jul-02
R37-1053-105	-10.6	-4.4	22140	25-Jul-02	10-Jul-02
R37-1053-106	-10.7	-4.3	22223	19-Jul-02	3-Jul-02
R37-1053-107	-10.0	-4.8	22327	12-Jul-02	26-Jun-02
R37-1053-108	-10.5	-4.3	22437	7-Jul-02	21-Jun-02
R37-1053-109	-10.1	-4.2	22518	1-Jul-02	14-Jun-02
R37-1053-110	-8.7	-4.3	22623	25-Jun-02	8-Jun-02
R37-1053-111	-9.4	-4.9	22723	18-Jun-02	1-Jun-02
R37-1053-112	-9.3	-4.9	22835	12-Jun-02	25-May-02
R37-1053-113	-9.0	-4.9	22934	6-Jun-02	18-May-02
R37-1053-114	-9.5	-4.0	23035	31-May-02	12-May-02
R37-1053-115	-10.9	-3.8	23131	25-May-02	5-May-02
R37-1053-116	-10.6	-2.7	23224	19-May-02	28-Apr-02
R37-1053-117	-10.1	-1.6	23332	27-Apr-02	3-Apr-02
R37-1053-118	-10.6	-2.1	23689	21-Apr-02	27-Mar-02
R37-1053-119	-11.3	-2.4	23792	14-Apr-02	20-Mar-02
R37-1053-120	-11.6	-2.5	23892	9-Apr-02	14-Mar-02
R37-1053-121	-11.5	-3.0	23974	3-Apr-02	6-Mar-02
R37-1053-122	-11.4	-3.6	24087	28-Mar-02	27-Feb-02
R37-1053-123	-11.2	-2.9	24184	22-Mar-02	21-Feb-02
R37-1053-124	-11.5	-3.2	24280	16-Mar-02	14-Feb-02
R37-1053-125	-10.9	-3.2	24377	11-Mar-02	8-Feb-02
R37-1053-126	-10.7	-2.5	24464	4-Mar-02	1-Feb-02

Table B.1 Continued

Sample ID	$\delta^{13}C$ (‰, VPDB)	$\delta^{18}O$ (‰, VPDB)	dist. from base (μm)	untuned date	tuned date
R37-1053-127	-11.0	-2.1	24572	27-Feb-02	26-Jan-02
R37-1053-128	-10.9	-2.5	24647	21-Feb-02	19-Jan-02
R37-1053-129	-11.3	-2.5	24754	15-Feb-02	12-Jan-02
R37-1053-130	-11.3	-3.1	24854	9-Feb-02	5-Jan-02
R37-1053-131	-11.3	-2.8	24953	2-Feb-02	29-Dec-01
R37-1053-132	-10.9	-3.2	25056	28-Jan-02	23-Dec-01
R37-1053-133	-11.0	-3.4	25145	22-Jan-02	16-Dec-01
R37-1053-134	-10.7	-3.0	25246	16-Jan-02	9-Dec-01
R37-1053-135	-9.7	-2.4	25337	10-Jan-02	2-Dec-01
R37-1053-136	-10.6	-2.8	25438	5-Jan-02	27-Nov-01
R37-1053-137	-11.3	-2.9	25520	30-Dec-01	19-Nov-01
R37-1053-138	-11.8	-3.2	25626	24-Dec-01	13-Nov-01
R37-1053-139	-11.6	-3.8	25724	18-Dec-01	6-Nov-01
R37-1053-140	-11.5	-4.2	25824	1-Dec-01	18-Oct-01
R37-1053-141	-11.4	-3.7	26096	26-Nov-01	11-Oct-01
R37-1053-142	-11.0	-3.3	26187	20-Nov-01	5-Oct-01
R37-1053-143	-11.7	-4.2	26282	14-Nov-01	28-Sep-01
R37-1053-144	-11.9	-4.3	26375	8-Nov-01	22-Sep-01
R37-1053-145	-12.1	-4.3	26472	2-Nov-01	15-Sep-01
R37-1053-146	-12.1	-4.7	26568	27-Oct-01	8-Sep-01
R37-1053-147	-11.9	-4.5	26664	22-Oct-01	2-Sep-01
R37-1053-148	-11.6	-3.9	26756	17-Oct-01	27-Aug-01
R37-1053-149	-11.9	-3.9	26837	10-Oct-01	19-Aug-01
R37-1053-150	-12.2	-4.1	26952	4-Oct-01	12-Aug-01
R37-1053-151	-11.8	-3.8	27052	28-Sep-01	5-Aug-01
R37-1053-152	-11.3	-4.0	27153	22-Sep-01	30-Jul-01
R37-1053-153	-11.0	-4.4	27251	16-Sep-01	23-Jul-01
R37-1053-154	-11.0	-4.1	27343	10-Sep-01	16-Jul-01
R37-1053-155	-10.7	-4.1	27450	4-Sep-01	9-Jul-01
R37-1053-156	-10.7	-4.4	27547	29-Aug-01	2-Jul-01
R37-1053-158	-10.9	-4.2	27646	16-Aug-01	18-Jun-01
R37-1053-159	-10.9	-4.1	27849	11-Aug-01	12-Jun-01
R37-1053-160	-10.9	-4.2	27932	5-Aug-01	5-Jun-01
R37-1053-161	-10.6	-4.4	28037	30-Jul-01	29-May-01
R37-1053-162	-10.6	-3.3	28136	23-Jul-01	22-May-01
R37-1053-163	-10.8	-2.7	28238	18-Jul-01	16-May-01
R37-1053-164	-9.7	-3.7	28331	11-Jul-01	8-May-01
R37-1053-165	-10.1	-3.4	28444	5-Jul-01	1-May-01

Table B.1 Continued

Sample ID	$\delta^{13}C$ (‰, VPDB)	$\delta^{18}O$ (‰, VPDB)	dist. from base (μm)	untuned date	tuned date
R37-1053-166	-10.9	-3.7	28545	29-Jun-01	24-Apr-01
R37-1053-167	-10.2	-2.7	28638	23-Jun-01	17-Apr-01
R37-1053-169	-10.9	-3.6	28746	13-Jun-01	6-Apr-01
R37-1053-170	-10.9	-3.7	28895	7-Jun-01	30-Mar-01
R37-1053-171	-11.0	-3.0	29003	1-Jun-01	23-Mar-01
R37-1053-172	-10.9	-2.9	29101	26-May-01	17-Mar-01
R37-1053-173	-10.7	-2.3	29192	20-May-01	10-Mar-01
R37-1053-174	-10.1	-3.2	29288	15-May-01	4-Mar-01
R37-1053-175	-10.1	-3.0	29375	10-May-01	26-Feb-01
R37-1053-176	-10.2	-3.1	29467	4-May-01	20-Feb-01
R37-1053-177	-9.4	-2.5	29554	27-Apr-01	12-Feb-01
R37-1053-178	-9.0	-2.7	29669	21-Apr-01	5-Feb-01
R37-1053-179	-9.0	-2.6	29764	16-Apr-01	29-Jan-01
R37-1053-180	-9.6	-2.7	29860	11-Apr-01	24-Jan-01
R37-1053-181	-10.5	-2.3	29940	4-Apr-01	16-Jan-01
R37-1053-182	-10.1	-4.0	30046	29-Mar-01	9-Jan-01
R37-1053-183	-9.7	-2.2	30143	25-Mar-01	3-Jan-01
R37-1053-184	-10.0	-2.0	30219	19-Mar-01	26-Dec-00
R37-1053-185	-9.5	-2.1	30320	12-Mar-01	19-Dec-00
R37-1053-186	-9.1	-3.4	30423	7-Mar-01	12-Dec-00
R37-1053-187	-10.2	-3.4	30504	1-Mar-01	5-Dec-00
R37-1053-188	-11.1	-3.2	30600	24-Feb-01	28-Nov-00
R37-1053-189	-11.2	-3.2	30690	18-Feb-01	20-Nov-00
R37-1053-190	-11.0	-4.1	30793	12-Feb-01	13-Nov-00
R37-1053-191	-10.6	-4.0	30886	7-Feb-01	6-Nov-00
R37-1053-192	-10.3	-4.3	30975	1-Feb-01	30-Oct-00
R37-1053-193	-10.5	-4.3	31069	26-Jan-01	23-Oct-00
R37-1053-194	-10.4	-3.5	31163	22-Jan-01	17-Oct-00
R37-1053-195	-10.5	-3.5	31236	15-Jan-01	8-Oct-00
R37-1053-196	-11.0	-3.4	31347	9-Jan-01	1-Oct-00
R37-1053-197	-11.1	-3.2	31443	3-Jan-01	23-Sep-00
R37-1053-198	-11.1	-3.3	31541	29-Dec-00	17-Sep-00
R37-1053-199	-11.1	-3.4	31621	23-Dec-00	9-Sep-00
R37-1053-200	-11.0	-3.7	31728	17-Dec-00	1-Sep-00
R37-1053-201	-10.9	-3.6	31827	11-Dec-00	25-Aug-00
R37-1053-202	-11.0	-3.7	31927	6-Dec-00	19-Aug-00
R37-1053-203	-10.7	-3.6	32005	1-Dec-00	12-Aug-00
R37-1053-204	-11.1	-4.1	32087	24-Nov-00	3-Aug-00

Table B.1 Continued

Sample ID	$\delta^{13}C$ (‰, VPDB)	$\delta^{18}O$ (‰, VPDB)	dist. from base (μm)	untuned date	tuned date
R37-1053-207	-10.8	-4.0	32205	5-Nov-00	11-Jul-00
R37-1053-208	-11.0	-4.1	32503	31-Oct-00	4-Jul-00
R37-1053-209	-11.1	-3.8	32593	24-Oct-00	26-Jun-00
R37-1053-210	-11.4	-4.3	32703	18-Oct-00	18-Jun-00
R37-1053-211	-10.9	-4.4	32800	12-Oct-00	10-Jun-00
R37-1053-212	-10.8	-3.0	32905	6-Oct-00	3-Jun-00
R37-1053-214	-10.9	-2.7	33000	25-Sep-00	20-May-00
R37-1053-215	-11.2	-3.3	33187	18-Sep-00	11-May-00
R37-1053-216	-10.4	-3.5	33298	11-Sep-00	3-May-00
R37-1053-217	-10.3	-3.5	33404	5-Sep-00	25-Apr-00
R37-1053-218	-11.0	-4.0	33506	31-Aug-00	18-Apr-00
R37-1053-219	-11.5	-3.3	33599	23-Aug-00	9-Apr-00
R37-1053-220	-10.8	-2.7	33719	16-Aug-00	31-Mar-00
R37-1053-221	-10.9	-3.0	33834	10-Aug-00	23-Mar-00
R37-1053-222	-11.2	-3.1	33940	4-Aug-00	16-Mar-00
R37-1053-223	-11.4	-3.0	34029	29-Jul-00	7-Mar-00
R37-1053-224	-11.3	-2.8	34141	22-Jul-00	28-Feb-00
R37-1053-225	-10.9	-2.8	34253	15-Jul-00	19-Feb-00
R37-412-259	-11.0	—	666	19-May-87	18-Apr-87
R37-412-258	-11.7	-5.7	784	12-May-87	12-Apr-87
R37-412-257	-12.1	-4.9	888	5-May-87	7-Apr-87
R37-412-256	-13.0	—	1008	28-Apr-87	1-Apr-87
R37-412-255	-12.6	-3.6	1130	20-Apr-87	25-Mar-87
R37-412-254	-12.7	-5.0	1276	11-Apr-87	18-Mar-87
R37-412-253	-12.8	-5.0	1371	5-Apr-87	13-Mar-87
R37-412-252	-12.6	-6.2	1496	28-Mar-87	6-Mar-87
R37-412-251	-12.8	—	1608	21-Mar-87	28-Feb-87
R37-412-250	-12.4	—	1710	15-Mar-87	23-Feb-87
R37-412-249	-12.3	—	1830	7-Mar-87	16-Feb-87
R37-412-248	-12.3	—	1917	2-Mar-87	11-Feb-87
R37-412-247	-12.2	-5.6	1984	26-Feb-87	8-Feb-87
R37-412-246	-11.3	-4.8	2073	20-Feb-87	3-Feb-87
R37-412-245	-10.9	-5.2	2176	14-Feb-87	28-Jan-87
R37-412-244	-11.0	—	2286	7-Feb-87	22-Jan-87
R37-412-243	-10.1	-5.6	2383	1-Feb-87	17-Jan-87
R37-412-242	-10.5	-5.0	2455	27-Jan-87	13-Jan-87
R37-412-240/241	-9.8	-4.5	2570	20-Jan-87	6-Jan-87

Table B.1 Continued

Sample ID	$\delta^{13}C$ (‰, VPDB)	$\delta^{18}O$ (‰, VPDB)	dist. from base (μm)	untuned date	tuned date
R37-412-239	-8.9	—	2752	9-Jan-87	27-Dec-86
R37-412-238	-9.9	-6.1	2860	2-Jan-87	21-Dec-86
R37-412-237	-10.4	-5.7	2961	27-Dec-86	15-Dec-86
R37-412-236	-11.5	—	3060	20-Dec-86	9-Dec-86
R37-412-235	-10.3	—	3154	15-Dec-86	3-Dec-86
R37-412-234	-10.8	-4.6	3262	8-Dec-86	27-Nov-86
R37-412-233	-12.9	-3.9	3363	1-Dec-86	21-Nov-86
R37-412-232	-12.5	—	3455	26-Nov-86	15-Nov-86
R37-412-231	-12.1	—	3577	18-Nov-86	8-Nov-86
R37-412-230	-12.7	—	3667	12-Nov-86	2-Nov-86
R37-412-229	-12.5	—	3768	6-Nov-86	27-Oct-86
R37-412-228	-12.7	—	3874	31-Oct-86	20-Oct-86
R37-412-227	-12.9	-5.4	3973	24-Oct-86	14-Oct-86
R37-412-226	-12.1	-5.2	4077	18-Oct-86	8-Oct-86
R37-412-225	-12.2	—	4181	11-Oct-86	1-Oct-86
R37-412-224	-12.9	—	4291	4-Oct-86	24-Sep-86
R37-412-223	-12.7	-7.1	4389	28-Sep-86	18-Sep-86
R37-412-221	-12.5	-5.7	4568	17-Sep-86	6-Sep-86
R37-412-220	-12.4	-6.1	4661	11-Sep-86	31-Aug-86
R37-412-219	-12.5	—	4769	5-Sep-86	24-Aug-86
R37-412-218	-12.3	-5.7	4872	29-Aug-86	17-Aug-86
R37-412-217	-12.2	-5.1	4987	22-Aug-86	10-Aug-86
R37-412-216	-12.1	—	5073	17-Aug-86	4-Aug-86
R37-412-215	-12.2	-5.4	5174	10-Aug-86	28-Jul-86
R37-412-214	-11.7	—	5262	5-Aug-86	22-Jul-86
R37-412-213	-11.9	—	5344	31-Jul-86	17-Jul-86
R37-412-212	-11.9	-4.8	5424	26-Jul-86	12-Jul-86
R37-412-211	-11.4	-5.6	5523	19-Jul-86	5-Jul-86
R37-412-210	-11.6	-6.0	5617	14-Jul-86	29-Jun-86
R37-412-209	-9.7	-4.6	5704	8-Jul-86	23-Jun-86
R37-412-208	-11.6	-5.8	5794	2-Jul-86	17-Jun-86
R37-412-207	-10.6	-5.5	5881	27-Jun-86	11-Jun-86
R37-412-206	-10.0	-5.5	6056	16-Jun-86	30-May-86
R37-412-205	-10.0	-5.9	6155	10-Jun-86	24-May-86
R37-412-204	-9.2	-5.2	6245	4-Jun-86	17-May-86
R37-412-203	-10.4	—	6338	30-May-86	11-May-86
R37-412-202	-11.7	-5.1	6432	24-May-86	5-May-86
R37-412-201	-12.2	-5.0	6799	1-May-86	10-Apr-86

Table B.1 Continued

Sample ID	$\delta^{13}C$ (‰, VPDB)	$\delta^{18}O$ (‰, VPDB)	dist. from base (μm)	untuned date	tuned date
R37-412-200	-12.0	-3.7	6899	24-Apr-86	3-Apr-86
R37-412-199	-12.4	-4.6	6991	19-Apr-86	28-Mar-86
R37-412-198	-12.0	-4.3	7087	13-Apr-86	21-Mar-86
R37-412-197	-12.2	-3.9	7189	6-Apr-86	14-Mar-86
R37-412-196	-11.7	-3.4	7293	31-Mar-86	8-Mar-86
R37-412-195	-12.1	-5.0	7370	26-Mar-86	2-Mar-86
R37-412-194	-12.4	-5.6	7478	19-Mar-86	23-Feb-86
R37-412-193	-12.2	-5.6	7572	13-Mar-86	17-Feb-86
R37-412-192	-12.0	-5.2	7667	7-Mar-86	11-Feb-86
R37-412-191	-11.9	—	7787	28-Feb-86	3-Feb-86
R37-412-190	-12.4	-4.7	7862	23-Feb-86	29-Jan-86
R37-412-189	-12.0	-5.7	7966	17-Feb-86	22-Jan-86
R37-412-188	-12.0	-4.6	8054	11-Feb-86	17-Jan-86
R37-412-187	-12.3	-4.4	8158	5-Feb-86	10-Jan-86
R37-412-186	-12.1	-4.5	8242	31-Jan-86	5-Jan-86
R37-412-185	-12.0	-4.6	8352	24-Jan-86	29-Dec-85
R37-412-184	-11.8	-4.6	8428	19-Jan-86	24-Dec-85
R37-412-183	-11.4	-4.6	8498	15-Jan-86	20-Dec-85
R37-412-182	-11.2	-4.2	8657	5-Jan-86	11-Dec-85
R37-412-181	-11.0	-3.5	8814	26-Dec-85	1-Dec-85
R37-412-180	-11.1	-4.2	8955	17-Dec-85	23-Nov-85
R37-412-179	-11.2	-4.2	9111	7-Dec-85	14-Nov-85
R37-412-178	-11.8	-4.1	9265	28-Nov-85	6-Nov-85
R37-412-177	-10.2	—	9416	18-Nov-85	28-Oct-85
R37-412-001	-12.4	-4.9	9447	16-Nov-85	27-Oct-85
R37-412-002	-12.5	-4.3	9515	7-Nov-85	19-Oct-85
R37-412-003	-12.3	-5.5	9616	31-Oct-85	13-Oct-85
R37-412-004	-12.5	-4.9	9723	23-Oct-85	6-Oct-85
R37-412-005	-12.5	-5.1	9842	14-Oct-85	29-Sep-85
R37-412-006	-12.2	-5.1	9934	7-Oct-85	23-Sep-85
R37-412-171/172	-11.7	-5.4	10037	28-Sep-85	16-Sep-85
R37-412-008	-11.7	-5.3	10139	22-Sep-85	11-Sep-85
R37-412-009	-11.9	-5.1	10238	15-Sep-85	5-Sep-85
R37-412-010	-12.5	-5.2	10339	7-Sep-85	30-Aug-85
R37-412-168	-12.1	-5.4	10436	28-Aug-85	23-Aug-85
R37-412-012	-12.0	-5.3	10533	24-Aug-85	19-Aug-85
R37-412-013	-12.4	-5.4	10626	17-Aug-85	14-Aug-85
R37-412-014	-12.3	-5.2	10723	10-Aug-85	9-Aug-85

Table B.1 Continued

Sample ID	$\delta^{13}C$ (‰, VPDB)	$\delta^{18}O$ (‰, VPDB)	dist. from base (μm)	untuned date	tuned date
R37-412-015	-12.3	-5.0	10825	2-Aug-85	3-Aug-85
R37-412-016	-12.5	-4.9	10923	26-Jul-85	28-Jul-85
R37-412-017	-12.1	-4.9	11022	18-Jul-85	23-Jul-85
R37-412-018	-12.0	-4.4	11112	12-Jul-85	18-Jul-85
R37-412-019	-11.9	-4.5	11215	4-Jul-85	12-Jul-85
R37-412-020	-12.1	-4.2	11310	27-Jun-85	7-Jul-85
R37-412-021	-11.9	-4.5	11415	19-Jun-85	1-Jul-85
R37-412-022	-12.1	-4.7	11514	12-Jun-85	25-Jun-85
R37-412-023	-11.9	-4.2	11609	5-Jun-85	20-Jun-85
R37-412-024	-11.6	-4.4	11708	29-May-85	14-Jun-85
R37-412-025	-12.0	-4.9	11802	22-May-85	9-Jun-85
R37-412-026	-12.1	-2.8	11910	14-May-85	3-Jun-85
R37-412-027	-12.3	-4.3	12004	7-May-85	29-May-85
R37-412-028	-10.7	-3.4	12105	29-Apr-85	23-May-85
R37-412-029	-11.7	-4.3	12202	22-Apr-85	17-May-85
R37-412-030	-10.2	-5.5	12303	15-Apr-85	11-May-85
R37-412-031	-10.2	-4.8	12405	7-Apr-85	5-May-85
R37-412-032	-11.8	-4.0	12501	31-Mar-85	30-Apr-85
R37-412-033	-12.4	-4.9	12617	22-Mar-85	23-Apr-85
R37-412-034	-12.5	-4.5	12722	15-Mar-85	16-Apr-85
R37-412-035	-12.6	-5.9	12832	6-Mar-85	10-Apr-85
R37-412-036	-11.9	-5.4	12939	26-Feb-85	3-Apr-85
R37-412-037	-12.3	-5.7	13054	18-Feb-85	27-Mar-85
R37-412-038	-12.6	-5.2	13152	11-Feb-85	21-Mar-85
R37-412-039	-11.6	-5.4	13277	1-Feb-85	13-Mar-85
R37-412-041	-12.5	-5.1	13386	24-Jan-85	6-Mar-85
R37-412-042	-12.3	-5.8	13490	17-Jan-85	27-Feb-85
R37-412-043	-12.4	-5.4	13600	8-Jan-85	20-Feb-85
R37-412-044	-12.4	-4.9	13717	31-Dec-84	13-Feb-85
R37-412-045	-11.5	-4.2	13814	24-Dec-84	6-Feb-85
R37-412-046	-10.8	-5.6	13931	15-Dec-84	29-Jan-85
R37-412-047	-10.3	-5.2	14042	7-Dec-84	22-Jan-85
R37-412-048	-10.4	-4.1	14150	29-Nov-84	15-Jan-85
R37-412-049	-11.2	-4.3	14256	21-Nov-84	7-Jan-85
R37-412-050	-11.0	-3.8	14366	13-Nov-84	31-Dec-84
R37-412-051	-10.6	-4.8	14517	2-Nov-84	20-Dec-84
R37-412-052	-10.8	—	14606	26-Oct-84	14-Dec-84
R37-412-053	-9.2	-5.4	14708	18-Oct-84	7-Dec-84

Table B.1 Continued

Sample ID	$\delta^{13}C$ (‰, VPDB)	$\delta^{18}O$ (‰, VPDB)	dist. from base (μm)	untuned date	tuned date
R37-412-054	-12.6	-4.2	14822	10-Oct-84	29-Nov-84
R37-412-055	-12.8	-4.1	14933	2-Oct-84	21-Nov-84
R37-412-056	-12.5	-4.7	15043	24-Sep-84	13-Nov-84
R37-412-057	-12.4	—	15160	15-Sep-84	5-Nov-84
R37-412-058	-12.3	-4.6	15268	7-Sep-84	28-Oct-84
R37-412-059	-12.1	-4.2	15381	30-Aug-84	20-Oct-84
R37-412-060	-12.4	-4.2	15479	22-Aug-84	12-Oct-84
R37-412-063	-12.9	-6.1	15609	13-Aug-84	3-Oct-84
R37-412-064	-12.9	-4.9	15729	4-Aug-84	24-Sep-84
R37-412-065	-12.3	-5.7	15851	26-Jul-84	15-Sep-84
R37-412-066	-13.1	-4.7	15961	18-Jul-84	7-Sep-84
R37-412-067	-12.4	-5.8	16079	9-Jul-84	29-Aug-84
R37-412-068	-13.0	-6.5	16194	30-Jun-84	20-Aug-84
R37-412-069	-11.7	-4.8	16333	20-Jun-84	10-Aug-84
R37-412-070	-12.6	-3.2	16498	8-Jun-84	28-Jul-84
R37-412-071	-12.7	-2.2	16628	29-May-84	18-Jul-84
R37-412-072	-12.5	-2.2	16755	20-May-84	9-Jul-84
R37-412-073	-12.7	-4.2	16915	8-May-84	26-Jun-84
R37-412-074	-12.5	-4.9	17024	30-Apr-84	18-Jun-84
R37-412-075	-12.5	-5.0	17102	24-Apr-84	12-Jun-84
R37-412-076	-12.2	-4.8	17212	16-Apr-84	3-Jun-84
R37-412-077	-12.3	-4.8	17308	9-Apr-84	27-May-84
R37-412-078	-12.3	-4.9	17398	2-Apr-84	20-May-84
R37-412-079	-12.0	-4.1	17483	27-Mar-84	14-May-84
R37-412-080	-12.0	-4.2	17603	18-Mar-84	4-May-84
R37-412-081	-11.9	-5.6	17694	11-Mar-84	27-Apr-84
R37-412-082	-12.2	-4.9	17795	4-Mar-84	20-Apr-84
R37-412-083	-12.4	-5.0	17899	25-Feb-84	12-Apr-84
R37-412-084	-12.3	-4.5	17995	18-Feb-84	4-Apr-84
R37-412-085	-11.9	-4.0	18097	10-Feb-84	28-Mar-84
R37-412-086	-11.7	-3.9	18195	3-Feb-84	20-Mar-84
R37-412-087	-12.0	-4.5	18276	28-Jan-84	14-Mar-84
R37-412-088	-12.1	-5.1	18372	21-Jan-84	7-Mar-84
R37-412-089	-12.2	-3.4	18469	14-Jan-84	28-Feb-84
R37-412-090	-12.1	-4.7	18567	7-Jan-84	21-Feb-84
R37-412-091	-11.8	-4.7	18655	31-Dec-83	14-Feb-84
R37-412-092	-11.3	-4.4	18756	24-Dec-83	6-Feb-84
R37-412-093	-11.4	-4.1	18855	16-Dec-83	30-Jan-84

Table B.1 Continued

Sample ID	$\delta^{13}C$ (‰, VPDB)	$\delta^{18}O$ (‰, VPDB)	dist. from base (μm)	untuned date	tuned date
R37-412-094	-9.6	-2.1	18958	9-Dec-83	22-Jan-84
R37-412-095	-9.9	-2.6	19050	2-Dec-83	15-Jan-84
R37-412-096	-10.2	-2.2	19179	22-Nov-83	6-Jan-84
R37-412-097	-10.8	-2.5	19287	14-Nov-83	29-Dec-83
R37-412-098	-12.2	-3.9	19374	8-Nov-83	22-Dec-83
R37-412-099	-12.5	-2.8	19480	31-Oct-83	14-Dec-83
R37-412-101	-11.9	-4.5	19572	24-Oct-83	8-Dec-83
R37-412-102	-11.4	-4.2	19650	18-Oct-83	2-Dec-83
R37-412-103	-12.0	-4.0	19767	10-Oct-83	23-Nov-83
R37-412-104	-11.7	-5.4	19850	3-Oct-83	17-Nov-83
R37-412-105	-12.4	-4.1	19944	27-Sep-83	10-Nov-83
R37-412-106	-12.4	-4.9	20035	20-Sep-83	3-Nov-83
R37-412-107	-12.5	-4.6	20105	15-Sep-83	29-Oct-83
R37-412-108	-12.3	-4.5	20202	7-Sep-83	21-Oct-83
R37-412-109	-12.4	-5.2	20284	1-Sep-83	15-Oct-83
R37-412-110	-11.7	-5.2	20337	28-Aug-83	11-Oct-83
R37-412-111	-12.0	-4.7	20443	21-Aug-83	3-Oct-83
R37-412-112	-11.8	-3.8	20537	14-Aug-83	26-Sep-83
R37-412-113	-12.0	-4.9	20643	6-Aug-83	17-Sep-83
R37-412-114	-11.8	-5.4	20747	29-Jul-83	9-Sep-83
R37-412-115	-12.3	-5.1	20834	23-Jul-83	2-Sep-83
R37-412-116	-11.8	-4.8	20923	16-Jul-83	26-Aug-83
R37-412-117	-11.5	—	20999	10-Jul-83	20-Aug-83
R37-412-118	-11.8	-5.1	21104	3-Jul-83	11-Aug-83
R37-412-119	-11.5	-4.6	21182	27-Jun-83	5-Aug-83
R37-412-120	-11.0	-4.7	21283	19-Jun-83	28-Jul-83
R37-412-121	-11.3	-4.6	21399	11-Jun-83	18-Jul-83
R37-412-122	-11.6	-4.8	21505	3-Jun-83	9-Jul-83
R37-412-123	-9.8	-4.4	21582	28-May-83	2-Jul-83
R37-412-124	-9.4	—	21662	22-May-83	25-Jun-83
R37-412-125	-10.4	-3.8	21759	15-May-83	16-Jun-83
R37-412-126	-9.2	-3.9	21872	7-May-83	6-Jun-83
R37-412-127	-9.9	-4.4	21945	1-May-83	30-May-83
R37-412-128	-9.9	-3.0	22016	26-Apr-83	24-May-83
R37-412-129	-10.6	—	22108	19-Apr-83	15-May-83
R37-412-130	-10.9	—	22202	12-Apr-83	6-May-83
R37-412-131	-10.8	—	22294	5-Apr-83	28-Apr-83
R37-412-132	-11.9	-4.4	22385	30-Mar-83	19-Apr-83

Table B.1 Continued

Sample ID	$\delta^{13}C$ (‰, VPDB)	$\delta^{18}O$ (‰, VPDB)	dist. from base (μm)	untuned date	tuned date
R37-412-133	-12.2	-4.2	22441	26-Mar-83	13-Apr-83
R37-412-134	-12.3	-4.0	22515	20-Mar-83	6-Apr-83
R37-412-135	-12.2	-4.4	22589	15-Mar-83	30-Mar-83
R37-412-136	-12.1	-4.8	22679	8-Mar-83	21-Mar-83
R37-412-137	-12.4	-5.7	22773	1-Mar-83	12-Mar-83
R37-412-138	-12.7	-4.6	22850	23-Feb-83	4-Mar-83
R37-412-139	-12.5	-5.7	22937	17-Feb-83	23-Feb-83
R37-412-140	-13.1	-5.3	23032	10-Feb-83	14-Feb-83
R37-412-141	-12.8	-4.8	23121	3-Feb-83	5-Feb-83
R37-412-142	-12.3	-3.3	23216	27-Jan-83	26-Jan-83
R37-412-143	-12.2	-5.1	23301	21-Jan-83	17-Jan-83
R37-412-144	-10.5	-3.8	23390	14-Jan-83	8-Jan-83
R37-412-145	-9.9	-3.8	23484	7-Jan-83	30-Dec-82
R37-412-146	-11.1	-5.2	23569	1-Jan-83	21-Dec-82
R37-412-147	-11.4	-4.8	23668	25-Dec-82	11-Dec-82
R37-412-148	-10.5	-5.8	23800	15-Dec-82	28-Nov-82
R37-412-149	-10.1	-4.9	23900	8-Dec-82	18-Nov-82
R37-412-150	-10.9	-5.0	23988	1-Dec-82	9-Nov-82
R37-412-151/152	-11.2	—	24211	15-Nov-82	17-Oct-82
R37-412-153	-11.9	—	24304	8-Nov-82	8-Oct-82
R37-412-154	-12.2	-5.0	24419	30-Oct-82	27-Sep-82
R37-412-155	-12.4	-4.8	24521	22-Oct-82	17-Sep-82
R37-412-156	-12.3	-5.4	24638	14-Oct-82	5-Sep-82
R37-412-157	-12.4	-4.9	24735	7-Oct-82	27-Aug-82
R37-412-158	-12.3	-6.0	24846	28-Sep-82	16-Aug-82
R37-412-159	-12.1	-4.5	24956	20-Sep-82	5-Aug-82
R37-412-160	-12.2	—	25032	15-Sep-82	28-Jul-82
R37-412-162	-12.2	-5.2	25154	6-Sep-82	17-Jul-82
R37-412-163	-12.1	-4.1	25251	29-Aug-82	7-Jul-82
R37-412-164	-11.2	-4.1	25364	14-Aug-82	28-Jun-82

Table B.2
Stable carbon and nitrogen isotope profile data from tail hair with tuned and untuned dates

Hair ID	$\delta^{13}C$ (‰, VPDB)	$\delta^{15}N$ (‰, AIR)	dist. from prox end (mm)	untuned date	tuned date
R37-060927	-20.5	12.4	2.5	31-Aug-06	16-Sep-06
R37-060927	-20.6	12.3	7.5	24-Aug-06	9-Sep-06
R37-060927	-21.9	12.3	12.5	16-Aug-06	1-Sep-06
R37-060927	-21.2	12.3	17.5	7-Aug-06	23-Aug-06
R37-060927	-21.7	12.1	22.5	30-Jul-06	15-Aug-06
R37-060927	-21.8	12.7	27.5	22-Jul-06	7-Aug-06
R37-060927	-21.5	13.0	32.5	13-Jul-06	29-Jul-06
R37-060927	-20.5	13.1	37.5	5-Jul-06	21-Jul-06
R37-060927	-20.4	12.9	42.5	26-Jun-06	12-Jul-06
R37-060927	-20.6	12.3	47.5	18-Jun-06	4-Jul-06
R37-060927	-19.8	11.8	52.5	10-Jun-06	26-Jun-06
R37-060927	-20.3	11.5	57.5	5-Jun-06	21-Jun-06
R37-060927	-21.1	9.9	62.5	30-May-06	15-Jun-06
R37-060927	-19.2	10.6	67.5	17-May-06	2-Jun-06
R37-060927	-18.5	11.2	72.5	4-May-06	20-May-06
R37-060927	-17.9	11.1	77.5	22-Apr-06	8-May-06
R37-060927	-18.1	11.3	82.5	12-Apr-06	28-Apr-06
R37-060927	-20.6	9.9	87.5	3-Apr-06	19-Apr-06
R37-060927	-22.3	8.5	92.5	25-Mar-06	10-Apr-06
R37-060927	-22.4	9.0	97.5	16-Mar-06	1-Apr-06
R37-060927	-22.6	8.7	102.5	8-Mar-06	24-Mar-06
R37-060927	-22.6	8.4	107.5	27-Feb-06	15-Mar-06
R37-060927	-22.5	8.5	112.5	18-Feb-06	6-Mar-06
R37-060927	-22.5	8.5	117.5	9-Feb-06	25-Feb-06
R37-060927	-22.8	8.4	122.5	1-Feb-06	17-Feb-06
R37-060927	-22.5	8.4	127.5	23-Jan-06	8-Feb-06
R37-060927	-22.4	8.4	132.5	14-Jan-06	30-Jan-06
R37-060927	-22.4	8.4	137.5	5-Jan-06	21-Jan-06
R37-060927	-22.5	8.1	142.5	28-Dec-05	13-Jan-06
R37-060927	-22.1	8.7	147.5	19-Dec-05	4-Jan-06
R37-060927	-21.5	8.9	152.5	10-Dec-05	26-Dec-05
R37-060927	-21.8	9.8	157.5	1-Dec-05	17-Dec-05
R37-060927	-22.2	9.6	162.5	23-Nov-05	9-Dec-05
R37-060927	-21.9	9.8	167.5	14-Nov-05	30-Nov-05
R37-060927	-22.5	10.3	172.5	5-Nov-05	21-Nov-05
R37-060927	-22.1	9.9	177.5	27-Oct-05	12-Nov-05
R37-060927	-22.2	10.0	182.5	19-Oct-05	4-Nov-05

Table B.2 Continued

Hair ID	$\delta^{13}C$ (‰, VPDB)	$\delta^{15}N$ (‰, AIR)	dist. from prox end (mm)	untuned date	tuned date
R37-060927	-22.1	11.0	187.5	10-Oct-05	26-Oct-05
R37-060927	-22.1	11.5	192.5	1-Oct-05	17-Oct-05
R37-060927	-22.1	12.1	197.5	22-Sep-05	8-Oct-05
R37-060927	-21.9	12.4	202.5	14-Sep-05	30-Sep-05
R37-060927	-21.7	11.8	207.5	5-Sep-05	21-Sep-05
R37-060927	-21.5	12.0	212.5	27-Aug-05	12-Sep-05
R37-060927	-21.7	12.6	217.5	18-Aug-05	3-Sep-05
R37-060927	-21.9	12.2	222.5	10-Aug-05	26-Aug-05
R37-060927	-21.4	12.3	227.5	2-Aug-05	18-Aug-05
R37-060927	-21.2	12.1	232.5	24-Jul-05	9-Aug-05
R37-060927	-20.7	12.0	242.5	8-Jul-05	24-Jul-05
R37-060927	-20.7	12.0	247.5	30-Jun-05	16-Jul-05
R37-060927	-21.1	11.7	252.5	22-Jun-05	8-Jul-05
R37-060927	-20.8	12.0	257.5	14-Jun-05	30-Jun-05
R37-060927	-21.2	11.8	262.5	5-Jun-05	21-Jun-05
R37-060927	-21.2	11.6	267.5	28-May-05	13-Jun-05
R37-060927	-21.2	11.9	272.5	20-May-05	5-Jun-05
R37-060927	-20.9	11.5	277.5	12-May-05	28-May-05
R37-060927	-21.4	11.2	282.5	4-May-05	20-May-05
R37-060927	-22.9	10.5	287.5	26-Apr-05	12-May-05
R37-060617	-21.0	11.1	2.5	12-Jun-06	—
R37-060617	-21.4	9.9	7.5	4-Jun-06	—
R37-060617	-19.9	11.2	12.5	27-May-06	—
R37-060617	-19.0	10.8	17.5	18-May-06	—
R37-060617	-19.0	10.6	22.5	10-May-06	—
R37-060617	-18.2	11.2	27.5	2-May-06	—
R37-060617	-18.2	11.2	32.5	23-Apr-06	—
R37-060617	-18.2	11.1	37.5	15-Apr-06	—
R37-060617	-22.8	8.4	42.5	7-Apr-06	—
R37-060617	-22.5	8.5	47.5	29-Mar-06	—
R37-060617	-22.6	9.0	52.5	21-Mar-06	—
R37-060617	-22.7	8.6	57.5	13-Mar-06	—
R37-060617	-22.7	8.4	62.5	4-Mar-06	—
R37-060617	-22.6	8.5	67.5	24-Feb-06	—
R37-060617	-22.5	8.6	72.5	16-Feb-06	—
R37-060617	-22.7	8.4	77.5	7-Feb-06	—
R37-060617	-22.6	8.4	82.5	30-Jan-06	—
R37-060617	-22.6	8.3	87.5	22-Jan-06	—

Table B.2 Continued

Hair ID	$\delta^{13}C$ (‰, VPDB)	$\delta^{15}N$ (‰, AIR)	dist. from prox end (mm)	untuned date	tuned date
R37-060617	-21.9	9.0	92.5	13-Jan-06	—
R37-060617	-22.6	8.4	97.5	5-Jan-06	—
R37-060617	-22.4	8.2	102.5	28-Dec-05	—
R37-060617	-22.7	8.2	107.5	19-Dec-05	—
R37-060617	-22.0	9.5	112.5	11-Dec-05	—
R37-060617	-21.7	8.6	117.5	3-Dec-05	—
R37-060617	-22.3	9.9	122.5	24-Nov-05	—
R37-060617	-22.3	9.4	127.5	16-Nov-05	—
R37-060617	-22.0	10.0	132.5	8-Nov-05	—
R37-060617	-22.5	10.0	137.5	30-Oct-05	—
R37-060617	-22.4	10.0	142.5	22-Oct-05	—
R37-060617	-22.1	10.5	147.5	14-Oct-05	—
R37-060617	-21.7	11.3	152.5	5-Oct-05	—
R37-060617	-22.1	11.9	157.5	27-Sep-05	—
R37-060617	-21.8	12.5	162.5	19-Sep-05	—
R37-060617	-21.6	11.7	167.5	10-Sep-05	—
R37-060617	-21.9	11.9	172.5	2-Sep-05	—
R37-060617	-21.6	11.6	177.5	25-Aug-05	—
R37-060617	-21.5	12.0	182.5	16-Aug-05	—
R37-060617	-21.1	12.1	187.5	8-Aug-05	—
R37-060617	-20.7	12.2	192.5	31-Jul-05	—
R37-060617	-20.8	12.1	197.5	22-Jul-05	—
R37-060617	-20.5	12.1	202.5	14-Jul-05	—
R37-060617	-20.5	11.9	207.5	6-Jul-05	—
R37-060617	-20.5	11.9	212.5	27-Jun-05	—
R37-060617	-20.9	11.9	217.5	19-Jun-05	—
R37-060617	-20.8	11.6	222.5	11-Jun-05	—
R37-060617	-20.3	11.4	227.5	2-Jun-05	—
R37-060617	-22.6	10.5	232.5	25-May-05	—
R37-060617	-22.3	10.8	237.5	17-May-05	—
R37-060617	-21.2	11.6	242.5	8-May-05	—
R37-060617	-21.5	10.9	247.5	30-Apr-05	—
R37-060617	-22.4	10.8	252.5	22-Apr-05	—
R37-060617	-22.1	10.7	257.5	13-Apr-05	6-May-05
R37-060617	-20.8	10.1	262.5	5-Apr-05	28-Apr-05
R37-060617	-20.9	10.5	267.5	28-Mar-05	21-Apr-05
R37-060617	-20.8	11.1	272.5	19-Mar-05	13-Apr-05
R37-060617	-21.6	10.7	277.5	11-Mar-05	6-Apr-05
R37-060617	-21.3	10.9	282.5	3-Mar-05	29-Mar-05

Table B.2 Continued

Hair ID	$\delta^{13}C$ (‰, VPDB)	$\delta^{15}N$ (‰, AIR)	dist. from prox end (mm)	untuned date	tuned date
R37-060617	-21.1	11.7	287.5	22-Feb-05	22-Mar-05
R37-060617	-21.1	11.5	292.5	14-Feb-05	14-Mar-05
R37-060617	-21.6	11.9	297.5	6-Feb-05	7-Mar-05
R37-060617	-21.7	10.3	302.5	28-Jan-05	27-Feb-05
R37-060617	-21.6	11.2	307.5	20-Jan-05	20-Feb-05
R37-060617	-21.2	11.9	312.5	12-Jan-05	12-Feb-05
R37-060617	-21.4	10.9	317.5	3-Jan-05	5-Feb-05
R37-021101	-21.9	12.1	2.5	27-Oct-02	22-Nov-02
R37-021101	-22.3	12.1	7.5	19-Oct-02	13-Nov-02
R37-021101	-21.7	12.3	12.5	10-Oct-02	4-Nov-02
R37-021101	-22.1	12.4	17.5	2-Oct-02	26-Oct-02
R37-021101	-21.4	12.9	22.5	23-Sep-02	17-Oct-02
R37-021101	-22.3	13.4	27.5	15-Sep-02	8-Oct-02
R37-021101	-21.6	14.2	32.5	6-Sep-02	29-Sep-02
R37-021101	-21.4	12.9	37.5	29-Aug-02	20-Sep-02
R37-021101	-21.2	12.9	42.5	20-Aug-02	11-Sep-02
R37-021101	-21.5	12.6	47.5	12-Aug-02	2-Sep-02
R37-021101	-21.6	12.6	52.5	3-Aug-02	24-Aug-02
R37-021101	-21.7	12.5	57.5	26-Jul-02	15-Aug-02
R37-021101	-23.0	12.2	62.5	17-Jul-02	6-Aug-02
R37-021101	-21.7	13.3	67.5	9-Jul-02	25-Jul-02
R37-021101	-20.8	12.5	72.5	30-Jun-02	13-Jul-02
R37-021101	-20.8	12.0	77.5	22-Jun-02	1-Jul-02
R37-021101	-19.4	12.3	82.5	13-Jun-02	18-Jun-02
R37-021101	-18.9	12.4	87.5	5-Jun-02	7-Jun-02
R37-021101	-19.7	12.8	92.5	27-May-02	28-May-02
R37-021101	-19.2	12.7	97.5	19-May-02	18-May-02
R37-021101	-21.3	11.4	102.5	10-May-02	3-May-02
R37-021101	-21.9	11.3	107.5	2-May-02	19-Apr-02
R37-021101	-21.1	11.2	112.5	23-Apr-02	4-Apr-02
R37-021101	-21.6	10.6	117.5	15-Apr-02	25-Mar-02
R37-021101	-22.1	10.5	122.5	6-Apr-02	14-Mar-02
R37-021101	-22.3	10.5	127.5	29-Mar-02	4-Mar-02
R37-021101	-22.3	11.1	132.5	20-Mar-02	21-Feb-02
R37-021101	-22.5	10.8	137.5	12-Mar-02	11-Feb-02
R37-021101	-21.8	11.5	142.5	3-Mar-02	31-Jan-02
R37-021101	-21.9	11.4	147.5	23-Feb-02	27-Jan-02
R37-021101	-21.5	11.5	152.5	14-Feb-02	22-Jan-02

Table B.2 Continued

Hair ID	$\delta^{13}C$ (‰, VPDB)	$\delta^{15}N$ (‰, AIR)	dist. from prox end (mm)	untuned date	tuned date
R37-021101	-21.8	11.2	157.5	6-Feb-02	17-Jan-02
R37-021101	-22.4	10.8	162.5	29-Jan-02	13-Jan-02
R37-021101	-22.5	10.8	167.5	20-Jan-02	8-Jan-02
R37-021101	-22.8	10.6	172.5	12-Jan-02	—
R37-021101	-22.4	11.2	177.5	3-Jan-02	—
R37-021101	-21.9	10.9	182.5	26-Dec-01	—
R37-021101	-22.4	11.2	187.5	17-Dec-01	—
R37-021101	-21.4	11.2	192.5	9-Dec-01	—
R37-021101	-19.9	11.4	197.5	30-Nov-01	—
R37-021101	-21.7	11.3	202.5	22-Nov-01	—
R37-021101	-22.4	10.6	207.5	13-Nov-01	—
R37-021101	-22.1	10.1	212.5	5-Nov-01	—
R37-020204	-22.5	10.4	2.5	20-Dec-01	—
R37-020204	-22.1	10.5	7.5	16-Dec-01	—
R37-020204	-22.9	10.4	12.5	11-Dec-01	5-Jan-02
R37-020204	-22.4	10.2	17.5	7-Dec-01	1-Jan-02
R37-020204	-22.0	10.9	22.5	30-Nov-01	27-Dec-01
R37-020204	-21.4	11.4	27.5	23-Nov-01	23-Dec-01
R37-020204	-21.9	11.1	32.5	16-Nov-01	16-Dec-01
R37-020204	-20.4	11.2	37.5	6-Nov-01	9-Dec-01
R37-020204	-19.9	11.5	42.5	26-Oct-01	2-Dec-01
R37-020204	-22.2	11.0	47.5	16-Oct-01	22-Nov-01
R37-020204	-22.3	9.8	52.5	5-Oct-01	11-Nov-01
R37-020204	-22.5	10.0	57.5	24-Sep-01	1-Nov-01
R37-020204	-22.1	10.9	62.5	13-Sep-01	21-Oct-01
R37-020204	-21.6	11.7	67.5	2-Sep-01	10-Oct-01
R37-020204	-21.7	11.6	72.5	22-Aug-01	29-Sep-01
R37-020204	-22.7	11.0	77.5	11-Aug-01	18-Sep-01
R37-020204	-22.6	10.7	82.5	30-Jul-01	7-Sep-01
R37-020204	-22.8	11.0	87.5	19-Jul-01	27-Aug-01
R37-020204	-22.8	11.2	92.5	8-Jul-01	15-Aug-01
R37-020204	-22.2	10.9	97.5	29-Jun-01	4-Aug-01
R37-020204	-21.7	10.8	102.5	20-Jun-01	24-Jul-01
R37-020204	-21.7	11.0	107.5	12-Jun-01	15-Jul-01
R37-020204	-21.7	10.9	112.5	3-Jun-01	6-Jul-01
R37-020204	-21.8	10.9	117.5	25-May-01	28-Jun-01
R37-020204	-22.0	11.0	122.5	12-May-01	19-Jun-01
R37-020204	-21.9	11.2	127.5	5-May-01	10-Jun-01

Table B.2 Continued

Hair ID	$\delta^{13}C$ (‰, VPDB)	$\delta^{15}N$ (‰, AIR)	dist. from prox end (mm)	untuned date	tuned date
R37-020204	-21.5	11.3	135.0	30-Apr-01	28-May-01
R37-020204	-21.6	11.4	142.5	25-Apr-01	21-May-01
R37-020204	-21.8	11.2	147.5	21-Apr-01	16-May-01
R37-020204	-21.4	11.7	152.5	14-Apr-01	11-May-01
R37-020204	-20.7	11.2	157.5	7-Apr-01	7-May-01
R37-020204	-21.4	10.6	162.5	1-Apr-01	30-Apr-01
R37-020204	-22.0	11.3	167.5	25-Mar-01	23-Apr-01
R37-020204	-21.7	10.7	172.5	18-Mar-01	17-Apr-01
R37-020204	-22.1	10.4	177.5	12-Mar-01	10-Apr-01
R37-020204	-21.8	10.6	182.5	5-Mar-01	3-Apr-01
R37-020204	-21.8	10.5	187.5	2-Mar-01	28-Mar-01
R37-020204	-21.7	10.5	192.5	23-Feb-01	21-Mar-01
R37-020204	-21.2	11.6	195.0	16-Feb-01	18-Mar-01
R37-020204	-21.2	11.9	200.0	10-Feb-01	11-Mar-01
R37-020204	-20.7	10.4	205.0	3-Feb-01	4-Mar-01
R37-020204	-20.7	10.5	210.0	27-Jan-01	26-Feb-01
R37-020204	-20.6	11.5	215.0	21-Jan-01	19-Feb-01
R37-020204	-20.7	11.5	220.0	14-Jan-01	12-Feb-01
R37-020204	-19.4	11.8	225.0	8-Jan-01	6-Feb-01
R37-020204	-19.1	11.6	230.0	2-Jan-01	30-Jan-01
R37-020204	-19.8	12.1	235.0	28-Dec-00	24-Jan-01
R37-020204	-19.2	12.0	240.0	22-Dec-00	18-Jan-01
R37-020204	-21.3	10.6	245.0	16-Dec-00	13-Jan-01
R37-020204	-21.3	10.3	250.0	10-Dec-00	7-Jan-01
R37-020204	-21.1	10.3	255.0	5-Dec-00	1-Jan-01
R37-020204	-20.5	10.7	260.0	29-Nov-00	26-Dec-00
R37-020204	-21.1	10.1	265.0	25-Nov-00	21-Dec-00
R37-020204	-19.8	10.1	270.0	17-Nov-00	15-Dec-00
R37-010125	-19.3	11.9	5.0	17-Jan-01	—
R37-010125	-21.2	10.7	10.0	10-Jan-01	—
R37-010125	-21.4	10.2	15.0	3-Jan-01	—
R37-010125	-20.9	10.3	20.0	27-Dec-00	—
R37-010125	-20.4	10.5	25.0	19-Dec-00	—
R37-010125	-21.3	10.2	30.0	12-Dec-00	—
R37-010125	-20.7	10.1	35.0	5-Dec-00	—
R37-010125	-19.9	10.3	40.0	28-Nov-00	11-Dec-00
R37-010125	-20.7	10.8	45.0	20-Nov-00	3-Dec-00
R37-010125	-22.2	10.0	50.0	13-Nov-00	25-Nov-00

Table B.2 Continued

Hair ID	$\delta^{13}C$ (‰, VPDB)	$\delta^{15}N$ (‰, AIR)	dist. from prox end (mm)	untuned date	tuned date
R37-010125	-21.6	10.0	55.0	6-Nov-00	17-Nov-00
R37-010125	-21.8	9.6	60.0	30-Oct-00	9-Nov-00
R37-010125	-21.0	10.5	65.0	22-Oct-00	1-Nov-00
R37-010125	-21.1	10.1	70.0	15-Oct-00	24-Oct-00
R37-010125	-21.0	10.6	75.0	8-Oct-00	16-Oct-00
R37-010125	-20.9	10.6	80.0	1-Oct-00	7-Oct-00
R37-010125	-21.2	10.5	85.0	23-Sep-00	28-Sep-00
R37-010125	-21.4	10.4	90.0	16-Sep-00	19-Sep-00
R37-010125	-21.2	10.8	95.0	9-Sep-00	10-Sep-00
R37-010125	-21.6	10.8	100.0	2-Sep-00	1-Sep-00
R37-010125	-21.6	10.0	105.0	25-Aug-00	23-Aug-00
R37-010125	-21.4	9.9	110.0	18-Aug-00	14-Aug-00
R37-010125	-21.9	10.6	115.0	11-Aug-00	5-Aug-00
R37-010125	-22.0	10.7	120.0	4-Aug-00	28-Jul-00
R37-010125	-21.8	10.4	125.0	27-Jul-00	19-Jul-00
R37-010125	-21.5	10.3	130.0	20-Jul-00	10-Jul-00
R37-010125	-21.8	10.5	135.0	13-Jul-00	1-Jul-00
R37-010125	-21.5	10.8	140.0	6-Jul-00	22-Jun-00
R37-010125	-21.9	10.6	145.0	28-Jun-00	13-Jun-00
R37-010125	-21.6	10.6	150.0	21-Jun-00	4-Jun-00
R37-010125	-22.1	10.8	155.0	14-Jun-00	26-May-00
R37-010125	-22.0	10.9	160.0	7-Jun-00	17-May-00
R37-010125	-22.0	11.4	165.0	30-May-00	8-May-00
R37-010125	-21.0	11.0	170.0	23-May-00	30-Apr-00
R37-010125	-20.8	10.9	175.0	16-May-00	21-Apr-00
R37-010125	-22.0	10.3	180.0	9-May-00	12-Apr-00
R37-010125	-21.8	10.1	185.0	1-May-00	3-Apr-00
R37-010125	-21.2	10.7	190.0	24-Apr-00	25-Mar-00
R37-010125	-21.2	10.6	195.0	17-Apr-00	16-Mar-00
R37-010125	-21.1	10.2	200.0	10-Apr-00	7-Mar-00
R37-010125	-21.7	10.2	205.0	2-Apr-00	27-Feb-00
R37-010125	-21.9	11.4	210.0	26-Mar-00	18-Feb-00
R37-010125	-21.8	10.5	215.0	19-Mar-00	9-Feb-00
R37-010125	-21.5	10.5	220.0	12-Mar-00	1-Feb-00
R37-010125	-21.6	10.8	225.0	4-Mar-00	23-Jan-00
R37-010125	-21.9	10.8	230.0	26-Feb-00	14-Jan-00
R37-010125	-22.3	10.3	235.0	19-Feb-00	5-Jan-00
R37-010125	-22.1	10.0	240.0	12-Feb-00	27-Dec-99
R37-010125	-21.8	10.1	245.0	4-Feb-00	18-Dec-99

Table B.2 Continued

Hair ID	$\delta^{13}C$ (‰, VPDB)	$\delta^{15}N$ (‰, AIR)	dist. from prox end (mm)	untuned date	tuned date
R37-010125	-21.1	10.5	250.0	28-Jan-00	9-Dec-99
R37-010125	-20.0	10.9	255.0	21-Jan-00	30-Nov-99
R37-010125	-20.1	10.8	260.0	14-Jan-00	21-Nov-99
R37-010125	-21.0	10.7	265.0	6-Jan-00	12-Nov-99
R37-010125	-21.4	10.9	270.0	30-Dec-99	4-Nov-99

APPENDIX C

DATA TABLES ASSOCIATED

WITH CHAPTER 5

Table C.1
Measurements of angle (θ) between tusk axis and growth increments and calculated radial growth rate in μm/week from ivory slab M640

Slab	θ (°)	um/day	um/week
M640	7.33	18.0	126.0
M640	8.02	19.7	138.0
M640	7.28	17.9	125.1
M640	7.94	19.5	136.6
M640	8.24	20.3	141.8
M640	7.63	18.7	131.2
average	**7.74**	**19.0**	**133.1**
stdev	**0.39**	**3.0**	**20.7**

Growth rate (um/day) =(TAN(RADIANS(angle))*axial growth rate)/365.25*1000

14C growth rate data	
51.1	axial mm/yr
7.5	2σ

Table C.2

Angle of appostion (α) measurements from molar thin sections

Thin Section	α (°)	dist. from cervix (mm)	Thin Section	α (°)	dist. from cervix (mm)
Misha_Rm3.5	2.87	85.7	IMNH-40368	5.23	100.8
Misha_Rm3.5	3.10	52.7	IMNH-40368	5.93	98.8
Misha_Rm3.5	3.37	32.7	IMNH-40368	5.38	101.6
Misha_Rm3.5	4.00	3.6	IMNH-40368	4.92	93.2
			IMNH-40368	6.15	92.1
TE-95_Rm3.7	3.15	104.3	IMNH-40368	6.35	89.5
TE-95_Rm3.7	2.80	97.9	IMNH-40368	5.21	80.0
TE-95_Rm3.7	3.44	94.1	IMNH-40368	5.99	78.4
TE-95_Rm3.7	3.39	91.6	IMNH-40368	4.16	73.9
TE-95_Rm3.7	3.16	61.8	IMNH-40368	5.57	72.6
TE-95_Rm3.7	3.21	61.8	IMNH-40368	5.80	70.2
TE-95_Rm3.7	3.39	61.0	IMNH-40368	6.27	54.9
TE-95_Rm3.7	3.37	58.9	IMNH-40368	6.47	51.2
TE-95_Rm3.7	3.31	57.6	IMNH-40368	5.83	43.4
TE-95_Rm3.7	3.39	52.5	IMNH-40368	6.11	42.2
TE-95_Rm3.7	3.14	46.0	IMNH-40368	6.43	33.2
TE-95_Rm3.7	3.37	39.1	IMNH-40368	7.17	23.3
TE-95_Rm3.7	3.33	37.5	IMNH-40368	7.61	18.2
TE-95_Rm3.7	3.37	34.0	IMNH-40368	8.20	11.4
TE-95_Rm3.7	4.79	1.3	IMNH-40368	9.48	5.3
			IMNH-40368	10.21	12.1
			IMNH-40368	11.82	2.0
			IMNH-40368	9.36	1.6
			IMNH-40368	10.93	2.0

Table C.3
Stable carbon and oxygen isotope profile data from M640 tusk dentin

Sample ID	$\delta^{13}C$ (‰, VPDB)	$\delta^{18}O$ (‰, VPDB)	dist. from base (μm)	date
M640-001	-13.0	-12.6	8834	16-Jan-07
M640-003	-13.3	-12.0	9213	21-Dec-06
M640-005	-13.9	-12.0	9627	23-Nov-06
M640-007	-14.0	-12.0	10026	27-Oct-06
M640-009	-13.8	-11.5	10414	30-Sep-06
M640-011	-13.9	-12.3	10812	3-Sep-06
M640-013	-14.5	-13.2	11201	7-Aug-06
M640-015	-14.5	-13.1	11548	15-Jul-06
M640-017	-14.7	-12.9	11941	18-Jun-06
M640-019	-14.8	-14.1	12359	21-May-06
M640-021	-14.3	-13.7	12761	23-Apr-06
M640-023	-14.0	-14.0	13319	16-Mar-06
M640-025	-13.4	-13.3	13696	19-Feb-06
M640-027	-13.8	-14.1	14104	22-Jan-06
M640-029	-13.8	-14.0	14497	26-Dec-05
M640-031	-13.8	-13.7	14869	1-Dec-05
M640-032	-13.2	-13.0	14990	22-Nov-05
M640-033	-12.9	-12.9	15088	16-Nov-05
M640-034	-12.9	-13.3	15197	8-Nov-05
M640-035	-13.2	-13.2	15295	2-Nov-05
M640-036	-13.3	-13.5	15383	27-Oct-05
M640-037	-13.2	-13.5	15487	20-Oct-05
M640-038	-13.2	-13.1	15591	12-Oct-05
M640-039	-13.1	-12.7	15695	5-Oct-05
M640-040	-13.2	-12.4	15799	28-Sep-05
M640-041	-13.1	-11.7	15902	21-Sep-05
M640-042	-12.9	-11.6	15990	15-Sep-05
M640-043	-12.9	-11.2	16152	4-Sep-05
M640-044	-13.0	-11.1	16303	25-Aug-05
M640-045	-12.7	-11.4	16407	18-Aug-05
M640-046	-13.0	-12.3	16501	11-Aug-05
M640-047	-13.0	-12.5	16600	5-Aug-05
M640-048	-12.8	-12.5	16699	29-Jul-05
M640-049	-12.8	-12.4	16803	22-Jul-05
M640-050	-12.8	-12.5	16881	17-Jul-05
M640-051	-13.1	-12.7	16980	10-Jul-05
M640-052	-12.9	-13.2	17079	3-Jul-05
M640-053	-12.8	-13.3	17188	26-Jun-05

Table C.3 Continued

Sample ID	$\delta^{13}C$ (‰, VPDB)	$\delta^{18}O$ (‰, VPDB)	dist. from base (μm)	date
M640-054	-12.7	-13.4	17261	21-Jun-05
M640-055	-12.4	-13.7	17366	14-Jun-05
M640-056	-12.7	-14.4	17470	6-Jun-05
M640-057	-12.3	-13.5	17559	31-May-05
M640-058	-12.3	-13.9	17663	24-May-05
M640-059	-12.7	-13.7	17752	18-May-05
M640-060	-12.6	-13.5	17867	10-May-05
M640-061	-11.2	-13.0	17945	5-May-05
M640-062	-8.9	-11.1	18055	28-Apr-05
M640-063	-6.0	-9.1	18139	22-Apr-05
M640-064	-5.0	-8.7	18259	14-Apr-05
M640-065	-5.6	-9.3	18348	8-Apr-05
M640-066	-4.9	-9.1	18442	1-Apr-05
M640-067	-5.7	-9.9	18536	26-Mar-05
M640-068	-5.8	-9.6	18656	18-Mar-05
M640-069	-6.5	-9.7	18755	11-Mar-05
M640-070	-7.2	-9.8	18844	5-Mar-05
M640-072	-7.9	-9.3	19047	19-Feb-05
M640-073	-8.3	-9.1	19146	12-Feb-05
M640-074	-8.5	-9.4	19229	7-Feb-05
M640-075	-8.4	-9.8	19323	31-Jan-05
M640-076	-8.2	-9.6	19422	24-Jan-05
M640-077	-8.0	-9.8	19490	20-Jan-05
M640-079	-8.6	-9.9	19611	12-Jan-05
M640-080	-8.0	-9.8	19700	6-Jan-05
M640-081	-7.5	-9.6	19799	30-Dec-04
M640-082	-7.6	-9.8	19893	23-Dec-04
M640-083	-8.3	-10.4	19987	17-Dec-04
M640-084	-8.4	-10.8	20065	12-Dec-04
M640-085	-8.4	-10.0	20190	3-Dec-04
M640-086	-7.7	-10.2	20295	26-Nov-04
M640-088	-7.7	-10.3	20494	12-Nov-04
M640-089	-8.0	-10.4	20588	6-Nov-04
M640-090	-8.2	-10.4	20698	30-Oct-04
M640-091	-5.9	-9.9	20792	23-Oct-04
M640-092	-5.8	-9.3	20880	17-Oct-04
M640-093	-6.0	-9.5	20982	10-Oct-04
M640-094	-7.9	-9.5	21092	3-Oct-04
M640-096	-12.5	-8.7	21264	21-Sep-04

Table C.3 Continued

Sample ID	$\delta^{13}C$ (‰, VPDB)	$\delta^{18}O$ (‰, VPDB)	dist. from base (μm)	date
M640-098	-9.3	-8.6	21462	7-Sep-04
M640-100	-12.3	-9.1	21660	25-Aug-04
M640-102	-12.7	-9.1	21854	12-Aug-04
M640-105	-12.2	-9.2	22172	21-Jul-04
M640-106	-12.2	-8.5	22276	14-Jul-04
M640-108	-12.2	-8.8	22479	30-Jun-04
M640-110	-12.3	-9.2	22687	16-Jun-04
M640-115	-12.1	-8.2	23172	14-May-04
M640-120	-7.4	-7.7	23657	11-Apr-04
M640-125	-7.1	-8.6	24137	9-Mar-04
M640-130	-6.0	-10.0	24638	4-Feb-04
M640-135	-6.0	-10.7	25117	3-Jan-04
M640-140	-5.1	-9.2	25474	9-Dec-03
M640-145	-4.1	-9.4	25844	14-Nov-03
M640-150	-3.8	-7.9	26397	7-Oct-03
M640-155	-3.5	-7.7	26883	4-Sep-03
M640-160	-4.1	-7.6	27331	5-Aug-03
M640-165	-5.9	-7.8	28238	4-Jun-03
M640-170	-9.1	-8.0	29170	1-Apr-03
M640-175	-5.0	-9.0	30134	26-Jan-03

Table C.4
Micromill stable isotope profile data from Misha Rm3.5b enamel

Sample ID	$\delta^{13}C$ (‰, VPDB)	$\delta^{18}O$ (‰, VPDB)	dist. from EDJ (μm)
Misha Rm6.5-001	-13.0	-13.6	2200
Misha Rm6.5-002	-12.1	-13.6	2100
Misha Rm6.5-003	-12.5	-14.0	2000
Misha Rm6.5-004	-12.6	-14.6	1900
Misha Rm6.5-005	-12.7	-14.5	1800
Misha Rm6.5-006	-12.7	-14.8	1700
Misha Rm6.5-007	-12.7	-14.5	1600
Misha Rm6.5-008	-12.4	-14.0	1500
Misha Rm6.5-009	-12.4	-14.6	1400
Misha Rm6.5-010	-12.9	-14.8	1350
Misha Rm6.5-011	-12.9	-14.3	1300
Misha Rm6.5-012	-12.6	-13.8	1250
Misha Rm6.5-013	-12.4	-13.7	1200
Misha Rm6.5-014	-12.3	-13.9	1150
Misha Rm6.5-015	-12.4	-14.2	1100
Misha Rm6.5-016	-12.3	-14.4	1050
Misha Rm6.5-017	-12.3	-14.6	1000
Misha Rm6.5-018	-12.3	-14.3	950
Misha Rm6.5-019	-11.8	-13.8	900
Misha Rm6.5-020.5	-11.3	-14.0	800
Misha Rm6.5-022	-11.0	-13.9	750
Misha Rm6.5-023	-9.2	-12.5	700
Misha Rm6.5-024	-9.1	-12.9	650
Misha Rm6.5-025	-9.9	-13.2	600
Misha Rm6.5-026	-9.1	-13.6	550
Misha Rm6.5-027	-8.6	-13.2	500
Misha Rm6.5-028	-8.9	-13.5	450
Misha Rm6.5-029	-8.0	-12.6	400
Misha Rm6.5-030	-7.9	-12.4	350
Misha Rm6.5-031	-7.7	-12.0	300
Misha Rm6.5-033	-7.9	-12.3	250
Misha Rm6.5-034	-8.0	-12.2	200
Misha Rm6.5-035	-8.5	-12.6	150
Misha Rm6.5-036	-8.6	-12.5	100
Misha Rm6.5-037	-8.8	-11.6	50
Misha Rm6.5-038	-9.6	-11.7	0

Table C.5
LA-GC-IRMS stable isotope profile data from Misha Rm3.5b enamel

Sample ID	Scan #	(‰, VPDB) $\delta^{13}C^{a}$	(‰, VPDB) $\delta^{18}O^{b}$	dist. from EDJ (μm)	comment
Profile 1: 54mm					
Misha_uCT-B_29	1	-10.2	-10.6	226	
Misha_uCT-B_30	2	-7.4	-10.8	374	
Misha_uCT-B_31	3	-6.4	-10.7	589	
Misha_uCT-B_32	4	-6.2	-11.2	705	
Misha_uCT-B_33	5	-12.1	-14.3	913	
Misha_uCT-B_34	6	-12.3	-13.2	1100	
Misha_uCT-B_35	7	-12.2	-14.3	1268	
Misha_uCT-B_36	8	-12.5	-14.4	1447	
Misha_uCT-B_37	9	-12.9	-14.3	1663	
Misha_uCT-B_38	10	-13.5	-14.6	1842	
Misha_uCT-B_39	11	-14.1	-14.4	2095	3 minor char
Misha_uCT-B_40	12	-15.3	-15.4	2368	5 char
Misha_uCT-B_41	13	-18.1	-14.3	2653	5 char
Profile 2: 71mm					
Misha_uCT-B_14	1	-3.1	-9.3	163	
Misha_uCT-B_15	2	-3.2	-10.0	429	
Misha_uCT-B_16	3	-5.1	-10.1	576	
Misha_uCT-B_17	4	-9.5	-9.2	729	
Misha_uCT-B_18	5	-11.3	-10.1	945	
Misha_uCT-B_19	6	-10.4	-10.8	1066	
Misha_uCT-B_20	7	-7.7	-12.4	1239	
Misha_uCT-B_21	8	-7.8	-12.1	1368	
Misha_uCT-B_22	9	-7.2	-11.3	1518	
Misha_uCT-B_23	10	-6.5	-10.8	1734	
Misha_uCT-B_24	11	-11.5	-14.1	1903	
Misha_uCT-B_25	12	-12.6	-14.0	2058	
Misha_uCT-B_26	13	-13.8	-13.8	2266	
Misha_uCT-B_28	14	-17.1	-16.0	2800	char

Table C.5 Continued

Sample ID	Scan #	(‰, VPDB) $\delta^{13}C^{a}$	(‰, VPDB) $\delta^{18}O^{b}$	dist. from EDJ (μm)	comment
Profile 3: 80mm					
Misha_uCT-B_13	1	-7.2	-9.5	216	
Misha_uCT-B_1	2	-7.5	-9.9	332	
Misha_uCT-B_2	3	-10.2	-9.2	592	
Misha_uCT-B_3	4	-9.7	-9.4	847	
Misha_uCT-B_4	5	-6.2	-10.6	1055	
Misha_uCT-B_5	6	-14.0	-10.3	1368	
Misha_uCT-B_6	7	-16.5	-10.4	1529	
Misha_uCT-B_7	8	-16.7	-10.8	1726	
Misha_uCT-B_8	9	-8.2	-12.3	1879	
Misha_uCT-B_9	10	-8.7	-12.4	2156	
Misha_uCT-B_10	11	-9.7	-12.3	2300	1 minor char
Misha_uCT-B_11	12	-12.9	-12.6	2568	3 char
Misha_uCT-B_12	13	-19.3	-11.7	2789	5 char

a) $^{13}\varepsilon^{*}_{\text{laser-acid}} = -0.9$; b) $^{18}\varepsilon^{*}_{\text{laser-acid}} = -7.4$

Table C.6
Conventionally sampled stable isotope profile data from Misha_Rm3.5 enamel

Sample ID	$\delta^{13}C$ (‰, VPDB)	$\delta^{18}O$ (‰, VPDB)	dist. from cervix (mm)	sample depth (mm)
Misha Rm3.5-100	-12.1	-12.7	0.0	0.5
Misha Rm3.5-105	-12.8	-14.0	5.8	0.8
Misha Rm3.5-110	-12.3	-13.9	11.4	0.9
Misha Rm3.5-115	-12.5	-14.2	16.2	0.8
Misha Rm3.5-120	-12.3	-13.8	20.3	0.9
Misha Rm3.5-125	-12.1	-14.0	26.3	0.9
Misha Rm3.5-130	-12.6	-15.0	31.3	0.8
Misha Rm3.5-132	-12.6	-14.5	33.0	0.8
Misha Rm3.5-134	-12.5	-14.9	35.0	0.8
Misha Rm3.5-136	-12.6	-14.2	37.5	0.8
Misha Rm3.5-138	-12.7	-14.1	39.1	0.7
Misha Rm3.5-140	-12.5	-14.0	40.8	0.8
Misha Rm3.5-142	-12.7	-13.9	42.6	0.8
Misha Rm3.5-144	-12.8	-13.7	44.7	0.9
Misha Rm3.5-146	-13.2	-14.7	46.9	1.0
Misha Rm3.5-148	-12.9	-14.6	49.1	0.9
Misha Rm3.5-150	-13.0	-14.8	51.2	0.9
Misha Rm3.5-152	-13.3	-15.2	52.8	0.9
Misha Rm3.5-154	-13.1	-15.0	54.6	0.8
Misha Rm3.5-156	-13.1	-15.0	56.5	0.8
Misha Rm3.5-158	-12.9	-14.7	58.5	0.9
Misha Rm3.5-160	-12.4	-13.9	60.2	0.9
Misha Rm3.5-162	-12.5	-14.1	62.3	0.9
Misha Rm3.5-164	-12.8	-14.0	64.5	0.8
Misha Rm3.5-166	-13.0	-14.0	66.3	0.6
Misha Rm3.5-168	-12.3	-14.5	68.1	0.8
Misha Rm3.5-170	-10.0	-12.1	70.5	0.7
Misha Rm3.5-172	-9.0	-11.3	72.2	0.7
Misha Rm3.5-174	-9.6	-10.8	74.6	1.4
Misha Rm3.5-176	-10.0	-11.0	76.6	1.0
Misha Rm3.5-178	-9.9	-10.9	79.0	0.9
Misha Rm3.5-180	-10.6	-10.4	80.5	1.0
Misha Rm3.5-182	-11.4	-11.2	82.3	1.0
Misha Rm3.5-184	-10.9	-10.1	84.4	0.9
Misha Rm3.5-186	-11.0	-10.3	86.7	0.9
Misha Rm3.5-190	-10.9	-10.1	88.5	0.9
Misha Rm3.5-188	-10.2	-10.1	90.3	0.9
Misha Rm3.5-192	-11.1	-10.5	91.9	1.1

Table C.6 Continued

Sample ID	$\delta^{13}C$ (‰, VPDB)	$\delta^{18}O$ (‰, VPDB)	dist. from cervix (mm)	sample depth (mm)
Misha Rm3.5-194	-12.0	-11.1	94.0	1.0
Misha Rm3.5-196	-11.6	-10.5	96.2	1.0
Misha Rm3.5-198	-10.1	-10.1	98.1	1.0
Misha Rm3.5-200	-6.9	-9.8	100.0	1.3
R37 Rm6.8-000b	-10.4	-1.6	0.0	0.7
R37 Rm6.8-002b	-10.9	-1.6	1.5	0.7
R37 Rm6.8-004b	-10.3	-1.8	3.8	0.9
R37-Rm6.8-006	-10.3	-1.5	6.4	0.7
R37-Rm6.8-008	-10.2	-1.7	8.1	1.2
R37-Rm6.8-010	-10.5	-1.5	10.0	1.0
R37-Rm6.8-012	-10.6	-1.2	12.1	0.9
R37-Rm6.8-014	-10.7	-1.2	13.7	1.1
R37-Rm6.8-016	-10.5	-1.0	15.7	0.9
R37-Rm6.8-018	-10.5	-1.0	17.8	1.2
R37-Rm6.8-020	-10.2	-0.6	20.2	1.3
R37-Rm6.8-022	-10.2	-1.0	21.7	0.9
R37-Rm6.8-024	-10.9	-0.8	24.7	0.8
R37-Rm6.8-026	-10.8	-0.6	26.7	1.0
R37-Rm6.8-028	-10.8	-0.6	28.5	1.0
R37-Rm6.8-030	-10.9	-1.3	30.3	0.9
R37-Rm6.8-032	-11.0	-1.5	32.2	1.1
R37-Rm6.8-034	-10.8	-1.2	34.2	1.0
R37-Rm6.8-036	-11.0	-1.1	36.4	1.0
R37-Rm6.8-038	-10.9	-1.4	38.4	1.1
R37-Rm6.8-040	-10.7	-1.5	39.9	1.4
R37-Rm6.8-042	-11.1	-1.8	42.5	1.0
R37-Rm6.8-044	-10.9	-1.4	44.4	1.4
R37-Rm6.8-046	-11.0	-1.5	46.0	1.0
R37-Rm6.8-048	-10.8	-0.9	48.1	0.9
R37-Rm6.8-050	-11.1	-0.5	49.9	1.0
R37-Rm6.8-052	-11.1	-1.1	51.9	0.9
R37-Rm6.8-054	-11.3	-1.5	54.2	1.0
R37-Rm6.8-056	-11.0	-1.3	56.0	0.9
R37-Rm6.8-058	-10.6	-1.5	58.3	0.9
R37-Rm6.8-060	-11.0	-1.6	60.0	1.1
R37-Rm6.8-062	-11.0	-1.5	62.2	1.1
R37-Rm6.8-064	-10.9	-1.2	63.9	1.3
R37-Rm6.8-066	-11.0	-1.3	66.4	1.1

Table C.6 Continued

Sample ID	$\delta^{13}C$ (‰, VPDB)	$\delta^{18}O$ (‰, VPDB)	dist. from cervix (mm)	sample depth (mm)
R37-Rm6.8-068	-11.4	-1.6	68.4	1.0
R37-Rm6.8-070	-11.2	-1.3	69.9	1.1
R37 Rm6.8-072	-11.3	-1.4	72.5	1.1
R37-Rm6.8-074	-11.0	-1.3	74.4	1.1
R37-Rm6.8-076	-11.1	-1.2	76.4	0.7
LACM-06	-5.2	-2.6	6.0	1.0
LACM-08	-5.8	-1.5	8.0	1.0
LACM-10	-5.9	-1.8	10.0	1.0
LACM-13	-6.5	-1.5	13.0	1.0
LACM-15	-8.0	-1.7	15.0	1.0
LACM-16.5	-8.4	-1.8	16.5	1.0
LACM-19	-8.2	-1.8	19.0	1.0
LACM-21	-8.2	-1.6	21.0	1.0
LACM-22	-8.3	-1.6	22.0	1.0
LACM-26	-8.4	-1.8	26.0	1.0
LACM-27	-8.1	-2.0	27.0	1.0
LACM-28	-7.3	-2.1	28.0	1.0
LACM-30	-6.6	-2.5	30.0	1.0
LACM-32.5	-4.9	-1.7	32.5	1.0
LACM-35	-4.8	-1.5	35.0	1.0
LACM-36	-4.7	-1.1	36.0	1.0
LACM-38	-5.0	-1.5	38.0	1.0
LACM-41	-5.0	-1.1	41.0	1.0
LACM-43	-5.3	-1.9	43.0	1.0
LACM-45	-7.1	-1.7	45.0	1.0
LACM-48	-6.7	-1.7	48.0	1.0
LACM-50	-7.8	-1.6	50.0	1.0
IMNH-40368-10	-8.3	-13.5	10.0	2.5
IMNH-40368-12	-8.8	-13.7	12.0	2.5
IMNH-40368-14	-9.2	-14.1	14.0	2.5
IMNH-40368-16	-9.2	-13.6	16.0	2.5
IMNH-40368-18	-9.6	-13.6	18.0	2.5
IMNH-40368-20	-9.9	-13.2	20.0	2.5
IMNH-40368-22	-9.9	-13.4	22.0	2.5
IMNH-40368-24	-9.7	-13.3	24.0	2.5
IMNH-40368-26	-8.5	-13.3	26.0	2.5
IMNH-40368-28	-8.8	-13.4	28.0	2.5

Table C.6 Continued

Sample ID	$\delta^{13}C$ (‰, VPDB)	$\delta^{18}O$ (‰, VPDB)	dist. from cervix (mm)	sample depth (mm)
IMNH-40368-30	-9.7	-13.7	30.0	2.5
IMNH-40368-32	-9.7	-13.7	32.0	2.5
IMNH-40368-34	-8.9	-12.5	34.0	2.5
IMNH-40368-36	-9.4	-13.1	36.0	2.5
IMNH-40368-38	-10.0	-13.2	38.0	2.5
IMNH-40368-40	-9.9	-13.3	40.0	2.5
IMNH-40368-42	-9.9	-13.2	42.0	2.5
IMNH-40368-44	-10.0	-13.6	44.0	2.5
IMNH-40368-46	-9.9	-13.5	46.0	2.5
IMNH-40368-48	-9.9	-13.4	48.0	2.5
IMNH-40368-50	-9.9	-13.0	50.0	2.5
IMNH-40368-52	-9.9	-12.9	52.0	2.5
IMNH-40368-54	-10.0	-12.3	54.0	2.5
IMNH-40368-56	-10.0	-13.5	56.0	2.5
IMNH-40368-58	-10.0	-13.5	58.0	2.5
IMNH-40368-60	-10.0	-13.6	60.0	2.5
IMNH-40368-62	-10.0	-13.2	62.0	2.5
IMNH-40368-64	-10.2	-13.4	64.0	2.5
IMNH-40368-66	-10.2	-13.4	66.0	2.5
IMNH-40368-68	-10.2	-13.2	68.0	2.5
IMNH-40368-70	-10.1	-13.5	70.0	2.5
IMNH-40368-72	-10.2	-13.3	72.0	2.5
IMNH-40368-74	-10.1	-13.1	74.0	2.5
IMNH-40368-76	-9.9	-13.2	76.0	2.5
IMNH-40368-78	-10.4	-13.0	78.0	2.5
IMNH-40368-80	-10.2	-13.3	80.0	2.5
IMNH-40368-82	-10.3	-12.9	82.0	2.5
IMNH-40368-84	-10.2	-13.2	84.0	2.5
IMNH-40368-86	-10.2	-13.5	86.0	2.5
IMNH-40368-88	-10.4	-13.3	88.0	2.5
IMNH-40368-90	-10.1	-13.0	90.0	2.5
IMNH-40368-92	-10.3	-13.1	92.0	2.5
IMNH-40368-94	-10.2	-12.6	94.0	2.5
IMNH-40368-96	-10.2	-13.6	96.0	2.5
IMNH-40368-98	-10.3	-13.0	98.0	2.5
IMNH-40368-100	-9.8	-13.1	100.0	2.5